THÈSE

Pour obtenir le grade de

DOCTEUR DE L'UNIVERSITÉ GRENOBLE ALPES

École doctorale : I-MEP² - Ingénierie - Matériaux, Mécanique, Environnement, Energétique, Procédés, Production
Spécialité : 2MGE - Matériaux, Mécanique, Génie civil, Electrochimie
Unité de recherche : CEA LETI - Laboratoire d'électronique et de technologie de l'information

Structures ferroélectriques à base d'oxyde de hafnium-zirconium par dépôt de couches atomiques pour les mémoires émergentes

Advanced ferroelectric hafnium-zirconium oxide structures deposited by Atomic Layer Deposition for emerging memory applications

Présentée par :

Amanda MALLMANN TONELLI

Direction de thèse :

Vincent JOUSSEAUME DIRECTEUR DE RECHERCHE, CEA - Leti	Directeur de thèse
Messaoud BEDJAOUI INGENIEUR CHERCHEUR, CEA Leti Grenoble	Co-encadrant de thèse
Laurent GRENOUILLET INGENIEUR CHERCHEUR, CEA	Co-encadrant de thèse

Rapporteurs :

Nicholas BARRETT
DIRECTEUR DE RECHERCHE, CEA centre de Paris-Saclay
Damien DELERUYELLE
PROFESSEUR DES UNIVERSITES, INSA Lyon

Thèse soutenue publiquement le **9 octobre 2025**, devant le jury composé de :

Elisabeth BLANQUET, DIRECTRICE DE RECHERCHE, CNRS délégation Alpes	Présidente
Vincent JOUSSEAUME, DIRECTEUR DE RECHERCHE, CEA centre de Grenoble	Directeur de thèse
Nicholas BARRETT, DIRECTEUR DE RECHERCHE, CEA centre de Paris-Saclay	Rapporteur
Damien DELERUYELLE, PROFESSEUR DES UNIVERSITES, INSA Lyon	Rapporteur
Mickaël GROS-JEAN, INGENIEUR HDR, STMicroelectronics	Examinateur
Christophe LABBE, PROFESSEUR DES UNIVERSITES, Université de Caen Normandie	Examinateur

Invités :

Laurent Grenouillet
INGENIEUR DE RECHERCHE, CEA-Leti
Messaoud Bedjaoui
INGENIEUR DE RECHERCHE, CEA-Leti

Per aspera ad astra

Acknowledgements

First of all, I would like to express my deep gratitude to all the members of the jury for the honor they have bestowed upon me by evaluating my thesis work. I am sincerely thankful for the time and effort you have devoted to reviewing my manuscript. Your insightful comments, corrections, and suggestions will undoubtedly contribute to improving and elevating the quality of this work, for which I am truly grateful.

I would like to express my sincere gratitude to my supervisors, Messaoud and Laurent, for their guidance and support throughout this work. I am especially thankful to my PhD director, Vincent, for his trust, availability, and constant encouragement during these years. His mentorship has been invaluable, both scientifically and personally, and his enthusiasm and rigor have greatly inspired me. Through their advice and collaboration, I have not only deepened my professional knowledge but also developed important personal skills that will remain with me beyond this thesis.

This thesis would not have been possible without the contribution of many people involved in the fabrication, characterization, and electrical measurements of the devices. I am deeply thankful to Nicolas G., Zineb, Nicolas V., Julien M., Arthur, Julien P., Jean-Baptiste and Simon for their essential help and expertise, from the cleanroom processing to the material and electrical characterizations. Working alongside you has been both enriching and rewarding.

I would also like to warmly thank all my colleagues from SDEP and LDMC for their daily support, shared coffees, and countless discussions that made each day in the lab more enjoyable. Special thanks to Mathieu, Sylvain, Benjamin, Renzo, Clément, and Mohamad for your camaraderie, humor, and constant readiness to help. My deepest thanks also go to my dear friends, the filles du BCC, for their friendship, kindness, and for being there during both the challenging and joyful moments of this adventure.

Finally, I wish to express my deepest gratitude to all my personal friends and, above all, to my family and loved ones. Your unconditional support, patience, and love have been my foundation and my greatest strength throughout these years.

To all of you — colleagues, mentors, friends, and family — I extend my heartfelt thanks. This work would not have been possible without your presence, generosity, and encouragement.

Thank you from the bottom of my heart.

Résumé

Les avancées rapides de l'intelligence artificielle, de l'apprentissage automatique et de l'Internet des objets ont conduit à une demande croissante pour des technologies de mémoire plus efficaces, mettant en évidence les limites des solutions traditionnelles telles que la SRAM, la DRAM et la mémoire flash NAND. Parmi les alternatives émergentes, les mémoires ferroélectriques suscitent un intérêt croissant en raison de leur scalabilité, de leur non-volatilité et de leur compatibilité avec les procédés CMOS modernes.

Cette thèse explore le potentiel des matériaux à base de HfO_2, en particulier des couches minces de HfO_2 dopé au zirconium (HZO), en tant que candidats pour les technologies de mémoires non volatiles de nouvelle génération. Elle propose une analyse comparative entre des structures ferroélectriques monocouches (solution solide) et multicouches, en examinant l'influence de la composition, des matériaux d'électrodes, des conditions de recuit et de la réduction d'épaisseur sur leurs performances structurelles et électriques. Une attention particulière est portée aux configurations multicouches, souvent considérées comme pouvant favoriser la réponse ferroélectrique via un contrôle plus fin de l'architecture d'empilement. Cependant, les résultats obtenus dans cette étude montrent que cette amélioration n'est pas systématique et que les multicouches ne présentent pas nécessairement de meilleures performances que les structures monocouches.

Le dépôt en couches atomiques (ALD) joue un rôle central dans cette étude, grâce à sa capacité à produire des films minces avec une précision atomique en termes de composition et d'épaisseur. Cette technique permet la fabrication de systèmes complexes tels que les nanolaminés et les multicouches périodiques. Les objectifs principaux de cette recherche sont d'étudier les propriétés intrinsèques des matériaux à base de HZO tout au long des étapes de fabrication de structures Metal-Ferroelectric-Metal (MFM), et de corréler ces caractéristiques structurales avec leurs performances électriques, à l'aide de techniques combinées de caractérisations structurales, physico-chimiques et d'imagerie.

En explorant en profondeur leur comportement et leurs performances, cette thèse contribue à faire progresser la compréhension et l'application des matériaux ferroélectriques à base de HfO_2 dans les technologies mémoire.

Mots clés : Oxyde d'hafnium, Ferroélectrique, Structures multicouches, Dépôt par couches atomiques, Condensateurs Métal-Ferroélectrique-Métal, Films minces, Technologies de mémoire

Abstract

The rapid advancement of artificial intelligence, machine learning, and the Internet of Things has led to an increasing demand for more efficient memory technologies, exposing the limitations of traditional solutions like SRAM, DRAM, and NAND flash. Among the emerging alternatives, ferroelectric memories have garnered significant attention due to their scalability, non-volatility, and seamless compatibility with modern CMOS processes. Since the discovery of ferroelectricity in doped HfO_2 thin films in 2011, HfO_2-based materials have shown great potential in memory applications.

This thesis investigates the potential of HfO_2-based materials, particularly Zr-doped HfO_2 (HZO) thin films, as candidates for next-generation non-volatile memory technologies. The study offers a comparative analysis of single-layer (solid solution) and multilayer ferroelectric structures, examining how composition, electrode materials, annealing conditions, and thickness scaling influence their structural and electrical performances. Particular attention is given to multilayer configurations, which are often considered as a way to enhance the ferroelectric response through finer control of the stack architecture. However, the results obtained in this study show that such improvement is not systematic, and that multilayers do not necessarily exhibit better performance than single-layer structures.

Atomic layer deposition (ALD) plays a key role in this work due to its capability of growing thin films with atomic-level precision in both composition and thickness. This technique enables the development of complex systems such as nanolaminates and periodic multilayers, which offer promising solutions for improving the performance of ferroelectric devices. The main objectives of this research are to investigate the intrinsic properties of HZO-based materials and their evolution throughout the stages of Metal-Ferroelectric-Metal (MFM) capacitor fabrication, while also establishing correlations between these structural characteristics and their electrical performance, using a combination of structural, physicochemical, and imaging techniques.

By thoroughly exploring their behavior and performance, this thesis contributes to advancing the understanding and potential application of HfO_2-based ferroelectric materials in memory technologies.

Keywords : Hafnium Oxide, Ferroelectric, Multilayer structures, Atomic layer deposition, Metal-Ferroelectric-Metal capacitors, Thin films, Memory technologies

List of conferences

This work led to participation in several international conferences:

- A. Mallmann Tonelli *et al.*, **HfZrO-based Structures by ALD for Embedded Ferroelectric Non-Volatile Memories**, in *2023 EUROCVD / Baltic ALD*, 2023.
- A. Mallmann Tonelli *et al.*, **Ultrathin HfO_2–ZrO_2 Multilayer Structures by ALD for Embedded Ferroelectric Non-Volatile Memories**, in *AVS 24th International Conference on Atomic Layer Deposition (ALD 2024)*, 2024.
- A. Mallmann Tonelli *et al.*, **Optimizing Ultrathin HfO_2-ZrO_2 Structures by ALD for BEOL-Compatible Ferroelectric Non-Volatile Memories**, in *Materials for Advanced Metallization Conference (MAM 2025)*, 2025.
- A. Mallmann Tonelli *et al.*, **Impact of Layer Configuration on Ultrathin HfO_2-ZrO_2 Structures for Ferroelectric Non-Volatile Memories**, in *European Materials Research Society (EMRS 2025)*, 2025. — *Ferroic Young Researcher Award.*

Two patents ware also submitted.

- A. Mallmann Tonelli *et al.*, **Procedures for the preparation of a ferroelectric multilayer device**, December 2024.
- A. Mallmann Tonelli (second author) *et al.*, **Material and thin-film stack system for antiferroelectric capacitors and fabrication processes**, December 2024.

Contents

Acknowledgements i

Résumé ii

Abstract iii

List of conferences iv

Table of contents v

List of figures ix

List of Tables xiii

Acronyms xiv

Introduction xviii

1 Context, state of the art and goal of the thesis 1
1 The need for more energy efficient memory technologies . . . 3
1.1 Emergent non-volatile memories . . . 6
1.1.1 Ferroelectric Memories . . . 8
1.1.2 MFM . . . 10
2 Ferroelectric materials . . . 12
2.1 Historical advancements in ferroelectricity . . . 12
2.2 Properties of ferroelectrics . . . 13
2.3 HfO_2: from high-k dielectrics to ferroelectric memories . . . 14
2.4 Formation and stabilization of the ferroelectric phase in HfO_2-based films 15
2.4.1 Deposition techniques . . . 16
2.4.2 Impact of different precursors on ALD deposition . . . 16
2.4.3 Doping effect . . . 17
2.4.4 Influence of the electrodes . . . 17
2.4.5 Effect of annealing . . . 18
2.5 Intrinsic phenomena in ferroelectric HfO_2-based films . . . 18
3 Comparing single-matrix and multilayer ferroelectric structures . . . 21
4 The importance of thickness reduction in ferroelectric capacitors . . . 23
5 Objectives of the thesis . . . 25

2 Experimental techniques and methodologies 27

1 Deposition techniques . . . 29
1.1 ALD deposition of ferroelectric layers . . . 29
1.2 Deposition of metallic layers by PVD or CVD . . . 32
2 Material characterization . . . 35
2.1 X-ray Reflectometry . . . 35
2.2 Wavelength Dispersive X-Ray Fluorescence . . . 37
2.3 X-ray Diffraction . . . 37
2.4 Transmission Electron Microscopy . . . 41
2.5 Secondary-Ion Mass Spectrometry . . . 42
2.6 X-ray Photoelectron Spectroscopy . . . 43
2.7 Bow measurement . . . 44
3 Fabrication of the studied electrical devices . . . 47
3.1 300 mm MFM structures . . . 47
3.2 Annealing . . . 47
4 Methodologies for electrical characterization . . . 49
4.1 PUND : a technique to extrapolate ferroelectric metrics . . . 49
4.1.1 Basic method . . . 49
4.1.2 Experimental measurements . . . 51
4.2 Quasi-static I-V characteristics . . . 51
5 Chapter Summary and Conclusions . . . 54

3 10 nm HZO 1:1 Thin Film 55
1 Introduction . . . 57
2 10 nm HZO as a reference material: from material to device performance . . . 58
2.1 Intrinsic characteristics of as-deposited HZO . . . 58
2.2 Intrinsic properties of 10 nm HZO after electrode deposition and annealing 62
2.3 Electrical performance of capacitors . . . 65
2.4 General conclusion . . . 67
3 Impact of top electrode configurations on the ferroelectric performance of HZO capacitors . . . 68
3.1 Top electrode configurations and fabrication details . . . 68
3.2 Intrinsic properties of the electrode films . . . 68
3.3 Evaluation of stress evolution through bow analysis in HZO capacitors . . 71
3.4 Influence of top electrode configurations on electrical performance of HZO capacitors . . . 73
3.5 General conclusion . . . 75
4 Chapter Summary and Conclusions . . . 77

4 Composition and Thickness Scaling in HZO Solid Solution Films 78
1 Introduction . . . 80
2 Influence of Hf/Zr compositions on the properties of 10 nm HZO thin films . . . 81
2.1 Composition tuning of HfO_2–ZrO_2 solid solutions via ALD . . . 81
2.2 Correlation between composition and ferroelectric performance . . . 82
2.3 General conclusion . . . 85
3 Thickness effects on the properties of HZO 1:1 thin films . . . 86
3.1 Thickness and thermal effects on HZO thin films . . . 86
3.2 Electrical properties of HZO thin films: impact of thickness and annealing temperature . . . 87
3.3 Correlation between polarization and XRD intensity in HZO films . . . 92
3.4 Benchmark . . . 93

3.5 General conclusion . . . 95
4 Composition engineering for stabilizing ferroelectricity in ultrathin films . . . 97
4.1 Crystallization trends across composition and thickness . . . 97
4.2 Composition-driven variations in electrical results . . . 99
4.3 General conclusion . . . 102
5 Chapter Summary and Conclusions . . . 103

5 Multilayer engineering for enhanced ferroelectric performance 104
1 Introduction . . . 106
2 6 nm multilayer structures . . . 107
2.1 Structural and compositional features of 6 nm HfO_2–ZrO_2 multilayers . . . 107
2.2 Impact of multilayer design on ferroelectric response . . . 110
2.2.1 Evolution of remanent polarization and coercive voltage as a function of electrical cycling . . . 111
2.2.2 Wake-up behavior and multilayer loop characteristics . . . 112
2.2.3 Hypotheses on mechanisms influencing polarization in 6 nm multilayers . . . 113
2.2.4 Leakage current and breakdown characteristics . . . 115
2.2.5 Correlation between crystallographic texture and ferroelectric performance . . . 116
2.3 General conclusion . . . 118
3 6 nm multilayers with different compositions . . . 120
3.1 Structural and compositional analysis of 6 nm multilayers with varying Hf/Zr ratios . . . 120
3.2 Electrical properties of 6 nm HfO_2/ZrO_2 multilayers with varying composition . . . 122
3.3 General conclusion . . . 125
4 Ultra-thin multilayers: tuning ferroelectric performance with reduced ZrO_2 content 126
4.1 Structural and composition characterization of ZrO_2-reduced ultra-thin multilayers . . . 126
4.2 Ferroelectric stability in sub-6 nm capacitor structures . . . 128
4.3 General conclusion . . . 131
5 Benchmark . . . 133
6 Chapter Summary and Conclusions . . . 136

Conclusion et perspectives 137
1 Discussion and conclusions . . . 137
2 Perspectives . . . 139

Appendices 141
1 Spectroscopic Ellipsometry . . . 141
2 EDX-based chemical composition analysis throughout the fabrication of 10 nm HZO films . . . 142
3 ToF-SIMS profiling of 10 nm HZO with TiN top electrode . . . 143
4 Fine characterization of 10 nm HZO: investigating wake-up mechanisms . . . 144
4.1 MFM coupons . . . 145
4.2 Grazing incident wide angle X-ray scattering . . . 146
4.3 Crystallinity results via GIWAXS measurements . . . 147
4.4 Extended X-ray absorption fine structure . . . 147
4.5 Local atomic environment analysis via EXAFS . . . 150

5 Effect of etching sequence on ferroelectric response 151
6 XRR analysis of 6 nm multilayer structures 152
7 XRR analysis of 6 nm multilayer structures with different compositions 153
8 XRR analysis of ultra-thin multilayers 154

Texte de synthèse en français **156**
9 Contexte et opportunités des matériaux ferroélectriques à base d'oxyde d'hafnium 156
10 Dépôt par ALD des couches ferroélectriques à base d'HfO_2 et ZrO_2 157
11 Approches expérimentales de caractérisation 158
12 Comportement ferroélectrique des films de solution solide $Hf_{1-x}Zr_xO_2$ 158
13 Structures multicouches HfO_2/ZrO_2 : vers la ferroélectricité à l'échelle nanométrique160
14 Avancées et perspectives sur les films ferroélectriques ultrafins de HfO_2 161

Bibliography **163**

List of figures

1.1 Growth of AI model size and memory capacity over time. . . . 3
1.2 Memory pyramid describing the hierarchy . . . 5
1.3 Schematic representation of operating mechanisms in emerging non-volatile memories. . . . 6
1.4 Way to encode information within a ferroelectric . . . 9
1.5 FE memory cells . . . 9
1.6 Structure of piezoelectric material . . . 12
1.7 Classification of crystal geometries according to their symmetries, or crystal classes 14
1.8 HfO_2-based ferroelectric. . . . 15
1.9 Summary of issue in HfO_2-based ferroelectric. . . . 19
1.10 Schematic superlattices stack . . . 21
1.11 Capacitor thickness reduction . . . 23

2.1 Sketches of the working principles of ALD . . . 30
2.2 Schematic of ALD window and growth per cycle . . . 31
2.3 Photograph of the ASM Polygon Pulsar thermal ALD reactor used for the deposition of HfO_2-based ferroelectric films in this study. . . . 31
2.4 Schematic comparison of two ALD-based deposition strategies for HfO_2-ZrO2 thin films. . . . 32
2.5 XRR measurement . . . 35
2.6 X-ray reflection and refraction at the air-material interface as a function of the angle of incidence . . . 36
2.7 Schematic diagram of an X-ray diffraction (XRD) measurement setup . . . 38
2.8 In-plane XRD diffractogram for HZO 10 nm annealed at 400°C . . . 39
2.9 XRD of 10 nm HZO thin film with and without etching of top electrode after 400°C anneal . . . 40
2.10 Cross-sectional TEM image and EDX line scan across multilayer stack . . . 41
2.11 SIMS profile of HfO_2 films . . . 42
2.12 XPS profile of HZO thin film . . . 44
2.13 Wafer deformation measurement . . . 45
2.14 Sketches of the tested 300 mm MFM structures and photograph of a patterned 300 mm wafer . . . 47
2.15 Temperature–time profiles for two anneal recipes . . . 48
2.16 PUND sequence and its related P-V curve . . . 49
2.17 Schematic of a quasi-static voltage sweep typically used and example of a quasi-static I–V curve for a 10 nm HZO film . . . 52

3.1 XRR analysis of a 10 nm HZO film as deposited and ellipsometry uniformity map 58

3.2 GPC for films deposited using ALD . . . 59
3.3 Polar maps of the Hf and Zr atomic percentage distributions measured by WDXRF 60
3.4 XPS analysis of a 10 nm HZO film as deposited . . . 61
3.5 Depth-resolved SIMS analysis of a 10 nm HZO film as deposited . . . 62
3.6 Structural characterization of a 10 nm HZO film at different stages of the fabrication process . . . 63
3.7 Cross-sectional TEM of the MFM stack with a 10 nm HZO layer at different process stages. . . . 64
3.8 EDX line profiles showing the elemental distribution across the MFM stack with a 10 nm HZO layer at different process stages. . . . 65
3.9 P-E loops of HZO 10 nm samples annealed at different conditions. . . . 66
3.10 In-plane XRD patterns of TiN bottom electrode used in all MFM structures throughout this study . . . 69
3.11 In-plane XRD patterns of TiN electrodes with different deposition conditions . . 69
3.12 Evolution of stress during different processing steps for TiN- and W-based electrodes. . . . 70
3.13 Evolution of delta bow during different processing steps for TiN- and W-based electrodes . . . 72
3.14 Evolution of remanent polarizarion and coercive voltage for 10 nm HZO samples with different top electrodes annealed at 400°C for 1 h . . . 73
3.15 Current density for 10 nm HZO samples with different top electrodes annealed at 400°C for 1 h . . . 74
3.16 Comparison of $2P_r$ at the first cycle with different TiN (002) peak intensities and top electrode stress characteristics. . . . 75

4.1 Zr/(Hf + Zr) atomic ratio of 10-nm HZO films versus cycle ratio, measured by WDXRF . . . 81
4.2 XRD results of 10 nm HZO as-deposited films with different stoichiometries . . . 83
4.3 XRD results of 10 nm HZO films with different stoichiometries after TiN/W deposition and annealing . . . 83
4.4 (P–E) measurement results of 10 nm HZO films with different stoichiometries after TiN/W deposition and annealing . . . 84
4.5 Wake-up effect of 10 nm HZO films with different stoichiometries after TiN/W deposition and annealing . . . 85
4.6 XRD results of HZO 1:1 thin films with different thicknesses and annealing conditions . . . 87
4.7 PUND results of HZO 1:1 thin films with different thicknesses and annealed at 400°C . . . 88
4.8 PUND results of HZO 1:1 thin films with different thicknesses and annealed at 500°C . . . 89
4.9 Remanent polarization, coercive voltage and coercive field behaviors of HZO 1:1 thin films with different thicknesses and annealing conditions . . . 89
4.10 Current density for HZO layers of different thicknesses and annealing conditions 90
4.11 Comparison of breakdown field for HZO layers of different thicknesses (4nm, 5nm, 6nm, and 10nm) and annealing conditions . . . 91
4.12 Relationship between remanent polarization XRD peak intensity at 30.5° for HZO 1:1 thin films with different thicknesses and annealing conditions . . . 92
4.13 Benchmark of $2P_r$ for HZO thin films with a 1:1 composition across various thicknesses. . . . 94

4.14 Zr/(Hf + Zr) atomic ratio of ultrathin HZO films versus cycle ratio, measured by WDXRF . . . 97
4.15 As deposited density evolution of 4, 5, and 6 nm HZO films as a function of the precursors ratio . . . 98
4.16 XRD patterns of HZO films with thicknesses of 4 nm, 5 nm, and 6 nm annealed at 500°C . . . 99
4.17 Pr and Vc as a function of Zr composition for HZO films annealed at 500°C . . . 100
4.18 Current density for HZO layers of different thicknesses (4nm, 5nm, 6nm) and compositons . . . 100
4.19 Comparison of breakdown for HZO layers of different thicknesses (4nm, 5nm, 6nm) and compositons . . . 101

5.1 Schematic representation of the 6 nm multilayer configurations . . . 107
5.2 In-plane XRD measurements for multilayered HfO_2/ZrO_2 stacks after integration with TiN/W top electrode, annealing at 500°C for 15 min . . . 109
5.3 P-E loops of 6 nm multilayer samples annealed at 500°C for 15 min . . . 111
5.4 Remanent polarization and coercive voltage evolution for 6 nm multilayer samples annealed at 500°C for 15 min . . . 112
5.5 Trends in remanent polarization for 6 nm HfO_2/ZrO_2 based multilayer structures with different starting oxides (HfO_2 or ZrO_2) and varying unit layer thicknesses . 113
5.6 Current density as a function of the electric field and breakdown field for different multilayer configurations and single-layer HZO . . . 115
5.7 Correlation between remanent polarization XRD peak intensity at 30.5° for 6 nm HfO_2/ZrO_2 multilayers . . . 116
5.8 Correlation between unit layer thickness and both initial remanent polarization ($2P_r$) and normalized area ratio of the orthorhombic (200) to (111) XRD reflections 117
5.9 Schematic representation of the 6 nm multilayer with different compositions . . . 120
5.10 In-plane XRD patterns of HfO_2/ZrO_2 multilayers compared with their corresponding HZO solid-solution counterparts . . . 122
5.11 P–E loops as a function of cycling for different 6 nm structures annealed at 500°C for 15 min. . . . 123
5.12 Evolution of remanent polarization and coercive voltage as a function of cycling for different structures and compositions. . . . 123
5.13 E_{BD} comparison for HZO and multilayer structures at 6 nm thickness . . . 124
5.14 XRD characterization of 5 and 4 nm multilayer structures after top electrode deposition and annealing at 500°C for 15 minutes . . . 127
5.15 TEM images of 5 and 4 nm multilayer structures after TiN/W top electrode deposition and annealing at 500°C for 15 minutes . . . 128
5.16 P-E loops of 5 nm ultrathin structures at different cycling stages and annealed at 500°C for 15 min . . . 129
5.17 P-E loops of 4 nm ultrathin structures at different cycling stages with TiN/W top electrodes and annealed at 500°C for 15 min . . . 130
5.18 Coercive voltage and coercive field for ultrathin HZO and multilayer films . . . 130
5.19 Comparison of electrical characteristics for ultrathin HZO and multilayer films . 131
5.20 Benchmark of $2P_r$ for HfO_2/ZrO_2 multilayers thin films across various total thicknesses . . . 134

21 Schematic representation of spectroscopic ellipsometry . . . 141
22 EDX analysis of a 10 nm HZO film as deposited . . . 142
23 EDX analysis of a 10 nm HZO film after top electrode deposition . . . 143

24 EDX characterization of a 10 nm HZO film with TiN as the bottom and top electrode after 400°C anneal for 1 hour 143
25 ToF-SIMS of 10 nm HZO with TiN bottom and top electrode after annealing . . 144
26 PTA photolithography mask and sketches of the tested MFM coupons 145
27 GIWAXS measurement 146
28 GIWAXS patterns of HZO solid solution capacitors after 1 and 10^5 electrical cycles 148
29 EXAFS measurement 148
30 textitk^2-weighted EXAFS spectra at the Hf L_3-edge for samples 1, 2, 3, 4, and 6 151
31 Comparison of $2P_r$ at the first cycle with different TiN peak intensities and stress conditions 152
32 XRR measurements for 6 nm multilayer structures with varying unit layer thicknesses and stacking sequences 153
33 XRR measurements for 6 nm multilayer structures with different compositions . 154
34 XRR results of 5 and 4 nm multilayer structures 154

List of Tables

1.1 Benchmark comparison of conventional and emerging memory devices across key performance metrics [17]. 7

1.2 Key deposition methods for ferroelectric HfO_2-based thin films, with main advantages, limitations, and integration notes. 16

3.1 Summary of the top electrode configurations used in this study, including material stacks, deposition techniques, generator types, and processing temperatures. . . . 68

4.1 Summary of HZO film characteristics as a function of Hf:Zr ratio, including thickness and density determined by XRR, and atomic percentages determined by WDXRF Measurements were performed on 300 mm wafers. 82

5.1 Experimental details for 6 nm multilayer configurations exhibiting Hf/Zr compositions (as determined by WDXRF analysis) alongside the corresponding ALD pulse parameters used in their fabrication. 108

5.2 Fitted thicknesses of individual layers in Ti/TiN/HfO_2/ZrO_2 multilayer structures, based on XRR analysis. Each configuration includes a Ti/TiN bottom electrode stack followed by alternating HfO_2 (H) and ZrO_2 (Z) layers. Densities were fixed at 4.5 g/cm^3 for Ti, 4.95 g/cm^3 for TiN, 9.68 g/cm^3 for HfO_2, and 5.68 g/cm^3 for ZrO_2. 108

5.3 Experimental details for 6 nm multilayer configurations with alternating HfO_2 (H) and ZrO_2 (Z) layers. Atomic compositions were determined by WDXRF, and layer thicknesses were extracted by XRR fitting. Densities used in the fitting were fixed at 4.5 g/cm^3 for Ti, 4.95 g/cm^3 for TiN, 9.68 g/cm^3 for HfO_2, and 5.68 g/cm^3 for ZrO_2. Interface roughness was limited to 0.5 nm. 121

5.4 Experimental details and structural parameters for 5 and 4 nm multilayer configurations. The stack includes Ti/TiN bottom electrodes followed by alternating HfO_2 (H) and ZrO_2 (Z) layers. Atomic compositions were determined by WDXRF and thicknesses were extracted from XRR analysis. 126

5 Description of EXAFS samples analyzed. 150

Acronyms

AI Artificial Intelligence

ALD Atomic Layer Deposition

BE Bottom Electrode

BEOL Back-End-Of-Line

BTO Barium Titanate,$BaTiO_3$

CMOS Complementary Metal-Oxide-Semiconductor

CSD Chemical Solution Deposition

CTE Coefficient of thermal expansion

CVD Chemical Vapor Deposition

DC Direct Current

DRAM Dynamic Random Access Memory

DUT Device Under Test

EDX Energy Dispersive X-ray

EM Electron Microscope

EXAFS Extended X-ray Absorption Fine Structure

FE Ferroelectric

FeCAP Ferroelectric Capacitor

FeFET Ferroelectric Field Effect Transistor

FeRAM Ferroelectric Random Access Memory

FIB Focused Ion Beam

FTJ Ferroelectric Tunnel Junction

FWHM Full Width at Half Maximum

GIWAXS Grazing-Incidence Wide-Angle X-ray Scattering

GIXRD Grazing Incidence X-ray Diffraction

GPC Growth per Cycle

GPU Graphical Processing Unit

HAXPES Hard X-ray photoelectron spectroscopy

HZO Hafnium oxide doped with Zirconium

ICP Inductively Coupled Plasma

IoT Internet of Things

m- Monoclinic

MFM Metal-Ferroelectric-Metal

ML Machine learning

MOSFET Metal-Oxide-Semiconductor Field-Effect Transistor

MRAM Magnetic Random Access Memory

NLA Nanosecond Laser Anneal

NVM Non Volatile Memory

o- Orthorhombic

PCM Phase Change Memory

PEALD Plasma Enhanced Atomic Layer Deposition

PLD Pulsed Laser Deposition

PTA Advanced Technological Plateform (french acronym)

PUND Positive Up Negative Down

PVD Physical Vapor Deposition

PZT Lead zirconate titanate, $PbZr_XTi_{1-X}O_3$

RF Radio frequency

RRAM Resistive Random Access Memory

RTA Rapid Thermal Anneal

ShL Shortloop

SIMS Secondary-Ion Mass Spectrometry

SMU Source Measurement Unit

SRAM Static Random Access Memory

SSP Seam Suppressed Process

t- Tetragonal

TE Top Electrode

TEM Transmission Electron Microscope

TOF-SIMS Time-of-flight Secondary-Ion Mass Spectrometry

WDXRF Wavelength Dispersive X-Ray Fluorescence

WGFMU Waveform Generator/Fast Measurement Unit

XANES X-ray Absorption Near Edge Structure

XAS X-ray absorption spectroscopy

XPS X-ray photoelectron spectroscopy

XRD X-ray Diffraction

XRF X-ray fluorescence

XRR X-ray reflectometry

List of Symbols

Symbol	Measure Unit	Designation
E_{BD}	$[MV/cm]$	Breakdown Field
E_c	$[MV/cm]$	Coercive electric field
E_g	$[eV]$	Band gap
I_{FE}	$[A]$	Ferroelectric current
I_{DIEL}	$[A]$	Dielectric current
I_{LEAK}	$[A]$	Leakage current
J	$[A/cm^2]$	Current density
$2P_r$	$[\mu C/cm^2]$	Remanent polarization
S	$[cm^2]$	Area of the device
t	$[s]$	Time
T	$[K]$	Temperature of the device
t_{FE}	$[nm]$	Thickness of the FE layer
V	$[V]$	Voltage
V_C	$[V]$	Coercive voltage
V_{TE}	$[V]$	Voltage applied at TE
θ	$[\circ]$	Incident angle
λ	[Å]	Wave length
ν	$[Hz]$	Frequency of a photon

Introduction

The increasing demand for non-volatile memories in emerging technologies such as artificial intelligence, edge computing, and the Internet of Things has intensified the search for scalable, low-power alternatives to conventional memory devices. Among the most promising candidates are ferroelectric capacitors based on hafnium oxide (HfO_2) and its doped or alloyed derivatives, particularly hafnium–zirconium oxide (HZO). These materials stand out for their full compatibility with CMOS processes, scalability down to a few nanometers, and their ability to retain ferroelectric properties even at reduced thicknesses.

However, as device integration advances, achieving robust and reliable ferroelectric behavior at the nanoscale becomes increasingly challenging. Device performance depends not only on the intrinsic properties of the ferroelectric material but also on the interplay between composition, film thickness, thermal treatments, and electrode interfaces. In parallel, the introduction of alternative structural designs, such as multilayer stacks, has opened new paths to modulate ferroelectric properties, although their benefits must be critically assessed in practical implementations.

This thesis investigates these aspects through a comprehensive study of ultrathin HZO-based ferroelectric layers, focusing on how processing parameters and structural configurations influence key properties such as remanent polarization, coercive field, leakage, and wake-up behavior during electrical cycling. The experimental approach is based on the fabrication of MFM (Metal-Ferroelectric-Metal) capacitors, where the ferroelectric layers are deposited by atomic layer deposition (ALD), and integration is carried out on 300 mm wafers. The ferroelectric response is systematically evaluated and correlated with the material's structure using a combination of electrical measurements and material characterization techniques, including X-ray diffraction (XRD). To further investigate the local atomic environment and its evolution during cycling, extended X-ray absorption fine structure (EXAFS) analysis was carried out at a synchrotron facility; however, these results are still under interpretation.

Chapter 1 frames the problem and motivation: it surveys the limits of established memory technologies, introduces ferroelectric memories with a historical perspective, and motivates the study of Metal–Ferroelectric–Metal (MFM) structures based on HfO_2. It compares single-matrix and multilayer architectures, emphasizes the importance of thickness reduction, and states the key objectives of the thesis.

Chapter 2 introduces the experimental methodologies, from the fabrication of ferroelectric

capacitors using ALD, PVD and CVD, to the material characterization techniques applied to probe film thickness, density, phase, and chemical composition. Techniques such as XRR, XRD (GIXRD and in-plane), TEM, EDX, SIMS, and XPS are presented alongside the electrical characterization (PUND and quasi-static I–V) essential for evaluating device performance.

Chapter 3 focuses on 10 nm-thick HZO layers with a 1:1 Hf:Zr ratio, used as a reference structure to investigate the influence of fabrication steps such as top electrode deposition and annealing. The chapter analyzes how different electrode configurations affect mechanical stress and ferroelectric performance, and presents a preliminary investigation into the physical origins of the wake-up effect through structural and electrical characterization.

Chapter 4 explores the effects of varying global composition and scaling thickness on the structural and functional properties of HZO films. It examines how deviations from the 1:1 Hf/Zr ratio and reductions in film thickness to 6, 5, and 4 nm impact phase stabilization, polarization, leakage current, and dielectric properties. The chapter emphasizes the challenges of achieving robust ferroelectricity in ultrathin films and identifies strategies based on composition engineering to mitigate these limitations.

Chapter 5 focus on the multilayer HfO_2/ZrO_2 structures and examines how changes in stacking order, composition, and unit layer thickness influence ferroelectric properties. By adjusting the sequence of HfO_2 and ZrO_2 layers, the study explores ways to enhance polarization, stabilize the orthorhombic phase, and reduce leakage currents. Particular attention is given to how the choice of starting and ending layers, as well as scaling to sub-5 nm thicknesses, affects crystallization behavior and overall device performance.

Rather than isolating individual effects, the study aims to develop a broader understanding of how material properties evolve throughout each stage of the fabrication process. By exploring variables such as composition, annealing conditions, total thickness, and the use of multilayer architectures, this work contributes to identifying process–structure–property relationships that support the development of ultrathin ferroelectric layers suitable for integration in next-generation memory devices.

Ultimately, this work aims to define robust process windows and material configurations suitable for integration into ferroelectric memory devices, particularly under the thermal and structural constraints imposed by BEOL fabrication. Through this approach, the thesis provides insights into how processing conditions and design choices affect the ferroelectric behavior of ultrathin HfO_2-based layers at the device level.

Chapter 1

Context, state of the art and goal of the thesis

Objectives

In this chapter, a progressive approach will first outline the current demand for more efficient memory technologies by providing an overview of the limitations faced by existing systems. Emerging solutions, such as ferroelectric memories, will be introduced, focusing on the development of HfO_2-based materials. A historical perspective on ferroelectric materials will justify the relevance of studying Metal-Ferroelectric-Metal (MFM) structures in this thesis. Comparative analyses between single-matrix and multilayer ferroelectric structures will be presented, highlighting the potential advantages of multilayers. The importance of thickness reduction in ferroelectric capacitors will be emphasized. Finally, the key objectives of this thesis will be detailed in the concluding section.

Contents

1 The need for more energy efficient memory technologies . . . **3**
1.1 Emergent non-volatile memories . . . 6
2 Ferroelectric materials . . . **12**
2.1 Historical advancements in ferroelectricity . . . 12
2.2 Properties of ferroelectrics . . . 13
2.3 HfO_2: from high-k dielectrics to ferroelectric memories . . . 14
2.4 Formation and stabilization of the ferroelectric phase in HfO_2-based films . . . 15
2.5 Intrinsic phenomena in ferroelectric HfO_2-based films . . . 18
3 Comparing single-matrix and multilayer ferroelectric structures . . . **21**
4 The importance of thickness reduction in ferroelectric capacitors . . . **23**
5 Objectives of the thesis . . . **25**

1 The need for more energy efficient memory technologies

As modern computing continues to advance, the need for more efficient memory technologies has become increasingly urgent. The growing complexity of data-intensive applications, including artificial intelligence (AI), machine learning (ML), autonomous systems, and the Internet of Things (IoT), is placing unprecedented demands on existing memory hierarchies. This is particularly evident in the training of large AI models, which now require exponentially more computing power.

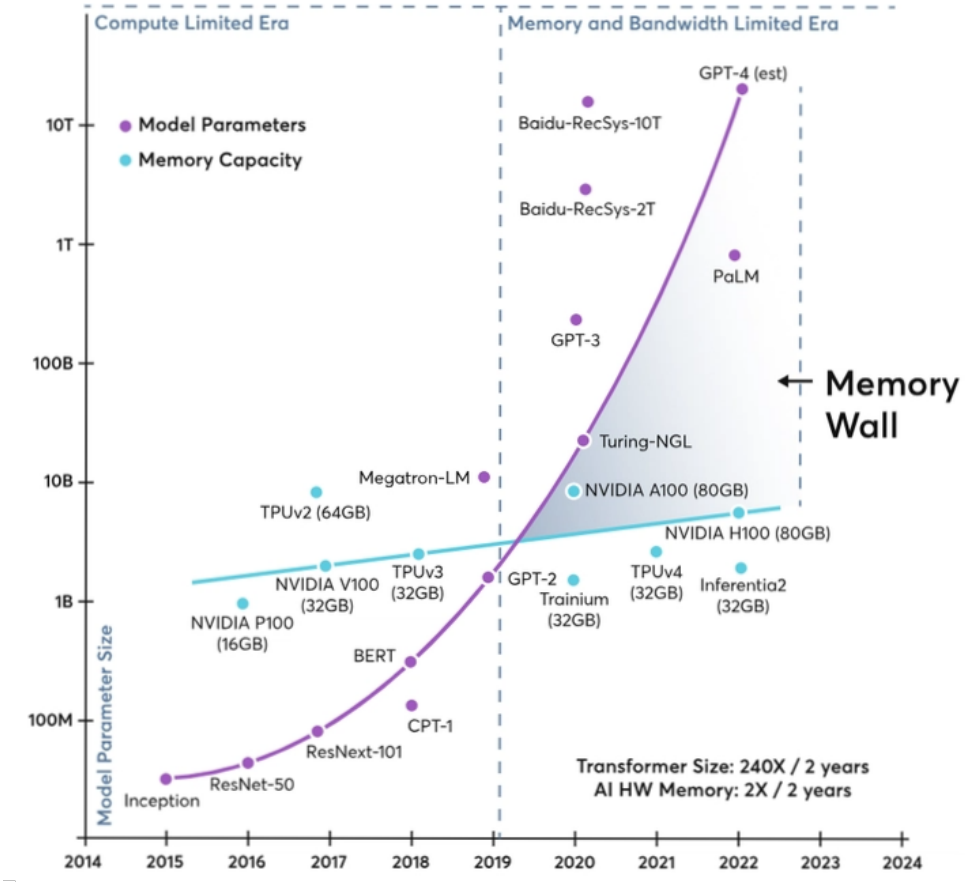

Figure 1.1: Growth of AI model size and memory capacity over time. The trend reveals an exponential increase in model complexity, with a comparatively modest growth in memory capacity. Data are from [1].

Fig. 1.1 plots years on the x-axis and model parameter size on the y-axis, showing the growth of AI models in terms of their parameter counts, that is, the total number of adjustable values that define model size and complexity. Over the past decade, parameter sizes have grown from millions (e.g., Inception, ResNet) to hundreds of billions and even trillions (e.g., GPT-3, PaLM, Baidu RecSys, and the estimated GPT-4). This trend highlights the exponential increase in model complexity compared with the more modest improvements in hardware memory capacity.

The resulting disparity, referred to as the "memory wall", marks the transition from a compute-limited regime to one constrained by memory capacity and bandwidth. In this regime, the primary bottlenecks are not the arithmetic throughput of processors but rather the ability

to store large parameter sets and to transfer data efficiently between memory and processing units. Overcoming this limitation necessitates advances in high-speed, high-capacity memory architectures capable of sustaining the demands of large-scale AI workloads [2].

Recent advancements in energy-efficient AI models highlight the role of hardware in reducing power consumption and operational costs. DeepSeek AI, for instance, has achieved up to 40% greater efficiency than OpenAI's ChatGPT, probably due to a combination of factors, including algorithmic improvements and hardware integration. Despite using less powerful Nvidia chips due to restrictions, DeepSeek increased its market share from 5% in 2021 to 15% in 2024, emphasizing the competitive advantage of optimized computing systems [3]. However, relying on less powerful processors does not preclude the possibility of memory hardware optimizations having been implemented to mitigate the bottleneck. By reducing data movement, improving bandwidth utilization, and enhancing memory access efficiency, such optimizations can lower latency, increase throughput, and improve hardware utilization, ultimately leading to faster training, more efficient inference, and reduced energy consumption.

As AI adoption grows, reliance on GPUs and scalable memory will continue to rise. GPUs, which demand high bandwidth and massive parallel processing capabilities, place increasing pressure on conventional memory systems. However, traditional memory technologies face significant limitations in terms of power consumption, latency, and scalability. Projections estimate the GPU market will reach $435,760 million by 2030, growing at a compound annual growth rate (CAGR) of 31.59%, which will only be sustainable with significant advances in memory performance and energy efficiency [2, 3].

In parallel, the expansion of IoT devices is generating vast volumes of data, further exposing the "processor-memory gap", a performance bottleneck known as the "memory wall," originally described by Wulf and McKee in 1995 [4]. This issue stems partly from the industry's division between processor and memory technology development, which has slowed coordinated progress.

Traditional memory technologies such as Static Random Access Memory (SRAM), Dynamic Random Access Memory (DRAM), and NAND flash are now facing fundamental limitations. SRAM and DRAM are volatile and require constant power to retain data, leading to high energy consumption. DRAM also suffers from relatively high latency, as accessing data from off-chip memory introduces delays, and frequent refresh operations further increase power consumption in large-scale systems [5, 6]. NAND flash, while non-volatile, has slower access times and endurance issues, and all three face scaling challenges due to leakage, variability, and reduced reliability at smaller nodes [7–9].

Volatile memories are those that lose stored information once power is removed, whereas non-volatile memories retain data without the need for continuous power supply. Within processors, volatile memories such as SRAM and DRAM are employed in caches and main memory, where fast access is required to match processor throughput. Non-volatile memories such as NAND flash, on the other hand, are used primarily for long-term storage (e.g., solid-state drives). In the context of AI systems, volatile memories are essential for providing rapid access to parameters and intermediate results during training and inference, while non-volatile storage is necessary to hold the massive datasets and pre-trained models on which these systems rely.

To overcome these challenges, a shift toward emerging memory technologies is essential (as shown in **Fig. 1.2**). Promising candidates such as Resistive RAM (ReRAM), Phase-Change Memory (PCM), Spin-Transfer Torque Magnetic RAM (STT-MRAM), and Ferroelectric RAM (FeRAM or FeFET-based devices) offer the potential to combine fast access, low power consumption, and non-volatility. These technologies could bridge the gap between traditional volatile and non-volatile memories, addressing the performance and efficiency needs of next-generation computing systems [10].

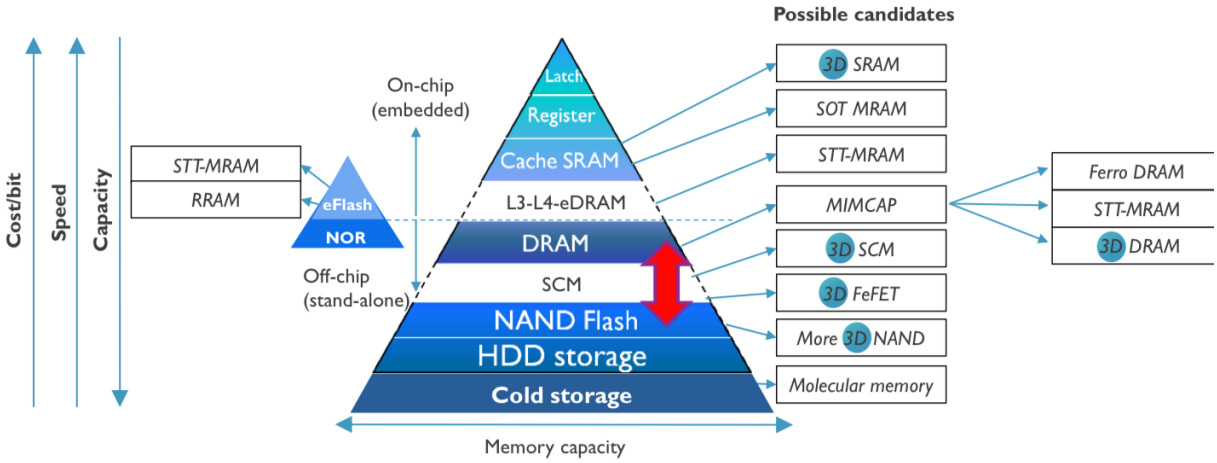

Figure 1.2: Emerging memories and their use in the storage/memory hierarchy. Source: [11].

1.1 Emergent non-volatile memories

In light of the limitations of conventional memory technologies, research has increasingly focused on alternative solutions that offer improved speed, endurance, and scalability. This section presents an overview of emergent non-volatile memories and their potential.

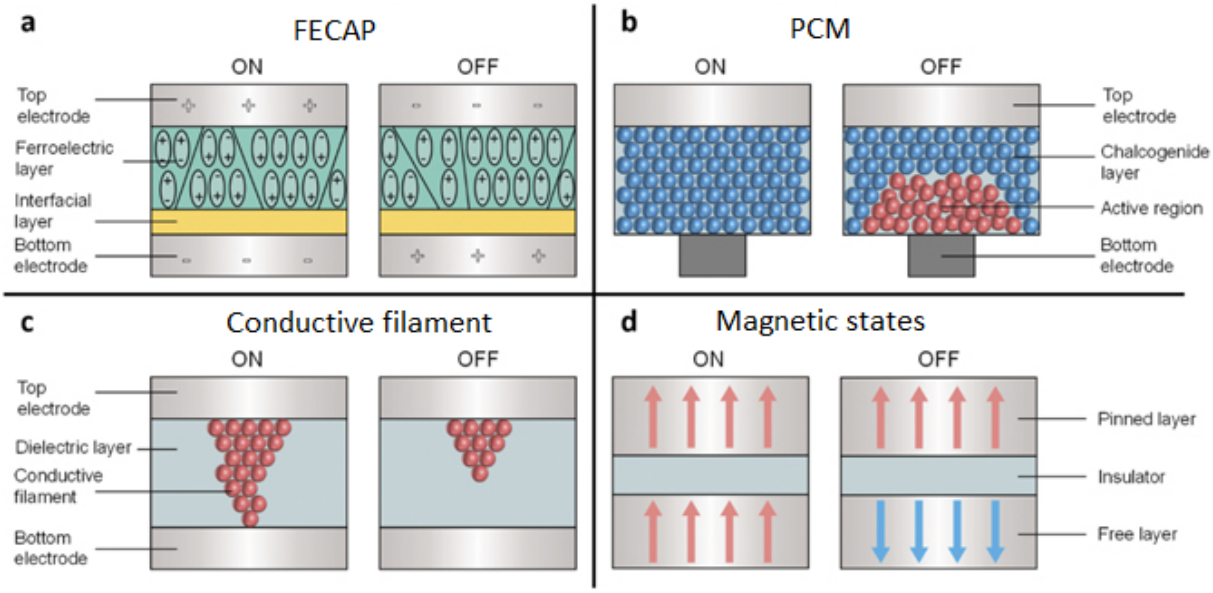

Figure 1.3: Different mechanisms of the representative emerging memory technologies including FeCAP, PCM, RRAM, and MRAM. **a.** Ferroelectric capacitor (FeCAP), where data storage is based on the reversible polarization switching of the ferroelectric layer between two stable polarization states. **b.** Structure of the PCM, where data is stored through the reversible transition of a chalcogenide layer between the crystalline (low-resistance) and amorphous (high-resistance) phases. **c.** Conductive-filament of a RRAM, where the switching is driven by the formation and rupture of conductive filaments within a dielectric layer. **d.** Magnetic states of a MRAM device, where information is encoded in the relative orientation of magnetic moments in a magnetic tunnel junction (MTJ), with low resistance for parallel alignment and high resistance for antiparallel alignment. Images are from [12]

Several NVM technologies are at the forefront of memory innovation, each with unique properties and potential applications:

- **Ferroelectric capacitor (FeCAP), Fig. 1.3a**: uses a ferroelectric layer sandwiched between two metal electrodes, and forms the core of a ferroelectric random-access memory (FeRAM) cell, which follows a one-transistor–one-capacitor (1T1C) architecture. When a voltage is applied to a ferroelectric material, its internal dipoles align with the electric field. After the voltage is removed, part of this alignment remains, creating two stable polarization states that store binary information. It offers lower latency than traditional DRAM, high endurance compared with most other emerging memories, and non-volatility, allowing it to retain data even when power is turned off. However, FeRAM's density is typically lower than other NVM technologies, which limits its storage capacity in some applications [13].

- **Phase-Change Memory (PCM), Fig. 1.3b**: a chalcogenide active layer is sandwiched between two metal electrodes. The phase transition is controlled by a heater element, which modulates the temperature of the active layer. When the applied voltage induces a heating level below the melting temperature, the device gradually transitions from a high resistance state (HRS) to a low resistance state (LRS) as the material crystallizes. Conversely, when the heater raises the temperature above the melting point and the material is rapidly quenched, it returns to the amorphous phase, switching the device from LRS to HRS. PCM stores data by altering the phase of the chalcogenide material between amorphous and crystalline states. It offers better endurance than NAND flash and significantly faster read speeds. PCM is well-suited for applications requiring large amounts of data to be written quickly, but its relatively high write energy can be a limitation [14].

- **Conductive-filament of a Resistive RAM (RRAM), Fig. 1.3c**: a dielectric layer is sandwiched between two metal electrodes. It operates by changing the resistance of a material to store information. The change in resistance states originates from the formation and rupture of conductive filaments. This technology offers high read and write speeds and low power consumption, with the ability to retain data without power. Its endurance is high, making it suitable for both embedded memory and storage-class memory applications [15].

- **Magnetic states of a Magnetoresistive RAM (MRAM), Fig. 1.3d**: an insulator layer is sandwiched between two ferromagnetic metal electrodes. The resistance change across the barrier is caused by the different configurations of the magnetic moments in the two electrodes. It stores data using magnetic storage elements, offering a good combination of speed, endurance, and non-volatility. Its performance is close to DRAM in terms of speed, with better energy efficiency and the added benefit of persistent data storage. MRAM has attracted significant interest for use in embedded systems and computing applications [16].

Table 1.1 summarizes key performance metrics for conventional and emerging memory devices, providing a benchmark comparison in terms of energy consumption, speed, endurance, retention, and scalability.

Table 1.1: Benchmark comparison of conventional and emerging memory devices across key performance metrics [17].

	eSRAM	**eDRAM**	**FG Flash**	**RRAM**	**PCM**	**MRAM**	**FeRAM**
Energy/bit	1 fJ	1 pJ	100 pJ	>10 pJ	100 pJ	>10 pJ	1 pJ
Cell size (F^2)	$\sim$ 120	40	50	60	60	50	50
Write speed	<2 ns	10–50 ns	1–100 μs	50 ns	10–100 ns	10 ns	10 ns
Read speed	<2 ns	10–50 ns	$\sim$10–100 ns	1–20 ns	2 ns	1–20 ns	5 ns
Latency	<1 ns	>10 ns	μs range	<100 ns	<100 ns	>10 ns	>10 ns
Endurance	10^{16}	10^{16}	10^5	10^5–10^7	10^5–10^7	10^6–10^{15}	10^{12}
Retention	Volatile	Refresh	10 yrs	10 yrs	10 yrs	10 yrs	10 yrs
Scalability	High	High	Medium	High	High	Medium	Medium

While FeRAM may not offer the same storage density as some other memory technologies, its balance of speed, endurance, and non-volatility positions it as a strong candidate for a variety of embedded systems and energy-efficient applications. The core of this study focuses on the ferroelectric material that makes FeRAM possible. The upcoming sections will delve into the fundamental mechanisms of ferroelectricity, exploring how the material's intrinsic properties enable its role in memory technologies and assessing its potential to meet the challenges posed by modern data-intensive applications.

1.1.1 Ferroelectric Memories

The operation of ferroelectric memories relies on the two stable polarization states of the ferroelectric material, which correspond to opposite orientations of electric dipoles within the capacitor and are used to encode binary information (**Fig. 1.4**). These dipoles can be switched between two stable orientations by applying an electric field across the ferroelectric layer (**Fig. 1.4**b). This switching behavior gives rise to the characteristic ferroelectric hysteresis curve, which is defined by four key parameters:

- two coercive voltages (*i.e.* V_c^+, V_c^-) which determine the electric fields at which polarization can switch from one state to another
- two remanent polarizations (*i.e.* P_R^+, P_R^-), representing the residual polarization at zero electric field across the ferroelectric layer.

It is important to distinguish remanent polarization ($2P_R$) from saturation polarization (P_S). While the P_S corresponds to the maximum dipole alignment achievable under strong electric fields, only $2P_R$ remains after the field is removed and thus encodes the non-volatile information. In practical memory applications, the difference between the two stable remanent states, $2P_R$, defines the usable polarization window. This metric is technologically relevant because it directly determines the signal margin available for reliable data readout.

The principle of writing in ferroelectric memory is based on this hysteresis curve. By applying an electric field higher than the absolute coercive field, all the ferroelectric dipoles can be oriented in a specific direction. This orientation remains stable even when the electric field is turned off, enabling non-volatile information encoding.

Although ferroelectric memories share the same underlying programming principle, they differ in terms of structure and reading methods (**Fig. 1.5**). There are three types of ferroelectric memories: FeFET, FeRAM, and FTJ.

While FeRAM resembles DRAM in that both use a capacitor-based storage element and rely on destructive readout, FeFET and FTJ differ fundamentally in their operation. FeFETs are transistors whose non-volatility arises from the control of the channel by the polarization state of the ferroelectric gate dielectric, enabling non-destructive reading through a polarization-induced modulation of the channel current. In contrast, FTJs store information through a polarization-dependent change in tunnel resistance across the junction, also allowing non-destructive readout.

FeRAM stores data using the polarization state of a ferroelectric capacitor connected with a selection transistor, as shown in **Fig. 1.5**a. Since the polarization state cannot be directly read,

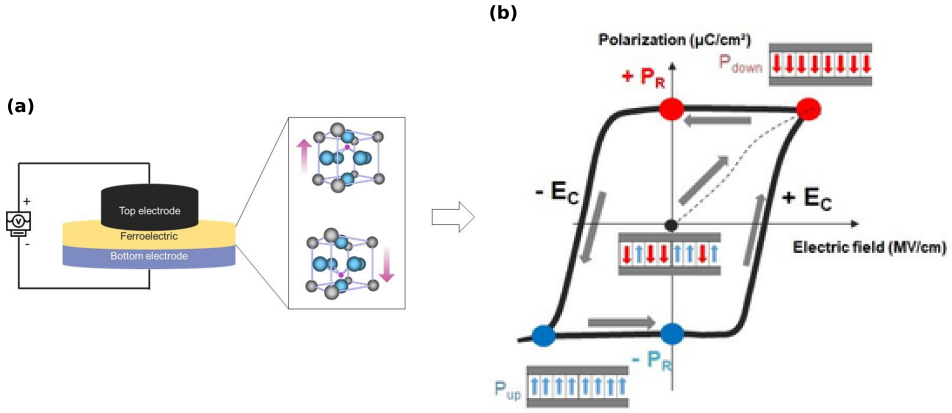

Figure 1.4: **a.** Schematic of a metal–ferroelectric–metal (MFM) capacitor structure used in FeRAM devices. **b.** Binary states ("1" and "0") are encoded by aligning dipoles upward or downward. These states can be changed by applying voltage higher than the coercive voltages (V_C^+ and V_C^-) and they are stable when the voltage is switched off, leading to the remanent polarization (P_R^+ and P_R^-).

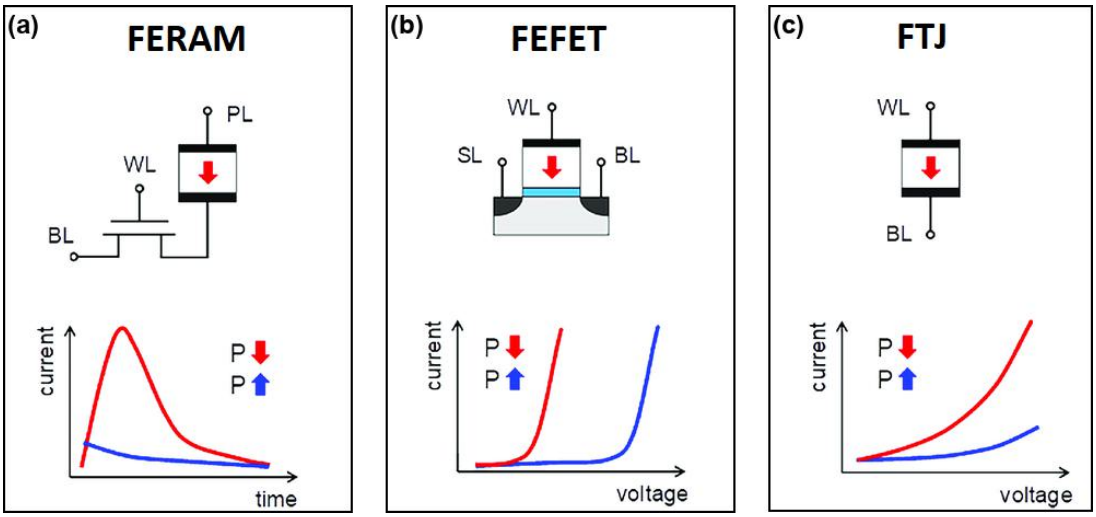

Figure 1.5: FE memory cells can be categorized into three types. **a.** FeRAM cells, where data storage occurs in the capacitor and the connected transistor serves as a switch. **b.** A FeFET cells, where the charge storage medium is the ferroelectric layer embedded in the FET gate stack. **c.** FTJs, which utilize the ultrathin tunnel barrier sandwiched between two different metals. In FTJs, the change in ferroelectric polarization direction leads to an asymmetric barrier potential, resulting in different barrier heights for tunneling electrons depending on the polarization direction, thereby enabling resistive switching. Adapted from [18].

a voltage above the coercive value is applied, generating a current that is sensed via the bitline, an inherently destructive process that requires rewriting the cell after reading. Despite this drawback, FeRAM is regarded as one of the most energy-efficient emerging memory technologies, particularly within the class of ferroelectric memories, as its capacitor-based structure requires very low switching voltages and currents compared to resistive or phase-change mechanisms. The typical structure includes a Metal-Ferroelectric-Metal (MFM) capacitor stack, integrated in a One Transistor–One Capacitor (1T–1C) architecture. This design has been demonstrated in

16 kbit arrays at the 130 nm node with TiN/HfO_2:Si/TiN capacitors integrated into the BEOL [19].

A major challenge for FeRAM is scalability [20]. As nodes shrink, capacitance and polarization decrease, compromising readability. To address this, 3D capacitors, similar to those used in DRAM, are being explored, requiring conformal deposition techniques such as Atomic Layer Deposition (ALD) to ensure reliable high-aspect-ratio ferroelectric integration.

In contrast, FeFET, shown in **Fig. 1.5**b, integrates the ferroelectric oxide directly into the gate stack of the transistor. In this architecture, the ferroelectric layer acts as the gate dielectric, and its polarization state modulates the channel conductivity beneath it, thereby storing information. It offers advantages like high sensing current, fast switching, and analog behavior via partial polarization control. Despite challenges such as fatigue, charge trapping, and integration complexity, FeFETs are promising for embedded non-volatile memories and AI hardware. Recent demonstrations of 3D FeFET arrays show potential for high-density, logic-compatible memory [21].

Finally, FTJ, shown in **Fig. 1.5**c, is a two-terminal device with a thin ferroelectric layer whose polarization modulates tunneling resistance. States like "Pup" and "Pdown" alter the electrostatic profile, enabling binary data storage via tunable current flow. Its simple structure makes FTJ a strong candidate for high-density non-volatile memory [22].

Each ferroelectric memory, FeRAM, FeFET, and FTJ, has distinct strengths suited to different domains: FeRAM for embedded low-power systems, FeFET for logic and neuromorphic integration, and FTJ for ultra-dense memory arrays [23, 24].

1.1.2 MFM

The core component of a FeRAM device is the ferroelectric capacitor, which is responsible for storing data by exploiting the polarization properties of ferroelectric materials. The basic structure of a ferroelectric capacitor typically consists of a Metal-Ferroelectric-Metal (MFM) stack. In this configuration, a thin ferroelectric layer is sandwiched between two metal electrodes.

The MFM stack operates as follows:

- **Electrodes:** These are the conductive layers on both sides of the ferroelectric material. They serve as the contact points through which an electric field is applied across the ferroelectric layer.
- **Ferroelectric Layer:** This is the central layer that exhibits ferroelectric properties. Materials like hafnium oxide (HfO_2) or lead zirconate titanate (PZT) are commonly used. The polarization of this layer can be switched by applying an electric field greater than the coercive voltage, allowing the storage of binary information (1 or 0).

When a voltage is applied across the metal electrodes, the dipoles within the ferroelectric layer align in a particular direction, creating a polarized state. The alignment of these dipoles is stable even when the voltage is removed, allowing the capacitor to retain information (non-volatility).

The MFM configuration is fundamental to the operation of memory technologies such as FeRAM and FTJ, where the information is encoded in the polarization state of the ferroelectric film. In this thesis, the device architecture under investigation is based on the MFM structure, with a particular focus on HfO_2-based ferroelectric capacitors. The work will explore the fabrication, integration challenges, downscaling effects, and the resulting electrical and structural characteristics of these capacitors, aiming to improve the understanding of their behavior in memory applications.

2 Ferroelectric materials

2.1 Historical advancements in ferroelectricity

The discovery of ferroelectricity traces back to 1920 when Joseph Valasek conducted experimental studies on Rochelle salt [25]. This material was already known for its piezoelectric behavior, but Valasek's research was driven by prior observations of its anomalous response to external forces and electric fields. Unlike typical piezoelectric materials, Rochelle salt exhibited nonlinear charge generation under mechanical stress and a dielectric response that varied with applied voltage [26].

Despite its groundbreaking role in identifying ferroelectricity, Rochelle salt was limited for applications due to its high solubility in water [27]. It was not until the 1940s that a significant breakthrough occurred with the discovery of barium titanate ($BaTiO_3$ or BTO). Unlike Rochelle salt, BTO demonstrated high dielectric permittivity and stable ferroelectric properties, making it the first widely studied practical ferroelectric material [28]. Beyond its macroscopic dielectric response, $BaTiO_3$ also became a model system for understanding ferroelectric domain structures [29, 30].

By the 1950s, further advancements led to the exploration of materials such as lead titanate ($PbTiO_3$ or PTO), lead zirconate titanate ($Pb(ZrTi)O_3$ or PZT). **Fig. 1.6 i**llustrates the perovskite ABO_3 crystal structure and the ferroelectric distortion of PZT. **Fig. 1.6 a** shows the ideal centrosymmetric cubic structure, in which the centers of positive and negative charges coincide, resulting in no net polarization. **Fig. 1.6 b** depicts the tetragonal phase of PZT, where displacement of the B-site cation relative to the oxygen octahedron generates local dipoles, giving rise to spontaneous ferroelectric polarization. PZT, particularly in its tetragonal phase, exhibited robust ferroelectric properties and found widespread applications in transducers, actuators, sensors, and ferroelectric memory [31].

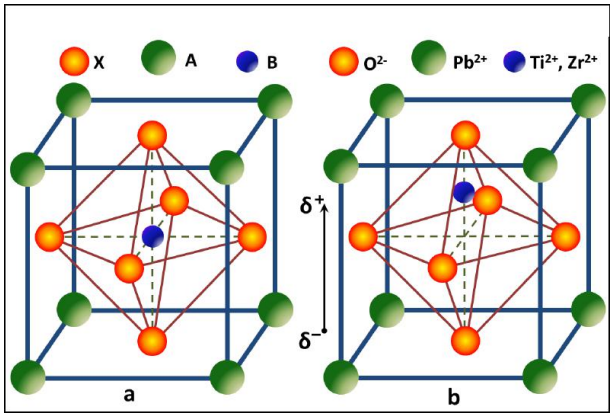

Figure 1.6: a. Cubic centrosymmetric ABO_3 phase, where A-site cations (Pb^{2+}, green) occupy cube corners, the B-site cation (Ti^{4+}/Zr^{4+}, blue) is at the body center, and O^{2-} anions (red) form an octahedron. **b.** Tetragonal ferroelectric distortion, where off-centering of the B-site cation and oxygen sublattice generates dipoles (δ^+/δ^-), giving rise to a spontaneous polarization along the tetragonal axis that can be reversed by an external electric field. [32].

PZT adopts a perovskite crystal structure, which can exhibit different symmetries depending

on composition and temperature. In its ferroelectric tetragonal phase, the unit cell is slightly elongated along one axis, giving it a distorted cubic structure. This distortion is caused by the off-center displacement of the Ti^{4+} or Zr^{4+} cation within the oxygen octahedron, breaking the centrosymmetry and giving rise to a spontaneous polarization. The displacement direction can be reversed by applying an external electric field, which is the basis of its ferroelectric behavior. Depending on the Zr/Ti ratio, PZT can also adopt rhombohedral or monoclinic phases, but the tetragonal phase is most commonly associated with strong ferroelectric response [32]. More precisely, polarization in a ferroelectric material is defined as the dipole moment per unit volume. While individual dipoles originate from ionic displacements within each unit cell, the measurable polarization corresponds to the collective contribution of these dipoles across the crystal lattice.

In 1993, PZT became the first ferroelectric material used in semiconductor memory, enabling the development of a 4 kbit FeRAM [33]. However, despite its strong ferroelectric properties, PZT presents several challenges that hinder its adoption in modern ferroelectric memory technologies. One major drawback is its reliance on lead (Pb), which raises environmental and regulatory concerns, making it incompatible with CMOS fabrication processes that demand lead-free materials. Furthermore, thickness scaling remains a critical issue due to the continuous trend toward device miniaturization. The coercive field (E_c), defined as the electric field required to switch the polarization of the ferroelectric material, is relatively low in PZT ($E_c <$ 0.1 MV/cm) compared to $Hf_{0.5}Zr_{0.5}O_2$ ($E_c \approx 1$ MV/cm) [34]. Consequently, PZT films on the order of 100 nm are required to achieve operating voltages in the 1.5–5 V range. Such thicknesses are not easily compatible with advanced technology nodes, particularly regarding patterning, where small lateral dimensions are needed.

These limitations have driven the search for alternative ferroelectric materials that are more suitable for integration into silicon-based technologies. Among the most promising candidates are hafnium oxide-based compounds, which offer improved scalability, CMOS compatibility, and the potential to overcome the key challenges associated with PZT.

2.2 Properties of ferroelectrics

Ferroelectricity occurs in crystalline or polycrystalline materials with a polar, non-centrosymmetric crystal structure. As illustrated in **Fig. 1.7 a**, ferroelectrics are a subset of pyroelectric materials, which separates electric charge in response to temperature changes [35]. Unlike linear dielectrics, where polarization induced by the distortion of the electron cloud and atomic nuclei disappears when the applied electric field is removed, a relative displacement of anions and cations within the unit lattice cell of a ferroelectric persists even without an electric field.

This displacement, resulting from the non-centrosymmetric nature of the lattice (**Fig. 1.7 b**), causes the centers of positive and negative charges to remain offset, producing a spontaneous polarization within the unit cell. This remanent polarization remains stable even after the external electric field is removed and can be reversed by applying an electric field of opposite polarity. The electric displacement field in ferroelectric materials includes both the non-switching dielectric response and the switching behavior of the spontaneous polarization [37].

Ferroelectric materials can be grown as single crystals or as polycrystalline films. Regardless

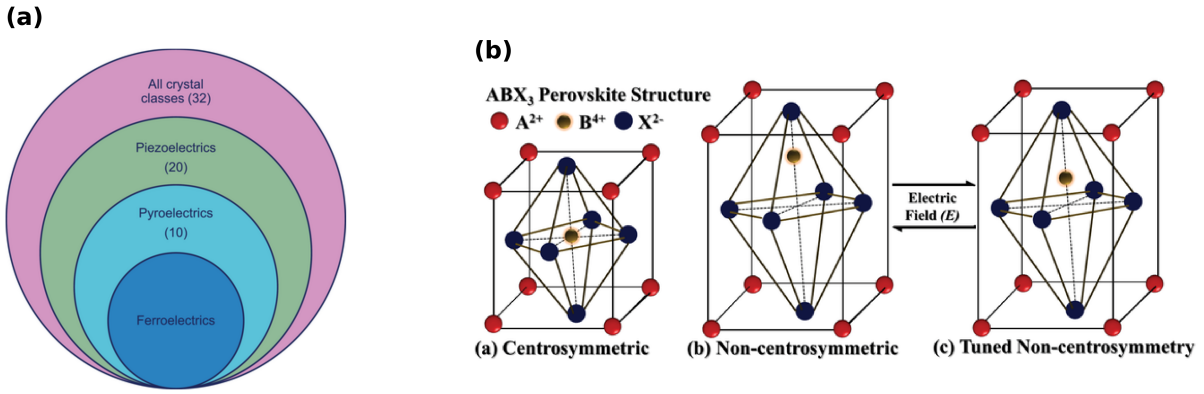

Figure 1.7: a. Relationship between dielectric, piezoelectric, pyroelectric, and ferroelectric materials. **b.** Perovskite structure with symmetric, non-centrosymmetric arrangements. Tuning of the degree of non-centrosymmetry by means of an external stimulus [36].

of crystallinity, ferroelectrics exhibit domains, regions in which electric dipoles are uniformly aligned to minimize elastic and electrostatic energies. The boundaries between domains are known as domain walls. In single crystals, polarization reversal proceeds mainly through domain nucleation and domain wall motion, while in polycrystalline films the presence of grains introduces additional structural constraints that affect domain configurations [38].

2.3 HfO_2: from high-k dielectrics to ferroelectric memories

Historically valued in the nuclear industry for its high neutron absorption coefficient, HfO_2 possesses a large bulk modulus, strong chemical stability, and a high melting point, making it well-suited for structural applications [39, 40].

At the beginning of the 2000s, HfO_2 began replacing SiO_2 as the gate insulator in MOSFETs, thanks to its high dielectric permittivity and stability on silicon. In recent years, the microelectronics industry has widely adopted HfO_2 as a high-k gate dielectric to mitigate excessive tunneling leakage currents in ultra-thin SiO_2 gates, a challenge exacerbated by device scaling [41]. Beyond transistor applications, HfO_2's unique properties, including a relatively large electronic bandgap and high dielectric constant, have made it an essential material for various technologies, including metal-insulator-metal (MIM) capacitors in DRAM [42].

The discovery of ferroelectricity in doped HfO_2 thin films, first reported in 2011 [43], has significantly advanced the development of ferroelectric memories by enabling compatibility with CMOS, scalability, and the elimination of toxic lead. Böscke *et al.* first demonstrated ferroelectricity in SiO_2-doped HfO_2 thin films deposited via ALD [43]. This ferroelectric behavior is attributed to the formation of a non-centrosymmetric orthorhombic phase (space group $Pca2_1$), a metastable phase not found in the phase diagram of HfO_2 [43]. Since this breakthrough, extensive experimental and theoretical studies have been conducted, deepening our understanding of HfO_2-based ferroelectric materials and their promising applications [44–51].

2.4 Formation and stabilization of the ferroelectric phase in HfO_2-based films

The stabilization of the metastable ferroelectric orthorhombic phase (o-phase) in HfO_2-based films is a complex process influenced by multiple factors. As previously discussed, this phase is not thermodynamically favorable under standard conditions, requiring careful engineering of deposition and processing parameters.

Unlike PZT, which crystallizes in the perovskite ABO_3 structure, ferroelectric HfO_2 belongs to the fluorite family of oxides (AO_2) [45]. The ideal fluorite structure, exemplified by CaF_2, is cubic (space group $Fm\bar{3}m$) and consists of a face-centered cubic (FCC) arrangement of cations, with anions occupying all the tetrahedral interstitial sites. In doped HfO_2-based ferroelectrics, the cation sublattice is primarily composed of Hf atoms partially substituted by dopant species such as Zr, Si, Y, Al, or Gd, while O^{2-} anions occupy the tetrahedral positions. Each cation is coordinated by eight oxygen anions, and each oxygen is coordinated by four cations. The most thermodynamically stable phase of HfO_2 at ambient conditions is monoclinic, which is centrosymmetric and therefore non-ferroelectric. Ferroelectricity emerges when doping, strain, or reduced dimensions stabilize a metastable non-centrosymmetric orthorhombic phase (space group $Pca2_1$), in which asymmetric displacements of the oxygen sublattice relative to the mixed cation lattice generate a spontaneous polarization. This mechanism is fundamentally distinct from the polarization in perovskite ferroelectrics and highlights the unique structural origin of ferroelectricity in HfO_2-based systems.

Fig. 1.8b provides a qualitative diagram describing the influence of key process parameters on the crystallinity and phase transitions of doped HfO_2 thin films. The model shows that higher thermal budgets, lower dopant concentrations, or greater film thicknesses favor the formation of the monoclinic phase, while the opposite conditions promote tetragonal or cubic phases. The orthorhombic ferroelectric phase exists near the boundary between these paraelectric phases. The relative importance of these parameters varies with the type of dopant used, allowing targeted optimization for desired ferroelectric behavior.

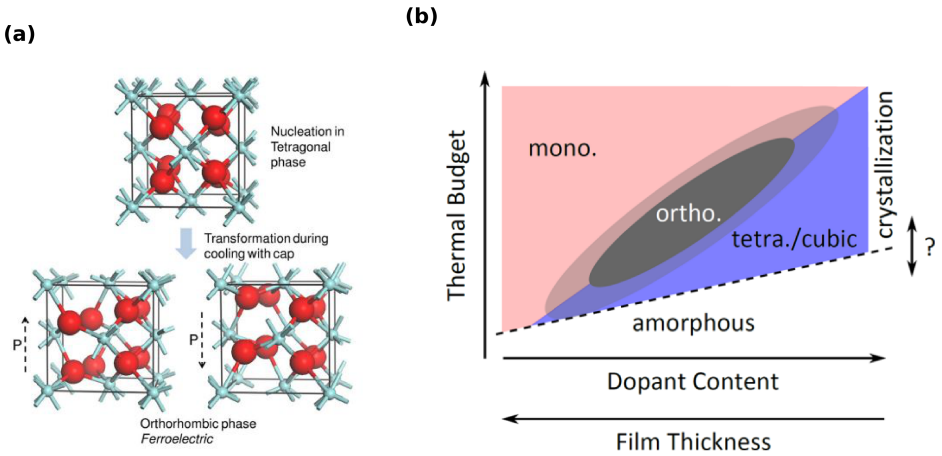

Figure 1.8: a. The formation of the orthorhombic phase proceeds by transformation from the tetragonal phase during cooling with a cap [43]. **b.** Qualitative model of the phase transitions of HfO_2 influenced by the most important process parameters [52].

2.4.1 Deposition techniques

Table 1.2: Key deposition methods for ferroelectric HfO_2-based thin films, with main advantages, limitations, and integration notes.

Method	Advantages	Limitations	Notes
ALD	Precise thickness control; high uniformity; CMOS-compatible	Sensitive to precursor and process conditions	Most used for scalable integration [44]
PVD	Low-temp deposition; low carbon contamination	Poor step coverage; dopant and stoichiometry control challenges	Low $2P_r$ in reactive sputtering [53, 54]
CSD	Low cost; large-area potential	Inhomogeneity and stoichiometric variation	Promising for low-cost uses [44]
PLD	Good compositional control; o- and rhombohedral phase stabilization	High temperature; costly equipment	Used in lab-scale demonstrations [55]

Various deposition methods have been employed to fabricate ferroelectric HfO_2-based thin films, each offering distinct advantages and posing specific challenges in terms of microstructure control, phase stabilization, and integration compatibility. **Table 1.2** summarizes the key characteristics of the most commonly used techniques, including their strengths, limitations, and relevance for scalable device applications [44, 53–55].

Among the available deposition techniques, ALD has emerged as the most promising approach for producing ferroelectric HfO_2-based thin films. ALD provides sub-nanometer control over thickness, excellent film uniformity across large areas, and conformal coverage of high-aspect-ratio structures, all of which are crucial for advanced device architectures. Its self-limiting surface reactions enable precise stoichiometry control and facilitate the incorporation of dopants at low concentrations with high reproducibility. Importantly, ALD is already widely adopted in the semiconductor industry for high-k dielectrics, ensuring full compatibility with CMOS process flows and scalability to high-volume manufacturing. These features position ALD as the most attractive deposition method for integrating ferroelectric HfO_2 into next-generation memory and logic devices. For this reason, the thin films investigated in this work were fabricated by ALD, and the specific process conditions will be described later in the manuscript.

2.4.2 Impact of different precursors on ALD deposition

In ALD, precursor selection strongly influences the structural and electrical properties of HfO_2 thin films [56]. Organometallic precursors (e.g., hafnium alkylamides) offer high volatility and low-temperature deposition but often lead to carbon contamination from residual ligands, which can degrade dielectric properties and increase leakage. Achieving high film purity with these precursors typically requires strong oxidants like ozone or plasma [57].

When optimized, organometallic precursors can yield dense and even crystalline films during deposition. Such crystallinity, observed in some cases, can contribute to enhanced ferroelectric performance by promoting favorable phase formation [58]. For instance, a 10 nm ferroelec-

tric HfO_2-based film with controlled carbon levels reached remanent polarization values near 40 $\mu C/cm^2$ [59–61]. This is linked to reduced lateral grain size and the stabilization of metastable orthorhombic phase, rather than the non-ferroelectric tetragonal and monoclinic phases.

In contrast, halide precursors like $HfCl_4$, used in this work, offer advantages in terms of film purity by significantly reducing carbon contamination. During the ALD cycle, the oxidant reacts with the metal–chlorine precursor complex, breaking the metal–Cl bond and replacing it with oxygen. This ligand-exchange reaction releases chlorine as a volatile byproduct (e.g., HCl), leaving behind a metal–oxygen bond. Nevertheless, they may introduce chlorine residues during deposition, which is why high processing temperatures and effective oxidant exposure are essential to minimize Cl incorporation. Although they require higher deposition temperatures and present challenges due to their low vapor pressure, a well-optimized halide-based ALD process can produce dense, low-defect films with minimal impurities [57].

$HfCl_4$ is also a well-established precursor for high-k HfO_2 deposition in transistor gate stacks, valued for its ability to form high-purity and conformal films [62]. Notably, both $HfCl_4$ and $ZrCl_4$ originate as byproducts of the nuclear industry, where they are recovered during the separation and purification of hafnium and zirconium [63]. Their reuse in microelectronics adds a valuable sustainability aspect to their application.

2.4.3 Doping effect

A wide variety of dopant elements has been explored to stabilize ferroelectricity in HfO_2-based thin films. Ferroelectricity has been observed in $Hf_{1-x}M_xO_2$ films (10 nm), where M represents dopant metals such as Si, Zr, Y, Al, Gd, Sr, and La, typically deposited by ALD [64–66]. The prevailing understanding is that the ferroelectric phase emerges from the high-temperature tetragonal (t) phase upon cooling. Dopants inhibit the transformation into the thermodynamically stable monoclinic (m) phase by lowering the formation energy of metastable o- phase, thus facilitating ferroelectric behavior [44].

Among these dopants, Zr is particularly effective for two main reasons. First, Zr can be incorporated at concentrations exceeding 50% due to its similar chemical and structural properties to Hf, whereas other dopants typically remain stable at <20%. By alternating Hf and Zr precursors in a 1:1 ratio via ALD, highly homogeneous and reproducible $Hf_{0.5}Zr_{0.5}O_2$ (HZO) films can be manufactured at a mass-production scale. Second, HZO films can exhibit ferroelectricity at relatively low processing temperatures, as the crystallization temperature of ZrO_2 is lower than other high-k dielectrics [66].

2.4.4 Influence of the electrodes

The choice of electrodes directly affects the formation and switching behavior of the ferroelectric phase in HZO, influencing both crystal phase stability and polarization characteristics. Common electrode materials include TiN, TaN, Pt, Ni, and W, each affecting the ferroelectric response through a combination of mechanical stress, interfacial reactions, and their ability to screen polarization charges. Inadequate screening can result in a depolarization field that opposes the spontaneous polarization, potentially suppressing or destabilizing the ferroelectric state [67].

Mechanical stress is one important factor, particularly in HZO films sandwiched between top and bottom electrodes, as it can help stabilize the orthorhombic ferroelectric phase. However, electrode-induced stress is not the only contributor. Interfacial chemistry and oxygen vacancy dynamics also play critical roles. For example, Kim *et al.* showed that HZO films annealed at 400°C after TiN top electrode deposition exhibited significantly higher remanent polarization compared to those annealed before electrode deposition [68]. While this was initially attributed to the capping layer effect, where tensile stress from the top electrode promotes the orthorhombic phase, other concurrent mechanisms such as suppression of oxygen loss and altered interface formation may also contribute to the observed behavior.

Moreover, the electrode material can significantly influence the chemical stability of the HZO layer. Nitride-based electrodes like TiN and TaN can scavenge oxygen from the ferroelectric film during processing, resulting in the formation of interfacial oxides and an increase in oxygen vacancy concentration. These vacancies may accumulate near the electrode interface or migrate through the ferroelectric layer, modifying local electronic structure and altering the effective work function. Such changes impact not only phase stability but also endurance and retention in HZO-based devices [69].

2.4.5 Effect of annealing

The annealing temperature is crucial for stabilizing the ferroelectric orthorhombic phase in polycrystalline HfO_2- and ZrO_2-based films. For FeRAM applications, annealing must be BEOL-compatible (< 500°C) to integrate with CMOS technology, though the optimal temperature depends on dopant type, concentration, and processing conditions.

Several annealing techniques are employed to optimize phase formation, including Rapid Thermal Annealing (RTA), furnace annealing, and Nanosecond Laser Annealing (NLA), each offering distinct advantages. RTA is widely used due to its rapid heating and cooling cycles, which minimize undesirable diffusion effects and interfacial reactions while promoting controlled crystallization [70]. Furnace annealing, while providing a uniform temperature distribution, can lead to extended exposure effects that influence dopant redistribution and grain growth [71]. In contrast, NLA enables ultra-fast crystallization by delivering localized high-energy pulses, reducing overall thermal impact on underlying layers [72].

Beyond temperature control, mechanical stress induced during annealing plays a significant role in stabilizing the ferroelectric phase. The mismatch in thermal expansion coefficients between materials in the MFM stack can introduce tensile strain during thermal cycling, facilitating the formation of the ferroelectric orthorhombic phase [73].

2.5 Intrinsic phenomena in ferroelectric HfO_2-based films

The discovery of ferroelectricity in thin films of HfO_2-based materials has sparked significant interest due to their potential for scaling and integration in advanced memory devices. Despite these advantages, HZO ferroelectric thin films are not without their challenges.

Generally, the observed hysteresis in the pristine state (corresponding to the first cycle,

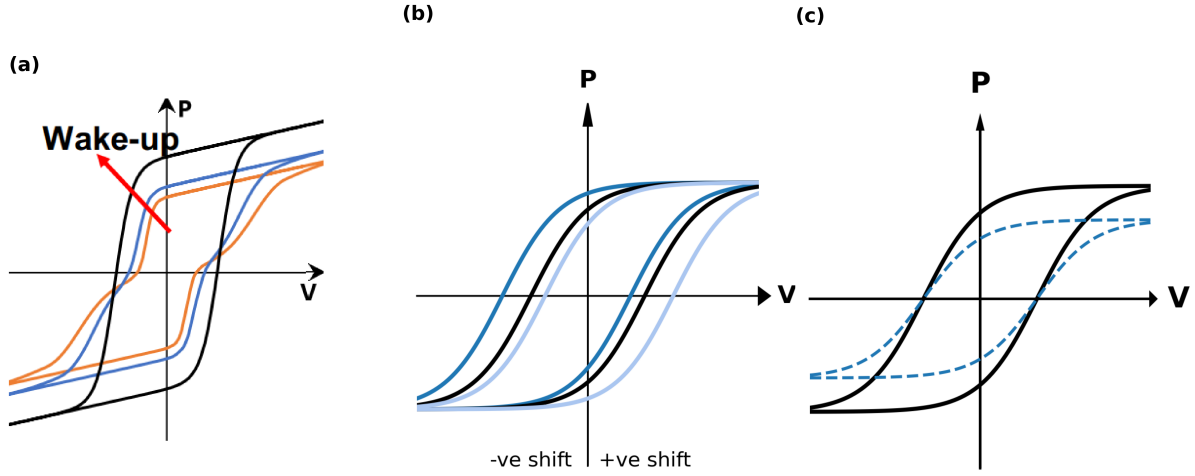

Figure 1.9: a. Wake-up, increasing the remanent polarization and coercive voltage distribution. **b.** Imprint, causing a bias-shift on the hysteresis loop. **c.** Fatigue, causing a decrease in the remamnent polarization. The desired polarization behavior is represented by the black curve, while the colored curves illustrate the respective phenomena affecting the ferroelectric response.

colored curves in **Fig. 1.9**a) is pinched, but it opens up during cycling. This increase in remanent polarization after several switching cycles is known as the wake-up effect, **Fig. 1.9**a. One proposed explanation for this phenomenon is a phase transformation from the tetragonal (antiferroelectric) to the orthorhombic (ferroelectric) phase, supported by changes in the dielectric constant during cycling [74–76].

Alternatively, the wake-up effect has also been linked to the redistribution of defects, particularly oxygen vacancies introduced during processes such as ALD and annealing. These vacancies can create an internal electric field that initially destabilizes the ferroelectric polarization, leading to a pinched loop. As cycling progresses, the redistribution of these defects reduces the internal field and allows for more uniform dipole switching, resulting in increased remanent polarization [77, 78].

Another contributing factor is the depolarization field (E_{dep}) arising from incomplete screening at the electrodes and interfacial "dead layers." During the early cycles, carriers injected from the electrodes and mobile oxygen vacancies migrate toward interfaces and grain boundaries, where they become trapped and partially compensate the bound polarization charge. This charge redistribution could increase interfacial capacitance (and reduce the dead-layer impact), lowering E_{dep}, unpinning domains, and opening the loop, thus raising $2P_r$ [67, 79, 80].Despite these insights, there is still no consensus on the exact origin of the wake-up effect, and it is likely the result of a combination of mechanisms.

The imprint effect is another important characteristic in HfO_2-based ferroelectric materials (**Fig. 1.9**b). In this case, the colored curve represents a shifted hysteresis loop due to internal built-in fields, while the black curve corresponds to the ideal symmetric behavior. The imprint effect refers to a voltage shift in the polarization hysteresis loop, which can lead to increased operating voltages, degraded retention characteristics, and potential write failures in ferroelectric memory devices. This effect has been observed in HfO_2-based ferroelectric capacitors, even at

room temperature, during polarization retention [81]. The origin of imprint remains under debate; proposed mechanisms include the formation of an oxygen-vacancy concentration profile within the ferroelectric film and/or charge injection from the electrodes into an interfacial layer at the ferroelectric/electrode interface [82–85]. During operation, mobile carriers can drift and accumulate near the interfaces, leaving a residual internal field after the external bias is removed.

Endurance degradation, also known as fatigue, **Fig. 1.9**c, is also a significant issue in HfO_2-based ferroelectric materials. The colored curve illustrates the reduced remanent polarization after extensive cycling, while the black curve represents the desired stable ferroelectric response. Fatigue refers to the reduction in $2P_r$ after repeated cycling, limiting the material's long-term reliability. In conventional perovskite-based ferroelectrics, fatigue is often attributed to domain pinning caused by the accumulation of defects, such as oxygen vacancies, at the electrode interface or within the material. Similarly, in HZO films, fatigue is thought to arise from the generation and migration of oxygen vacancies, which pin ferroelectric domains and reduce their ability to switch effectively. Additionally, leakage currents and thermal defect generation during cycling can exacerbate breakdown and further accelerate the degradation process [86, 87].

Together, the wake-up effect, imprint, and fatigue represent key reliability concerns in HfO_2-based ferroelectrics. Reducing the wake-up effect is essential to minimize the number of cycles required to stabilize polarization, while controlling imprint is critical to ensure symmetric switching and retention stability. Addressing fatigue is equally important, as it directly impacts the endurance of ferroelectric devices.

3 Comparing single-matrix and multilayer ferroelectric structures

To further optimize important characteristics of ferroelectric films, superlattices have emerged as a promising alternative approach (**Fig. 1.10**). This development is specifically targeted at improving upon the reference material, which is the solid solution of $HfZrO_2$ with a 1:1 ratio of Hf and Zr. While the reference material provides a balanced ferroelectric performance, including decent remanent polarization (40 $\mu C/cm^2$ for 10 nm film with a BEOL anneal in [88]) and endurance. Nevertheless, challenges remain for HZO, including maintaining robust ferroelectricity at reduced thicknesses, improving endurance under extensive cycling, and mitigating leakage [44].

Superlattices have been proposed to address these limitations. They can enhance remanent polarization by 10–30%, reduce leakage currents by an order of magnitude, double endurance lifetimes, are also said to allow tailoring of the coercive field, and offer better reliability characteristics [47, 89–93].

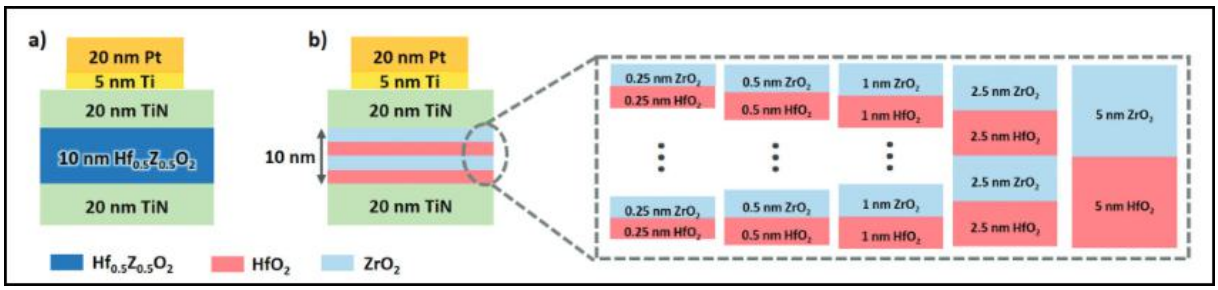

Figure 1.10: a. Schematic cross section of the metal-ferroelectric-metal (MFM) stack used to characterize the ferroelectric films. Figure a shows the reference device with the single phase HZO solid solution. **b.** illustrates the integration of the $[HfO_2/ZrO_2]$ superlattices into the MFM stack [89].

Although neither HfO_2 nor ZrO_2 are ferroelectric in their most stable forms, monoclinic paraelectric for HfO_2 and tetragonal antiferroelectric for ZrO_2, studies have demonstrated that their combination in a stacked architecture can induce ferroelectricity [94, 95]. This is attributed to the formation of polycrystalline superlattices with local epitaxial ordering within columnar grains, enabling the stabilization of the noncentrosymmetric orthorhombic ferroelectric phase.

One of the main motivations for employing superlattices is their potential to better stabilize the ferroelectric orthorhombic phase while reducing the fraction of the non-ferroelectric monoclinic phase. The layer stacking sequence appears to play a crucial role in this process. Some reports suggest that starting a multilayer structure with ZrO_2 promotes monoclinic phase formation, leading to lower remanent polarization [89, 96], whereas others indicate that the same configuration enhances 2Pr and endurance throughout cycling [47, 90]. These discrepancies highlight the complexity of superlattice behavior, suggesting that deposition conditions, layer thickness, and interface interactions significantly influence the final properties.

The thickness of each sublayer in superlattices is another critical factor that distinguishes them from the solid solution reference material. Research has shown that varying the thickness

of the HfO_2 and ZrO_2 layers affects lattice integrity, interface defects, and strain distribution [97, 98], directly influencing the final electrical performance of the material. A common finding across multiple studies is that thinner unit layers, provide the best ferroelectric properties. A 1 nm/1 nm thickness ratio of HfO_2 to ZrO_2 has been identified in multiple studies as delivering the highest remanent polarization and the lowest leakage current [89, 92, 98], outperforming the HZO solid solution. According to these same studies, this enhancement is likely due to the more effective management of mechanical stress at the interfaces between layers and thermal mismatch stress-induced distortion, which play a key role in the formation of different crystalline phases.

Despite this agreement on the advantages of ultrathin sublayers, there is no clear consensus on the most effective stacking configuration to achieve reproducible improvements over solid-solution HZO. There is still ambiguity as to whether the sequence should begin or end with HfO_2 or ZrO_2, and whether symmetric or asymmetric layer arrangements are more favorable. Moreover, it is still debated whether multilayer architectures can consistently surpass solid-solution HZO in addressing critical challenges such as endurance, leakage, wake-up behavior, and scalability. The overall ferroelectric properties of these multilayers are influenced by multiple interconnected factors, including unit layer thickness, layer stacking sequence, interface quality, and thermal processing. While some studies suggest that superlattices enhance remanent polarization and endurance, others report that certain configurations can lead to increased monoclinic phase fraction, affecting ferroelectric stability.

In addition to these structural considerations, the impact of thickness scaling in multilayer systems remains an open question. As ferroelectric layers continue to be reduced in total thickness to meet the demands of next-generation devices, it is unclear whether ultra-thin multilayers will retain their integrity throughout the full manufacturing process. This raises concerns about whether the enhanced properties observed in thicker multilayers will persist at reduced thicknesses or if additional trade-offs, such as increased leakage or reduced polarization stability, will emerge.

Questions still persist regarding the optimal sublayer thickness for achieving both high polarization and long-term reliability, the trade-off between leakage current and endurance, and the role of ferroelectric-electrode interfaces in determining switching behavior and device performance. Given these uncertainties, further investigation is crucial to unravel the mechanisms governing the behavior of these complex multilayer systems.

4 The importance of thickness reduction in ferroelectric capacitors

Despite the advantages of FE-HfO_2 materials, two crucial challenges must be addressed to meet the requirements for embedded FeRAM applications. The first major challenge is reducing the operating voltage. While HZO-based capacitors are typically deposited at thicknesses as low as 10 nm, they still exhibit a relatively high coercive field (E_c) of approximately 1.5 MV/cm. Given that the operating voltage is directly dependent on thickness and coercive field, a 10 nm-thick FE-HfO_2 capacitor still requires around 3 V for operation, which is significantly higher than that of conventional FeRAMs based on PZT, where 100 nm-thick films typically exhibit coercive fields below 0.1 MV/cm [99]. This high voltage requirement remains a critical limitation for scaling FE-HfO_2 into advanced silicon technologies, where lower voltage operation is essential for energy efficiency and compatibility with embedded systems [52].

A second key challenge is the limited breakdown tolerance of FE-HfO_2 materials. FE-HfO_2 suffers from an E_{BD} that is much closer to its operating field. This leads to premature dielectric breakdown during extended switching cycles, reducing device endurance and reliability [99].

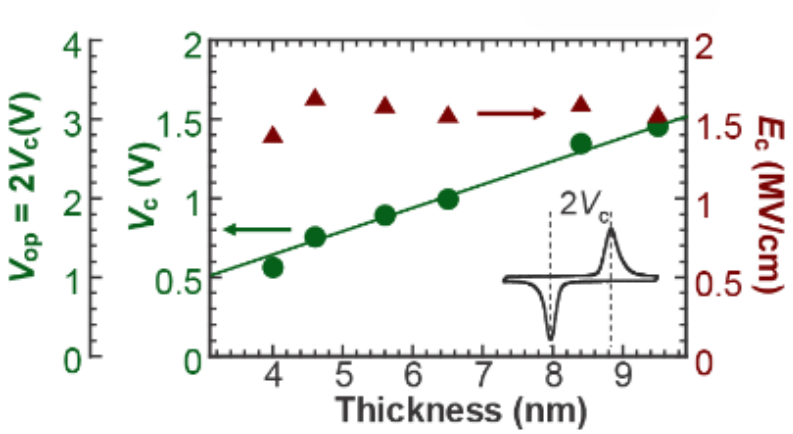

Figure 1.11: Coercive voltage V_C for ferroelectric capacitors with different HZO thicknesses. V_C decreases with decreasing HZO thicknes [99].

One of the most promising approaches to overcoming these limitations is reducing the total thickness of the ferroelectric layer. Thinner FE-HfO_2 capacitors enable lower operating voltages because the same coercive field can be reached with a smaller applied voltage. This makes them particularly attractive for high-performance memory applications, where low-power operation and energy efficiency are critical [18]. As seen in **Fig. 1.11**, the coercive voltage decreases with thinner layers, making these capacitors ideal for next-generation low-power embedded FeRAM solutions [100]. Additionally, it is found that the breakdown field is substantially improved in thinner HZO since the breakdown mechanism is dominated by the stress voltage, not the stress field, resulting in improved endurance characteristics for thinner films [99].

However, despite these benefits, further miniaturization of HZO films presents new challenges. One significant issue is the increased crystallization temperature required for ultra-thin

films. As the thickness decreases, it becomes more difficult to stabilize the desired ferroelectric orthorhombic phase, often requiring higher annealing temperatures. This is due to the higher energy barriers associated with crystallization in thinner layers, complicating integration into thermal budget-limited processes [101, 102].

While reducing the thickness of FE-HfO_2 is a promising strategy to lower operating voltages and enhance device endurance, its successful integration requires overcoming new material and processing challenges. Further investigations are essential to determine the ultimate limits of thickness scaling while ensuring reliable performance. In parallel, alternative processing methods, such as dopant content and optimized annealing, must be explored to enhance phase stability in ultra-thin films. Addressing these challenges will enable scalable, energy-efficient FeRAMs for next-generation memory applications.

5 Objectives of the thesis

The aim of this thesis is to develop and investigate ultrathin HfO_2-based ferroelectric layers deposited by ALD, fabricated into MFM capacitor structures. The capacitors are processed on 300 mm wafers to reflect industrial fabrication conditions, with the goal of understanding how material properties evolve throughout each stage of the MFM stack fabrication process. The study explores different structural configurations and compositions to assess their influence on ferroelectric behavior, focusing on properties such as crystallinity, morphology, and chemical composition. Although the work is centered on capacitor-level structures, the broader objective is to support the development of HfO_2-based ferroelectric layers for future application in integrated non-volatile memory arrays.

- **Investigate the impact of composition on ferroelectric properties**:

  This objective focuses on understanding how changing the ratio between HfO_2 and ZrO_2 affects the formation and stability of the ferroelectric metastable phase. By deliberately fabricating films with different Hf:Zr ratios, this study aims to observe how composition influences key ferroelectric properties such as remanent polarization, leakage current, and wake-up behavior. Both 10 nm and sub-10 nm structures are explored to identify which compositions best support stable and robust ferroelectric switching, contributing to the development of ultrathin ferroelectric films for memory applications.

- **Analyze the influence of top electrodes and crystallization anneal**:

  This study investigates how the choice of top electrode materials influences the crystallization behavior and structural characteristics of HfO_2-based thin films. Materials such as TiN and W are examined for their effect on film stress and crystallinity, and how these factors can affect phase formation and, consequently, electrical performance. Additionally, the impact of post-deposition annealing parameters, specifically temperature and duration, are explored to understand their effect on phase evolution and ferroelectric response. Particular attention is given to processing conditions that are compatible with BEOL integration, as this is essential for the practical implementation of ferroelectric materials in advanced memory devices. The aim is to clarify how these processing conditions contribute to the emergence and stability of ferroelectric behavior in ultrathin films.

- **Compare single-matrix and multilayer HfO_2/ZrO_2 structures**:

  By comparing single-matrix HZO films with multilayered HfO_2/ZrO_2 structures, this objective aims to investigate the potential advantages that multilayer designs offer in terms of electrical performance. The presence of internal interfaces in multilayers may act as barriers to leakage current and contribute to improved dielectric breakdown strength. Additionally, these interfaces can help limit defect propagation and support more stable polarization behavior. This comparison helps to determine whether multilayer configurations provide improved ferroelectric properties compared to single-matrix structures.

- **Understand the effects of thickness downscaling on ferroelectric performance**:

This objective aims to investigate the impact of reducing the total thickness of HZO structures from 10 nm and below and if these structures can maintain optimal ferroelectric properties while minimizing power consumption. Thinner ferroelectric films offer benefits for low-power operation and device scaling but may also introduce trade-offs in performance and stability. This study seeks to evaluate these effects and identify suitable processing conditions for maintaining reliable ferroelectric behavior at reduced dimensions.

This thesis explores ultrathin HfO_2-based ferroelectric layers for non-volatile memory applications, beginning with the foundational principles of ferroelectricity and the motivations behind adopting HfO_2-based systems. It follows a path through the experimental strategies used to develop and analyze these materials, emphasizing the relationship between structural properties and device behavior.

Chapter 2

Experimental techniques and methodologies

Objectives

Chapter 1 provided a comprehensive overview of HZO's promising role in ferroelectric memory applications, emphasizing its CMOS compatibility, scalability, and low-temperature ferroelectric properties. The current chapter delves into the key characterization methods and fabrication steps essential for developing sub-micrometer-sized ferroelectric capacitors (FeCAPs) compatible with back-end-of-line (BEOL) processes. It details the sample fabrication and deposition techniques, including atomic layer deposition (ALD) for ferroelectric layers and physical vapor deposition (PVD) and chemical vapor deposition (CVD) for metallic layers. Initial material characterization methods are introduced, followed by techniques to study processing steps, such as transmission electron microscopy (Transmission Electron Microscope (TEM)) and energy-dispersive X-ray spectroscopy (EDX). The crystallization of the ferroelectric layer is assessed through grazing-incidence X-ray diffraction (Grazing Incidence X-ray Diffraction (GIXRD)) and in-plane XRD, while TOF-SIMS and XPS provide detailed chemical insights. The chapter then explores the fabrication of the devices to investigate the properties of deposited stacks, followed by a description of optimized BEOL integration over 300 mm CMOS wafers. Finally, it highlights electrical characterization methods, including PUND and quasi-static I-V methods, to evaluate FeCAP performance. This descriptive chapter aims also to present limitation of characterization techniques, and constraints of the integration routes.

Contents

1 Deposition techniques **29**
1.1 ALD deposition of ferroelectric layers 29
1.2 Deposition of metallic layers by PVD or CVD 32
2 Material characterization **35**
2.1 X-ray Reflectometry 35
2.2 Wavelength Dispersive X-Ray Fluorescence 37
2.3 X-ray Diffraction 37
2.4 Transmission Electron Microscopy 41
2.5 Secondary-Ion Mass Spectrometry 42
2.6 X-ray Photoelectron Spectroscopy 43
2.7 Bow measurement 44
3 Fabrication of the studied electrical devices **47**
3.1 300 mm MFM structures 47
3.2 Annealing 47
4 Methodologies for electrical characterization **49**
4.1 PUND : a technique to extrapolate ferroelectric metrics 49
4.2 Quasi-static I-V characteristics 51
5 Chapter Summary and Conclusions **54**

1 Deposition techniques

The upcoming sections will explore the fabrication processes essential for developing the main stack of the MFM structure, which forms the core of ferroelectric memory devices. The ALD of ferroelectric materials will be discussed, a critical technique for creating uniform and high-quality ultrathin films. This will be followed by the deposition of metallic layers via Physical Vapor Deposition (PVD) and Chemical Vapor Deposition (CVD), highlighting their importance in forming the electrode interfaces.

1.1 ALD deposition of ferroelectric layers

Atomic Layer Deposition (ALD) is a precise thin-film growth technique based on self-limiting surface reactions. Precursor gases are introduced sequentially, each reacting only with the surface and not with itself, allowing the formation of one monolayer per cycle. Purge steps between precursors prevent unwanted reactions, enabling atomic-scale control over film thickness and composition.

During ALD, precursor molecules react with surface active sites (adsorption), avoiding any reaction in the gas phase. This selective interaction ensures a controlled layer formation. Precursor adsorption occurs through two main mechanisms: chemisorption and physisorption. Physisorption involves weak, low-energy bonds and is a reversible process without any chemical transformation of the adsorbed molecules. Conversely, chemisorption forms stronger, high-energy bonds, leading to irreversible chemical reactions that result in the formation of stable chemical bonds between the surface and the adsorbed molecules. In ALD, mainly chemisorption contributes to the actual deposition process, as it allows for the formation of a monolayer that covers the surface.

In this work, the HZO layers were deposited by thermal ALD, which involved the following steps, drawn in **Fig. 2.1 :**

1. Gaseous precursor A reacts with the substrate until a full conformal coat of the surface is obtained. In **Fig. 2.1 ,** a pulse of metal precursor $HfCl_4$ or $ZrCl_4$ reacts with surface –OH groups until saturation, forming surface –O–MCl_x species and releasing HCl as byproduct.

2. Excess of precursor A and byproducts are purged away. In **Fig. 2.1 ,** the excess precursor and HCl are removed.

3. Gaseous precursor B reacts with the ligands of precursor A until a full conformal coat with submonolayer is achieved. In **Fig. 2.1 ,** a pulse of H_2O hydrolyzes the remaining –Cl ligands, regenerates surface –OH, and converts the surface to –O–M–O– while producing additional HCl.

4. Again, excess species and byproducts are purged away. In **Fig. 2.1 ,** excess H_2O and byproducts are evacuated.

Repetition of ALD cycles allows for the deposition of layers with a constant Growth Per Cycle (GPC), enabling precise control over the final film thickness based on the total number of

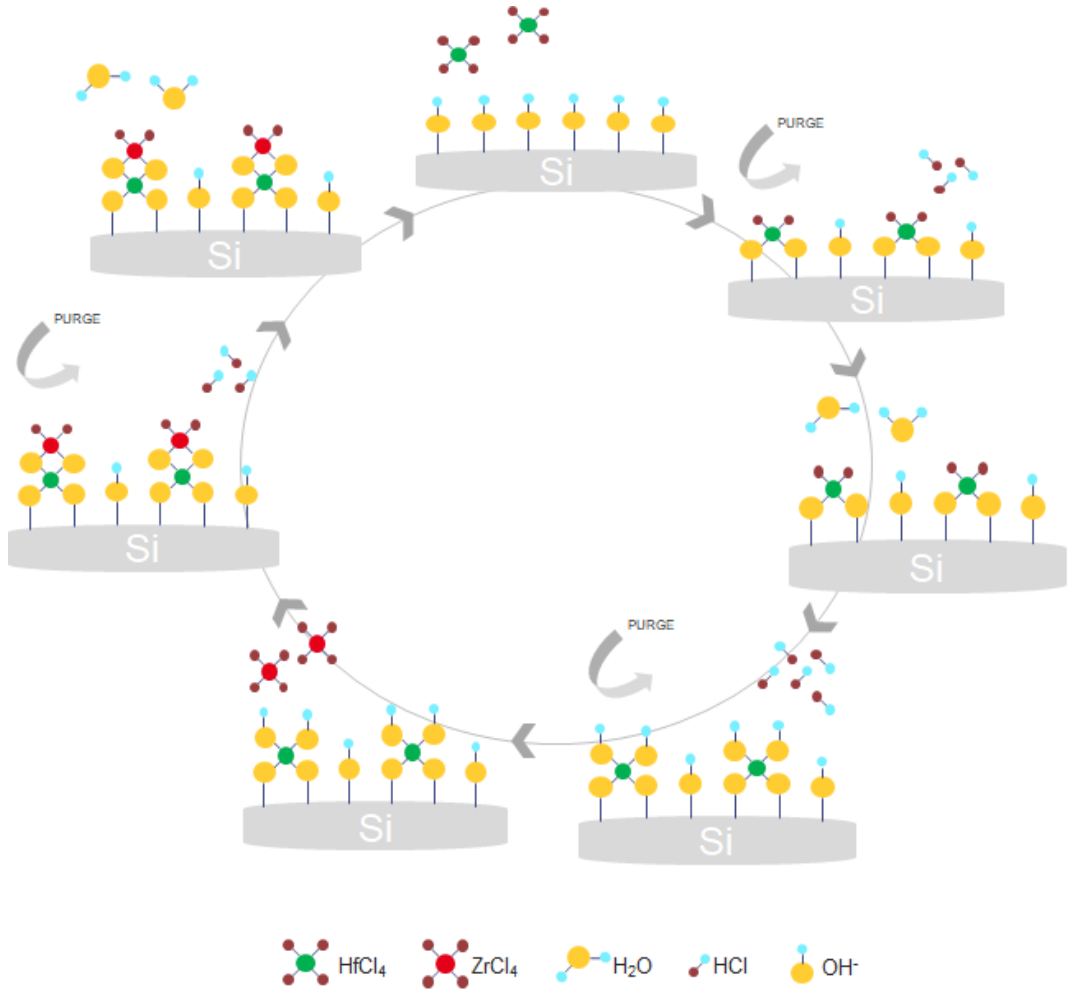

Figure 2.1: Sketches of the general principle of ALD. Each cycle consists of precursor adsorption ($HfCl_4/ZrCl_4$), purge, H_2O reaction to regenerate –OH groups, and a final purge, enabling controlled layer-by-layer growth.

cycles applied. GPC represents the average thickness increase per deposition cycle and reflects the efficiency and completeness of the surface reactions. This growth remains relatively constant within the so-called ALD temperature window, a specific temperature range where the precursor-surface interactions are optimized, self-limiting, and saturate the surface uniformly [103]. Within this window, each precursor pulse reacts only with the available surface sites, ensuring a linear and predictable film growth.

Outside this optimal window, the growth behavior deviates. At low temperatures (Regions 1–2), insufficient thermal energy may result in precursor condensation or incomplete reactions, limiting surface coverage and reducing GPC. Conversely, at elevated temperatures (Regions 3–4), precursor decomposition and desorption occur, deviating the process from ideal ALD mode and leading to non-uniform films or contamination [105–108]. These deviations are schematically illustrated in **Fig. 2.2 a**, which outlines the different growth regimes as a function of substrate temperature.

GPC is a critical parameter requiring careful calibration and is typically measured by ellip-

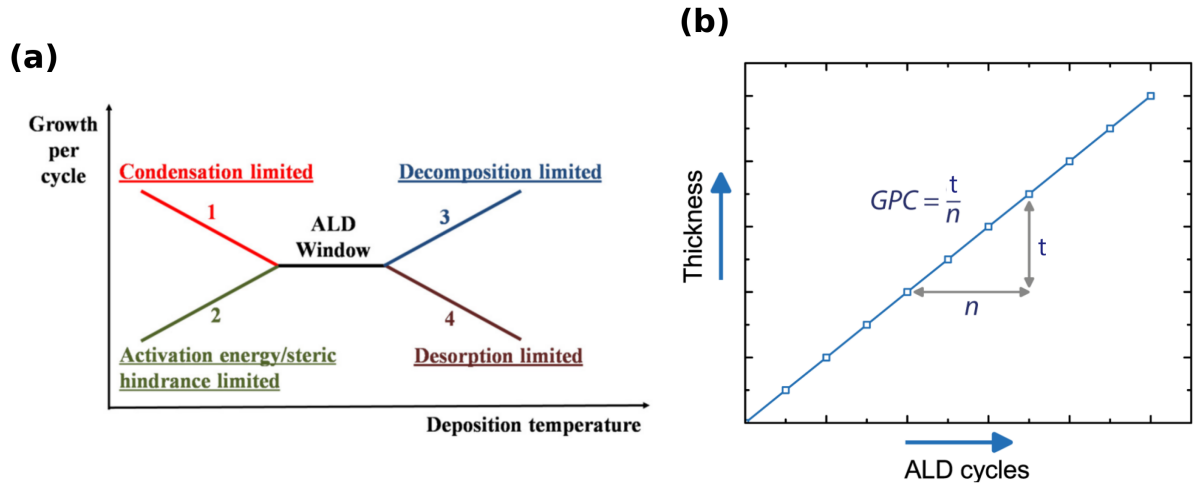

Figure 2.2: **a.** Schematic of ALD window [104]. **b.** The growth per cycle (GPC) can be defined as the slope of the thickness as a function of cycles.

sometry or reflectometry, **Fig. 2.2 b**. Stable GPC with increasing precursor dose and purge time indicates proper ALD mode. Otherwise, incomplete surface reactions or parasitic CVD may occur, leading to non-uniform films.

The ferroelectric films in this study were prepared by thermal ALD at 300°C using $HfCl_4$, $ZrCl_4$ as metal precursors and H_2O as the oxidant, with depositions performed in an ASM Polygon Pulsar chamber (photograph shown in **Fig. 2.3**). Each precursor pulse was followed by a N_2 purge to remove excess reactants and byproducts. The film thickness was controlled according to the GPC of each material, ensuring consistency with the established deposition process for precise layer thickness.

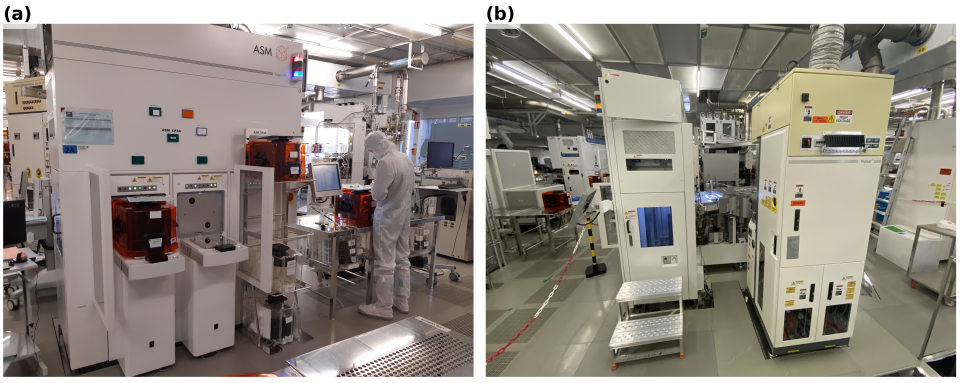

Figure 2.3: **a.** Fully automated ALD tool (ASM XP4) used in 300 mm cleanroom environment for large-scale integration and advanced process development. **b.** Photograph of the ASM Polygon Pulsar thermal ALD reactor used for the deposition of HfO_2-based ferroelectric films in this study.

The HZO solid solution was fabricated using the supercycle method seen in **Fig. 2.4 a**, which involves alternating individual ALD cycles of $HfCl_4$ and $ZrCl_4$ precursors, each followed by a water pulse to complete the oxidation step. This approach allows for atomic-level mixing of Hf

and Zr atoms within each growth cycle, resulting in a homogeneous composition throughout the film. By adjusting the ratio of HfO_2 to ZrO_2 cycles in each supercycle (e.g., 1:1 for $Hf_{0.5}Zr_{0.5}O_2$), it is possible to control the overall composition of the film.

In contrast, the multilayer structure in **Fig. 2.4 b** was deposited by sequentially stacking multiple cycles of HfO_2 and ZrO_2, forming compositionally distinct sublayers. The number of ALD cycles used for each oxide (x for HfO_2, y for ZrO_2) was determined based on the GPC of each material to achieve the desired sublayer thickness and the final thickness of the entire stack. This method enables control over both composition and layer stacking, offering a platform for engineering the internal interfaces, which can influence phase stabilization and ferroelectric properties.

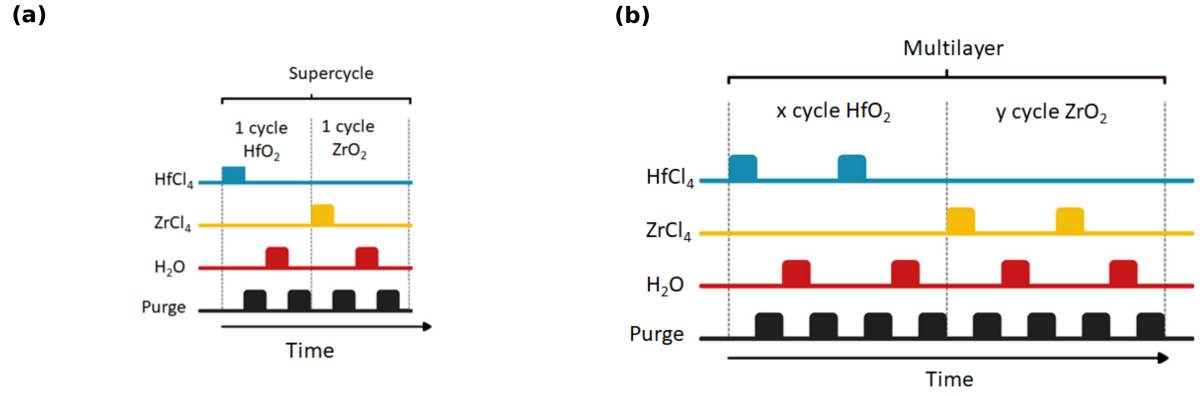

Figure 2.4: a. Supercycle approach used to fabricate $Hf_{1-x}Zr_xO_2$ solid solution films by alternating single ALD cycles of HfO_x and ZrO_y, promoting atomic-level mixing and uniform composition throughout the film. **b.** Multilayer approach used to deposit distinct HfO_2 and ZrO_2 layers by repeating x ALD cycles of HfO_2 followed by y cycles of ZrO_2, enabling defined interfaces and control of individual layer thickness and overall composition.

1.2 Deposition of metallic layers by PVD or CVD

In this thesis, the HfO_2-based layers were stacked between metallic layers deposited by physical vapor deposition (PVD) or chemical vapor deposition (CVD). All metal depositions were performed on an Endura platform from Applied Materials, using different chambers for each process.

PVD is a process used to deposit thin films by physically vaporizing a solid source material, such as a metal or ceramic, and transporting the vapor to a substrate in a vacuum or low-pressure environment, where it condenses to form a solid thin film. The main steps of PVD include:

1. A high-energy source, like sputtering or evaporation, heats and evaporates the material from the target.

2. The vaporized material is transported through the vacuum towards the substrate.

3. During transport, metallic atoms can react with reactive gases such as O_2, N_2, or CH_4, forming compounds like oxides, nitrides, or carbides.

4. The vapor condenses onto the substrate, covering its surface and forming a uniform thin film.

This technique was used to perform titanium nitride (TiN) deposition as bottom and top electrodes in the test vehicles. For TiN PVD, TiN is deposited by bombarding a titanium target with high-energy ions in a process known as sputtering. In this case, the titanium target is nitrided by a mixture of Ar and N_2 plasma, allowing the formation of TiN. The deposition is typically performed using a machine equipped with a DC power source applied to the target, although an RF generator can also be used depending on the material. Both configurations enable stable and efficient sputtering during the process. TiN films are highly valued for their hardness, corrosion resistance, and electrical conductivity, making them suitable for applications such as diffusion barriers in microelectronics and wear-resistant coatings. In this work, the deposition was carried out at room temperature.

The tungsten (W) metallic layer, also used as a top electrode, was deposited using the Seam Suppressed Process (SSP), a specialized technique in semiconductor manufacturing designed to deposit tungsten into vias and trenches while minimizing or eliminating seams and voids. This process is crucial for achieving low electrical resistivity, which is essential for ensuring efficient current flow in tungsten electrodes. Additionally, for electrodes, surface smoothness is critical to guarantee uniform contact with the semiconductor or dielectric materials.

The first step of the SSP is the CVD of titanium nitride (TiN), which serves as a crucial barrier and adhesion layer before W deposition. This TiN layer was deposited using Tetrakis(dimethylamido)titanium (TDMAT) as the precursor and nitrogen (N_2) as the carrier gas. The deposition occurs at a controlled temperature to ensure film uniformity. During the process, the precursor undergoes thermal decomposition in the presence of the carrier gas, leading to the formation of a conformal TiN layer. This step is essential for ensuring adhesion between the underlying material and the subsequently deposited tungsten while also acting as a diffusion barrier. The chamber pressure and precursor flow rates were precisely controlled to achieve a uniform TiN film of 10 nm thickness.

By following the SSP steps, a high-quality tungsten fill with minimal defects is achieved, making it ideal for applications in advanced semiconductor devices. The process involves the following key steps:

1. Deposition of a TiN barrier layer using CVD at 340°C to form a stable layer for tungsten deposition.

2. Exposure of the TiN layer to B_2H_6 to activate nucleation sites.

3. Deposition of a thin nucleation layer of tungsten (4-5 nm) using WF_6 at 380°C, ensuring uniform growth across the surface.

4. Bulk tungsten deposition over the nucleation layer, creating a thick, uniform, and seam-free tungsten layer for enhanced performance and reliability. This step is typically carried

out by continuing the WF_6-based process, enabling conformal growth over the nucleation layer.

The complete TiN CVD and W SSP deposition process lasts approximately 30 minutes, including about 20 minutes for the TiN step and 10 minutes for the W deposition.

2 Material characterization

2.1 X-ray Reflectometry

X-ray Reflectometry (XRR) is a non-destructive technique used to determine the thickness, density, and interface roughness of thin films by analyzing X-ray reflections at low incident angles. Interference patterns (Kiessig fringes) arise from reflections at film interfaces, as shown in the schematic in **Fig. 2.5**. Film thickness is extracted from fringe periodicity, density from the critical angle and amplitude, and roughness from fringe damping [109]. [110] showed that the analysis of the reflected intensity curve as a function of the glancing angle in the region of total reflection provides valuable information about near-surface structural properties. **Fig. 2.5** shows a typical reflectivity curve for a 10 nm HZO film, highlighting features used for structural analysis.

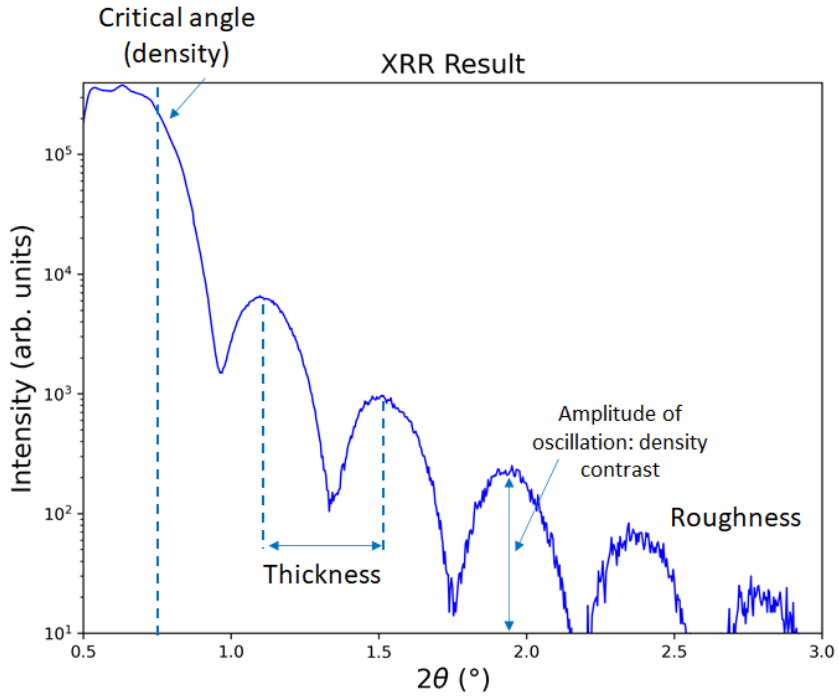

Figure 2.5: Example of XRR spectrum for an as deposited 10 nm-thick HZO layer on Si wafer. The critical angle and the information (density, thickness and roughness) extracted from the XRR spectrum are also pointed out.

When an electromagnetic wave hits a surface, Snell's law applies:

$$n_1 \sin i_1 = n_2 \sin i_2 \tag{2.1}$$

n_1 and n_2 are respectively the refractive indices of media 1 and 2 separated by an interface; i_1 is the angle between the incident beam and the normal to the interface. i_2 is the angle between the refracted beam and the normal (dotted lines in **Fig. 2.6**). In the case of X-rays, all the materials have a refractive index n_2 slightly lower than 1. Thus, it can be expressed as:

$$n_2 = 1 - \delta \tag{2.2}$$

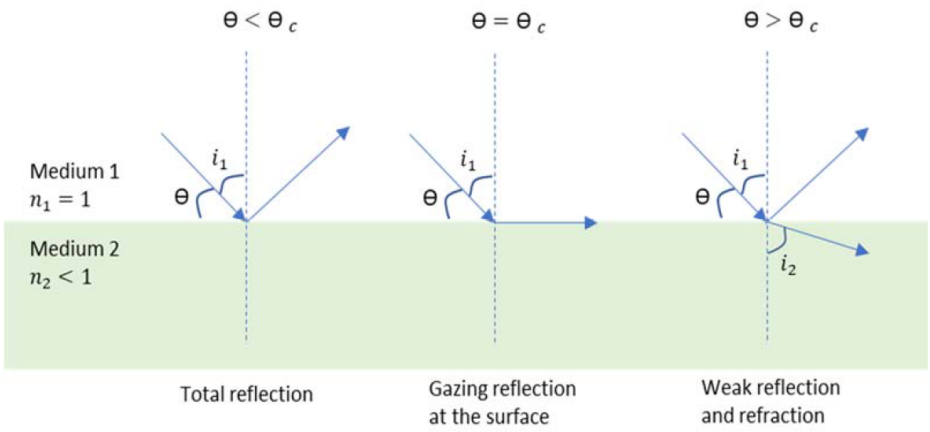

Figure 2.6: X-ray reflection and refraction at the air-material interface as a function of the angle of incidence θ.

The corrective term δ, which is of the order of 10^{-5} – 10^{-6}, is proportional to the electron density of the material ρ_e, to the electron radius r_e, and to the square of the incident beam wavelength λ:

$$\delta = \frac{\lambda^2}{2\pi} \cdot r_e \cdot \rho_e \tag{2.3}$$

Considering that in our case medium 1 is air (index $n_1 = 1$), the equation becomes:

$$\cos\theta = n_2 \cdot \sin(i_2) = (1 - \delta) \cdot \sin(i_2) \tag{2.4}$$

where θ is the angle between the sample surface and the incident beam. For a critical value θ_c, the reflected beam propagates by grazing the surface of the material ($i_2 = 90°$). Therefore, the critical angle is directly related to the electron density of the material, and it can be expressed as follows:

$$\cos\theta_c = 1 - \delta = 1 - \frac{\lambda^2}{2\pi} \cdot r_e \cdot \rho_e \tag{2.5}$$

If $\theta < \theta_c$ the entire beam is reflected outside the layer. This is the case of total reflection. If $\theta \geq \theta_c$ the incident beam is both reflected and refracted. From the measurement of θ_c, one deduces ρ_e, and hence the mass density if the composition of the studied material is known.

The refracted beam, which is then transmitted into the material, can be reflected and refracted each time it meets an interface (in the case of thin films, the interface between a capping layer and the film or the interface between the film and the substrate). This phenomenon gives rise to interferences between the first reflected beam and the successive reflected beams, being no longer in phase with the first one. The interference fringes, called Kiessig fringes, appear as oscillations on the XRR curve as a function of the scattering angle.

To a first approximation the period of the oscillations is proportional to the thickness of the thin film according to the relation:

$$t = \frac{\lambda}{2\,\Delta\theta} \tag{2.6}$$

With t the thickness of the film, λ the wavelength of the incident beam and $\Delta\theta$ the period of interference fringes. This relation is not valid for too small incident angles. The surface roughness r can be obtained from the amplitude of the fringes and the attenuation of the reflectivity curve.

In this study, XRR was employed to characterize the HZO layers. The experimental data were fitted using dedicated software to determine the structural properties of the films. For 300 mm wafers, XRR analysis was performed using the JVX XRR system (Jordan Valley) with a spot size of approximately 5 mm × 5 mm at $\theta = 10°$, utilizing a 50 μm × 5 mm slit and high-power X-ray sources (2 kW-15 kW). The fits for the 300 mm wafers were performed using Jordan Valley's software. For small samples (MFM coupons, that will be defined later), the analysis was conducted using the Empyrean system with a Cu source ($\lambda = 1.5406$ Å) at 45 kV and 40 mA, with incident slits set to 1/32°. The fitting for small samples was performed using the Panalytical software.

2.2 Wavelength Dispersive X-Ray Fluorescence

X-ray fluorescence (XRF) is a non-destructive analytical technique based on the photoelectric effect, widely used to determine elemental composition and mass deposition in bulk and thin films. In energy-dispersive XRF (EDXRF), the full emission spectrum is collected using a silicon drift detector, enabling fast analysis with small spot sizes (∼10 μm FWHM) but limited spectral resolution (≥120 eV). Wavelength-dispersive XRF (WDXRF), in contrast, employs crystals with defined lattice spacings mounted on a goniometer to selectively measure characteristic X-ray lines, offering higher resolution (5–25 eV) at the expense of larger measurement areas (≥10 mm) [111].

In this study, a Rigaku AZX400 WDXRF system was used to quantify Hf and Zr mass deposition and determine the Hf/Zr ratio in thin $Hf_xZr_{1-x}O_2$ films. The system operated at 30 kV and 100 mA to optimize excitation near the Zr-L_3 (2.223 keV) and Hf-M_5 (1.662 keV) absorption edges by enhancing Rh L-line emissions (Lα: 2.696 keV, Lβ: 2.834 keV). XRF intensities of Zr-Lα (2.044 keV) and Hf-Mα (1.646 keV) were measured using a Ge(111) crystal and a gas flow proportional counter. Due to the low XRF cross-section of oxygen, its quantification was not feasible in ultrathin ALD films.

In WDXRF, the absolute composition can be affected by systematic errors of up to 3% due to calibration uncertainties.

2.3 X-ray Diffraction

X-ray Diffraction (XRD) is a non-destructive technique used to analyze the atomic structure of crystalline materials. It relies on the constructive interferences of X-rays scattered by lattice planes, as described by Bragg's law:

$$2 \cdot d_{h,k,l} \cdot sin(\theta) = n_\lambda \cdot \lambda \tag{2.7}$$

where $d_{h,k,l}$ is the spacing between diffracting atomic planes, θ is the incident angle, n_λ is any integer, and λ is the wavelength of the beam. These specific directions appear as spots on the diffraction pattern called reflections.

XRD provides insights into crystallinity, phase composition, grain orientation, and strain. Different configurations and scanning modes allow selective probing of crystallographic planes, enabling structural analysis tailored to the sample's geometry and texture.

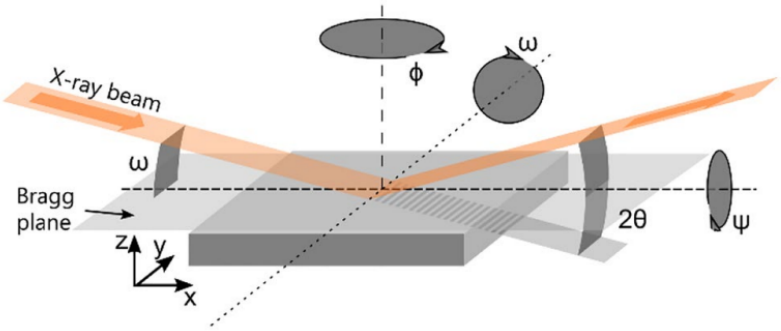

Figure 2.7: Schematic diagram of an X-ray diffraction (XRD) measurement setup [112]. Grazing Incidence XRD (GIXRD) is used to probe near-surface regions by keeping the incident beam at a shallow angle while scanning the detector. In-plane XRD rotates the sample and detector within the sample surface plane, allowing analysis of lattice planes oriented parallel to the film surface.

Although the diffraction peaks of these phases are very close and often overlap, XRD remains a valuable tool to assess structural trends in HfO_2-based films. As shown in **Fig. 2.7 ,** different measurement geometries such as grazing incidence and in-plane XRD can provide complementary information about crystallographic orientation and texture, even if full phase distinction is not achievable.

Grazing Incidence X-ray Diffraction (GIXRD) operates by fixing the incident angle (ω) at a small value (typically $< 5°$), limiting X-ray penetration to the uppermost layers of the sample. The detector then rotates through 2θ to capture scattered X-rays at various angles within the diffraction plane. This configuration emphasizes diffraction from planes oriented perpendicular to the surface, providing out-of-plane information such as lattice spacing and crystal orientation. In this study, GIXRD measurements were conducted using a PANalytical Empyrean diffractometer equipped with a Cu Kα radiation source ($\lambda = 1.5406$ Å) operated at 45 kV and 40 kV. The incident angle (α) was set to 0.5°, with an incident slit of $\frac{1}{2}°$, and the Parallel Plate Collimator (PPC) was set at 0.18° to ensure high-resolution diffraction patterns.

In contrast, in-plane X-ray Diffraction focuses on crystallographic planes parallel to the surface of the material. In this configuration, the X-ray beam enters the sample at a grazing angle (typically 1°), and the sample rotates within the surface plane while the detector performs a $\theta/2\theta$ scan. This setup enables diffraction from planes oriented parallel to the sample surface,

allowing for the detailed analysis of in-plane crystallographic properties such as lattice constants, grain orientation, and in-plane stress. In-plane XRD measurements were performed using a Rigaku SmartLab diffractometer, also equipped with a Cu Kα radiation source ($\lambda = 1.5406$ Å) operated at 45 kV. The incident optics included Sollers 0.5°, while the receiving optics were set with PPC at 0.228°. The incident angle (α) was fixed at 0.5° to optimize surface diffraction measurements.

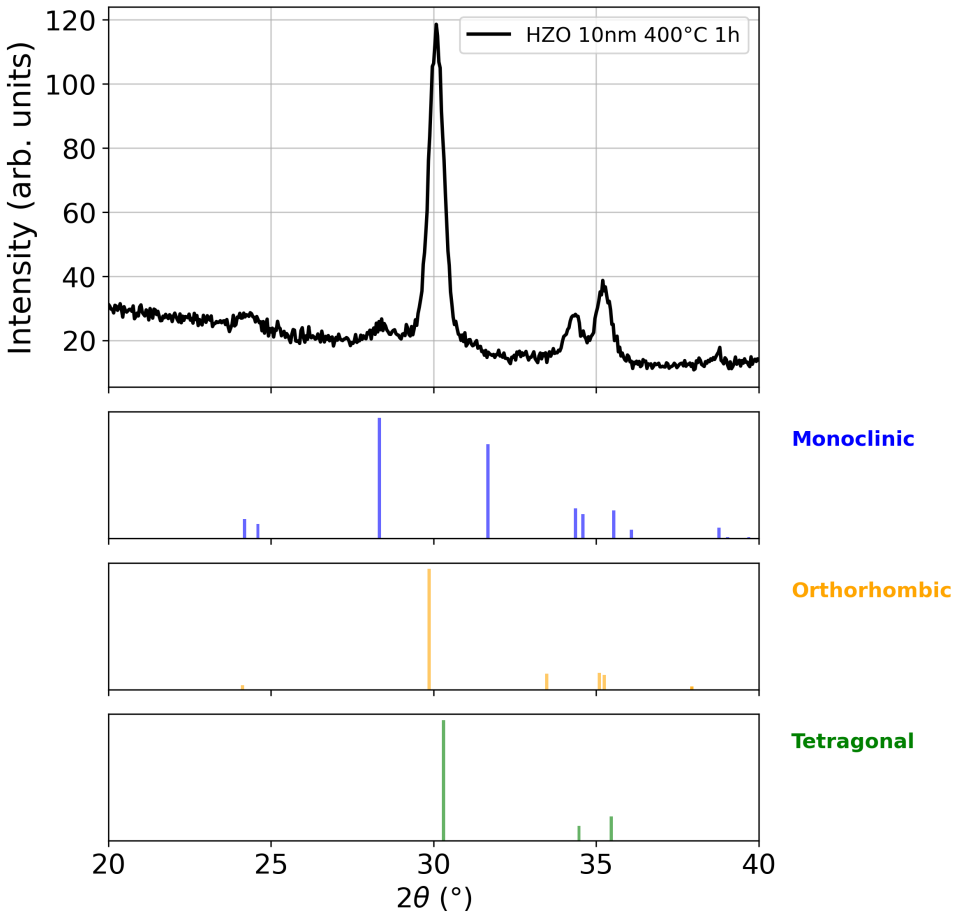

Figure 2.8: In-plane XRD diffractogram for HZO 10 nm annealed at 400°C comparing experimental data with reference diffraction patterns of different crystallographic phases.

As an example, the in-plane XRD spectra of HZO thin films is shown in **Fig. 2.8 ,** where θ positions of the peak indicate presence of Orthorhombic (o-), Tetragonal (t-) (both at 30.5°) and Monoclinic (m-) phases (at 28.5°). However, differentiating the o- and t- phases in HZO is particularly challenging and has already been reported in the literature [43, 52, 113]. This difficulty arises from the structural similarity between these two phases, as the orthorhombic phase can be considered a slight distortion of the tetragonal phase along one of the crystal axes [113]. Due to this subtle structural difference, their diffraction peaks often overlap, making precise phase identification complex. This challenge necessitates complementary analyses, such as electrical measurements or advanced structural characterization techniques, to confirm the presence and dominance of the ferroelectric o-phase over the non-ferroelectric t-phase.

The distinction between these phases is also reflected in their crystallographic space groups: the monoclinic phase belongs to the centrosymmetric $P2_1/c$ space group (JCPDF 00-034-0104), the tetragonal phase to $P4_2/nmc$ (JCPDF 04-011-8820), and the ferroelectric orthorhombic phase to the non-centrosymmetric $Pca2_1$ space group (JCPDF 04-005-5597). The close proximity of their diffraction peaks highlights the importance of combining XRD with other techniques for accurate phase analysis in HZO thin films.

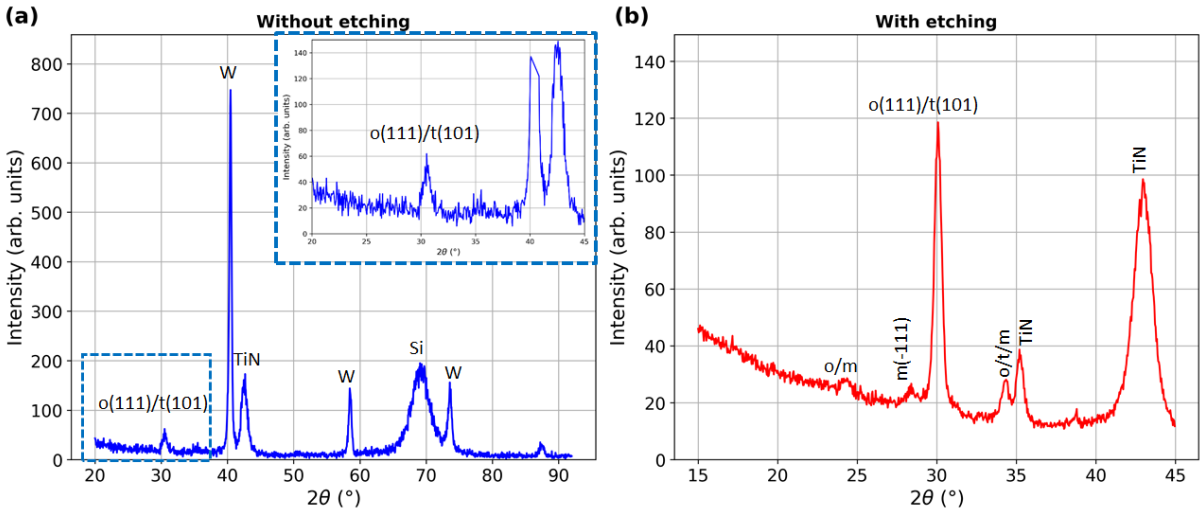

Figure 2.9: a. In-plane XRD of 10 nm HZO annealed thin film with TiN/W top electrode with zoomed-in o(111)/t(101) phases.**b.** In-plane XRD measurement of 10 nm HZO thin film after plasma etching process was applied to remove the top capping electrodes.

Another challenge in XRD analysis is the presence of a top electrode, such as tungsten, which absorbs a significant amount of X-rays and can interfere with the quality of the diffractogram. Tungsten, due to its high atomic number and strong scattering power, produces intense diffraction peaks that may overlap with or obscure signals from the underlying material, complicating the analysis of thin films. To overcome this, part of the XRD analyses in this work were performed after etching the top electrode. This approach minimizes the signal absorption caused by the electrode, enhancing the diffraction signal and resolution of the HZO diffraction peaks, and allowing for clearer observation of the material's crystallography. The details of the etching process used are described in (appendix Section 4.1).

An example of this improvement is shown in **Fig. 2.9 b**, highlighting the increased signal clarity and the removal of unwanted peaks after the electrode was removed. This is particularly evident when comparing the zoomed-in region of **Fig. 2.9 a**, where the signal is lower due to the interference from the top electrode. It is worth noting, however, that the selective etching of the top electrode may have also slightly affected the HZO layer. Although this potential etching of the ferroelectric film is difficult to quantify, due to the challenges associated with characterizing ultrathin layers post-etching, it remains a factor to consider when interpreting the structural results.

Similar plasma-based etching processes have been reported by [114], although their method used a lower SF_6 flow rate diluted with argon. In SF_6 plasma, reactive fluorine species chemically

attack the oxide and may incorporate into the film. In our case, XPS confirmed notable fluorine incorporation, though the affected HZO thickness could not be precisely quantified.

2.4 Transmission Electron Microscopy

Electron microscopy (EM) is a powerful characterization technique that uses a focused beam of electrons to visualize materials at the nanometer scale. Because electrons have much shorter wavelengths than visible light, EM offers significantly higher resolution, allowing observation of structural features that are beyond the reach of optical microscopy. Among the available techniques, Transmission Electron Microscopy (TEM) is particularly valuable for investigating internal structures, crystallographic orientation, and interfaces within thin films.

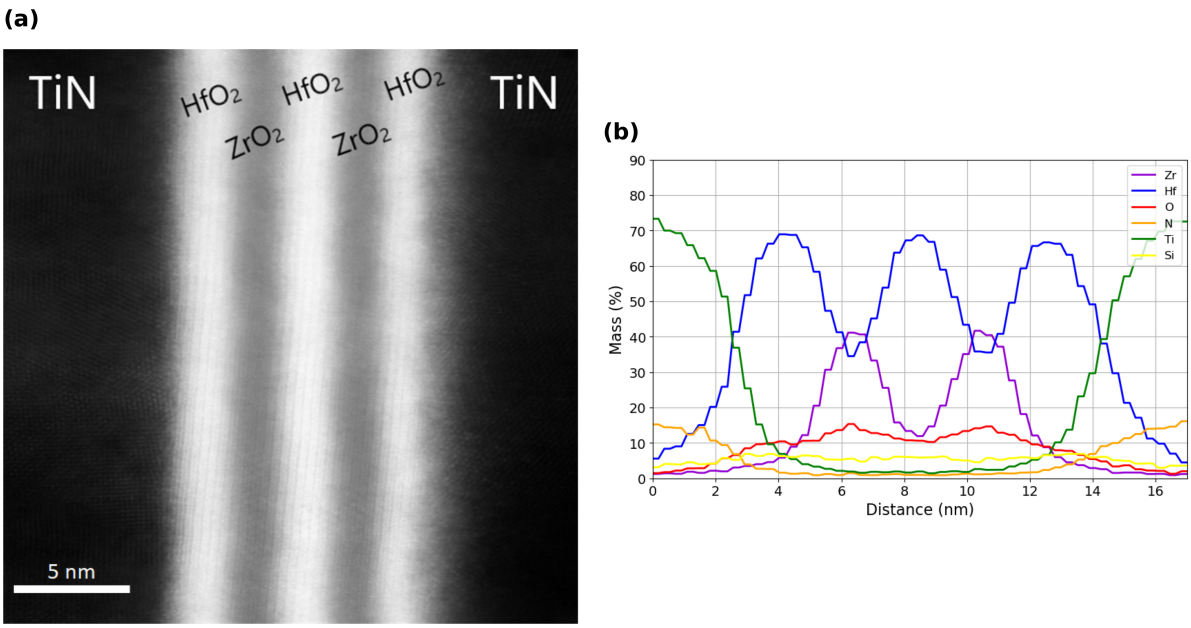

Figure 2.10: a. Cross-sectional TEM image of multilayerd HfO_2-based FE capacitors, demonstrating the crystallization of the FE layer at a low thermal budget. **b.** Corresponding EDX line scan across the stack, confirming the periodic chemical modulation of Hf and Zr, consistent with the designed multilayer architecture.

In this study, TEM was used to investigate various HfO_2-based ferroelectric samples, including both single-layer and multilayer structures. TEM was used to examine the developed stack architecture, assess crystallographic features, and, specifically for multilayer configurations, to verify the preservation and integrity of the individual layers after processing, as shown in **Fig. 2.10**a. Cross-sectional TEM images were acquired using a Titan 80–300 kV (Thermo Fisher Scientific) system.

Energy Dispersive X-ray Spectroscopy (EDX), used in conjunction with TEM, enables elemental analysis at the nanoscale, as shown in **Fig. 2.10**b. When the high-energy electron beam interacts with the sample, it can eject inner-shell electrons, resulting in the emission of X-rays with energies characteristic of each element. In this study, cross-sectional lamellae with a thickness of about 100 nm were prepared, which defines the probed volume for EDX. For heavy

elements such as Hf, Zr, and Ti, EDX in scanning TEM mode provides a spatial resolution of about 1–2 nm with reliable quantification. In contrast, for light elements such as O and N, the fluorescence yield is weaker and absorption stronger, leading to a practical resolution closer to 5–10 nm and reduced sensitivity (detection limit ∼1–2 at.% with lower accuracy). In this study, EDX was performed using the same equipment as TEM to confirm the chemical composition of the layers, complementing the structural insights obtained from high-resolution imaging.

Sample preparation for TEM was performed using Focused Ion Beam (FIB), which enables site-specific thinning of the material to electron transparency. This ensures high-resolution imaging while preserving key structural features.

2.5 Secondary-Ion Mass Spectrometry

Time-of-flight Secondary-Ion Mass Spectrometry (TOF-SIMS) is an analytical technique used to determine the composition of a material by sputtering its surface with a focused primary ion beam and analyzing the ejected secondary ions, as drawn in **Fig. 2.11 a**. When the primary ions hit the sample, they cause atoms and molecules from the surface to be ejected, some of which become ionized. These secondary ions are then collected and analyzed based on their mass-to-charge ratio using a mass spectrometer. ToF-SIMS is highly sensitive and can provide depth profiles, offering detailed compositional information as a function of depth, making it particularly useful for thin films, multilayers, and interface analysis [115].

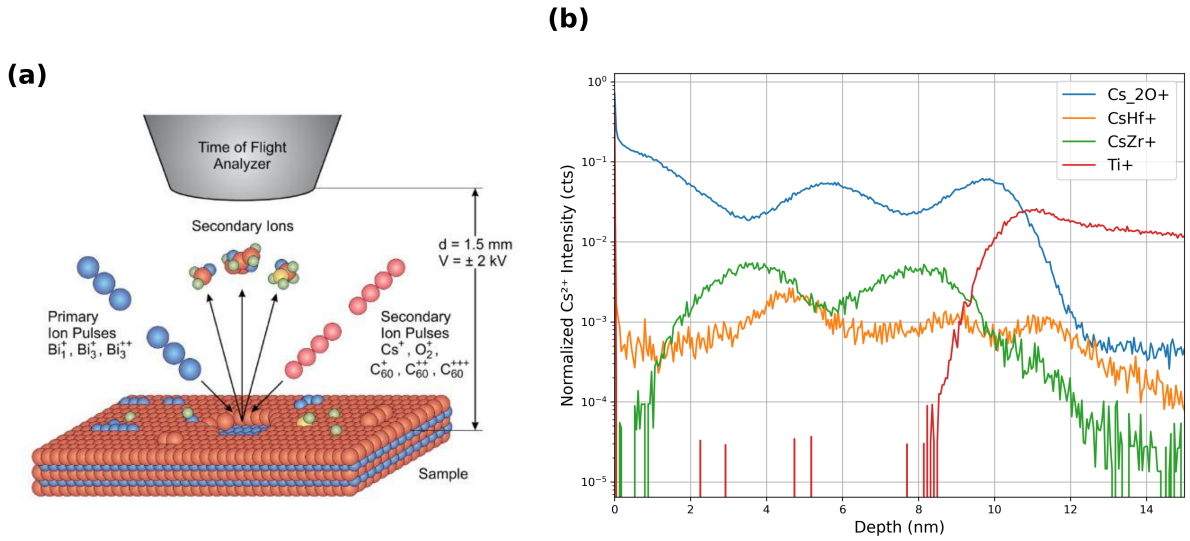

Figure 2.11: a. Principle of ToF-SIMS [116]. SIMS profile of **b.** as-deposited HfO_2/ZrO_2 multilayered thin film.

A time-of-flight (ToF) mass spectrometer works by sending short pulses of ions that generate secondary ions. These ions are then accelerated through a tube, and their arrival time at the detector is measured to determine their mass. ToF-SIMS is highly versatile, offering a broad mass range and high resolution.

In ToF-SIMS, matrix effects occur when the material's composition and structure affect the

ionization efficiency of ejected secondary ions, complicating quantitative analysis. The ionization yield varies not just with element concentration but also with the surrounding matrix, meaning different materials can alter detection intensities. This makes direct quantification challenging.

Depth limitations arise when analyzing very deep layers of a material, as the sputtering process can lead to changes in the surface morphology, such as roughening, which reduces depth resolution. This can make it difficult to maintain precise control over depth profiling for very thick samples or when trying to measure thin layers with high accuracy [117].

The ToF-SIMS analysis was performed using a ToF-SIMS instrument (Ion-ToF, Germany). Positive ion mode was chosen to optimize the detection of electropositive species such as Hf and Zr, which are key elements in our study. The primary ion source used for the measurement was Bi_3^+ with an energy of 25 keV and a current of 17.6 nA, scanning over a 90 μm × 90 μm area at a resolution of 128 × 128 pixels. The ion dose applied was 5.4×10^{13} ions/cm^2, ensuring adequate signal collection. The mass resolution achieved was $m/\Delta m > 10^3$.

No surface preparation was performed before the analysis. For depth profiling, Cs^+ ions were used as the sputtering source at 500 keV and 42 nA, with a raster size of 350 μm. The analysis was conducted in a non-interleaved mode with 1-second sputtering, 1-second pause, and one frame per shot per pixel. The detection limit was in the parts-per-billion (ppb) range, though depth profiling was considered unreliable for signals below ten counts.

The samples were not air-sensitive, and the analysis was performed in positive polarity mode (MCs mode). Additionally, a flood gun was used to neutralize charge effects on insulating oxides. The sputtering rate (x-axis calibration) was determined based on the oxide stack thickness, with an estimated etching rate of 0.05 nm/s on $HfZrO_X$.

2.6 X-ray Photoelectron Spectroscopy

X-ray photoelectron spectroscopy (XPS) is a surface-sensitive technique used to analyze the elemental composition and chemical states of materials. In XPS, high-energy photons irradiate the sample, ejecting core electrons from its constituent atoms. The basic working principle is illustrated in **Fig. 2.12 a**. The kinetic energy (KE) of these ejected electrons is measured, and their binding energy (BE) is calculated using [115]:

$$\mathrm{BE} = h\nu - \mathrm{KE} \tag{2.8}$$

where h is Planck's constant (6.63×10^{-34} J · s), and ν is the photon frequency.

Since each element has a unique set of binding energies for its core electrons, XPS enables elemental identification and chemical state analysis. These energies appear as distinct peaks in the XPS spectrum, and the intensity and position of these peaks allow identification of the elements and their corresponding chemical states. Additionally, the binding energy of an atom can shift depending on its chemical bonding environment, allowing XPS to provide crucial insights into a material's chemical state [118]. An example of survey spectrum can be seen in **Fig. 2.12 b**.

Despite its advantages, XPS is intrinsically limited to probing only a few nanometers of a

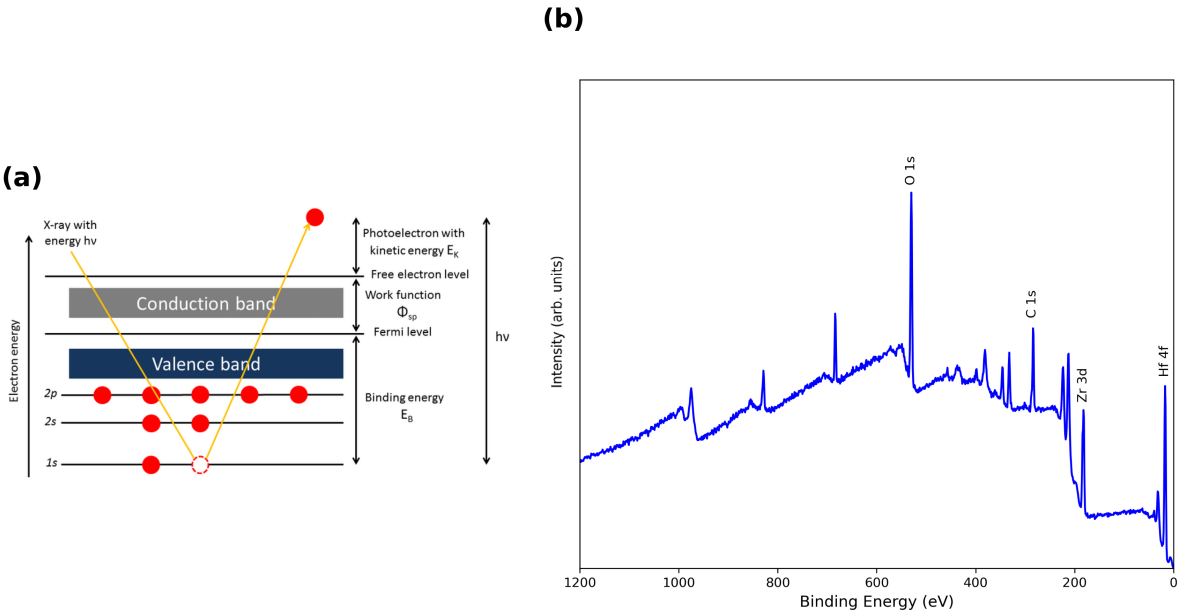

Figure 2.12: a. Principle of X-ray photoelectron spectroscopy [116]. **b.** Survey acquired by XPS on a HZO (10 nm) sample deposited on a TiN substrate.

material's depth. The effective information depth depends on the electron kinetic energy, the inelastic mean free path (λ), and the take-off angle. In our setup, the take-off angle is defined as the angle between the sample surface and the analyzer, with 45° as the default geometry. In this case, the analyzed thickness is approximated as $3\lambda \sin(\theta)$.

XPS measurements were performed using a Quantera spectrometer (Physical Electronics) equipped with a monochromatic Al Kα source ($h\nu$ = 1486.6 eV). The total energy resolution for high-resolution spectra was 0.6 eV. Analyses were carried out at 45° and 90° take-off angles. For reference, the inelastic mean free path of O 1s electrons in HfO_2 at ~1000 eV kinetic energy is ~1.9 nm, which is close to the value for Hf 4f electrons. The energy scale was calibrated using the C–C/C–H reference peak at 284.8 eV.

2.7 Bow measurement

Wafer bow analysis involves measuring and evaluating the curvature or warping of semiconductor wafers, which can result from stress during fabrication, temperature variations, or material properties. The 3-point measurement method is commonly employed, where the wafer is supported at three equidistant points, minimizing external stress while the deflection of its center is precisely measured [119]. This deflection indicates the wafer's curvature and is used to calculate the bow, **Fig. 2.13 a**.

The curvature of the wafer is characterized as either positive or negative, depending on the type of residual stress present, **Fig. 2.13 b**. A positive bow, where the center of the wafer bows upward relative to its edges (convex shape), indicates compressive stress in the film. Conversely, a negative bow, where the wafer edges bow upward relative to the center (concave shape), corresponds to tensile stress. These curvatures provide valuable insights into the stress

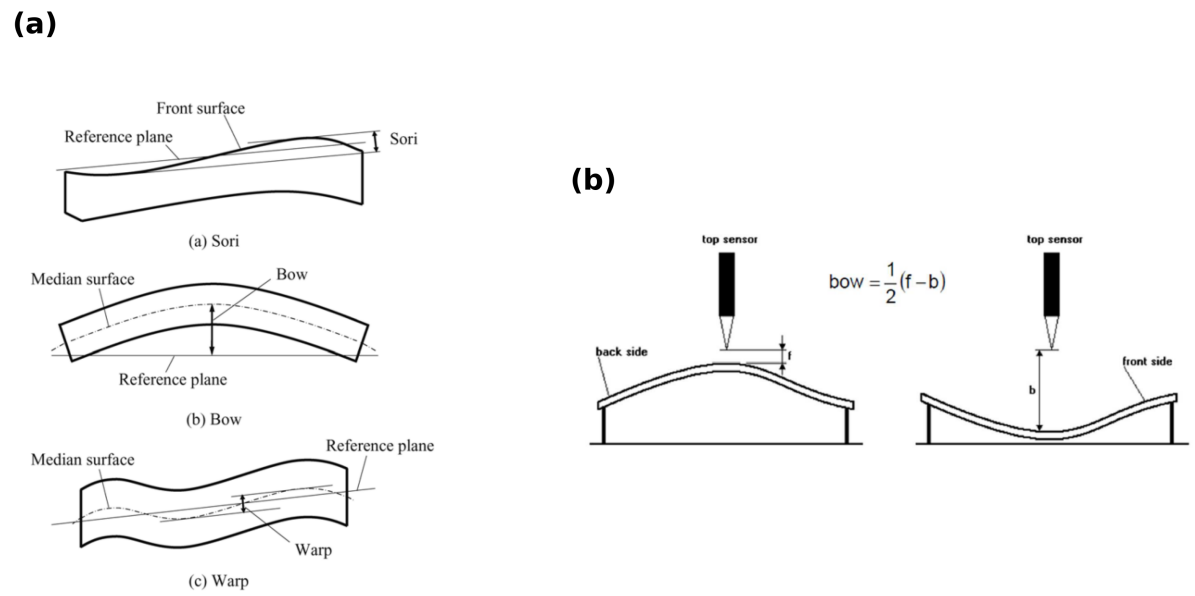

Figure 2.13: **a.** Illustration of definition of sori, bow and warp [120]. **b.** Wafer curvature [120].

distribution within the wafer.

The film stress can then be estimated with the Stoney relation written in terms of the substrate biaxial modulus E_S, $E_S = E/(1-\nu)$ and the change in curvature before (R_b) and after (R_a) deposition:

$$\sigma = \frac{E_S\, t_S^2}{6\, t_f} \left(\frac{1}{R_a} - \frac{1}{R_b} \right) \tag{2.9}$$

where t_S is the substrate thickness and t_f the (uniform) film thickness.

With this convention, the radius of curvature R derived from the wafer diameter D and the bow B is

$$R = -\left(\frac{D^2}{8B} + \frac{B}{2} \right) \tag{2.10}$$

In this study, bow measurements were performed using the FRT MICROPROF2, a non-contact optical profilometer equipped with both dual confocal and infrared interferometric sensors. Measurements followed the SEMI MF 534 standard, in which the wafer is supported at three equidistant points, and the bow is calculated as:

$$\text{Bow} = \frac{f - b}{2} \tag{2.11}$$

where the distance f is recorded between the center of the wafer's front surface and the sensor, and after flipping the wafer, the distance b is measured from the center of the back surface to the sensor.

It is crucial that the film thickness remains uniform, as variations or etched patterns can

distort the stress distribution and affect the calculation. This measurement is particularly important for evaluating the deformation resulting from different deposition processes, such as the use of various top electrodes, and for understanding the type and magnitude of stress they introduce into the wafer.

3 Fabrication of the studied electrical devices

3.1 300 mm MFM structures

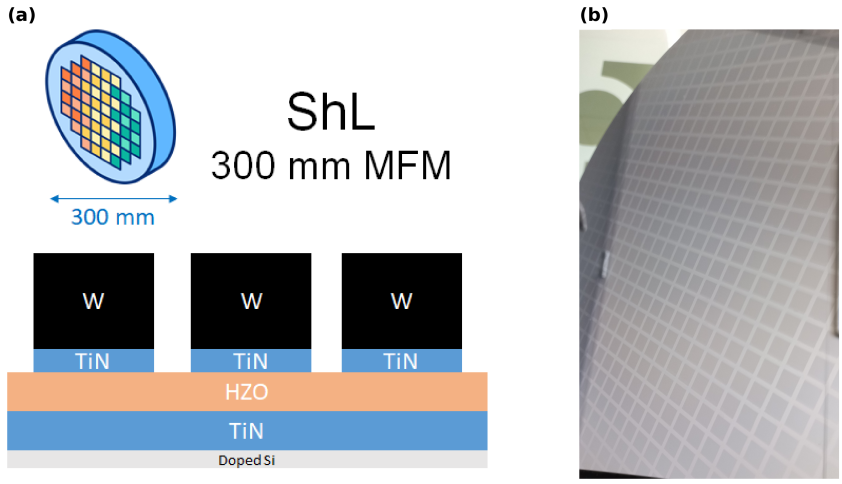

Figure 2.14: a. Sketches of the tested 300 mm MFM structures (shortloop capacitors) from CEA-Leti 300 mm wafers. **b.** Photograph of a patterned 300 mm wafer. A single wafer can accommodate several million capacitors, allowing for high-throughput testing and robust statistical analysis.

In this study, Short Loop (ShL) structures refer to Metal–Ferroelectric–Metal (MFM) capacitors fabricated on 300 mm wafers at CEA-Leti, as show in **Fig. 2.14**. These test structures are designed for fast material and stack screening, offering a simplified and time-efficient alternative to full memory matrix fabrication. Their 2D layout helps to isolate intrinsic properties of the ferroelectric stack from extrinsic effects related to integration.

The BE was made of Ti/TiN (5 nm/10 nm) deposited on Si substrates by PVD. The deposition of the HfO_2-based FE film was made by ALD at 300°C. On top of 10 nm-thick TiN and 70 nm-thick W top electrode (TE) layers were deposited by CVD and SSP. A negative-tone photoresist (TDMR-AR80, 840 nm thick) was then spin-coated for patterning, followed by lithography and reactive ion etching (RIE) to define the capacitors down to the ferroelectric layer.

Each capacitor has a circular surface with a diameter of 100 μm, corresponding to an effective surface area of approximately 7.85×10^{-5} cm^2. This defined surface was considered in all electrical measurements presented in this study, such as polarization and current density.

3.2 Annealing

HfO_2-based films are typically amorphous after the ALD process. Therefore, a subsequent temperature increase is crucial to crystallize the HfO_2-based layer into the FE orthorhombic (o-) phase. This temperature increase can occur during subsequent processing steps, such as the deposition of the top electrode, and/or through dedicated thermal annealing processes.

During this thesis, different anneal conditions were performed on the studied devices, in

order to get a first idea on the optimal anneal conditions. The optimal anneal conditions are the most favourable conditions for the crystallization of the ferroelectric layer leading to the best functionality of the devices under material choices and CMOS route constraints. Two different annealing processes were explored: one at 400°C for 1 hour, and another at 500°C for 15 minutes. Both were carried out under a nitrogen atmosphere in the same Tokyo Electron TELFORMULA batch furnace (TELFORMULA equipment).

The heating sequence involved an initial ramp where the temperature was increased up to 375 °C at a rate of 10 °C per minute, followed by a slower ramp reaching the final annealing temperature at 3 °C per minute, both with a N_2 flow of 10 Standard Liters per Minute (SLM). The annealing stage was then performed at either 400 °C or 500 °C, depending on the process, with the same N_2 flow sustained during this step. Finally, the system underwent a controlled cooling ramp down to 100 °C at a rate of 10 °C per minute.

Importantly, the furnace is stabilized at 100 °C prior to loading, and the sample enters at this temperature before undergoing the full heating sequence. As a result, the overall thermal exposure is longer than the nominal annealing step, as shown in **Fig. 2.15 .** The reported anneal duration refers specifically to the dwell time at the final target temperature (400 °C or 500 °C).

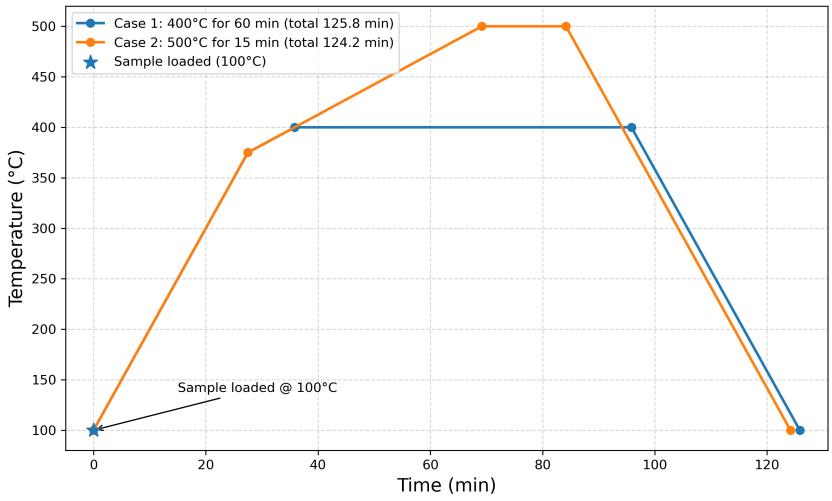

Figure 2.15: Temperature–time profiles for two anneal recipes. Sample loaded at 100 °C; ramp 10 °C min^{-1} to 375 °C, then 3 °C min^{-1} to 400 °C (60 min) or 500 °C (15 min); cool to 100 °C at 10 °C min^{-1}.

4 Methodologies for electrical characterization

This section focuses on the methodologies for electrical characterization employed to evaluate the performance and behavior of the ferroelectric materials. Techniques such as PUND and quasi-static I-V measurements are presented, providing key insights into the electrical properties and behaviors of the material.

4.1 PUND : a technique to extrapolate ferroelectric metrics

4.1.1 Basic method

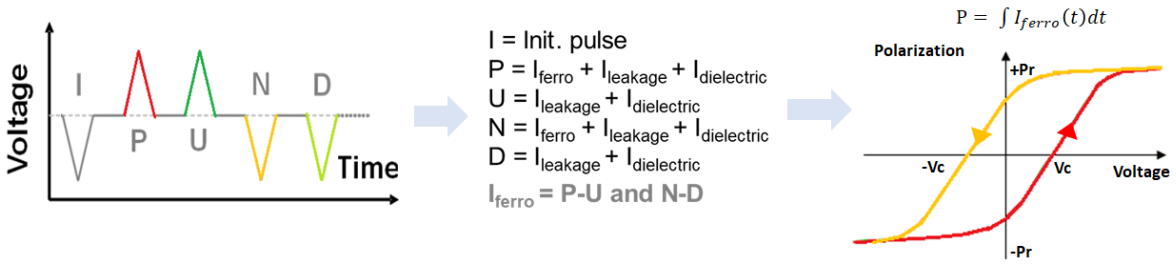

Figure 2.16: PUND sequence to measure the FE performance and P-V hysteresis loop resulting from the integration of I over time.

The investigation of FE properties ($2P_R$, E_C, V_C) relies on transient current measurements. Ferroelectric displacement current I_{FE} is the characteristic signature of ferroelectric switching. It arises due to the reversal of the dipoles under the action of an electric field. The integration of I_{FE} over time yields to the P-V curve. However, this I_{FE} is never measured alone, the dielectric displacement current (I_{DIEL}) and the static leakage current (I_{LEAK}) are overlayed on it. The amplitude of I_{DIEL} is proportional to the capacitance of the Device Under Test (DUT) and the ramping rate of the applied pulse ($I_{DIEL} = C_{tot}\ dV/dt$). As a result, parasitic contributions ($I_{DIEL} + (I_{LEAK})$) to the current may represent a non-negligible part of the total signal and may lead to an overestimation of the polarization. To tackle this overestimation, the Positive Up Negative Down (PUND) electrical characterization method can be used.

PUND corresponds to a specific sequence of voltage pulses applied to the sample so that $I_{DIEL} + I_{LEAK}$ can be separated from the switching current I_{FE}. It consists of a succession of five triangular signals (see **Fig. 2.16**):

- An initial negative pulse, I, which aligns all ferroelectric domains in one direction;
- A positive pulse, P, which contains the total amount of positive switched charges, both permanent and transient, as well as the dielectric response of the ferroelectric material: $I_P = I_{FE} + I_{LEAK} + I_{DIEL}$;
- A second positive pulse, U, which contains the positive transient polarization and the dielectric response: $I_U = I_{LEAK} + I_{DIEL}$;

- A negative pulse, N, which contains the total amount of negative switched charges, permanent and transient, and the dielectric response of the ferroelectric material: $I_N = I_{FE} + I_{LEAK} + I_{DIEL}$;
- A second negative peak, D, which contains the negative transient polarization and the dielectric response: $I_D = I_{LEAK} + I_{DIEL}$.

The subtractions P-U and N-D displacement signals lead to the current I_{FE}. By extracting only I_{FE}, PUND is the most pertinent method to characterize the FE response of a material [121].

To obtain a PUND hysteresis cycle, the integration must be performed as follows:

$$P^+ = \frac{1}{S} \int I_{\mathrm{PU}}\, dt \tag{2.12}$$

$$P^- = \frac{1}{S} \int I_{\mathrm{ND}}\, dt \tag{2.13}$$

where S is the surface area of the ferroelectric capacitor, P^+ is the polarization of the positive part, and P^- is the polarization of the negative part.

There are several important parameters of a ferroelectric material that can be extracted from hysteresis loops. The remanent polarization is the most frequently cited parameter because it serves as a figure of merit for ferroelectrics used in nonvolatile memory applications such as FeRAM. The remanent polarization is the total amount of switched charge within the ferroelectric film that remains stable when the electric field is removed. The remanent polarization (P_r) from the hysteresis loop is determined by:

$$P_r = \frac{P_r^+ + P_r^-}{2} \tag{2.14}$$

where P_r^+ is the positive remanent polarization and P_r^- is the negative remanent polarization.

In practical applications, the technologically relevant parameter is the switchable polarization, expressed as $2P_r$. It represents the full difference between the two remanent states and thus quantifies how much charge can be reversibly switched. Since memory operations rely on distinguishing between these two stable polarization states, $2P_r$ directly reflects the usable signal margin in ferroelectric-based devices.

The coercive field (E_c) is another key characteristic of a ferroelectric material because it represents the electric field required to switch ferroelectric dipoles within the material. When discussing P-V plots, the coercive field can be replaced by the coercive voltage (V_c), which is the voltage required to switch the ferroelectric polarization. The coercive field is calculated as:

$$E_c = \frac{V_c}{d} = \frac{|V_c^+| + |V_c^-|}{2d} = \frac{|E_c^+| + |E_c^-|}{2} \tag{2.15}$$

where d is the ferroelectric film thickness, and V_c is the coercive voltage.

4.1.2 Experimental measurements

In this thesis, the PUND was realised with an Agilent B1530A Waveform Generator/Fast Measurement Unit (WGFMU) from Keysight technologies. A first probe was connected to a first WGFMU, and applied the fast PUND pattern, while a second WGFMU set the second electrode to the ground, and measured the current. The voltage pulse sequence used during PUND measurements is illustrated in **Fig. 2.16**. No relaxation time was imposed during the electrical tests; however, a 10 ns interval is set between each measurement point by the WGFMU.

The ShL integration imposes to apply the voltage on BE, in order to have a good current/noise ratio. For the MFM coupons developed, this approach remains consistent, with the voltage continuing to be applied to the BE. The large BE area, especially the chuck connection in the wafer, can act as an antenna.

The first 10 cycles were performed at 10 kHz, with carefully controlled rise and fall times to facilitate gradual domain reorientation. Regarding the PUND sequence in this thesis, the pulse voltage and duration were fixed at respectively 4 V, 25 μs (10 kHz) for a MFM stack with a 10 nm thick HfO_2-based FE thin film. These pulse parameters were applied to guaranty the switch of all FE domains and a good resolution of I_{FE}. After the initial cycling phase, the frequency was raised to 100 kHz, enabling faster cycling for endurance evaluation.

Both the sampling time and the applied voltage were adjusted according to the film thickness. In addition, the PUND routine maintained a fixed number of 50 points per rise and fall ramp, which naturally resulted in shorter sampling times for thinner films and longer sampling times for thicker films. Similarly, the applied voltage was also adjusted by thickness to maintain a consistent electric field, with thinner films requiring lower voltages.

4.2 Quasi-static I-V characteristics

To fully understand the electrical performance of ferroelectric capacitors, it is essential to evaluate both their leakage current and breakdown voltage. The quasi-static I-V measurement technique provides a systematic approach to characterize these properties under controlled conditions.

Before the I–V sweep, a PUND initialization sequence is applied to align the ferroelectric domains, ensuring a stable and uniform polarization state across the device.

After this initialization, the SMU (Source Measurement Unit) applies a stepped voltage pattern with small increments, typically around 0.1 V, during the quasi-static I-V measurement. At each voltage step, a delay time (t_d) is introduced to allow the dipoles or domains within the ferroelectric material sufficient time to stabilize, minimizing transient effects, such as dielectric displacement currents. The maximum applied voltage varies with film thickness, 4 V for thinner films and up to 8 V for thicker ones.

Following the delay time, the current is recorded over a defined integration period (t_i) of 20 ms. The integration time is the fixed period during which current is measured, ensuring steady-state behavior is captured while minimizing noise and transient effects.

The total time for each voltage step is determined by the combination of t_d, t_i, and the

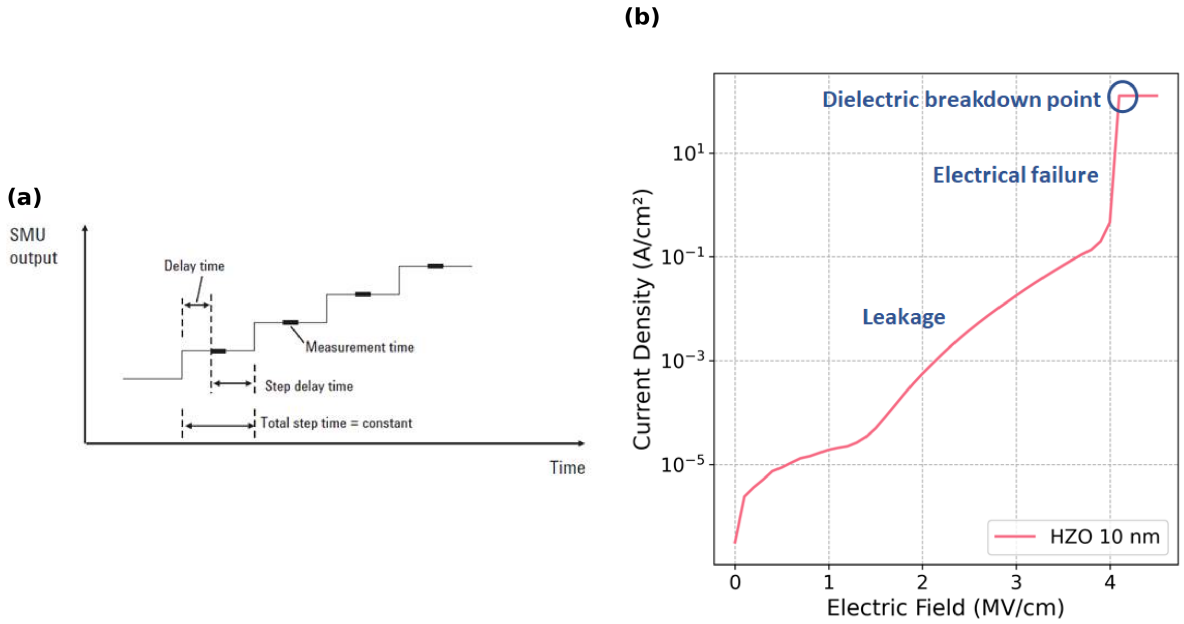

Figure 2.17: a. Schematic of a quasi-static voltage sweep typically used in current–voltage (I–V) measurements, showing the timing structure of each voltage step, including delay and measurement windows. **b.** Example of a quasi-static I–V curve for a 10 nm HZO film, showing characteristic leakage behavior followed by a steep current increase. The curve illustrates three distinct regions: leakage, progressive electrical failure, and the dielectric breakdown point, where the film loses its insulating properties.

time required by the measurement equipment, such as the Agilent B1500A device analyzer, to stabilize and measure the signal. This systematic timing approach, with consistent t_d and t_i across all voltage steps, ensures reproducible and comparable results throughout the voltage range. An example of the pulse sequence is shown in **Fig. 2.17 a**.

From the quasi-static I-V measurements (example of result in **Fig. 2.17 b**), the current density (J) is determined by normalizing the measured current (I) to the capacitor's top electrode surface area (S):

$$J = \frac{I}{S} \tag{2.16}$$

The leakage current behavior is analyzed as a function of the applied electric field and could insight into charge transport mechanisms such as Ohmic conduction, Poole-Frenkel emission, Schottky emission, or Fowler-Nordheim tunneling.

Breakdown voltage is identified in the I-V curve as a sudden, irreversible rise in current, indicating that the dielectric has lost its insulating properties. This can occur due to intrinsic material limitations or extrinsic factors like defects, grain boundaries, or interfacial imperfections.

To compare films of different thicknesses, the breakdown field (E_{bd}) is calculated as:

$$E_{bd} = \frac{V_{bd}}{t} \tag{2.17}$$

where t is the film thickness.

Two types of dielectric breakdown are usually distinguished. Hard breakdown is identified by irreversible increase in current, after which the dielectric completely loses its insulating properties. In contrast, soft breakdown corresponds to a more gradual rise in leakage current, where the dielectric remains partially insulating but degraded. In this work, only the hard breakdown will be addressed.

5 Chapter Summary and Conclusions

This chapter focuses on the experimental techniques and methodologies employed for the fabrication, characterization, and electrical testing of HfO_2-based ferroelectric materials studied in this thesis.

Regarding sample fabrication, the ALD deposition technique was employed to create the HfO_2-based structures, providing precise control over nanometric film thickness and enabling conformal deposition of the stack layers. Understanding the deposition processes, including ALD for the ferroelectric layers and PVD or CVD for the metallic electrodes, allows us to assess how these techniques influence the manufacturing process of the MFM test vehicle.

A comprehensive set of material characterization methods was employed not only to verify the successful fabrication of the samples but also to investigate their structural and chemical properties. XRR was used to extract film thickness, density, and interface roughness, which are indicators of deposition accuracy and film uniformity. XRD provided insight into crystallographic phases and texture. TEM allowed for high-resolution imaging of layer interfaces and microstructural features, while ToF-SIMS enabled depth profiling of the elemental composition, revealing potential interdiffusion or contamination across layers. Surface-sensitive techniques such as XPS and EDX contributed to the understanding of chemical composition and bonding states at the film surface and within specific regions of the stack, which can directly influence electrical properties.

Electrical measurements, including PUND and quasi-static I-V analysis, were used to extract key ferroelectric metrics such as remanent polarization, coercive field, wake-up behavior, and leakage current. These measurements enabled the correlation between the structural features of the film and its functional performance in capacitor configurations.

The methodologies presented in this chapter lay the foundation for understanding the relationships between deposition conditions, structural characteristics, and electrical behavior in HfO_2-based ferroelectric capacitors. This knowledge is essential for optimizing the fabrication process and ensuring reliable ferroelectric performance. The next chapters will focus on the experimental results obtained from these techniques, providing a detailed discussion on how variations in composition, thickness, and processing conditions influence the ferroelectric response and stability of the studied structures.

Chapter 3

10 nm HZO 1:1 Thin Film

Objectives

HfO_2-based ferroelectric materials are promising candidates for the implementation of BEOL-embedded ferroelectric non-volatile memories. However, their electrical performance must still be optimized to meet the stringent requirements of embedded FeRAM applications. This chapter focuses on 10 nm 1:1 HZO solid solution thin films, a benchmark material in ferroelectric research, and explores how electrode configurations influence their structural and functional properties.
Specifically, the chapter investigates the role of 10 nm HZO as a reference material, analyzing its evolution from the as-deposited state through electrode integration and annealing. It also examines how different top electrode configurations affect stress and impact the electrical behavior of the capacitors. In addition, an initial attempt to understand the physical mechanism underlying the wake-up effect is presented. These insights aim to support the development of optimized HZO thin films for next-generation memory technologies.

Contents

1 Introduction **57**
2 10 nm HZO as a reference material: from material to device performance **58**
2.1 Intrinsic characteristics of as-deposited HZO 58
2.2 Intrinsic properties of 10 nm HZO after electrode deposition and annealing 62
2.3 Electrical performance of capacitors 65
2.4 General conclusion 67
3 Impact of top electrode configurations on the ferroelectric performance of HZO capacitors . . . **68**
3.1 Top electrode configurations and fabrication details 68
3.2 Intrinsic properties of the electrode films 68
3.3 Evaluation of stress evolution through bow analysis in HZO capacitors 71
3.4 Influence of top electrode configurations on electrical performance of HZO capacitors . 73
3.5 General conclusion 75
4 Chapter Summary and Conclusions **77**

1 Introduction

This chapter explores the intrinsic and applied aspects of HZO, detailing the processes and parameters influencing its material properties and device performance.

The 10 nm-thick HZO structure has become a standard benchmark, widely used to study ferroelectric phase stabilization and electrical performance. Yet, even this well-studied configuration reveals complex dependencies on fabrication steps such as electrode deposition and annealing. Stress induced during processing, particularly from electrode materials, can influence phase formation, but its effects are not always straightforward.

This chapter provides a detailed analysis of these factors, using the 10 nm HZO structure as a reference system to understand material evolution from the as-deposited state through full device integration. It also examines how top electrode-induced stress influences ferroelectric behavior, and presents an initial investigation into the physical origins of the wake-up effect. Together, these insights contribute to a broader understanding of the interplay between process parameters, stress, and material functionality in HZO-based ferroelectrics.

2 10 nm HZO as a reference material: from material to device performance

Among the various ferroelectric HfO_2-based configurations, the 10 nm-thick $Hf_{0.5}Zr_{0.5}O_2$ (HZO) structure has become a widely used reference. This section focuses on the standard 10 nm HZO structure, analyzing how deposition, top electrode integration, and annealing impact its intrinsic properties and MFM electrical performance, serving as a baseline for comparison with other structures in this study.

2.1 Intrinsic characteristics of as-deposited HZO

HfO_2-ZrO_2 binary alloys are promising for memory applications due to their ability to stabilize the ferroelectric orthorhombic (o) phase (space group $Pca2_1$), especially at a 1:1 molar ratio, which promotes robust polarization and device reliability [122]. Ensuring consistent ferroelectric properties across fabrication conditions requires controlling factors such as composition, phase, grain size, and defects, parameters largely influenced by ALD processes [53].

The 10 nm HZO films were prepared by thermal ALD using the supercycle method described in Chapter 2 Section 2.1, **Fig. 2.4 ,** resulting in a homogeneous HZO matrix.

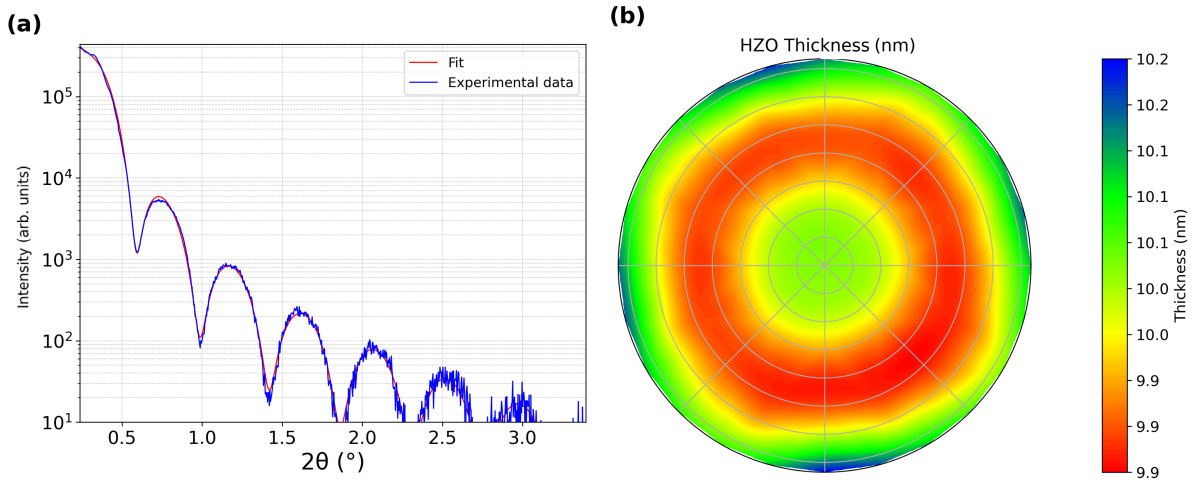

Figure 3.1: a. XRR analysis of a 10 nm HZO film as deposited on a Si substrate. The experimental data (blue) is accurately fitted (red), providing insight into film thickness, density, and roughness. XRR values represent the average from 3 measured points. b. Thickness uniformity map obtained for a 10 nm HZO film as deposited on a Si substrate by ellipsometry at 49 points across the sample surface. The standard deviation of the thickness was 0.95%, indicating excellent uniformity.

Fig. 3.1 a presents the XRR data for the as-deposited HZO thin film on a Si substrate, with the experimental curve (blue) closely matching the fitted model (red). The film density and thickness was obtained from the JVX software used to fit the measured reflectometry curves, as described in Chapter 2 Section 2.5. The fit yielded a thickness of 9.9 nm, an average density of 7.6 g/cm^3, and a surface roughness of 1Å, indicating good uniformity and control over the

deposition.

This density is lower than values reported in [123] and [124] for example, which can be attributed to differences in ALD process conditions. For example, a study using plasma-enhanced ALD at 180°C with organometallic precursors reported a higher HZO density of 8.18 g/cm^3 [123]. Another report showed that the use of H_2O_2 as an oxygen source led to a further increase in film density, reaching 8.50 g/cm^3 [124].

To further assess the spatial uniformity across the wafer, ellipsometry mapping was performed at 49 points, as shown in **Fig. 3.1 b** and described in appendix 1. The thickness map confirms the excellent uniformity of the film, with values varying only slightly around the 10 nm mark and following a radial pattern.

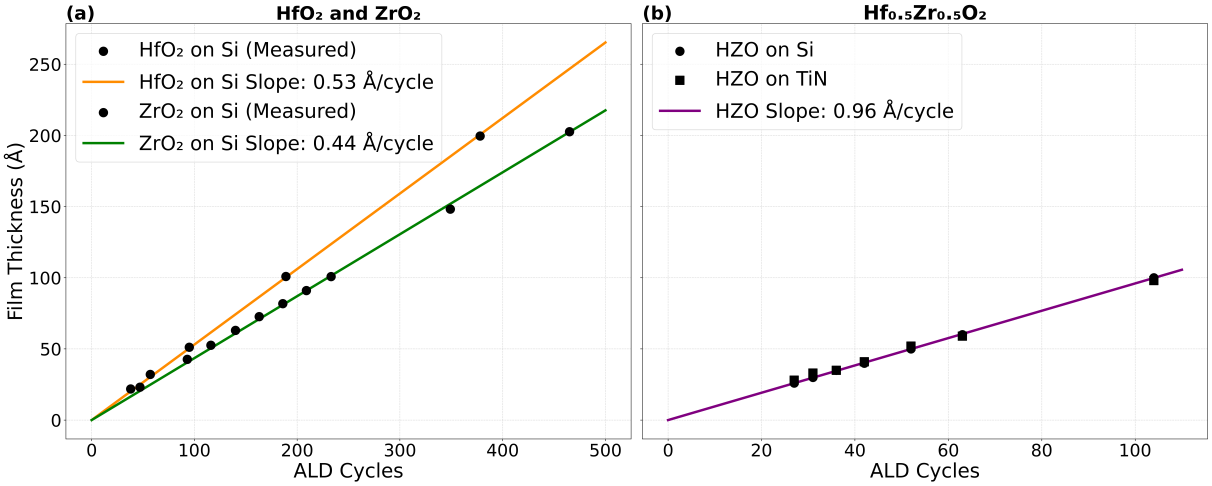

Figure 3.2: Film thickness as a function of ALD cycles for **a.** HfO_2 (orange curve) and ZrO_2 (green curve) on a Si substrate, and **b.** $Hf_{0.5}Zr_{0.5}O_2$ experimental measurements on Si and TiN substrates. Linear fits to the data are shown, with the slope corresponding to the growth per cycle (GPC) for each film. Thickness analysis was performed using X-ray reflectometry (XRR) measurements.

The GPC was determined from the linear evolution of film thickness with the number of ALD cycles, as measured by XRR. **Fig. 3.2 s**hown the GPC results for HfO_2, ZrO_2, and $Hf_{0.5}Zr_{0.5}O_2$ under the same ALD process conditions. These results highlight distinct differences in film growth rates. Since the ALD process parameters, such as temperature, precursor chemistry, and pulse timing, were held constant, the observed variations in GPC are attributed to differences in the reactivity of the precursors. HfO_2 exhibits a higher GPC of 0.53 Å/cycle compared to ZrO_2, which has a lower GPC of 0.44 Å/cycle. This difference likely arises from the higher reactivity of $HfCl_4$ relative to $ZrCl_4$ during surface reactions, as supported by prior studies on ALD precursor chemistry [125, 126]. For HZO, the apparent GPC increases to 0.96 Å/cycle, reflecting the combined deposition of both oxides in a supercycle, which leads to a cumulative growth effect, as described in Chapter 2 Section 2.1.

In **Fig. 3.2 b**, the growth of $Hf_{0.5}Zr_{0.5}O_2$ is shown for Si and TiN substrates. The data points indicate that the film thickness evolves similarly with the number of ALD cycles, regardless of the substrate. This suggests that the GPC growth mechanism is similar on both Si and TiN,

with no significant delay or change in growth rate.

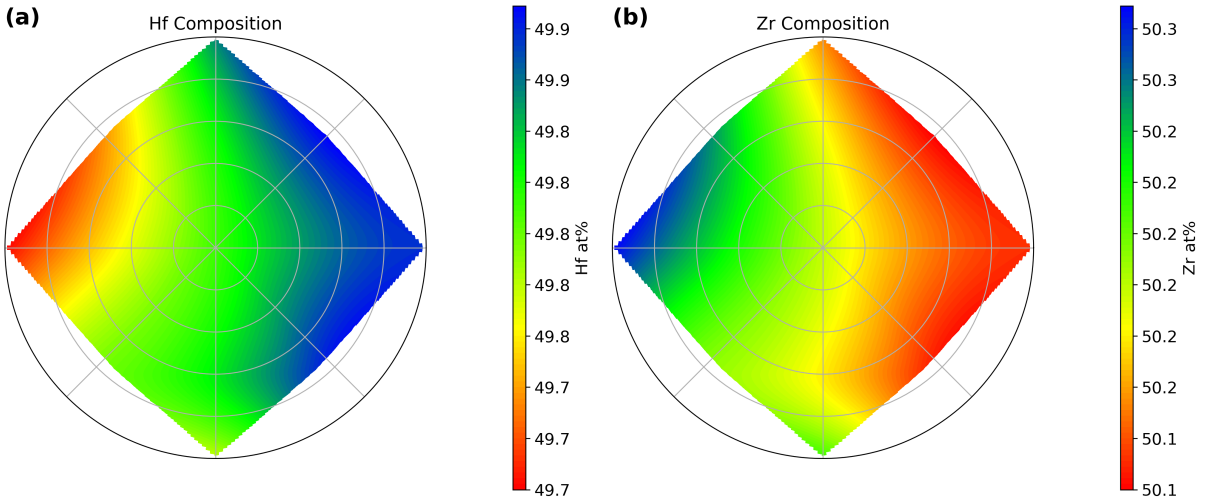

Figure 3.3: Polar maps of a 10 nm HZO film as deposited on a Si of **a.** Hf and **b.** Zr atomic concentrations across the wafer surface, obtained by 9-point WDXRF mapping.

The composition of the HZO thin film was analyzed using WDXRF and XPS to confirm stoichiometry and investigate surface chemistry. WDXRF measurements from a 9-point mapping in **Fig. 3.3 i**ndicate excellent uniformity across the wafer, with an average composition of Hf at%: 49.7 and Zr at%: 50.3. The slight variations observed in the spatial distribution of Hf and Zr may reflect the measurement uncertainty inherent to WDXRF. It is important to note that WDXRF does not detect light elements such as oxygen or chlorine, and therefore only provides information on the metallic (Hf and Zr) content of the film.

XPS analysis in as deposited **Fig. 3.4 f**urther complements these findings. The analysis reveals a Zr/(Hf + Zr) ratio of 0.54, an oxygen-to-metal (O/M) ratio of 1.8, and a carbon content of 15.2%, likely originating from surface contamination. The C 1s spectrum shown in **Fig. 3.4 d** includes the characteristic C–C/C–H peak, which was used to calibrate the binding energy scale. The energy axis was aligned by referencing this peak to 284.8 eV, ensuring consistent and accurate measurements across all spectra. The carbon species identified included C–C/C–H, C–O, and C=O bonds, with C–C/C–H being the dominant component, typically attributed to adventitious carbon commonly present as surface contamination.

In the O 1s region in **Fig. 3.4 a**, the main peak centered at 531.0 eV is consistent with oxygen in HfO_2 or ZrO_2 lattices. A smaller secondary peak at 531.5 eV is generally associated to non-lattice oxygen species. Surface adsorbates such as hydroxyl groups, carbonates, or water, as well as the sample's surface condition, can also influence the signal. The Zr 3d peaks observed at 182.2 eV and 184.6 eV in **Fig. 3.4 b** indicate that Zr is present in the 4+ oxidation state. Similarly, the Hf 4f peaks at 16.8 eV and 18.5 eV confirm the presence of Hf in a 4+ oxidation state in **Fig. 3.4 c**. Since Hf and Zr are isovalent, both adopt the same tetravalent oxidation state in $Hf_{0.5}Zr_{0.5}O_2$, confirming the expected chemical environment of the mixed oxide.

No evidence of Cl or F was observed in the XPS analysis, suggesting that, within the probed region, these elements are either absent or below the detection limit. Since WDXRF is not

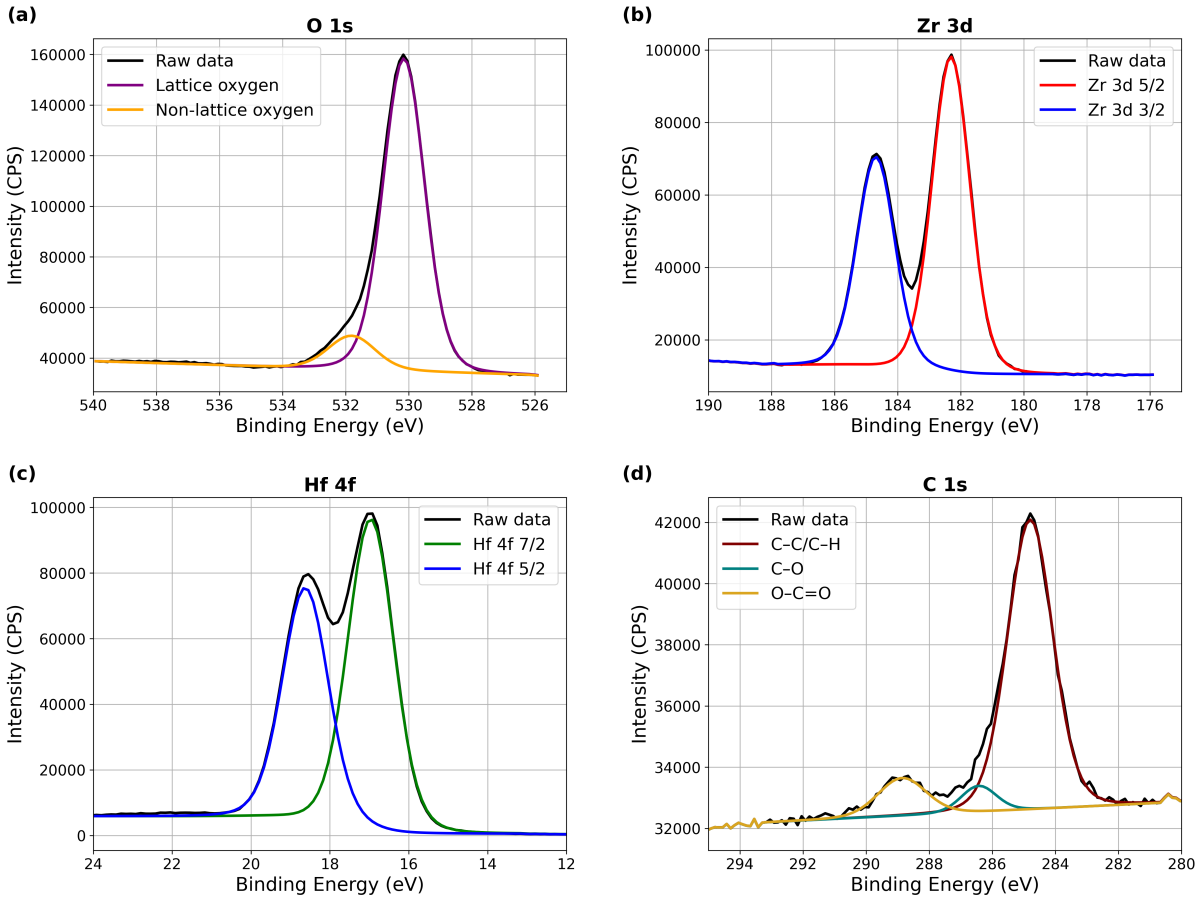

Figure 3.4: XPS core-level spectra of the as-deposited HZO film on Ti/TiN substrate for **a.** O 1s, **b.** Zr 3d, **c.** Hf 4f and **d.** C 1s.

sensitive to chlorine, its presence deeper within the film cannot be excluded based on WDXRF and XPS data alone. Moreover, it is important to note that XPS is a surface-sensitive technique, with an information depth of approximately 5 nm.

To further investigate the oxide formation at the interface with the bottom electrode, ToF-SIMS measurements were performed on as-deposited HZO samples on a 15 nm Ti/TiN bottom electrode, **Fig. 3.5 .** The figure presents the ToF-SIMS depth profile of the 10 nm HZO film, showing signals for Cs_2O^+, $CsHf^+$, and $CsZr^+$ across the layer. These signals remain relatively stable throughout the film and drop near the interface with TiN, consistent with the expected distribution of the primary elements.

The gradual decrease of Cs_2O^+ at the interface may suggest some oxygen diffusion into the TiN electrode, although given the ultrathin nature of the film, interdiffusion cannot be conclusively determined. It is important to note that interpreting the interface region is particularly delicate in this case. The roughness at the HZO/TiN interface may affect the ion yield during sputtering, altering the depth resolution and intensity of ToF-SIMS signals. This can lead to apparent broadening or shifts in signal profiles unrelated to actual chemical gradients.

Signals associated with Cs_2Cl^+ and Cs_2F^+ indicate chlorine and fluorine contamination, which may originate from residual precursor species or external sources like chamber surfaces or

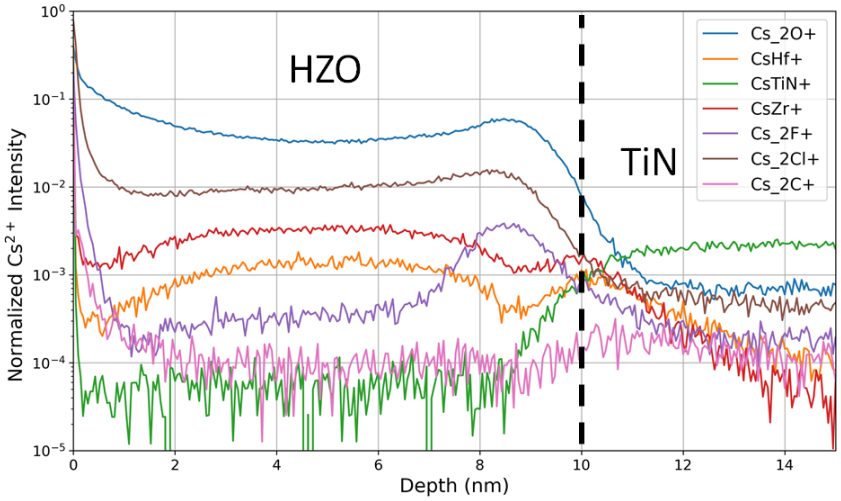

Figure 3.5: Depth-resolved ToF-SIMS analysis of a 10 nm HZO film as deposited. The graph illustrates the normalized Cs^+-based secondary ion intensities for key elements and species.

transfer containers. These species are not detected in XPS, highlighting the higher sensitivity of ToF-SIMS to trace impurities. However, due to differing ionization yields, ToF-SIMS signals are not directly quantitative and should be interpreted cautiously.

A weak Cs_2C^+ signal suggests limited carbon contamination, likely linked to atmospheric exposure. Overall, while ToF-SIMS provides valuable chemical depth profiling, the interpretation remains semi-quantitative and should be complemented by other techniques to assess film purity and interface quality.

2.2 Intrinsic properties of 10 nm HZO after electrode deposition and annealing

The ferroelectric properties of doped HfO_2 thin films are strongly influenced by the mechanical stress and built-in electric fields introduced by top electrodes such as TiN, TaN, and W [127]. These layers affect both stress and electrical performance. Annealing, in turn, drives key phase transitions needed to stabilize the ferroelectric orthorhombic (o-) phase [128]. This section analyzes the combined effects of electrode deposition and annealing temperature on the 10 nm HZO reference standard.

In-plane XRD analysis in **Fig. 3.6 s**hows the 10 nm HZO film at different stages of the fabrication process. The result confirms that the HZO layer is predominantly amorphous immediately after ALD deposition, as evidenced by the absence of distinct diffraction peaks in the bottom black curve. This result is consistent with the TEM image in **Fig. 3.7 a**, which shows a uniform HZO layer approximately 10 nm thick, as expected from the deposition conditions. The XRD measurement after top electrode deposition (middle black curve) was performed following the removal of the TiN/W layer (see in Chapter 2 Section 2.3), to improve signal resolution. The diffractogram reveals a reflection near 30.5°, typically associated with the orthorhombic or tetragonal (o/t) phase, along with features attributable to the monoclinic phase. These observations suggest partial crystallization of the film induced by the thermal budget of the 380°C

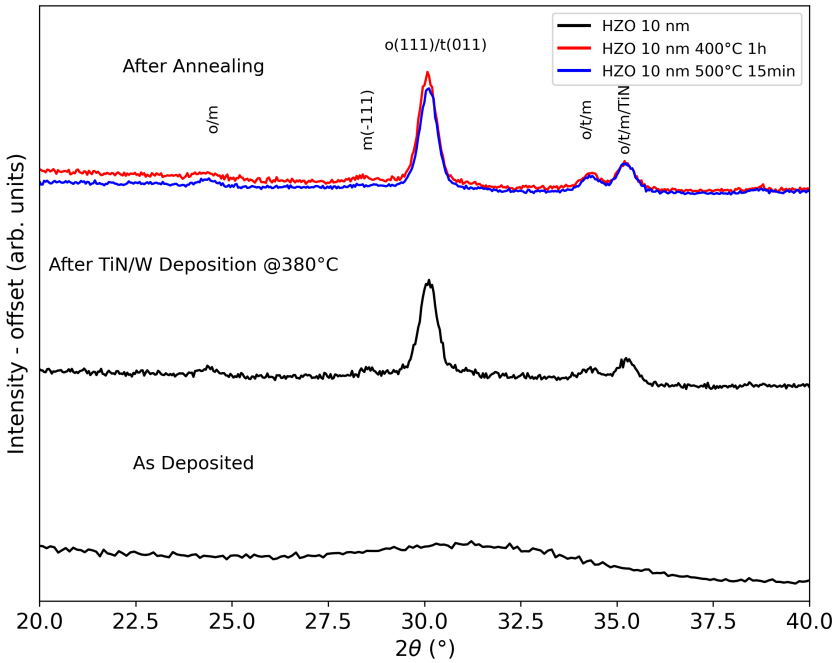

Figure 3.6: In-plane XRD patterns of a 10 nm HZO film acquired at different stages of the fabrication process: as-deposited (bottom, black), after TiN/W top electrode deposition at 380°C (middle, black), and after annealing at 400°C for 1 hour (top, red) or 500°C for 15 minutes (top, blue).

electrode deposition and the capping effect.

A broader diffraction feature also appears around 35°, often associated with the (200) planes of the orthorhombic phase and related to ferroelectric behavior due to polar axis orientation [129, 130]. However, this peak likely contains overlapping contributions from the (111) orientation of the TiN electrode, as well as from tetragonal (t(002), t(110)) and monoclinic (m(200), m(020)) reflections of HZO. Consequently, this peak should be interpreted cautiously, as it does not unambiguously confirm the presence of the orthorhombic ferroelectric phase.

Finally, the top curves (red and blue) in the in-plane XRD results shown in **Fig. 3.6 w**ere obtained after two different annealing processes: furnace annealing at 400°C for 1 hour and at 500°C for 15 minutes, as described in Chapter 2 Section 3.2. In both cases, the top electrode was etched before the XRD analysis. The interest in annealing at a higher temperature lies in promoting more complete crystallization of the HZO layer, which could improve ferroelectricity. The diffractogram for the 500°C anneal (blue curve) shows only minor differences compared to the 400°C, indicating that the overall crystallization of the HZO layer remains largely unchanged.

Cross-sectional TEM analysis shown in **Fig. 3.7 b**, corresponding to the same stack configuration with a TiN/W top electrode, reveals lattice fringes within the HZO layer, supporting the partial crystallization suggested by the in-plane XRD results. Further analysis in **Fig. 3.7 c** displays a sample after furnace annealing at 400°C for 1 hour. The TEM image confirms a more extensively crystallized HZO layer, while also revealing possible interfacial layers at both the top and bottom electrode interfaces.

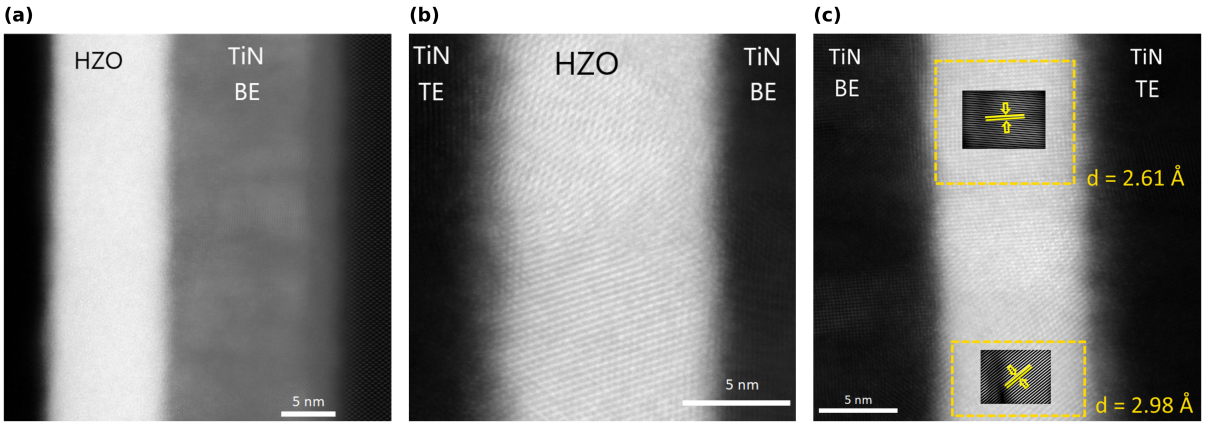

Figure 3.7: Cross-sectional TEM microscopy images of the MFM stack with a 10 nm HZO layer at different process stages. **a.** As-deposited HZO layer grown by ALD on a TiN bottom electrode **b.** After top electrode (TE) deposition at 380°C, with TiN used for both the TE and BE. Partial crystallization is visible. **c.** After furnace annealing at 400°C for 1 hour. Crystalline regions are now clearly distinguishable in the HZO layer, with lattice fringes indicating local crystalline order.

To better characterize the crystallographic nature of the film, a Fast Fourier Transform (FFT) was applied to a selected region of the annealed TEM image in **Fig. 3.7 c**. Filtering of the FFT patterns enabled the identification of lattice spacings corresponding to the $(200)_m$ and $(111)_o$ crystallographic planes, with measured d-spacings of 2.61Å and 2.98Å, respectively. These values are attributed to the coexistence of monoclinic and orthorhombic phases within the HZO solid solution structure after annealing.

It is important to note, however, that this observation is not statistical, as TEM only probes a localized region of the sample. While the TEM image in **Fig. 3.7 c** confirms the presence of crystallized regions, the cross-sectional TEM lamella is typically only ∼150 nm thick and represents a very small fraction of the film. Therefore, the presence of amorphous regions elsewhere in the sample cannot be excluded.

Moreover, a thin TiO_xN_y interfacial layer at the top interface cannot be ruled out. Given that TiN is known to act as an oxygen scavenger [131], and considering the high temperature involved in W deposition (see Chapter 2), interfacial oxygen redistribution may occur.

Fig. 3.8 presents the EDX line scans of the 10 nm HZO film at two different stages of the fabrication process. In **Fig. 3.8 a**, the HZO layer was analyzed just after deposition on a TiN bottom electrode (with no top electrode), while **Fig. 3.8 b** corresponds to the same structure after top electrode deposition and subsequent annealing at 400°C for 1 hour.

For the as-deposited sample (**Fig. 3.8 a**), the uniform signal profiles confirm the compositional homogeneity of the HZO film. The presence of Si and O signals above the HZO layer originates from the FIB lamella preparation, specifically due to the use of TEOS during focused ion beam (FIB)–induced deposition. After annealing (**Fig. 3.8 b**), the distribution of Hf and Zr remains broad and consistent, supporting the formation of a stable solid solution. The presence of O, N, and Ti signals is attributed to the oxide matrix and surrounding TiN electrodes,

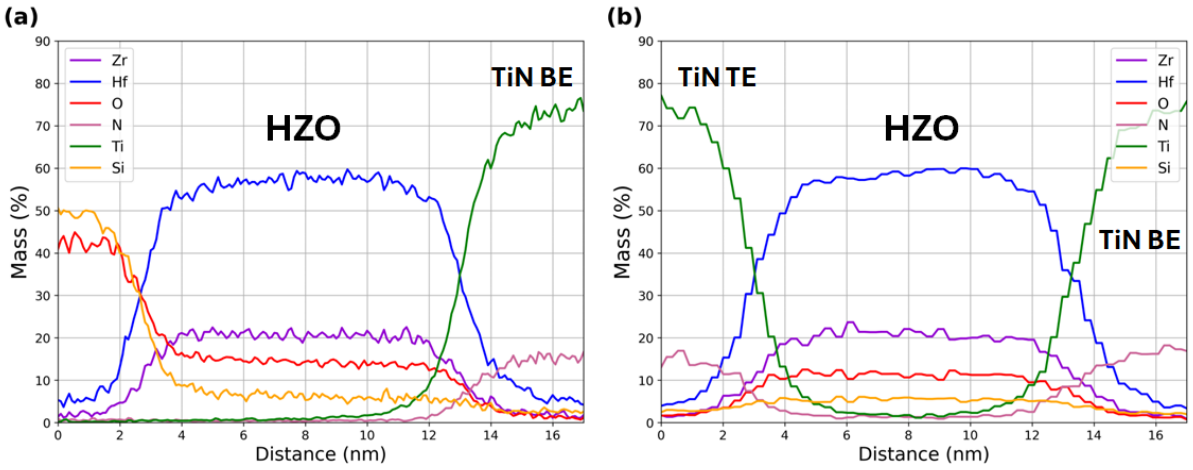

Figure 3.8: EDX line profiles showing the elemental distribution across the MFM stack with a 10 nm HZO layer at different process stages. **a.** As-deposited HZO layer grown by ALD on a TiN bottom electrode (BE), with no top electrode. **b.** After top electrode (TE) deposition and furnace annealing at 400°C for 1 hour.

as previously discussed. Full elemental distribution maps for these two stages are provided in appendix 2.

Complementary information on the compositional profile of the 10 nm HZO film with a 50 nm TiN PVD top electrode annealed at 400°C is provided in the appendix 3, where ToF-SIMS depth profiling confirms a uniform distribution of Hf, Zr, and O, along with the presence of residual chlorine, likely originating from the ALD process.

2.3 Electrical performance of capacitors

In-plane XRD results demonstrated the presence of a peak at 30.5° in **Fig. 3.6 ,** which can be attributed both to the ferroelectric orthorhombic phase and to a non-ferroelectric tetragonal phase. Hence, electrical characterization was performed to quantify the ferroelectric behavior. PUND measurements were carried out as described in Chapter 2.16, to extract ferroelectric parameters while avoiding parasitic non-ferroelectric currents. A triangular cycling protocol of ± 4 V at 10 kHz was applied for the initial 10 cycles to evaluate the evolution of $2P_r$ and E_c, and then at 100 kHz for the subsequent long-cycling measurement. Electrical tests were conducted on capacitors with a diameter of 100 μm.

Fig. 3.9 presents the polarization–electric field (P–E) loops of HZO 10 nm samples subjected to different annealing conditions: (a) without post-deposition annealing, (b) annealed at 400°C for 1 hour, and (c) annealed at 500°C for 15 minutes. All measurements were performed on the same MFM stack previously described, comprising a 15 nm-thick Ti/TiN bottom electrode, 10 nm-thick HZO with a 1:1 Hf:Zr composition, and a TiN/W top electrode.

The electrical characterization reveals an evolution of ferroelectric behavior with annealing. The unannealed sample already shows a measurable ferroelectric response, although with significantly lower polarization compared to the annealed samples. This suggests that some degree

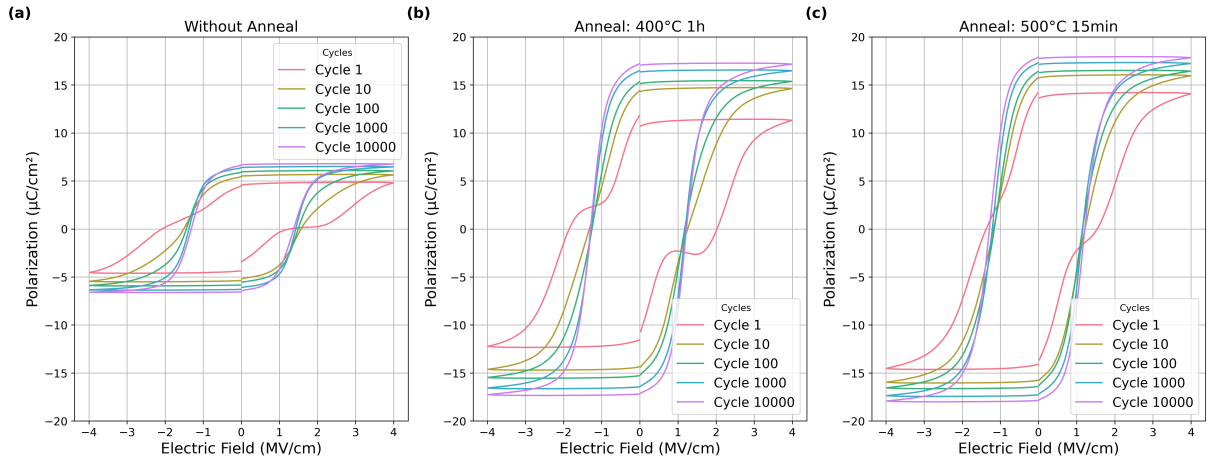

Figure 3.9: Polarization-electric field (P-E) loops of HZO 10 nm samples annealed at different conditions: **b.** without annealing, **b.** 400°C for 1 hour and **c.** 500°C for 15 minutes. The 500°C-annealed sample exhibits higher initial polarization and less pronounced wake-up effect. All measurements were performed on the same MFM stack previously described, comprising a 15 nm-thick Ti/TiN bottom electrode, 10 nm-thick HZO with 1:1 Hf:Zr composition, and a TiN/W top electrode.

of crystallization has occurred despite the absence of an explicit annealing step. The results are consistent with the structural analyses discussed earlier (**Fig. 3.6 a**nd **Fig. 3.7)**, where both XRD and cross-sectional TEM confirmed the presence of crystalline regions.

Comparing the samples annealed at 400°C and 500°C (**Fig. 3.9 b** and **Fig. 3.9 c**), only minor differences in $2P_R$ were observed. The sample annealed at 500°C exhibited a less pinched hysteresis in the pristine state and a slightly higher total polarization, with $2P_R$ values of 22 μC/cm^2 and 24 μC/cm^2 at 10^4 cycles for 400°C and 500°C, respectively. This suggests enhanced crystallization of the ferroelectric orthorhombic phase and reduced wake-up effect at 500°C. These findings are consistent with literature reports, which also show little difference in polarization between annealing at 400°C and 500°C, even though the absolute polarization values reported are higher (approximately 40 μC/cm^2) [132].

Unlike studies such as [133] and [134], where 400°C annealing resulted in amorphous films or weak polarization that required extensive cycling to induce ferroelectricity, the 400°C sample in this work exhibited good polarization after only 10 cycles, despite an initial wake-up effect. This suggests that the processing conditions used here were sufficient to partially crystallize the orthorhombic phase. While [135] reported higher $2P_r$ values, the small difference in polarization between the two annealing temperatures aligns with the trend observed in this study. Variations in results may be attributed to differences in ALD precursors and annealing methods (RTA vs. furnace). Still, the performance at 400°C is promising and compatible with BEOL requirements, supporting its potential for integration in memory applications.

To further investigate the origin of the observed wake-up effect, preliminary synchrotron-based Extended X-ray Absorption Fine Structure (EXAFS) and Grazing-Incidence Wide-Angle X-ray Scattering (GIWAXS) measurements were performed on 10 nm HZO 1:1 capacitors annealed at 400°C for 1 hour, fabricated as described in appendix Section 4.1. EXAFS provides

information on the local atomic environment around specific elements, while GIWAXS offers surface-sensitive insights into crystalline phase formation and texture. The samples were subjected to electrical cycling using PUND measurements, and structural analysis was conducted after selected cycle counts. According to the preliminary results detailed in the appendix 4, a structural evolution can already be observed during the initial 1–10 PUND cycles, suggesting that electrical cycling may actively influence phase transitions or atomic rearrangements. However, these findings remain under investigation, and further analysis is required to confirm the evolution and quantification of the phase fractions. The experimental procedures used for EXAFS and GIWAXS are also described in the appendix 4.2 and 4.4.

2.4 General conclusion

In this subchapter, the intrinsic characteristics and processing conditions of the standard 10 nm HZO material were evaluated, from deposition to device performance. Initial analysis confirmed the amorphous nature of the as-deposited films and highlighted the impact of top electrode deposition and subsequent annealing on crystallization. XRD results demonstrated the coexistence of orthorhombic, tetragonal, and monoclinic phases, with higher annealing temperature (500°C) leading to more pronounced crystallization. Electrical characterization confirmed ferroelectric behavior, emphasizing the role of annealing in reducing the wake-up effect and enhancing polarization.

Compared to the literature, the results obtained in this work highlight the potential of the sample annealed at 400°C, which exhibited early ferroelectric response despite a noticeable wake-up effect. This contrasts with other studies where ferroelectricity was not observed at this temperature due to insufficient crystallization. Although the improvement at 500°C was subtle, it is likely related to enhanced formation of the orthorhombic phase, resulting in slightly enhanced electrical performance. These findings reinforce the importance of thermal treatment in tuning ferroelectric properties and confirm the viability of HZO-based structures for integration into advanced memory technologies, offering a balance between performance and industry-compatible processing conditions.

This comprehensive analysis of the 10 nm HZO reference standard establishes a robust baseline for understanding the relationships between material processing, structural evolution, and electrical behavior. It provides a valuable benchmark for comparison with alternative material systems, including different Hf/Zr ratios, electrode configurations, and ultra-thin multilayered structures, which will be explored in the following subchapters.

3 Impact of top electrode configurations on the ferroelectric performance of HZO capacitors

As previously discussed, electrode materials play a key role in the integration of HZO-based ferroelectric capacitors. While TiN remains the standard choice, alternative materials have been explored to improve performance. Their influence on interfacial chemistry, work function, and thermal behavior can significantly affect crystallization, stress development, and the electrical properties of the film.

Electrodes also impact the structural characteristics of the HZO layer, such as crystallographic texture and stress state. In particular, electrode-induced stress, dependent on material type and thickness, can promote stabilization of the orthorhombic phase, essential for ferroelectricity.

In this study, the bottom electrode was fixed as a 15 nm Ti/TiN layer deposited by PVD, while different top electrode configurations were explored, varying the stacking materials, thickness, and deposition temperature. This approach aims to analyze how these parameters influence the structural and potentially ferroelectric behavior of the HZO capacitors, with particular attention to stress and crystallographic effects.

3.1 Top electrode configurations and fabrication details

The top electrode configurations studied are detailed in **Table 3.1**. Prior to the deposition of the top electrode, all samples underwent a degassing step at 200°C for 30 seconds.

Table 3.1: Summary of the top electrode configurations used in this study, including material stacks, deposition techniques, generator types, and processing temperatures.

Config.	Materials and Thicknesses	Deposition Technique and Generator	Temperature
1	10 nm TiN (CVD) + 50 nm TiN (PVD)	CVD + PVD (DC + RF)	340°C (CVD), Room (PVD)
2	60 nm TiN	PVD (DC + RF)	Room
3	10 nm TiN (CVD) + 70 nm W (SSP)	CVD + SSP (DC + RF)	380°C
4	60 nm TiN	PVD (DC only)	Room

The configurations were selected based on material availability, in-house expertise with deposition methods, and alignment with commonly reported setups in the literature. TiN and W are widely used in ferroelectric devices due to their known influence on the ferroelectric behavior of HZO, as previously discussed.

3.2 Intrinsic properties of the electrode films

Fig. 3.10 displays the in-plane XRD pattern of the 15 nm Ti/TiN bottom electrode, deposited by PVD (DC only) and used consistently across all MFM structures in this study. The XRD pattern reveals the presence of (111), (002), and (220) diffraction peaks, confirming the polycrystalline nature of the as-deposited TiN film.

The in-plane XRD analysis of the as-deposited TiN top electrodes in **Fig. 3.11 a** and **Fig. 3.11 b** reveals predominant (111), (002) and (220) crystalline orientations. While the

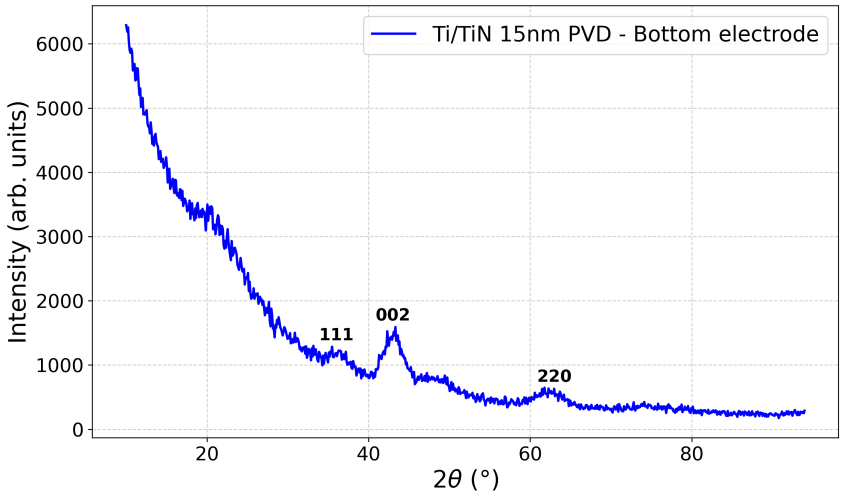

Figure 3.10: In-plane XRD pattern of the bottom electrode used in all MFM structures throughout this study. This electrode consists of a 15 nm thick Ti/TiN layer deposited by PVD (DC only) in a Si wafer.

crystallographic structure of the underlying HZO layer was not directly analyzed in this case, such orientations could influence its phase formation and stress state.

In the literature, studies have focused on TiN used as a top electrode, showing that a dominant (002) TiN orientation tends to correlate with a weaker orthorhombic (111) reflection, while a (111) TiN orientation is associated with a stronger presence of this reflection, suggesting more favorable conditions for stabilizing the ferroelectric phase [136, 137]. Although these findings refer to top electrodes, it is likely that the crystalline orientation of the bottom electrode during HZO deposition can similarly affect the preferential growth and phase stability of the ferroelectric layer.

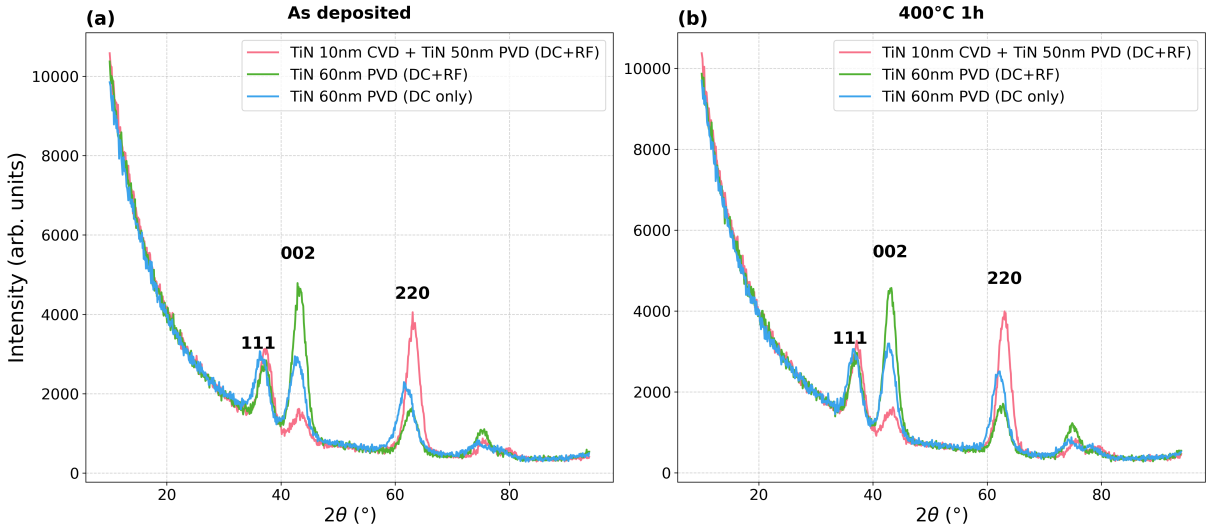

Figure 3.11: **a.** In-plane XRD patterns of **a.** as deposited TiN electrodes with different deposition conditions and **b.** after 400°C for 1 h annealing.

All metallic top electrode configurations examined exhibit similar intensity for the (111) reflection of TiN, indicating that this crystalline orientation is consistently present across samples. However, notable differences in the (002) peak intensity are observed. Specifically, TiN 60 nm PVD (Configuration 2) displays the strongest (002) reflection, whereas the TiN 10 nm CVD + TiN 50 nm PVD exhibit the lowest intensities for this peak, indicating a reduction in (002) orientation. Interestingly, the (220) reflection follows an inverse trend to the (002) peak, with higher (220) intensity observed in samples where the (002) orientation is reduced. Although this (220) orientation has not been directly linked in the literature to any specific impact on polarization, the trend may still influence the subsequent electrical performance.

Finally, the XRD results show that the intensities and 2θ positions of the (111), (002), and (220) peaks remain stable across all fabrication steps, as shown in **Fig. 3.11 a** and **Fig. 3.11 b**.

The stress evolution in the different metalic films, as shown in **Fig. 3.12 ,** reveals clear distinctions between TiN and W-based depositions. The stress was measured using the bow method, as described in Chapter 2 Sextion 2.7. TiN-based electrodes initially exhibit compressive stress, with values reaching approximately -7 GPa for the bilayer TiN 10 nm CVD + TiN 50 nm PVD, whereas the W-containing electrode starts in tensile stress (2 GPa). Upon annealing at 400°C, a significant stress relaxation occurs, where TiN structures transition from compressive to tensile stress, while the W-containing electrode shifts from tensile to nearly stress-free conditions.

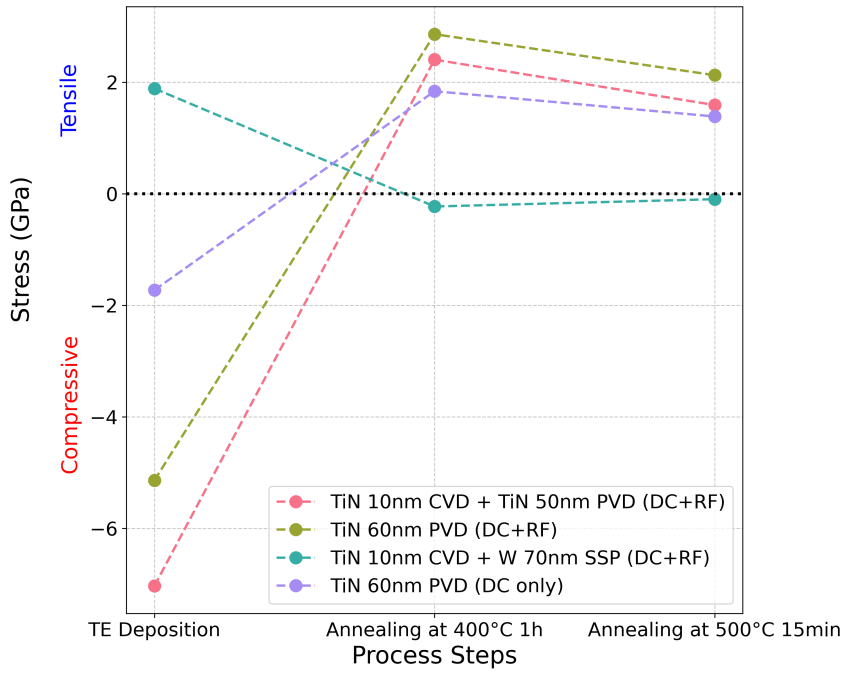

Figure 3.12: Evolution of stress during different processing steps for TiN- and W-based electrodes. The bow of the wafer was measured at three stages: after top electrode (TE) deposition, after annealing at 400°C for 1hour, and after annealing at 500°C for 15 minutes.

The presence of compressive stress in as-deposited TiN films can be primarily attributed to the atomic peening effect, a well-documented phenomenon in sputter-deposited films [138, 139]. During deposition, high-energy neutral gas atoms (such as Ar) collide with the growing

film, leading to atomic implantation and microplastic deformation. In our study, TiN-based electrodes initially exhibit strong compressive stress, especially in the bilayer TiN 10 nm CVD + TiN 50 nm PVD configuration, consistent with this mechanism.

Upon annealing, the observed stress transition from compressive to tensile in TiN electrodes suggests a film densification process that reduces the contribution of atomic peening-induced stress. The literature suggests that as grain size increases, the density of grain boundaries decreases, reducing the number of sites where excess atoms can accumulate, thereby alleviating compressive stress [138, 139]. In our results, annealing at 400°C facilitates a significant stress relaxation, with TiN structures transitioning from compressive to tensile stress, while the W-containing electrode shifts to a nearly stress-free state. This trend is also observed in samples annealed at 500°C, although the wafers were processed independently.

Although both configurations 2 and 4 use 60 nm TiN deposited by PVD, the differences in stress behavior can likely be attributed to the type of generator used during deposition. Configuration 2 employs both DC and RF generators, while Configuration 4 uses DC only, which may influence plasma conditions and, consequently, the film properties.

As reported in [140–142], superimposing an RF bias on DC sputtering enables direct tuning of substrate ion energy, yielding high-density TiN while maintaining control over intrinsic stress. By contrast, in DC-only sputtering the stress is modulated primarily by adjusting chamber pressure: higher pressure lowers ion energy and atomic peening, reducing stress but increasing film porosity. Thus, the generator scheme plausibly explains the stress differences between Configurations 2 (DC+RF) and 4 (DC).

Changing the DC power in a DC-only process does affect the plasma density and sputtering rate, but the ion energy at the substrate is only weakly influenced because the substrate potential is determined by the plasma conditions. As a result, DC power changes impact flux more than energy, meaning that pressure remains the dominant parameter for stress control in DC-only sputtering, while RF bias provides direct control over ion energy.

3.3 Evaluation of stress evolution through bow analysis in HZO capacitors

To better understand the mechanical evolution during fabrication, this study investigates the complete stack, enabling an evaluation of how each processing step affects the HZO layer.

Fig. 3.13 presents the evolution of wafer bow throughout key fabrication steps, after top electrode (TE) deposition, etching, and annealing—for both TiN- and W-based electrodes. In contrast to the previous analysis conducted on standalone metallic films, this stress evaluation was performed on full MFM stacks, including the TiN bottom electrode (BE) and the HZO layer, enabling a more direct assessment of the mechanical impact on the ferroelectric material.

The bow analysis in **Fig. 3.13 w**as carried out, as described in Chapter 2 Section 2.7, to evaluate the stress evolution at each processing stage and its impact on the HZO layer. Given that conventional stress calculations assume a continuous film, they may not be directly applicable after etching, where material removal modifies the sample geometry. Therefore, the delta bow approach is employed to track stress variations across different process steps, offering a comparative measure of the mechanical response of different electrode configurations.

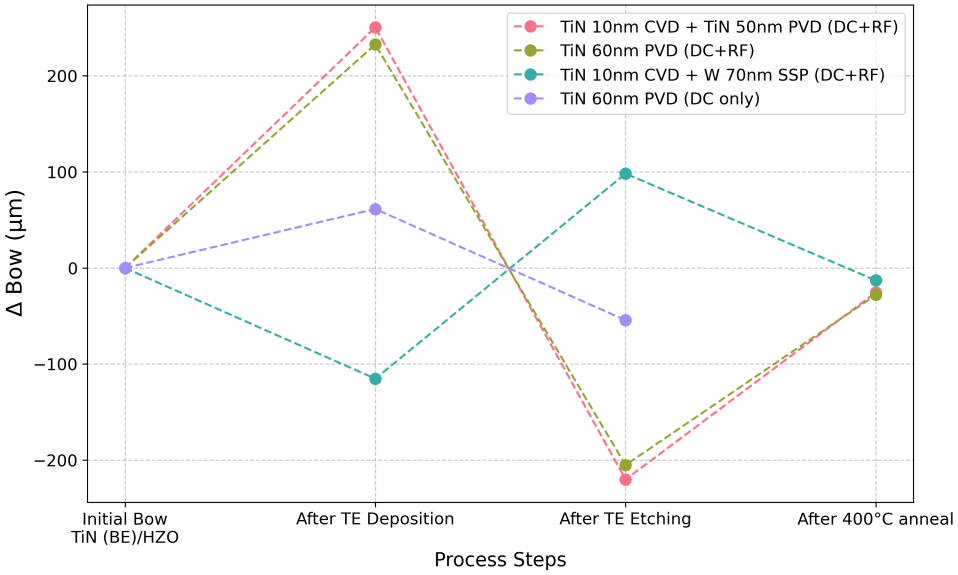

Figure 3.13: Evolution of delta bow during different processing steps for TiN- and W-based electrodes. The initial bow is set as the reference, followed by bow after top electrode (TE) deposition, after etching, and after annealing at 400°C for 1 h. The initial bow was measured on wafers with the TiN bottom electrode and HZO layer after ALD deposition

The results show that TiN-based electrodes induce high compressive stress after deposition, as seen by the increase in bow. In contrast, the W-based electrode initially exhibits tensile stress, resulting in a smaller bow magnitude. Etching introduces significant stress relaxation in most TiN-based samples, which shift toward a more tensile state, while the W-based sample becomes more compressive. This inversion may be attributed to either the discontinuity of the top electrode layer after etching, which limits the applicability of traditional stress estimation methods, or to material densification and structural evolution, as discussed in the previous section.

After annealing at 400°C, all samples show a more neutral bow, indicating overall stress relaxation and structural stabilization of the stack. However, even though delta bow decreases significantly after etching and annealing, local stress may still persist in regions where the top electrode remains, and could influence the ferroelectric behavior of the underlying HZO.

To further explore the relationship between mechanical stress and ferroelectric performance, electrical measurements were performed on etched capacitors both before and after the annealing step. The goal was to determine whether the reduction in wafer bow observed after etching and annealing **Fig. 3.13 c**orresponded to a full relaxation of stress within the active device area. As shown in **Fig. 31 a**nd detailed in appendix 5, the resulting $2P_R$ values were similar regardless of whether etching occurred before or after annealing. These results indicate that the observed relaxation in global stress, as measured by bow analysis, does not translate into a measurable change in ferroelectric polarization.

However, this does not exclude the presence of localized interfacial stress, especially underneath the remaining top electrode. Such localized effects may still influence domain behavior but are more difficult to quantify with wafer-scale methods. Therefore, while the global stress state

appears largely relaxed after annealing, local mechanical environments at the HZO/electrode interface may persist and subtly affect the material's electrical response.

3.4 Influence of top electrode configurations on electrical performance of HZO capacitors

The polarization evolution with cycling for the different top electrode configurations reveals distinct trends in remanent polarization ($2P_r$) and wake-up behavior in **Fig. 3.14 a**. Despite all configurations sharing TiN interfaces with the HZO layer, differences in polarization were observed among the different top electrodes.

It is important to note that all configurations were subjected to the same thermal treatment, annealing at 400°C for 1 h, and were based on 10 nm-thick HZO films. This ensures that the observed variations are primarily related to the top electrode configuration rather than differences in thermal budget or film thickness.

Configurations 1 and 3 exhibited the highest $2P_R$ values among all top electrode configurations analyzed, as seen in **Fig. 3.14 a**. While both demonstrated strong ferroelectric response, their behavior differed primarily during the initial electrical cycles. Configuration 1 (10 nm TiN via CVD + 50 nm TiN via PVD) shows a lower wake-up, suggesting a favorable initial ferroelectric state after annealing. In contrast, Configuration 3 (10 nm TiN via CVD + 70 nm W via SSP) displayed a more pronounced wake-up effect, characterized by a gradual increase in $2P_R$ during cycling. Although the polarization levels converge after 10^3 cycles, the wake-up characteristics differ between the two configurations. By comparison, Configuration 2 (60 nm TiN via PVD) shows a pronounced wake-up effect but achieves the lowest $2P_r$ among all configurations.

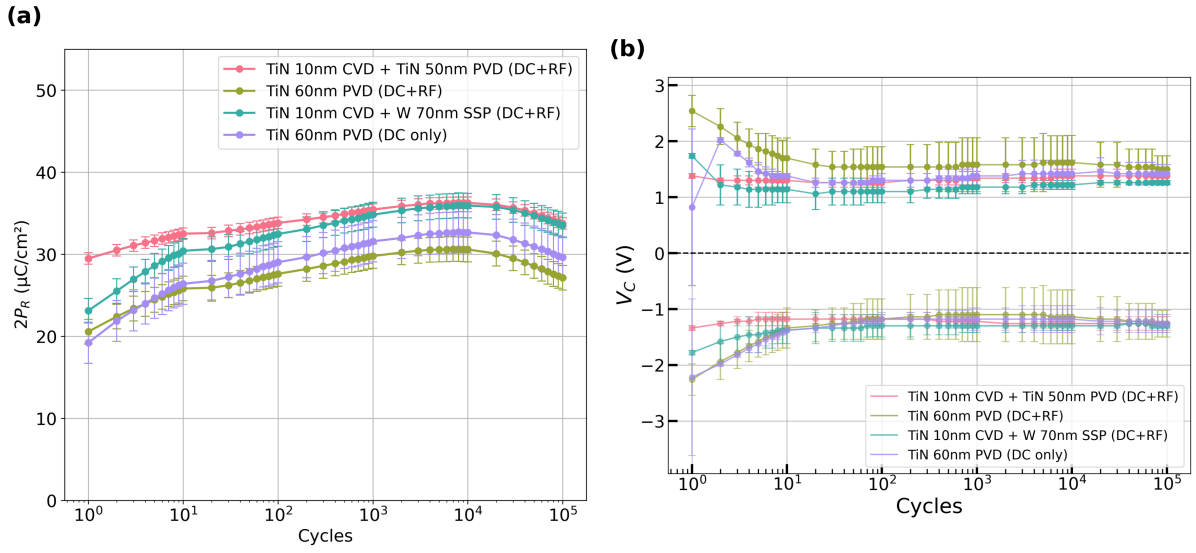

Figure 3.14: a. Evolution of remanent polarization ($2P_r$) and **b.** coercive voltage (V_C) as a function of cycling for different top electrode configurations annealed at 400°C for 1 h.

The coercive voltage (V_C) in **Fig. 3.14 b** exhibits a clear stabilization trend over cycling for all electrode configurations. Initial variations in V_C across the samples can be attributed

to the wake-up effect. As cycling progresses, the $|V_C|$ values gradually converge and stabilize around $\pm 1.3\,\mathrm{V}$ for all configurations. This convergence suggests that, despite differences in top electrode materials and deposition methods, the coercive voltage is primarily governed by the total thickness of the HZO layer.

The current density versus electric field plot (**Fig. 3.15)** confirms that all configurations exhibit similar leakage behavior, suggesting that leakage is also governed by the HZO thickness rather than the top electrode configuration. The curves shown represent the median response of approximately 20 capacitors per configuration, with very low variation across devices, justifying the use of the median as a reliable and representative indicator of leakage characteristics.

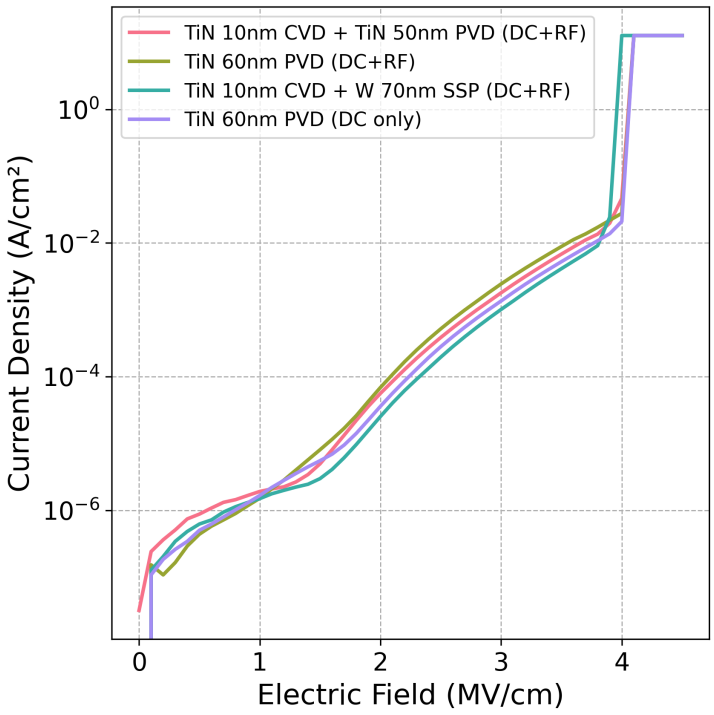

Figure 3.15: Current density as a function of the electric field for different top electrode configurations annealed at 400°C for 1 h.

To better understand the observed electrical behavior, a correlation with the previously discussed XRD and stress analyses was established, aiming to clarify the role of structural properties in the ferroelectric behavior. The in-plane XRD analysis revealed that Configuration 1 (10 nm TiN via CVD + 50 nm TiN via PVD) exhibited the lowest (002) TiN reflection intensities, indicating a weaker (002) TiN orientation compared to the other configurations. According to the literature already discussed in the previous subsection, reduced (002) orientation is supposed to promote the formation of the o-(111) ferroelectric phase, enhancing ferroelectric properties. This aligns with the high $2P_r$ observed in these samples. Conversely, TiN 60 nm PVD (configuration 2) displayed the strongest (002) TiN peak, suggesting a dominant (002) orientation, which is less favorable for stabilizing the ferroelectric phase. As a result, this configuration exhibited one of the lowest $2P_r$ values, reinforcing the correlation between crystallographic orientation and electrical performance, as shown in **Fig. 3.16 a**.

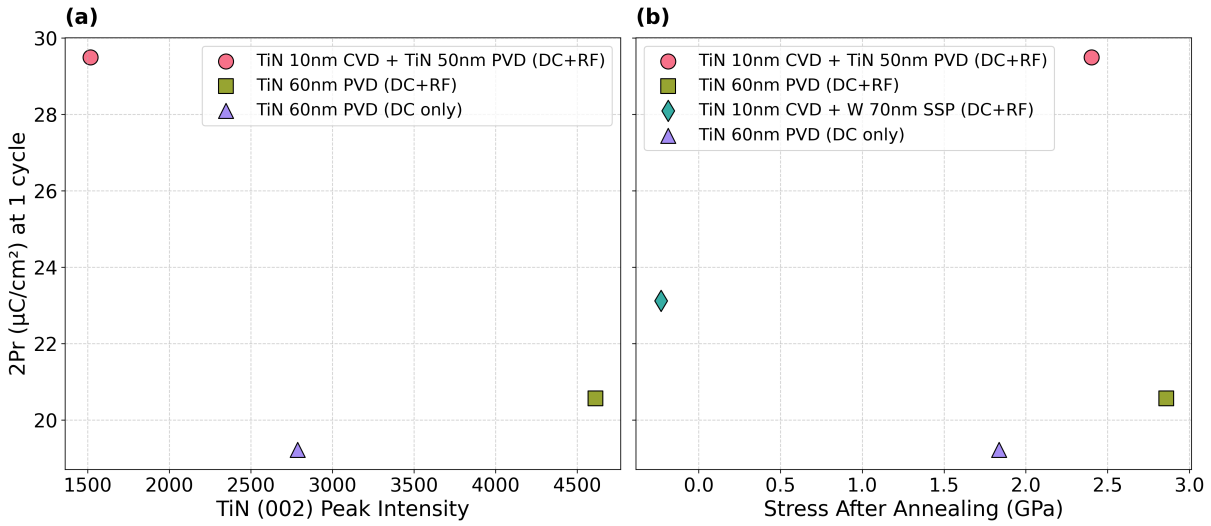

Figure 3.16: a. Relationship between in-plane XRD TiN (002) peak intensity and the initial $2P_r$ of films after 400°C for 1 h annealing. **b.** Correlation between stress after top electrode deposition and initial $2P_r$ values after annealing at 400°C for 1 h.

Similar to the observed correlation between TiN crystallographic orientation and polarization, an attempt was made to relate the stress state after top electrode deposition to the polarization in **Fig. 3.16 b**. Although the literature often highlights the role of mechanical stress, particularly tensile stress, in stabilizing the orthorhombic ferroelectric phase, no clear correlation can be established in our results. Regardless of whether the measured stress was compressive or tensile, after annealing at 400°C for 1 h, no consistent relationship with the initial $2P_R$ values is observed. These results suggest that macroscopic wafer-scale stress, as measured in this study, is not a determining factor in the ferroelectric response.

As shown in [49], the remanent polarization and switching field of $Hf_xZr_{1-x}O_2$ thin films can be tailored by modifying the in-plane strain within the film. However, the reference study is not directly comparable to our dataset. It analyzed material-level strain of the HZO by extracting in-plane strain from XRD peak positions and correlating it, together with DFT simulations, to phase stability (promotion of the $Pca2_1$ orthorhombic phase) and ferroelectric metrics (remanent polarization and switching field). The stacks used thin 10 nm TiN top electrodes and patterned capacitor dots. By contrast, our study evaluates macroscopic stress and wafer deformation (wafer bow/curvature) of the stacks, which averages over large areas; as such, the two approaches probe different stress scales and are not directly comparable.

3.5 General conclusion

This study highlights the impact of top electrode configurations on the structural, mechanical, and electrical properties of HZO-based ferroelectric capacitors.

Although initial stress states, compressive for TiN and tensile for TiN/W, are observed after top electrode deposition, these stresses relax substantially following etching and annealing steps. While the literature suggests that in-plane tensile stress promotes the formation of the

orthorhombic ferroelectric phase, no clear correlation is observed between the residual stress values and the final remanent polarization in this study.

In contrast, a more consistent relationship emerges between the TiN crystallographic orientation and ferroelectric performance. In-plane XRD results show that configurations with weaker TiN (002) orientation tend to exhibit higher $2P_r$ values, aligning with literature reports that associate this orientation with the promotion of the o-(111) phase in HZO. Conversely, a dominant (002) orientation correlates with lower polarization.

Electrical characterization further confirms that configurations with less-pronounced TiN (002) orientation exhibit higher remanent polarization and reduced wake-up effects. Leakage current remains similar across most configurations and are primarily governed by the HZO thickness.

Overall, these findings emphasize the critical role of electrode selection in optimizing ferroelectric performance. By tailoring crystallographic orientation and deposition conditions, it becomes possible to enhance polarization stability and overall device reliability.

4 Chapter Summary and Conclusions

This chapter established a baseline for HZO thin films, linking deposition, electrode integration, and thermal treatment to structure and device performance. Using the 10 nm HZO stack as a reference, we confirmed the amorphous as-deposited state and the role of annealing in crystallization and ferroelectric activation: films annealed at 400 °C already exhibit ferroelectric response, with noticeable wake-up, while a 500 °C anneal yields a modest improvement of polarization.

The impact of the top electrode was examined from mechanical and crystallographic viewpoints. Although initial stress states (compressive for TiN, tensile for W) are observed after top-electrode deposition, they relax substantially after etching and annealing; no clear correlation emerges between residual wafer bow and final $2P_r$. In contrast, a stronger and more reproducible link is found with TiN texture: configurations with a weaker TiN(002) orientation tend to show higher polarization and reduced wake-up, aligning with reports that favor environments stabilizing the o-(111) response.

These insights provide a coherent framework for the following subchapters, where we compare alternative Hf/Zr ratios, thickness reduction studies, and ultra-thin multilayer structures to further optimize ferroelectricity.

Chapter 4

Composition and Thickness Scaling in HZO Solid Solution Films

Objectives

Building on the insights gained from the study of 10 nm HZO reference structures, this chapter explores how variations in Hf/Zr composition and film thickness influence the structural and electrical properties of HZO thin films. Reducing the thickness of ferroelectric layers is of particular interest for enabling low-power operation in next-generation memory devices, as thinner films generally require lower switching voltages. However, aggressive downscaling also introduces challenges such as incomplete crystallization.

To address these limitations, particularly the deterioration of crystallization at low thicknesses and the need to reduce the operating voltage, this chapter investigates how composition engineering can be leveraged to compensate for the effects of thickness reduction. Deviations from the equimolar Hf:Zr ratio, whether toward Hf-rich or Zr-rich configurations, could offer pathways to stabilize the ferroelectric phase or improve other functional properties. Through a systematic analysis of structural and electrical data across multiple compositions and thicknesses, this chapter aims to identify the design conditions that allow polarization to be maintained or enhanced at reduced dimensions.

Contents

1 Introduction **80**
2 Influence of Hf/Zr compositions on the properties of 10 nm HZO thin films **81**
2.1 Composition tuning of HfO_2–ZrO_2 solid solutions via ALD 81
2.2 Correlation between composition and ferroelectric performance 82
2.3 General conclusion 85
3 Thickness effects on the properties of HZO 1:1 thin films **86**
3.1 Thickness and thermal effects on HZO thin films 86
3.2 Electrical properties of HZO thin films: impact of thickness and annealing temperature 87
3.3 Correlation between polarization and XRD intensity in HZO films 92
3.4 Benchmark 93
3.5 General conclusion 95
4 Composition engineering for stabilizing ferroelectricity in ultrathin films **97**
4.1 Crystallization trends across composition and thickness 97
4.2 Composition-driven variations in electrical results 99
4.3 General conclusion 102
5 Chapter Summary and Conclusions **103**

1 Introduction

Following the characterization of 10 nm HZO reference structures in the previous chapter, this section delves into the impact of Hf/Zr composition and film thickness scaling on the structural and electrical properties of the material. While the equimolar 1:1 Hf/Zr ratio is widely adopted due to its ability to stabilize the ferroelectric orthorhombic phase, deviations toward Hf- or Zr-rich compositions introduce distinct changes in phase formation and polarization behavior. These compositional variations play a key role in tailoring material performance to meet specific application requirements.

Reducing ferroelectric film thickness is highly attractive, as it enables lower coercive fields and reduced operating voltages, which are essential for energy-efficient memory and logic applications. However, as ferroelectric films are scaled down to 6, 5, and 4 nm, new challenges emerge. Ultrathin films often exhibit incomplete crystallization or a higher tendency toward non-ferroelectric phases, degrading key functional properties such as remanent polarization and endurance. This chapter explores how careful composition tuning can compensate for these scaling-related limitations and help preserve ferroelectric behavior at reduced dimensions.

Through the combined analysis of structural and electrical results, this chapter aims to clarify the interplay between composition, thickness, and phase stability in HZO films, and to identify promising directions for the development of next-generation ultrathin ferroelectric devices.

2 Influence of Hf/Zr compositions on the properties of 10 nm HZO thin films

The ferroelectric behavior of $Hf_xZr_{1-x}O_2$ thin films strongly depends on composition, with intermediate Hf:Zr ratios favoring enhanced polarization, while Hf-rich and Zr-rich extremes tend to stabilize non-ferroelectric monoclinic and antiferroelectric tetragonal phases, respectively, according to literature [122, 143].

This section discusses the impact of varying Hf/Zr ratios on the structural, electrical, and ferroelectric properties of 10 nm HZO thin films. By examining phase composition, polarization behavior, and their evolution upon thermal treatments, it aims to provide insights into how composition tuning can optimize the stabilization of the orthorhombic ferroelectric phase and improve device performance.

2.1 Composition tuning of HfO_2–ZrO_2 solid solutions via ALD

Different $Hf_xZr_{1-x}O_2$ thin films were deposited by ALD to explore the impact of composition on their structural and ferroelectric properties. A super-cycle approach in ALD was employed to control the Hf/Zr composition in the thin films. Each super-cycle consisted of an 'm' unit cycle for depositing HfO_2 and an 'n' unit cycle for depositing ZrO_2, allowing control over the stoichiometric ratio. In this study, different cycle ratios — among them 2:1, 1:1, and 1:2 — were used, resulting in Zr-rich, balanced, and Hf-rich compositions, respectively, with the thickness of the thin films fixed at approximately 10 nm.

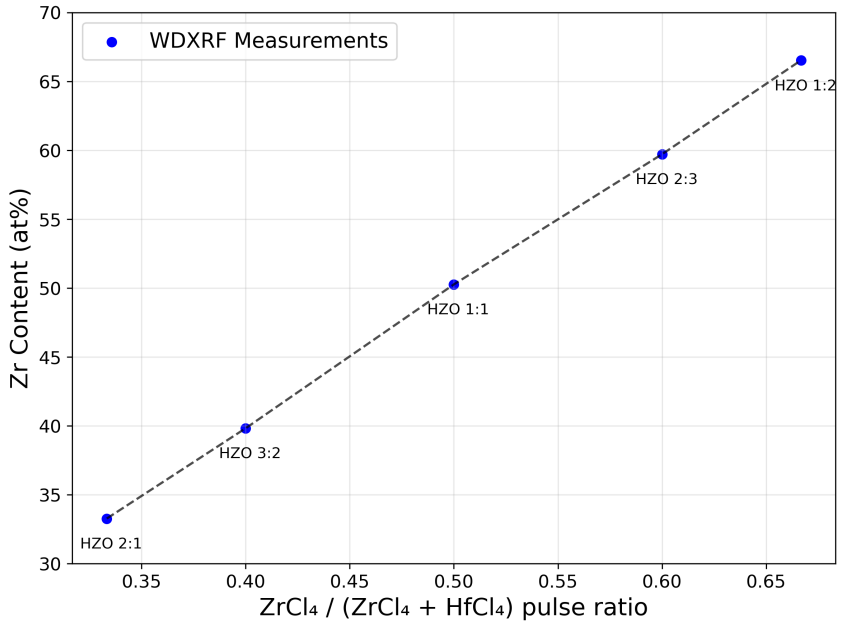

Figure 4.1: Zr/(Hf + Zr) atomic ratio of 10-nm-thick HZO thin films as a function of the Zr/(Hf + Zr) cycle ratio in the ALD process, measured by WDXRF.

The stoichiometric ratios of the HZO thin films were evaluated using WDXRF. As shown in **Fig. 4.1**, the measured Zr/(Hf + Zr) atomic ratios of 0.33, 0.5, and 0.66 are consistent with the

corresponding Zr/(Hf + Zr) cycle ratios in the ALD process, demonstrating a linear relationship between the ALD pulsing ratio and the resulting composition. The nearly identical GPC of the HfO_2 and ZrO_2 further ensure precise stoichiometric control in the mixed oxide films. This linear control highlights the capability of ALD to achieve predictable composition tuning, offering a robust platform for tailoring the ferroelectric properties of $Hf_xZr_{1-x}O_2$ thin films.

XRR measurements were performed on HZO films with 2:1, 1:1, and 1:2 Hf:Zr compositions. As summarized in **Table 4.1**, the density increases with higher Hf content. The Hf and Zr atomic percentages, measured by WDXRF, confirm the intended stoichiometry of each composition.

Table 4.1: Summary of HZO film characteristics as a function of Hf:Zr ratio, including thickness and density determined by XRR, and atomic percentages determined by WDXRF Measurements were performed on 300 mm wafers.

Ratio (Hf:Zr)	Thickness (nm)	Density (g/cm^3)	Hf at.%	Zr at.%
1:2	10.4	6.9	33.9	66.1
1:1	9.9	7.6	49.7	50.3
2:1	10.6	7.9	66.9	33.1

The differences in density reflect the composition variations induced by the ALD cycle ratios, specifically the relative proportions of Hf and Zr in the films. The higher density observed for the 2:1 composition is attributed to the greater Hf content, as HfO_2 has a higher density (9.6 g/cm^3 [144]) compared to ZrO_2 (5.6 g/cm^3) [145]. In contrast, the lower density for the Zr-rich (1:2) composition is due to the higher proportion of Zr in the material.

By comparing the measured densities with the expected linear values for each composition, calculated from the reference densities of HfO_2 and ZrO_2, the experimental densities are found to be consistently lower than the predicted ones. The deviation is minor for Zr-rich samples but becomes more pronounced for Hf-rich compositions, exceeding 0.5 g/cm^3. This discrepancy cannot be attributed solely to the intrinsic uncertainties of the XRR fitting procedure or the ∼3% uncertainty in the WDXRF composition measurements, and its origin remains under interpretation.

It should be noted that the density of HZO films could vary depending on the crystallinity of the material, as different crystalline phases (e.g., orthorhombic, tetragonal, or monoclinic) exhibit slightly different densities [146]. However, the films analyzed here are amorphous immediately after ALD deposition, as shown in **Fig. 4.2**. A broad feature is visible in the pattern, which may indicate the presence of nanocrystalline regions, but no distinct diffraction peaks corresponding to well-formed crystalline phases are observed at this stage. As a result, the observed density variations can be solely attributed to the differences in stoichiometry.

2.2 Correlation between composition and ferroelectric performance

After the top electrode deposition and subsequent annealing at 400°C for 1 hour, in-plane XRD analysis in **Fig. 4.3** shows the 10 nm HZO thin films and investigate the changes in their crystal structure based on their Zr content. All structures were fabricated with TiN/W top electrodes,

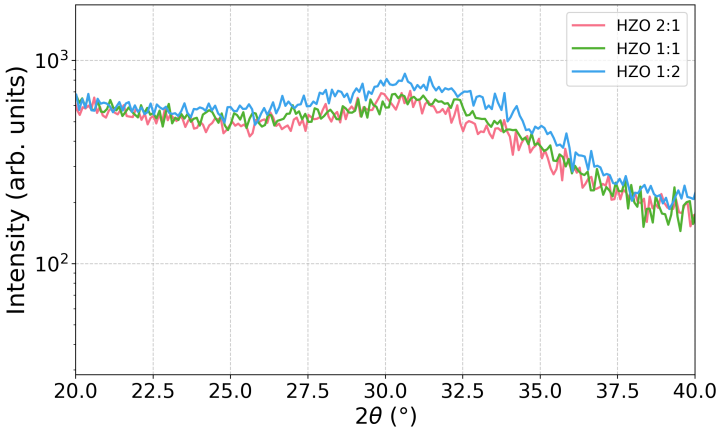

Figure 4.2: GIXRD results of 10 nm HZO as-deposited films in TiN with compositions 2:1, 1:1, and 1:2 Hf/Zr. The films are amorphous, as indicated by the absence of distinct crystalline peaks.

and the etching of the TE layer enabled direct observation of the HZO crystal phases. The results reveal that as the Hf content increases (or Zr content decreases), the monoclinic phase becomes more prominent, as indicated by strong peaks at 28.5° and 31°, which are the dominant reflections of this non-ferroelectric phase. This observation aligns with the inherent tendency of Hf-rich compositions to stabilize the monoclinic phase, which is a non-ferroelectric structure and has been associated with lower polarization values [122, 143].

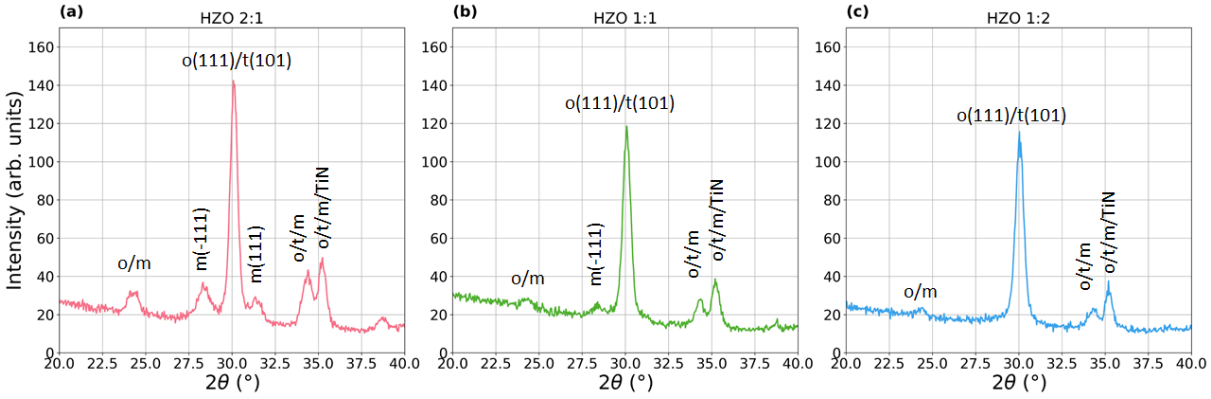

Figure 4.3: In-plane XRD patterns of 10 nm HZO thin films with compositions **a.** 2:1, **b.** 1:1 and **c.** 1:2 after TiN/W deposition and annealing at 400°C for 1 hour. Monoclinic phase peaks at 28.5° and 31° are more prominent in Hf-rich compositions, while the intensity of the 30.5° peak, commonly attributed to overlapping of the orthorhombic/tetragonal reflections, varies with composition, although no shift in its 2θ position is observed.

Interestingly, the peak at 30.5°, corresponding to the o/t phases, shows no significant shift in its position across the different compositions. This observation suggests that the material does not exhibit a strong preference for either the orthorhombic ferroelectric phase (which would shift left due to larger d-spacing) or the tetragonal antiferroelectric phase (which would shift right due to smaller d-spacing).

The polarization–voltage (P–V) characteristics of the MFM capacitors for the HZO thin

films with different compositions annealed at 400°C for 1 hour are shown in the **Fig. 4.4**.

The HZO 1:1 (**Fig. 4.4**b) exhibits the highest $2P_R$ across all cycles, aligning with expectations that the balanced Hf:Zr ratio is well-documented to stabilize the ferroelectric orthorhombic phase (o-phase), maximizing polarization [58, 122, 147].

In contrast, the HZO 1:2 (**Fig. 4.4**c) shows higher polarization compared to the 2:1 composition. After wake up, however, this enhanced polarization comes at the cost of a stronger antiferroelectric contribution, consistent with the known tendency of Zr-rich compositions to favor the tetragonal phase. As a result, more electrical cycling is required to stabilize the ferroelectric behavior.

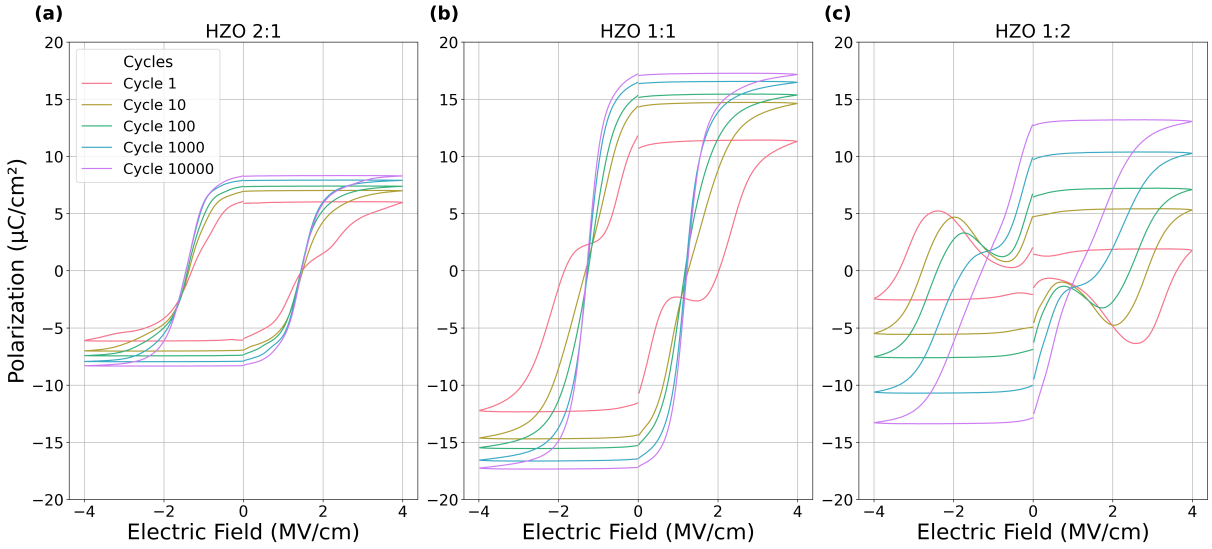

Figure 4.4: P–E loops for HZO films with **a.** 2:1, **b.** 1:1, and **c.** 1:2 Hf/Zr compositions after annealing at 400°C for 1 h

Meanwhile, the HZO 2:1, **Fig. 4.4**a, demonstrates intermediate polarization values, likely due to the reduced ferroelectric o-phase and the higher presence of the non-polar monoclinic phase, as the XRD analysis showed in **Fig. 4.3**a. However, the wake-up effect, observed as an evolution in polarization along cycling in **Fig. 4.5**, is less pronounced for the 2:1 composition compared to the 1:1 composition, revealing a more stable polarization behavior. This is likely due to the reduced Zr content, which limits the formation of the antiferroelectric tetragonal phase.

Recent studies, including those published by [148], provide valuable insights into the interplay between ferroelectric and non-ferroelectric phases in HZO thin films and their impact on device endurance. According to their findings, while maximizing the orthorhombic phase is critical for ferroelectricity, the presence of the monoclinic phase could help delay fatigue onset. This occurs because incoherent grain boundaries in mixed-phase films hinder the spread of pinned domains, enhancing endurance. Similarly, another study reports that epitaxial orthorhombic HZO films with greater monoclinic content exhibit improved endurance, while nearly single-crystalline films without parasitic phases suffer severe fatigue [149]. These findings suggest that monoclinic–orthorhombic grain boundaries reduce domain pinning propagation and offer a

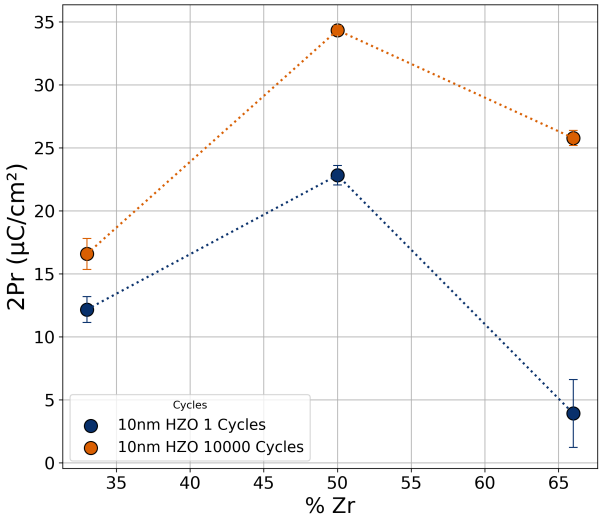

Figure 4.5: Remanent polarization (2Pr) as a function of Zr content in 10 nm HZO thin films, measured after 1 and 10000 cycles. This figure highlights the wake-up effect, observed as an increase in 2Pr with electrical cycling. All samples were annealed at 400°C for 1 h

strategy for increasing fatigue resistance in ferroelectric HZO-based devices.

2.3 General conclusion

In this subchapter, the impact of varying Hf/Zr ratios on the structural and ferroelectric properties of 10 nm HZO thin films is explored. The results show that the 1:1 composition (HZO 1:1) exhibits the highest remanent polarization, confirming that a balanced Hf/Zr ratio helps stabilize the orthorhombic phase, which is crucial for maximizing polarization. The Zr-rich composition (HZO 1:2) displays a higher wake-up effect, suggesting that increased Zr content enhances the cycling behavior of polarization, although this comes with a stronger antiferroelectric contribution.

In contrast, the Hf-rich composition (HZO 2:1) shows a greater presence of the monoclinic phase, as indicated by XRD analysis. Since the monoclinic phase is non-polar, its presence is typically associated with reduced remanent polarization. As a result, the Hf-rich films exhibit lower polarization values but demonstrate a more stable behavior with a less pronounced wake-up effect. The antiferroelectric contribution is notably reduced in Hf-rich films; however, this appears to have limited or no direct influence on device endurance. Interestingly, recent literature suggests that the presence of the monoclinic phase may improve device endurance by mitigating domain pinning. These findings highlight the importance of carefully tuning the Hf/Zr ratio to optimize the ferroelectric response of HZO films depending on the targeted device performance.

3 Thickness effects on the properties of HZO 1:1 thin films

The continuous push toward miniaturization in modern semiconductor technology has intensified the demand for ultrathin ferroelectric layers, especially for low-voltage and high-density applications. While HZO films offer key advantages, two main challenges remain for their use in embedded FeRAM: their high coercive field (about 1.5 MV/cm for 10 nm films), which leads to unacceptably high operating voltages for scaled logic, and the degradation of polarization and crystallization behavior as thickness decreases [99, 101, 150, 151].

This subchapter will delve into the effects of thickness reduction on the properties of HZO 1:1 thin films, focusing on the intricate relationship between thickness, crystallization behavior, and ferroelectric performance. By addressing these challenges, this discussion aims to identify processing conditions that preserve ferroelectricity while lowering the operating voltage, critical steps toward enabling ultrathin HZO integration into next-generation memory technologies.

3.1 Thickness and thermal effects on HZO thin films

In this study, the number of ALD cycles required to obtain the desired film thicknesses was determined based on the results presented in this chapter Section 2.1, using the GPC extracted from **Fig. 3.2 f**or the 1:1 HZO films deposited on TiN.

To investigate the impact of thickness reduction on the structural and ferroelectric properties of HZO 1:1 thin films, capacitors with film thicknesses of 10, 6, 5, and 4 nm were studied. The integrated capacitors were fabricated with the structure described in 3.1, consisting of a TiN/HZO/TiN-W MFM configuration. Two types of annealing processes were employed to crystallize the films: a furnace anneal at 400°C for 1 h or at 500°C for 15 min.

The presented results in **Fig. 4.6**a and **Fig. 4.6**b correspond to the in-plane XRD analysis performed after the etching of the top electrode. This analysis highlights the crystallographic structure of HZO 1:1 thin films with different thicknesses, under the two distinct annealing conditions. At 400°C, the 10 nm sample shows clear o(111)/t(101) peaks, while the 6 nm film exhibits weaker peaks, and the 5 and 4 nm films remain amorphous, likely due to insufficient energy for crystallization at low thickness.

When annealed at 500°C for 15 minutes, a marked improvement in crystallization is observed across most thicknesses. The 10 and 6 nm samples show stronger peaks, and the 5 nm sample also crystallizes. However, the 4 nm film remains mostly amorphous, indicating that even 500°C is still not sufficient for full crystallization at this thickness. These observations align with the expectation that thinner films require higher annealing temperatures to overcome the challenges posed by increased surface-area-to-volume ratios and interfacial energy [152].

Additionally, a peak is observed around 35°, which is present in some of the samples. This peak is commonly associated with the o(200) texture that contributes to enhanced polarization properties, as texture has been linked to improved ferroelectric phase formation, as discussed in [129]. The variation in the intensity of this peak across different thicknesses and annealing conditions suggests that the crystallization process is directly influenced by these parameters. While often linked to o(200) texture, its interpretation remains cautious due to possible overlap

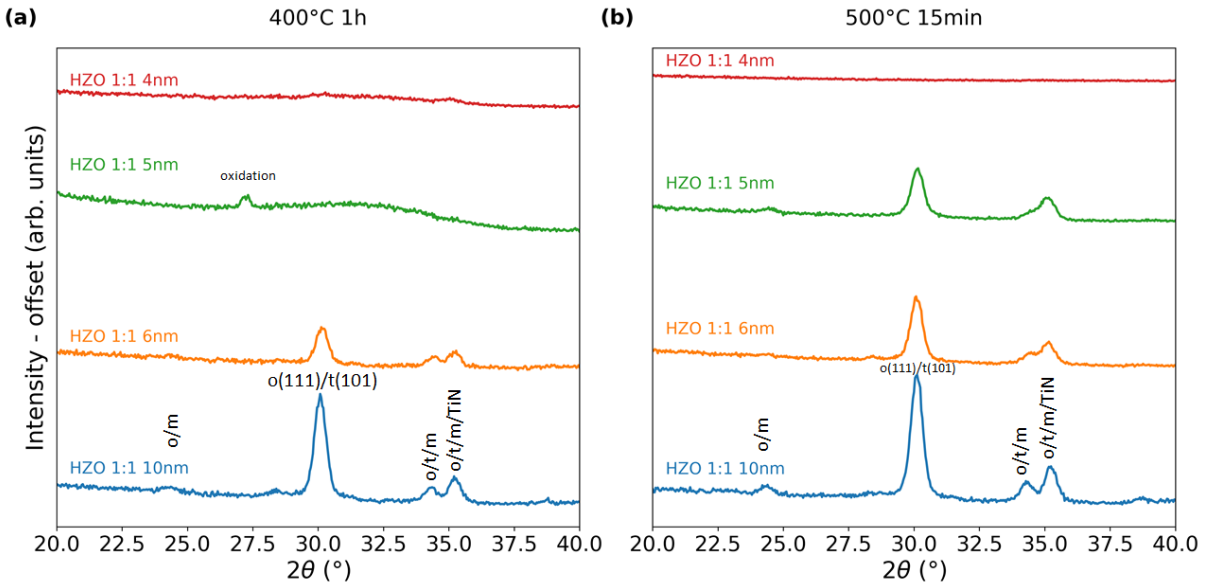

Figure 4.6: In-plane XRD analysis of HZO 1:1 thin films with thicknesses of 10 nm, 6 nm, 5 nm, and 4 nm after etching of the top electrode. The crystallization behavior is compared under two annealing conditions: **a.** 400°C for 1 hour and **b.** 500°C for 15 minutes.

with TiN(111) and non-ferroelectric phases, as discussed before.

Additional a low-intensity feature at 27°, labeled as "oxidation" in **Fig. 5.14**, is likely associated with surface oxidation of the exposed TiN or W electrodes following top electrode etching [153]. These signals are common artifacts in post-etch XRD measurements and are not related to the crystallinity of the ferroelectric layers.

These findings align with trends reported in the literature but also reveal key differences likely caused by process variations. Wang *et al.* observed clear o(111)/t(101) peaks near 30.5° in 3–6 nm HZO films after RTA at 450°C [151], whereas in this work, only the 5 nm sample showed such peaks after annealing at 500°C, with the 4 nm film remaining mostly amorphous. Lyu *et al.* also reported crystallization at 4 nm after RTA at 500°C [150], highlighting the strong influence of deposition conditions and MFM stack configuration. Additionally, Cho *et al.* demonstrated that both the ALD precursor chemistry and choice of oxidant impact crystallinity, with ozone enabling direct formation of crystalline HZO during deposition [58].

3.2 Electrical properties of HZO thin films: impact of thickness and annealing temperature

The ferroelectric properties of the HZO thin films were characterized through PUND analysis.

The 10 nm sample displays well-defined hysteresis loops, confirming successful crystallization and the presence of ferroelectric switching, as expected from the structural results. In contrast, the 6 nm film initially exhibits antiferroelectric-like behavior, which gradually evolves into ferroelectric response with continued cycling. This wake-up behavior suggests partial crystallization and indicates that the thermal budget at 400°C may not be sufficient to fully stabilize the orthorhombic phase at this thickness.

For the thinner films, the absence of hysteresis loops in the 5 nm and 4 nm samples annealed at 400°C, as shown in **Fig. 4.7**c and **Fig. 4.7**d, indicates a lack of ferroelectric switching. This is consistent with the in-plane XRD data in **Fig. 4.6**a, where no distinct diffraction peaks were observed for these thicknesses. The lack of both structural and electrical signatures of the ferroelectric phase suggests that the films remain largely amorphous under these annealing conditions.

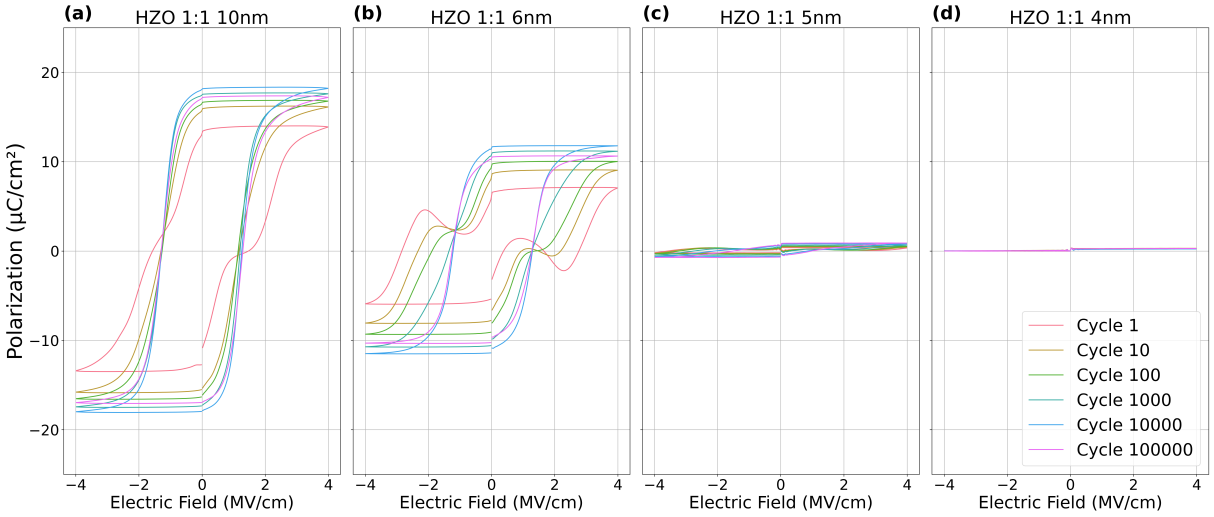

Figure 4.7: P-E loops of HZO 1:1 thin films annealed at 400°C for 1 h. The **a.** 4 nm and **b.** 5 nm samples remain amorphous, while the **c.** 6 nm sample shows partial ferroelectric behavior. The **d.** 10 nm sample displays clear ferroelectric characteristics.

At 500°C (**Fig. 4.8**), the ferroelectric response improves relative to 400°C. The 10 nm and 6 nm films show well-defined hysteresis from the outset, with the 10 nm sample exhibiting the highest remanent polarization and minimal wake-up. The 5 nm film starts with pinched (antiferroelectric-like) loops but evolves to clear ferroelectric behavior by 10^4 cycles. The 4 nm film remains antiferroelectric, indicating that, at this thickness, the thermal budget, as well as the overall MFM configuration employed, does not enable stabilization of the orthorhombic phase.

The 4 nm HZO annealed at 500 °C in this work exhibits lower polarization than the benchmark reported by Toprasertpong *et al.* [99]. In their study, a 4.0 nm HZO capacitor crystallized after a 500 °C/30 s rapid thermal anneal and reached $2P_r \approx 23\ \mu\mathrm{C\,cm^{-2}}$ at an operating field of 2.5 $\mathrm{MV\,cm^{-1}}$ after wake-up with 4 $\mathrm{MV\,cm^{-1}}$ pulses.

The difference can be attributed to variations in (i) ALD chemistry (chloride-based vs. metal–amide/H_2O, including the use of O_3 instead of H_2O and differences in deposition temperature), affecting impurity incorporation, nucleation density, and early phase formation; (ii) thermal budget/heating profile (long-ramp furnace anneal vs. short-duration RTA), influencing crystallization kinetics, grain size/texture, and orthorhombic phase formation at ultrathin thicknesses; (iii) electrode stack and patterning (25 nm TiN top/bottom with a 100 nm Al pad and dot capacitors), modifying interfacial constraint and in-plane strain; and (iv) the wake-up protocol, which sets the wake-up behaviour.

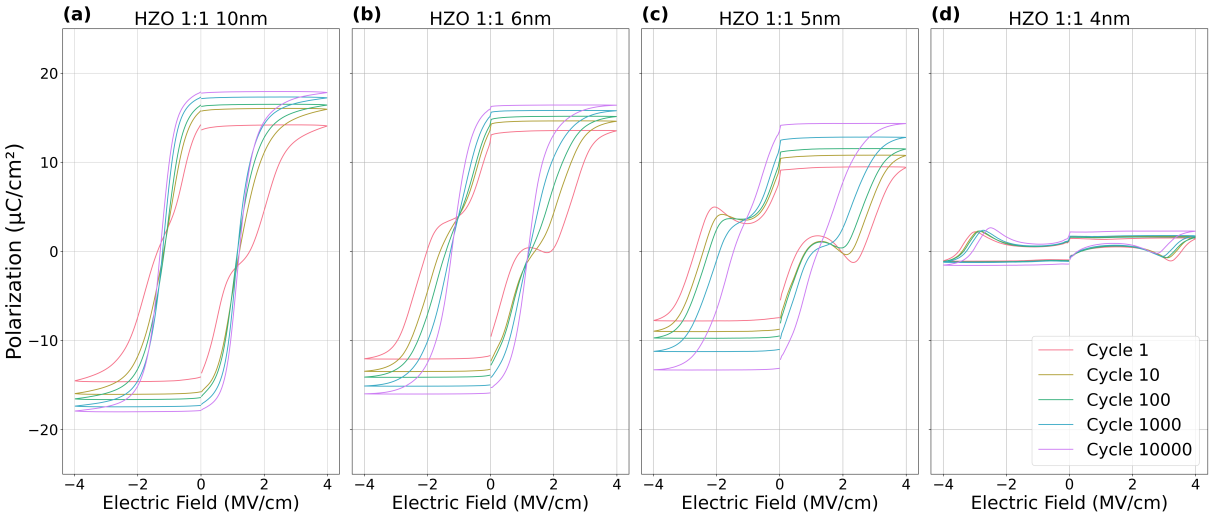

Figure 4.8: P-E loops of HZO 1:1 thin films annealed at 500°C for 15 min. The **a.** 4 nm sample shows antiferroelectric behavior, and the **b.** 5 nm sample fully transforms into a ferroelectric phase after 10^4 cycles. The **c.** 6 nm and **d.** 10 nm samples display robust ferroelectric behavior.

The results in **Fig. 4.9**a highlights the improvement in remanent polarization ($2P_r$) with increasing thickness and annealing temperature, demonstrating the influence of structural and thermal parameters on the ferroelectric properties. The data, obtained after 10^4 cycles from PUND measurements performed, show that higher annealing temperatures (500°C) significantly enhance $2P_r$, particularly for thinner films (5 nm and 6 nm), which initially display weak polarization due to incomplete crystallization.

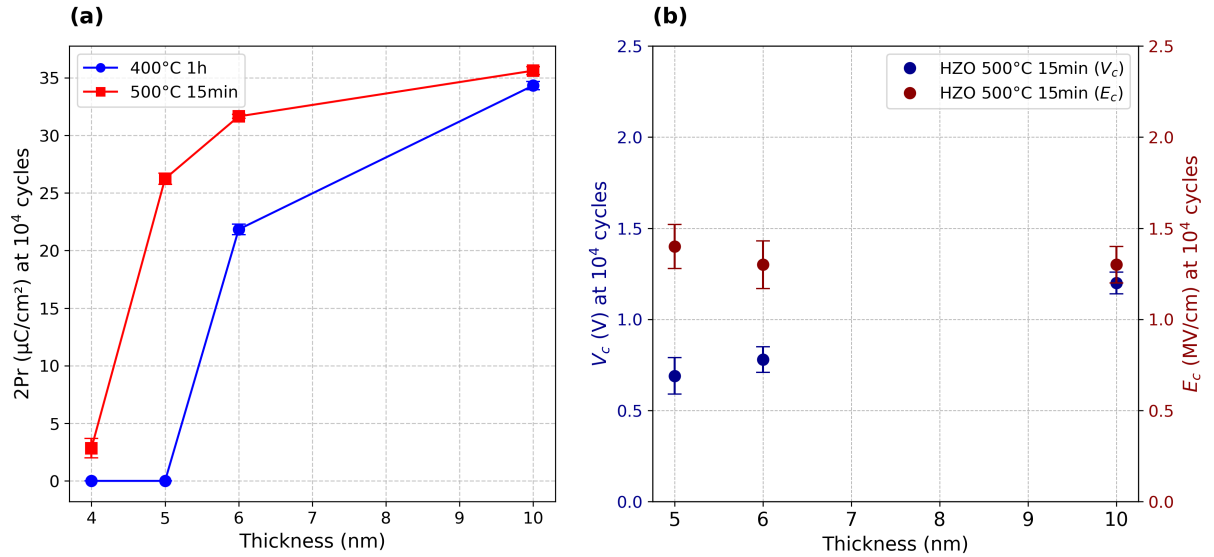

Figure 4.9: **a.** Remanent polarization ($2P_r$) of HZO 1:1 thin films after 10^4 cycles, showing improved $2P_r$ with increasing thickness and annealing temperature. **b.** Coercive voltage (V_c) and field (E_c) of HZO 1:1 thin films annealed at 500°C, with V_c decreasing for thinner films and E_c remaining constant.

The **Fig. 4.9**b shows the relationship between thickness and coercive voltage (V_c) as well as

the coercive field (E_c) for the same 1:1 composition annealed at 500°C. The data for the 4 nm sample is not included in the graph due to its antiferroelectric behavior, which persists even after annealing at higher temperatures. This result indicates that the ferroelectric phase can not stabilized at such a low thickness, consistent with previous observations.

The coercive voltage (V_c), measured after 10^4 cycles, decreases with reducing thickness, demonstrating the effectiveness of scaling in lowering the operating voltage. Meanwhile, the coercive field (E_c) remains relatively constant across all thicknesses, in agreement with prior studies that reported a similar behavior in HZO capacitors [99]. The constant E_c, independent of the HZO thickness, can be attributed to the polarization switching kinetics in thin HZO and has been theoretically predicted by the Landau-Ginzburg framework, as described in [99].

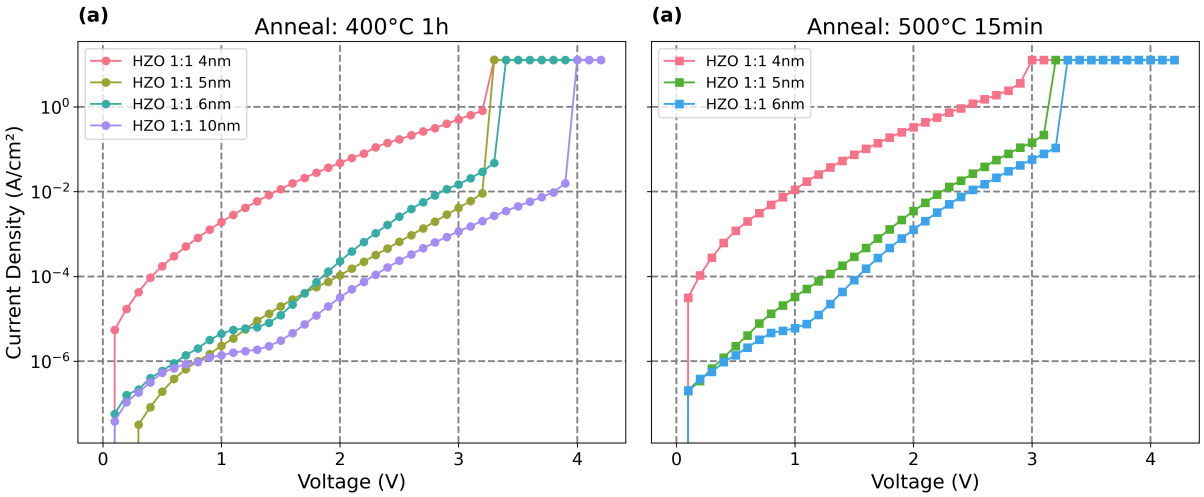

Figure 4.10: Current density (A/cm²) vs. Voltage (V) for HZO layers of different thicknesses (4, 5, 6, and 10 nm) **a.** annealed at 400°C for 1 hour and **b.** annealed at 500°C 15 min. Each curve represents the median response from 20 capacitors, ensuring results with very low dispersion and high reproducibility across devices.

The leakage current characteristics of HZO films exhibit a clear dependence on annealing temperature and film thickness. As seen in **Fig. 4.10**, the leakage current increases with the thermal budget of the annealing process. Samples annealed at 400 °C for 1 hour remain nanocrystalline and therefore present fewer conduction paths. In contrast, annealing at 500 °C for 15 minutes shows higher crystallization, leading to the formation of more grains and grain boundaries. These microstructural features, together with possible oxygen vacancy formation at higher temperatures [154], act as preferential pathways for charge transport, which explains the higher leakage currents observed at 500 °C.

Although the 4 nm HZO sample does not exhibit polarization or switching characteristics, it presents quasi-static I-V behavior comparable to that of the ferroelectric samples, even though each film displays its own particularities. However, the 4 nm HZO capacitor displays a high leakage current, exceeding that of the 10 nm film. This behavior is consistent with previous findings by Toprasertpong *et al.* [99], which show that HZO capacitors with thicknesses of 4.6 nm or more predominantly exhibit field-driven leakage, while devices with a thickness of

4 nm present significantly higher leakage currents likely due to an increased contribution of direct tunneling from the TiN electrodes through the thinner dielectric layer.

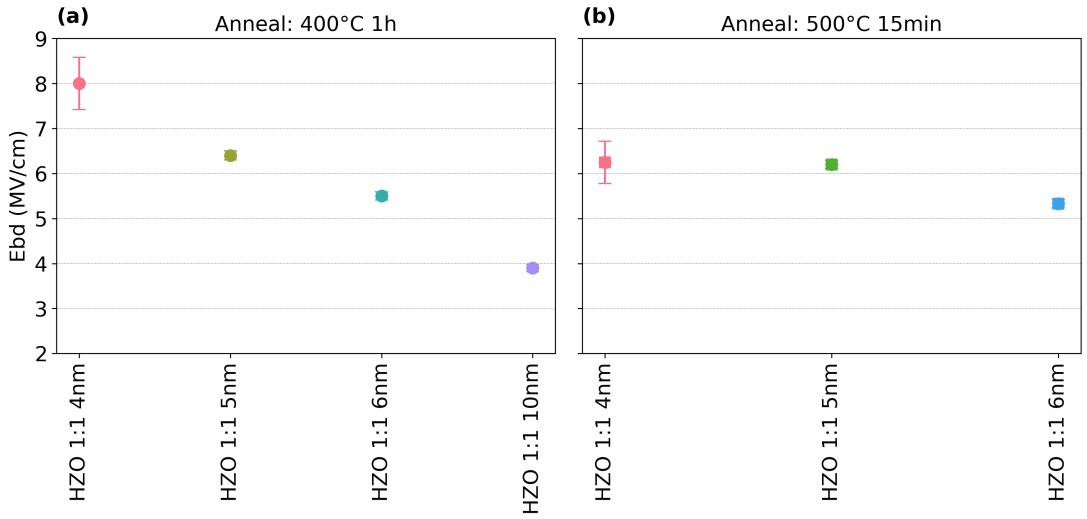

Figure 4.11: Comparison of breakdown field (E_{BD}) for different HZO thicknesses **a.** annealed at 400°C for 1 hour and **b.** annealed at 500°C 15 min.

Fig. 4.11 demonstrates that the breakdown field (E_{BD}) increases as the thickness of the HZO film decreases, especially for the samples annealed at 400°C, which is consistent with previous reports indicating that thinner ferroelectric films demonstrate greater breakdown tolerance under the same electric field [99]. This enhancement is especially evident in **Fig. 4.11**a, where the 4 nm films clearly show the highest E_{BD} values.

Consistent with prior reports [99], at the same applied field, the applied voltage is lower in thinner films. According to this reference, the injected electrons from the electrode have a lower injection energy, which causes less damage to the thin films. Thus, thinner films have more breakdown tolerance than thicker films under the same electric field, resulting in a higher E_{BD}. However, the detailed physical mechanism by which the electron energy injected from TiN electrodes triggers the breakdown of HZO is not yet clear and requires further investigation. This effect contributes to higher E_{BD} values in thinner films, reinforcing that thickness scaling is an effective approach for improving the breakdown tolerance of HZO-based FeRAMs.

From the increase in breakdown electric field E_{BD} in thin HZO films, we can expect an improvement in the endurance characteristics, which is a key challenge for FeRAMs using ferroelectric HZO. The ability to achieve higher breakdown tolerance in ultra-thin films suggests that thickness scaling is a viable strategy for enhancing device reliability, reducing operating voltages, and mitigating breakdown.

Furthermore, the breakdown field can be considered like an endurance assessment parameter, as it reflects the ability of the dielectric to withstand prolonged electrical stress without catastrophic failure. In this context, a higher E_{BD} indicates greater resistance to time-dependent dielectric breakdown (TDDB), which is commonly used as a reliability benchmark in microelectronics. Its relation to endurance arises from the margin between the coercive field and the breakdown field: the larger this difference, the longer the material can operate reliably.

3.3 Correlation between polarization and XRD intensity in HZO films

An attempt was made to correlate the remanent polarization ($2P_r$) with the intensity of the XRD peak at 30.5°, as shown in **Fig. 4.12**. This peak arises from overlapping contributions of the orthorhombic (o(111)) and tetragonal (t(101)) phases. Although these phases are structurally distinct, their diffraction patterns are highly similar, which makes precise deconvolution of the peak challenging. While the XRD signal provides insights into the degree of crystallization, it does not offer quantitative information on the fraction of the film that is crystallized, which may still contain amorphous regions.

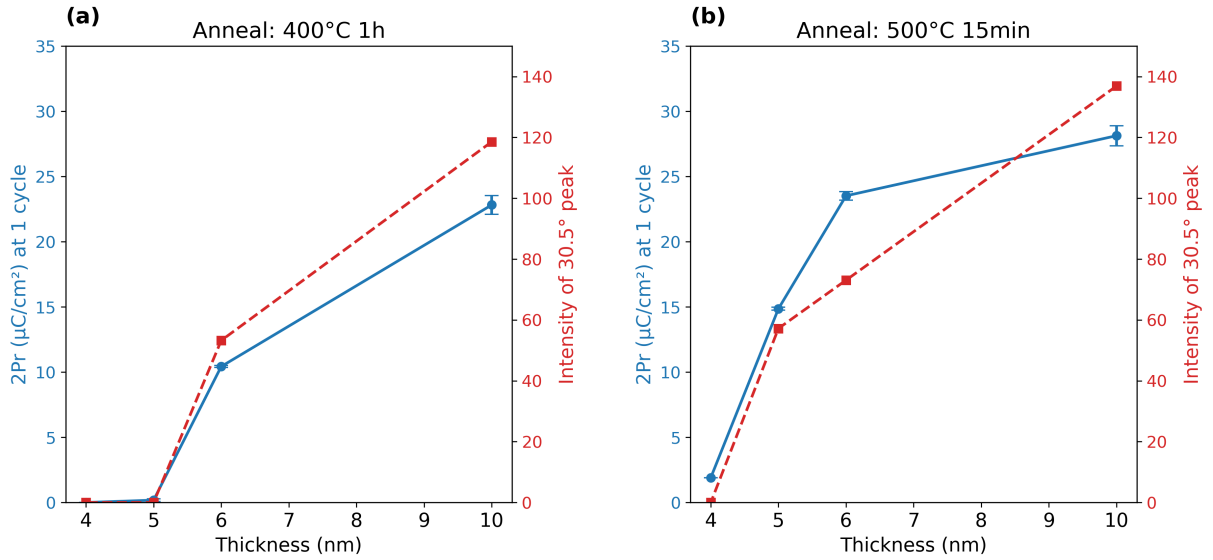

Figure 4.12: Relationship between remanent polarization ($2P_r$) and XRD peak intensity at 30.5° (o/t phases) for HZO 1:1 thin films annealed at **a.** 400°C and **b.** 500°C.

Despite the overlap, the intensity of the 30.5° peak can still serve as a useful indicator of the potential degree of crystallization. A stronger peak suggests higher structural ordering and, by extension, a larger volume fraction of the ferroelectric orthorhombic phase. The observed correlation shows that samples with greater peak intensity also exhibit higher $2P_r$ values, particularly in the 5 nm, 6 nm, and 10 nm films annealed at 500°C. This trend supports the interpretation that improved crystallization, regardless of the orthorhombic/tetragonal contributions, leads to enhanced polarization.

In contrast, the 4 nm films, which display neither significant peak intensity nor polarization, reflect the challenge of stabilizing the ferroelectric phase at such reduced thicknesses. As film thickness decreases, the energy barrier for the formation and stabilization of the orthorhombic phase increases, making it less energetically favorable for the material to crystallize into a polar phase [155]. This results in either an amorphous structure or the dominance of non-ferroelectric phases. These findings reinforce that the emergence of ferroelectric behavior in HZO is intrinsically linked to its structural evolution, with the orthorhombic phase playing a central role.

3.4 Benchmark

The benchmark analysis of remanent polarization across HZO thin films with a 1:1 composition in **Fig. 4.13** provides a comprehensive context for the studies presented in this work. By examining how film thickness and annealing conditions influence ferroelectric performance, and comparing these findings with results reported in the literature, this analysis effectively positions the outcomes of this manuscript within the broader field.

For the 10 nm thickness, the remanent polarization achieved in this study is comparable to the values typically reported in the literature for this type of film, as exemplified by Lehninger *et al.* [88]. This highlights the success of the processing conditions employed here in achieving robust ferroelectric performance. Consequently, these results underscore the competitive positioning of this work relative to similar studies.

Other studies have also reported values around 40 μC/cm^2, such as [68], which achieved $2P_r = 45$ μC/cm^2 by using a thick TiN top electrode to induce tensile stress during annealing. Even higher values, reaching 60–64 μC/cm^2, have been obtained under more aggressive processing conditions, as demonstrated in [156], through optimization of ozone exposure, interface engineering, and annealing at temperatures ranging from 500 to 800°C. However, these approaches exceed the BEOL thermal budget, limiting their industrial relevance and compatibility with standard integration flows.

In the intermediate thickness range of 6 nm and 5 nm, this study demonstrated high polarization values, further confirming the effectiveness of the annealing process in promoting ferroelectric phase crystallization. However, it is important to note that the annealing temperature used (500°C) exceeds BEOL-compatible limits. In contrast, other works, such as those by Lyu *et al.* and Wang *et al.* [151, 157], achieved comparable polarization at lower annealing temperatures, illustrating the potential for thermal budget optimization.

For films at 4 nm and below, this study encountered significant challenges in stabilizing the ferroelectric orthorhombic phase, resulting in negligible polarization. In contrast, studies by Toprasertpong *et al.* and Lyu *et al.* successfully achieved measurable polarization at 4 nm [99, 157]. Furthermore, Wang *et al.* reported even better results for thinner films while employing BEOL-compatible processes, emphasizing the feasibility of maintaining ferroelectric properties at extreme thickness scaling [151]. These comparisons highlight the opportunity for innovation in deposition and thermal processing methods to enable reliable ferroelectric performance in ultra-thin films.

It is also worth highlighting the recent advancements presented by [148], which reported a high-performance 3D stacked FeRAM architecture based on a doped HZO layer with a thickness of 5.7 nm. Their NVDRAM (non-volatile dynamic random access memory) technology demonstrated exceptional integration density and device performance, achieving a record-high effective $2P_r$ exceeding 55 μC/cm^2, measured using PUND at an operating voltage of 1.5 V, and maintaining endurance up to 10^{12} cycles. Although these results are highly relevant for future technological deployment, the lack of publicly available details regarding the material synthesis, stack formation, and processing conditions prevents a direct comparison with the experimental results presented in this study. Nevertheless, the achievement of A. Chavan *et al.* reinforces

the importance of ongoing efforts toward scalable, high-performance ferroelectric stacks, such as those developed in the present work.

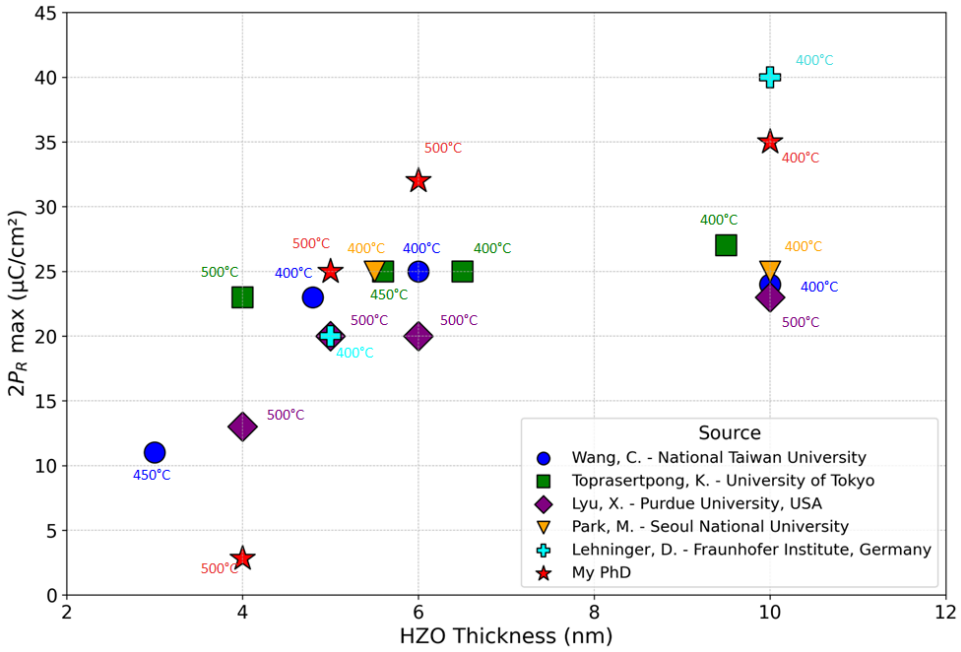

Figure 4.13: Benchmark of remanent polarization for HZO thin films with a 1:1 composition across various thicknesses.

The differences in processing methods used in this study and those reported in the literature can explain the variations observed in this benchmark comparison. These differences come from factors such as the ALD deposition process, annealing conditions, electrode selection, and overall device fabrication strategies.

Additionally, part of the discrepancy may stem from variations in the degree of crystallinity of the HZO films themselves. Since XRD only provides information about the crystalline portion of the material, we cannot precisely quantify how much of the film remains amorphous or how much is actually crystallized into the ferroelectric orthorhombic phase. This uncertainty makes direct performance comparisons more complex, as polarization values strongly depend on the volume fraction of the active ferroelectric phase.

The deposition process is a critical factor in determining the quality of HZO thin films. In this work, a thermal ALD process at 300°C with $HfCl_4$ and $ZrCl_4$ precursors was employed, ensuring controlled stoichiometry and film uniformity. In contrast, Lyu *et al.* [157] and Wang *et al.* [151] employed organometallic-based ALD and PEALD processes, respectively, achieving improved ferroelectric performance at similar thicknesses. Wang's use of PEALD with O_2 as the oxidant likely enhanced ligand removal and minimized carbon contamination, while also being associated with partial crystallization during deposition, as previously discussed [158]. While organometallic precursors are often associated with carbon incorporation, their successful application in these studies suggests that, when carefully optimized, they can yield high-performance ferroelectric films.

Electrode material and deposition method also significantly affect ferroelectric behavior. Lyu employed WN electrodes deposited by ALD, which are known for their oxygen scavenging behavior. This property can actively remove oxygen from the HZO layer near the interface, promoting the formation of oxygen vacancies that could help stabilizing the ferroelectric orthorhombic phase. In prior studies, such behavior has been shown to enhance ferroelectricity, with optimized WN-based structures, and a long endurance of $> 10^{10}$ cycles was also obtained [159]. Wang *et al.* used a metal stack consisting of a Pt bottom electrode and a TiN top electrode deposited by PEALD, which played a critical role in promoting the o-phase. As discussed in [160], the ALD TiN capping layer generated higher in-plane tensile stress than sputtered TiN and led to the formation of a TiO_xN_y interfacial layer, both contributing to improved crystallization and polarization. This approach enabled a $2P_r$ of 51.2 $\mu C/cm^2$ in sub-10 nm ALD films after annealing at only 400°C.

Annealing conditions also play a decisive role in determining the material's ferroelectric properties. This study employed a high annealing temperature of 500°C for 15 minutes, which facilitated the crystallization of the orthorhombic ferroelectric phase and resulted in high polarization values, particularly for the 6 nm and 5 nm films. However, this temperature exceeds BEOL compatibility limits. In contrast, Lyu *et al.* achieved comparable polarization values at 500°C using rapid thermal annealing for just 1 minute, which reduced thermal exposure while still stabilizing the ferroelectric phase. Similarly, Wang *et al.* and Lehninger *et al.* used lower annealing temperatures (400–450°C) with RTA for 60 seconds, achieving promising polarization results while adhering to BEOL constraints. These differences highlight the need for refining annealing processes to reduce thermal budgets without compromising ferroelectric performance.

Finally, the fabrication and measurement strategies employed by different studies contribute to the observed performance variations. Differences in capacitor size and electrical testing conditions, such as cycling protocols, frequencies, and field strengths, often not fully specified in the literature, can also play a significant role in the observed differences.

3.5 General conclusion

This study systematically explores the effects of thickness scaling and annealing conditions on the structural, electrical, and reliability properties of HZO thin films. In-plane XRD analysis reveals that while 10 nm films crystallize at BEOL-compatible temperatures (400°C), thinner films ($\leq$ 5 nm) require higher annealing temperatures (500°C) to stabilize the orthorhombic ferroelectric phase. However, at extreme scaling (4 nm), crystallization remains incomplete, which limits ferroelectric performance.

Electrical characterization shows that thinner films lower the coercive voltage (V_c), which benefits the reduction of operating voltages. However, at 4 nm, polarization ($2P_r$) is significantly reduced, with antiferroelectric behavior emerging and tunneling becoming the dominant leakage mechanism. Although 500°C annealing improves performance for 5–6 nm films, this temperature exceeds BEOL-compatible limits, suggesting the need for alternative annealing methods. Reliability studies confirm that thinner films generally exhibit higher breakdown fields (E_{BD}), although leakage associated with tunneling becomes a limitation at extreme thickness scaling.

Overall, this work highlights the trade-offs of thickness scaling: while ultrathin HZO films offer lower operating voltages and improved breakdown characteristics, achieving stable ferroelectricity at extreme scaling requires precise control of crystallization and interface properties. Further process optimization, including advanced annealing techniques and interface engineering, is critical for the integration of high-performance, scalable ferroelectric devices. This perspective is reinforced by the benchmark study, which demonstrates that improved electrical performance is achievable through optimized processing strategies.

4 Composition engineering for stabilizing ferroelectricity in ultrathin films

As shown previously, the stabilization of the ferroelectric orthorhombic phase in ultrathin HZO films remains a significant challenge as the thickness decreases below 10 nm. As the film thickness scales down, significant structural and phase-related transformations occur, driven by interface effects and changes in phase equilibrium.

In this context, adjusting the Zr ratio has emerged as a promising approach to mitigate undesired phase stabilization in ultrathin films. However, it remains unclear whether the compositional strategies effective at 10 nm are directly applicable at 6 nm or below, where the impact of interfaces becomes more pronounced and may alter the balance between ferroelectric and non-ferroelectric phases.

Tailoring the Zr ratio in ultrathin films can be an effective alternative to mitigate these structural and compositional effects, enabling improved performance even at reduced dimensions. In particular, adjusting the composition may help counteract the excessive stabilization of the tetragonal phase (t-phase), which is often favored in ultrathin films and known to degrade ferroelectricity. To this end, the investigation of composition optimization presented in this subchapter will primarily focus on 6, 5, and 4 nm films, where the challenges of phase stabilization and interface effects are most pronounced.

4.1 Crystallization trends across composition and thickness

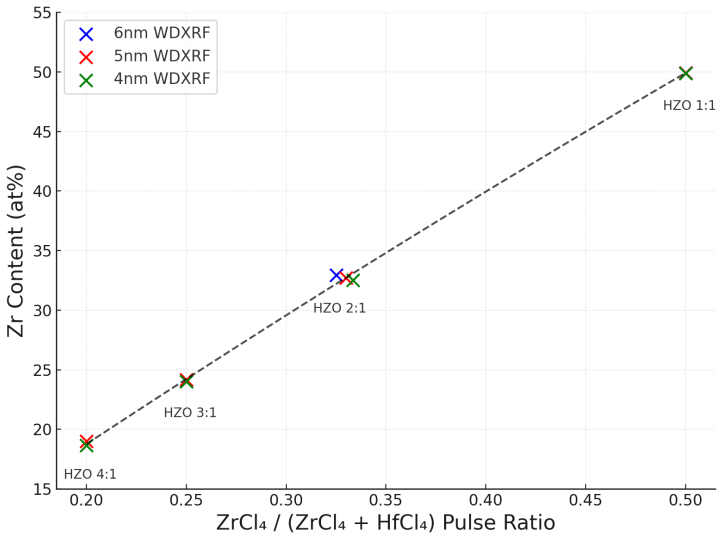

Figure 4.14: Zr/(Hf + Zr) atomic ratio of HZO films of varying thicknesses (6 nm, 5 nm, and 4 nm) films as a function of the Zr/(Hf + Zr) cycle ratio in the ALD process, measured by WDXRF. All films were deposited on a Ti/TiN substrate.

The results presented in the **Fig. 4.14 c**onfirms the clear linear relationship between the $ZrCl_4$ / ($ZrCl_4$ + $HfCl_4$) pulse ratio and the Zr content (at%) measured via WDXRF for films of varying thicknesses (6 nm, 5 nm, and 4 nm). This trend indicates that the ALD process main-

tains a predictable and stable stoichiometric control, where the precursor dose ratio directly influences the atomic composition of the deposited films. The consistency across thicknesses suggests that the ALD growth mechanism is well-controlled, with minimal deviation in composition as the film thickness decreases.

Notably, all thicknesses exhibit a nearly identical dependence on the precursor pulse ratio, confirming that composition control remains robust across different scaling conditions.

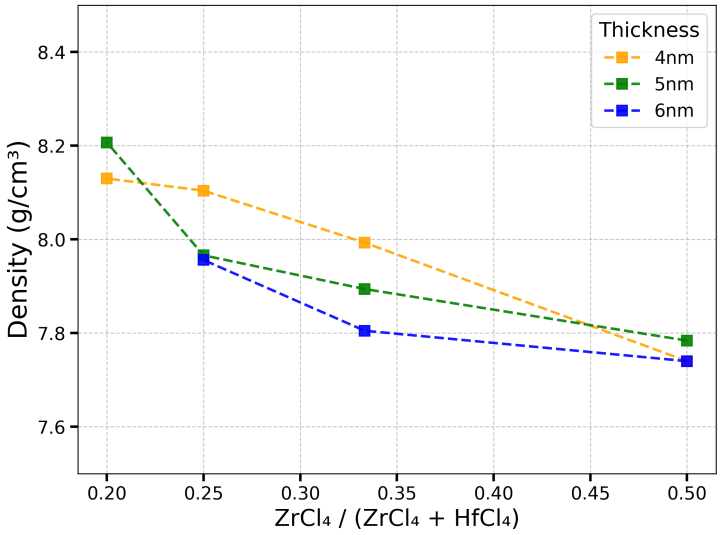

Figure 4.15: As deposited density evolution of 4 nm, 5 nm, and 6 nm HZO films as a function of the precursors ratio. The density was obtained via X-ray reflectometry on samples deposited on Si substrates. Measurements were performed at a single point near the center of the wafer.

The evolution of density as a function of the $ZrCl_4$ / ($ZrCl_4$ + $HfCl_4$) ratio for 4 nm, 5 nm, and 6 nm HZO films is presented in **Fig. 4.15 .** These films were developed using the GPC of HZO 1:1 as a reference for the ALD process. Since the deposition conditions were initially optimized for a 1:1 Hf:Zr ratio, variability in thickness and density across different Zr contents are expected, as the surface reactions and growth mechanisms for Zr-rich and Hf-rich compositions are not identical.

The density of the films decreases with increasing Zr content, consistent with the lower bulk density of ZrO_2 compared to HfO_2. HfO_2 has a density of 9.68 g/cm^3 [144], while ZrO_2 has 5.68 g/cm^3 [161]. This difference mainly results from the higher atomic mass of Hf relative to Zr, leading to denser HfO_2 structures. As a result, HZO compositions richer in Hf exhibit higher density, whereas increasing the Zr content causes a gradual reduction in density.

The fabrication process involved the deposition of HZO films, followed by annealing at 500°C for 15 minutes on structures with TiN/W top electrodes, with subsequent etching. This annealing temperature was selected based on previous studies, which demonstrated that higher temperatures enhance crystallization in ultrathin ferroelectric layers, thereby facilitating the formation of the desired phases.

The in-plane XRD in **Fig. 4.16 r**esults reveal significant differences in crystallization behavior across compositions and thicknesses, particularly in the evolution of the 30.5° peak, which

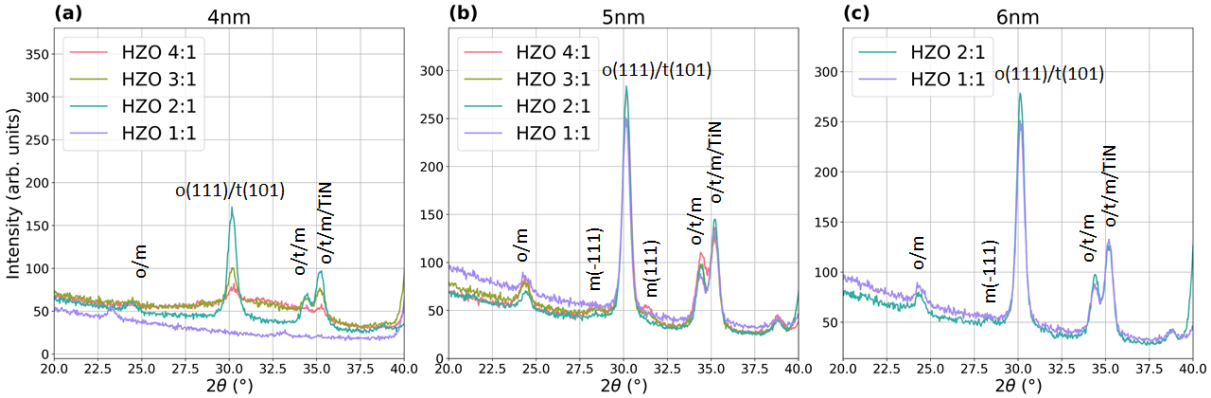

Figure 4.16: In-plane XRD patterns of HZO films with thicknesses of **a.** 4 nm, **b.** 5 nm, and **c.** 6 nm, highlighting the impact of composition on crystallization. Thicker films exhibit enhanced crystallinity and more defined diffraction peaks.

corresponds to the orthorhombic/tetragonal phases. As shown in **Fig. 4.16 a**, the 4 nm films demonstrate that crystallization is achievable under the applied thermal budget, even at this extreme thickness. Notably, the 4:1 and 1:1 compositions at 4 nm do not exhibit discernible peaks, strongly suggesting an amorphous structure.

As the thickness increases to 5 nm in **Fig. 4.16 b**, crystallization improves significantly. In particular, the 4:1, 3:1 and 2:1 samples show the highest intensity at 30.5°, suggesting a greater degree of crystallization. However, the 4:1 sample also presents a distinct peak at 28.5° and 31°, which correspond to the monoclinic phase. This behavior is expected, since higher HfO_2 content tends to favor the formation of the monoclinic phase, which is the most thermodynamically stable but non-ferroelectric structure [66].

At 6 nm, the XRD results in **Fig. 4.16 c** confirm the crystallization and phase formation of the films. Despite differences in absolute intensity, the 2:1 composition exhibits the most intense 30.5° peak, indicating strong crystallization of the orthorhombic/tetragonal phases. Additionally, a minor peak at 28.5° is observed in the 2:1 sample, suggesting a slight presence of the monoclinic phase.

4.2 Composition-driven variations in electrical results

PUND measurements were carried out to evaluate the performance of capacitors fabricated with HZO films of varying thicknesses and compositions.

Although all samples were annealed under the same conditions (500°C for 15 minutes), the 4 nm and 5 nm samples at the 2:1 composition were fabricated with a different top electrode configuration: TiN 10 nm CVD + TiN 50 nm PVD, while the rest of the samples used TiN 10 nm CVD + W 70 nm SSP. Despite the initial differences in polarization and wake-up, both configurations reached similar polarization values after 10^3 cycles (**Fig. 3.14 a**), as discussed in this chapter Section 3. With this consideration, the result in **Fig. 4.17 c**an be analyzed and interpreted focusing on the effects of different thicknesses and compositions.

At 5 and 6 nm, the 1:1 composition yielded the highest polarization, confirming that a bal-

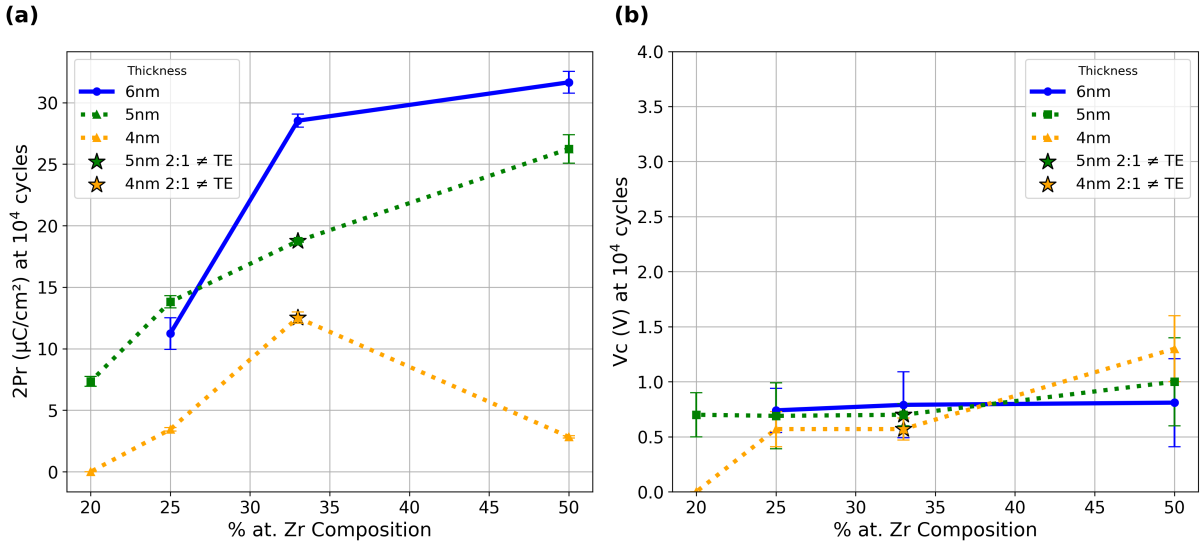

Figure 4.17: a. Remanent polarization (2Pr) and **b.** coercive voltage (Vc) as a function of Zr composition for HZO films annealed at 500°C. The 4 nm and 5 nm samples at 2:1 composition have a different top electrode configuration, TiN 10 nm CVD + TiN 50 nm PVD, whereas the rest of the samples have TiN 10 nm CVD + W 70 nm SSP as the top electrode.

anced Hf/Zr ratio is optimal at intermediate thicknesses. Hf-rich compositions showed poor ferroelectricity, likely due to increased monoclinic phase formation. For 4 nm films, the highest $2P_r$ was observed for the 2:1 composition, suggesting this composition better stabilizes the orthorhombic phase at ultrathin dimensions. The 1:1 and 4:1 samples shows low or no polarization, consistent with incomplete crystallization or amorphous structure, as supported by XRD discussed previously.

In **Fig. 4.17 b**, V_c remained relatively stable across most samples and was primarily thickness-dependent. The 4 nm 1:1 sample showed elevated V_c , possibly due to antiferroelectric behavior, while the 4 nm 4:1 sample showed no switching, consistent with its amorphous nature.

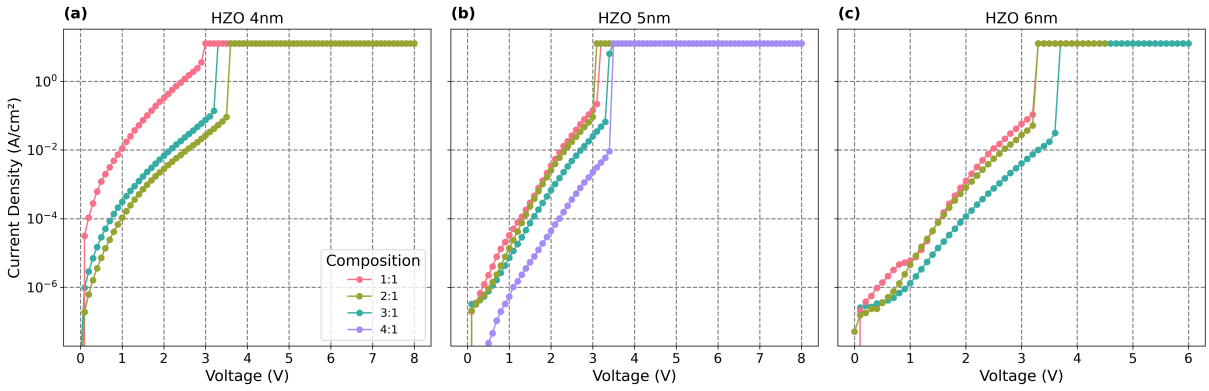

Figure 4.18: Current density (A/cm²) vs. Voltage (V) for HZO layers annealed at 500°C for 15 minutes for different and compositions (1:1, 2:1: 3:1, 4:1) and with **a.** 4 nm, **b.** 5 nm and **b.** 6 nm thickness. Each curve represents the median response from 20 capacitors, ensuring results with very low dispersion and high reproducibility across devices.

The leakage current behavior in HZO thin films exhibits complex dependencies on both thickness and composition, as illustrated in the quasi-static I-V characteristics in **Fig. 4.18 .** The 4 nm films exhibit the highest leakage current, which gradually decreases for the 5 and 6 nm films. This trend aligns with expectations for ultrathin dielectrics, where direct tunneling becomes the dominant charge transport mechanism as the physical thickness decreases. In the 4 nm 1:1 sample, in particular, the sharp increase in leakage suggests that the film is below the critical thickness necessary to effectively suppress tunneling currents.

In addition to thickness effects, composition plays a key role in leakage current behavior. The 3:1 and 4:1 compositions, which are Hf-rich, show lower leakage currents across the 5 and 6 nm thicknesses compared to the 1:1 and 2:1 compositions. This observation can be correlated with the breakdown field strength values shown in Figure **Fig. 4.19 .** The E_{BD} generally increases with Hf concentration, particularly for the 4 nm films, where the 3:1 and 4:1 compositions exhibit significantly higher E_{BD} compared to the 1:1 and 2:1 samples.

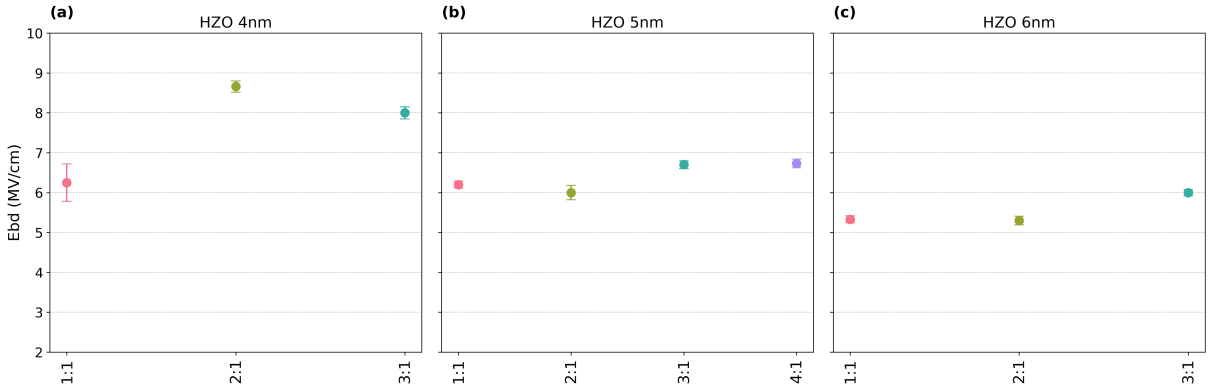

Figure 4.19: Comparison of breakdown field (E_{BD}) for HZO layers annealed at 500°C for 15 minutes for different and compositions (1:1, 2:1: 3:1, 4:1) and with **a.** 4 nm, **b.** 5 nm and **b.** 6 nm thickness.

This behavior aligns well with findings in the literature. According to [162], the bandgap of HZO films tends to increase with higher Hf incorporation, as confirmed through transmittance measurements. Moreover, density functional theory (DFT) calculations indicate that this trend is associated with hybridization between Zr 4d and Hf 5d orbitals, leading to modifications in the electronic structure. The same study also discussed XPS results, which suggested that Hf-rich compositions exhibit reduced oxygen vacancy concentrations, leading to a wider bandgap. This reduction in oxygen vacancies likely contributes to lower leakage currents and higher breakdown fields in Hf-rich films. It is important to note, however, that the HZO layers in that work were deposited by pulsed laser deposition (PLD) and had a thickness of 30 nm, which differs from the ALD-grown ultrathin films used in this study.

Further support comes from [163], which details how the bandgap of ferroelectric $Hf_{1-x}Zr_xO_2$ varies as a function of Zr concentration. It was observed that the bandgap exhibits a decreasing trend with increasing Zr content, implying that even a small fraction of Zr incorporation significantly reduces the bandgap and deteriorates the insulating properties. As described in the study, since ZrO_2 has a larger unit cell volume than HfO_2, this expansion leads to bandgap

reduction, which enhances charge transport and contributes to higher leakage currents and lower breakdown fields.

4.3 General conclusion

This study highlights the crucial role of composition and thickness in stabilizing the ferroelectric phase in ultrathin HZO films. As the film thickness scales below 10 nm, structural and phase-related transformations become increasingly significant, often leading to excessive stabilization of the tetragonal phase, which suppresses ferroelectricity. Through composition engineering, this work demonstrates that reducing the Zr content in ultrathin films mitigates this effect, promotes the formation of the orthorhombic ferroelectric phase, and enhances polarization.

For 4 nm films, the HZO 2:1 ratio emerges as the optimal composition, whereas for 5 and 6 nm films, the highest polarization appears at the 1:1 composition, indicating that the optimal composition shifts with thickness. This composition-dependent trend suggests that a delicate balance between Hf and Zr is required to stabilize the desired phase at different dimensions. In contrast, Hf-rich compositions (e.g., 4:1) exhibit poor ferroelectric performance due to their tendency to form the monoclinic phase, which is non-ferroelectric but thermodynamically stable.

In addition to polarization trends, the electrical properties of the films are investigated through leakage current and breakdown field measurements. The results show that Hf-rich compositions consistently exhibit lower leakage currents and higher breakdown fields, which can be attributed to a wider bandgap and reduced oxygen vacancy formation. This behavior aligns with literature reports indicating that Hf incorporation increases the bandgap and enhances dielectric stability by limiting charge transport pathways.

The findings of this study provide valuable insights for optimizing HZO films for ferroelectric applications. By carefully tailoring the Zr:Hf ratio through control of ALD supercycles, it becomes possible to overcome the phase stability challenges associated with ultrathin films, ensuring both high polarization and improved dielectric reliability. These results reinforce the importance of composition engineering as an effective strategy for achieving stable and scalable ferroelectricity in next-generation memory and electronic devices.

5 Chapter Summary and Conclusions

This chapter explores the impact of composition and thickness scaling on the structural and electrical properties of HZO thin films. The results demonstrate that stabilizing the ferroelectric orthorhombic phase becomes increasingly challenging at reduced thicknesses, requiring a careful balance of Hf/Zr composition and processing conditions.

The 1:1 Hf/Zr composition exhibits the highest remanent polarization for 10 thin films, confirming its ability to stabilize the ferroelectric phase. In contrast, Zr-rich compositions show stronger wake-up effects and antiferroelectric behavior, while Hf-rich compositions contain a greater fraction of the monoclinic phase, which, despite lowering polarization, may contribute to improved endurance according to the literature.

As thickness scales down to 6, 5, and 4 nm, significant structural and electrical changes emerge. At 4 nm, the ferroelectric response is strongly suppressed in the 1:1 composition, likely due to the dominance of a non-ferroelectric phase. Reducing the Zr ratio mitigates this effect, promoting better phase stabilization and polarization, while Hf-rich compositions remain largely amorphous or monoclinic, limiting their suitability for ultrathin ferroelectric applications.

Leakage current and breakdown field measurements further confirm that Hf-rich compositions exhibit lower leakage and higher breakdown fields, aligning with literature reports on bandgap widening and defect suppression. However, at 4 nm, leakage currents increase significantly due to direct tunneling effects, indicating that further optimization is needed to improve dielectric reliability at extreme thickness scaling.

Overall, this chapter provides insights into the key levers that influence ferroelectricity in ultrathin HZO. The results indicate that composition tuning and process conditions affect polarization as thickness is reduced. While scaling lowers operating voltage, maintaining stable polarization below 6 nm depends on a higher crystallization temperature. These observations outline practical directions for further optimization rather than definitive solutions.

Chapter 5

Multilayer engineering for enhanced ferroelectric performance

Objectives

Multilayer structures have emerged as a promising approach to enhance ferroelectric performance, particularly in ultrathin films where maintaining the orthorhombic phase stability becomes increasingly challenging. By layering HfO_2 and ZrO_2 in controlled thicknesses, researchers have reported improved polarization, reduced leakage currents, and enhanced endurance compared to single-layer HZO films of similar thickness. These advantages are attributed to the modulation of stress, defect density, and interface effects within the multilayers, which can promote the stabilization of the ferroelectric orthorhombic phase. Additionally, tailoring the composition and stacking order of the layers could allow fine-tuning of the electrical and structural properties, providing opportunities for optimized performance in non-volatile memory applications.

This chapter focuses on key aspects of multilayer structures, including how composition variations through unit layer thickness and stacking configurations influence ferroelectric behavior. It examines their role in stabilizing ferroelectric phases, optimizing polarization, and addressing challenges such as leakage currents and performance at ultrathin dimensions. These strategies offer a pathway to tune material properties for integration into next-generation ferroelectric devices.

Contents

1 Introduction **106**
2 6 nm multilayer structures **107**
2.1 Structural and compositional features of 6 nm HfO_2–ZrO_2 multilayers 107
2.2 Impact of multilayer design on ferroelectric response 110
2.3 General conclusion 118
3 6 nm multilayers with different compositions **120**
3.1 Structural and compositional analysis of 6 nm multilayers with varying Hf/Zr ratios . 120
3.2 Electrical properties of 6 nm HfO_2/ZrO_2 multilayers with varying composition 122
3.3 General conclusion 125
4 Ultra-thin multilayers: tuning ferroelectric performance with reduced ZrO_2 content **126**
4.1 Structural and composition characterization of ZrO_2-reduced ultra-thin multilayers . . 126
4.2 Ferroelectric stability in sub-6 nm capacitor structures 128
4.3 General conclusion 131
5 Benchmark **133**
6 Chapter Summary and Conclusions **136**

1 Introduction

Building upon the findings of the previous chapter, which focused on the properties of solid-solution HZO, this chapter explores how multilayer engineering influences ferroelectric performance, particularly in ultrathin structures below 10 nm. A key objective is to determine whether the electrical properties observed in solid-solution HZO persist when the material is structured as a multilayer. The study begins with 6 nm multilayers using a 50% HfO_2/ZrO_2 composition, as previous investigations identified this composition as the most promising for ferroelectric applications. In addition, compositions with 33% and 66% Zr are considered to explore the impact of Zr concentration on phase stability and polarization in this novel multilayered structures.

This chapter also investigates the impact of unit layer thickness. The relative thickness of HfO_2 and ZrO_2 sublayers is expected to influence the overall ferroelectric properties of the stack by influencing phase stability, defect formation and stress distribution. By analyzing different stacking configurations and unit layer dimensions, this study aims to establish whether an optimal structural arrangement can be achieved to maximize ferroelectric performance.

Further, the study delves into the implications of thickness scaling, investigating whether the behavior of multilayers remain effective as the total thickness is reduced to 5 nm and 4 nm. As observed in prior studies, extreme thickness reduction introduces new challenges, including increased interface effects, phase instability, leakage currents, and suppressed polarization. A critical aspect of this work is to determine whether multilayer architectures can mitigate these adverse effects and sustain ferroelectric performance at the nanometric scale.

By systematically analyzing composition, thickness, stacking order, initial and final layers, and unit layer thicknesses, this chapter aims to provide a deeper understanding of the trade-offs involved in multilayer integration. The findings will contribute to the ongoing efforts to optimize ferroelectric HZO for next-generation non-volatile memory technologies, highlighting both the potential advantages and intrinsic limitations of multilayer structures as a pathway for achieving stable, ultra-thin ferroelectric devices.

2 6 nm multilayer structures

The study of ferroelectric HZO has shown that composition and thickness play crucial roles in determining its electrical performance. In the previous Chapter 4, Sections 3 and 4 demonstrated that, at 6 nm thickness, the 1:1 Hf:Zr composition provides the highest remanent polarization ($2P_r$). In this context, this subchapter investigates whether a different structural approach, multilayers, can offer further improvements in electrical performance while maintaining these benefits.

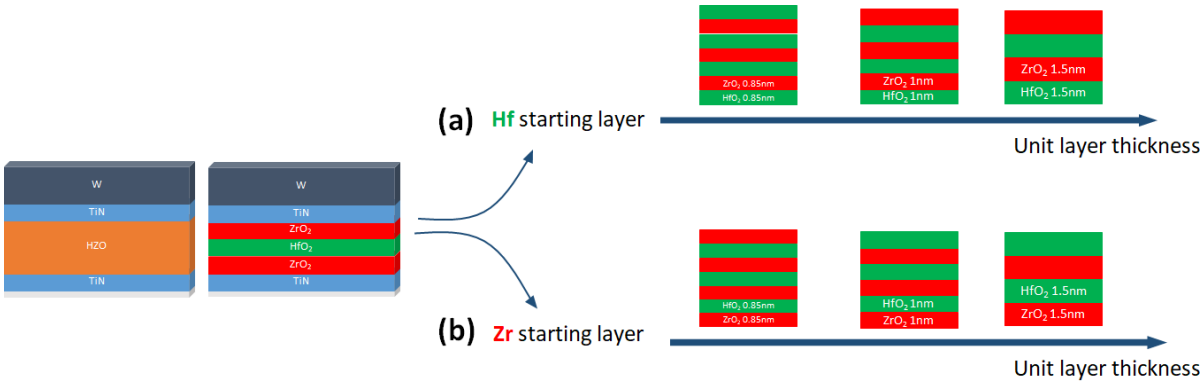

Figure 5.1: Schematic representation of the 6 nm multilayer configurations. Two types of structures were fabricated: **a.** HfO_2 starting and **b.** ZrO_2 configurations.

The fabrication of the multilayer structures followed the ALD process described in Chapter 2 Section 2.1. In the case of the superlattices, the deposition cycles required to achieve the desired HfO_2 and ZrO_2 sublayer thicknesses were determined based on the GPC of each individual material, measured on a Si substrate. By precisely controlling the number of cycles, the total film thickness was maintained at 6 nm, while different unit layer thicknesses were explored to study their influence on ferroelectric behavior.

Six different multilayer structures were developed using unit layer thicknesses of 1.5, 1.0, and 0.85 nm, with variations in the sequence of the initial and final oxides. These unit layers were repeated until reaching a total thickness of 6 nm. A schematic representation of these configurations is shown in **Fig. 5.1**, highlighting the stacking order and the variation in starting and ending layers.

2.1 Structural and compositional features of 6 nm HfO_2–ZrO_2 multilayers

In this study, the GPC values were determined from individual oxide depositions on Si substrates, with HfO_2 exhibiting a higher GPC (0.52 Å/cycle) than ZrO_2 (0.42 Å/cycle). These values were used to calculate the total number of ALD cycles required to achieve the target sublayer thicknesses for a 1:1 global composition, as shown in the **Table 5.1**.

Configurations with 1.5 nm and 1.0 nm unit layers were designed by alternating an equal number of HfO_2 and ZrO_2 sublayers. In the 0.85 nm unit layer configurations, consisting of seven layers, the compositional balance was further affected by the starting layer: stacks beginning with HfO_2 became Hf-rich, while those starting with ZrO_2 were Zr-rich.

The final compositions did not perfectly match these theoretical targets. Deviations were observed, with Hf consistently substoichiometric relative to Zr. This discrepancy could be attributed to the fact that oxide-to-oxide growth can lead to different GPC values compared to growth on the substrate, resulting in deviations from the expected composition. Moreover, both WDXRF and XRR introduce intrinsic uncertainties that may contribute to these discrepancies, potentially impacting the accuracy of the final reported composition and thickness.

Table 5.1: Experimental details for 6 nm multilayer configurations exhibiting Hf/Zr compositions (as determined by WDXRF analysis) alongside the corresponding ALD pulse parameters used in their fabrication.

Target Unit Thickness	Layers	Hf (at%)	Zr (at%)	ALD Cycles HfO_2	ALD Cycles ZrO_2
1.5 nm - HZHZ	4	45	55	56	70
1.5 nm - ZHZH	4	45	55	56	70
1 nm - HZHZHZ	6	45	55	57	69
1 nm - ZHZHZH	6	45	55	57	69
0.85 nm - HZHZHZH	7	52	48	64	60
0.85 nm - ZHZHZHZ	7	37	63	48	80

XRR measurements shown in **Table 5.2** were performed on as-deposited multilayer samples to estimate the individual layer thicknesses, prior to top electrode deposition or thermal annealing. To improve convergence, several constraints were applied to the fitting model. The densities of HfO_2 and ZrO_2 were fixed to their theoretical values (9.68 and 5.68 g/cm^3, respectively), and the interfacial roughness was limited to a maximum of 0.5 nm. However, the thickness of each individual HfO_2 and ZrO_2 sublayer was allowed to vary independently.

The Ti/TiN bottom electrode stack was included in the fitting model, with fixed densities of 4.5 g/cm^3 for Ti and 4.95 g/cm^3 for TiN, while their respective thicknesses were left as free parameters. These values were based on XRR measurements performed on the metal stack prior to the deposition of the multilayer. The target deposition thicknesses for these layers were 5 nm for Ti and 10 nm for TiN. Variability in the fitted Ti and TiN thicknesses was observed across samples, despite identical deposition conditions. They could result from actual deposition variability or more likely fitting limitations.

Table 5.2: Fitted thicknesses of individual layers in Ti/TiN/HfO_2/ZrO_2 multilayer structures, based on XRR analysis. Each configuration includes a Ti/TiN bottom electrode stack followed by alternating HfO_2 (H) and ZrO_2 (Z) layers. Densities were fixed at 4.5 g/cm^3 for Ti, 4.95 g/cm^3 for TiN, 9.68 g/cm^3 for HfO_2, and 5.68 g/cm^3 for ZrO_2.

Target Unit Thickness	Ti (nm)	TiN (nm)	Fitted H/Z Thicknesses (nm)
1.5 nm - HZHZ	5.8	8.8	1.4, 1.4, 1.6, 1.8
1.5 nm - ZHZH	4.1	9.1	1.8, 1.5, 1.4, 1.7
1 nm - HZHZHZ	5.7	8.4	1, 1, 1, 0.9, 1.2, 1.2
1 nm - ZHZHZH	5.2	9.5	0.8, 1.1, 0.9, 0.9, 1, 1
0.85 nm - HZHZHZH	4.7	9.4	0.85, 0.91, 0.93, 0.76, 0.82, 0.91, 0.85
0.85 nm - ZHZHZHZ	4.5	9.7	0.88, 0.93, 0.78, 0.95, 0.86, 0.93, 0.93

Despite these challenges, the extracted parameters offer an approximation of the unit layer thicknesses. The corresponding XRR fitting curves for both configurations are provided in the appendix 6.

In-plane XRD measurements in **Fig. 5.2 a** were performed on multilayered HfO_2/ZrO_2 stacks after integration with a TiN/W top electrode, annealing at 500°C for 15 min, and subsequent etching of the top electrode to enable direct access to the ferroelectric layer, in order to analyze the resulting crystal structure. As discussed in the previous chapter, this annealing condition led to improved electrical performance in the 6 nm films. All samples exhibit well-defined diffraction peaks, confirming successful crystallization of the films under these processing conditions.

A prominent diffraction peak appears near 30.5° in all patterns, commonly associated with the planes of the orthorhombic (o) or tetragonal (t) phases. No systematic peak shift is observed across the different samples. However, noticeable differences in peak intensity are present, which may be linked to subtle changes in crystallinity or phase fraction.

According to previous reports [89, 96], multilayer structures starting with a ZrO_2 sublayer tend to promote the formation of the monoclinic (m) phase, which is typically evidenced by diffraction peaks around 28.5° and 31°. However, in the present study, no such peaks are detected in any of the measured configurations, including those starting with a ZrO_2 layer, indicating an effective suppression of the dominant m-phase orientations across all samples.

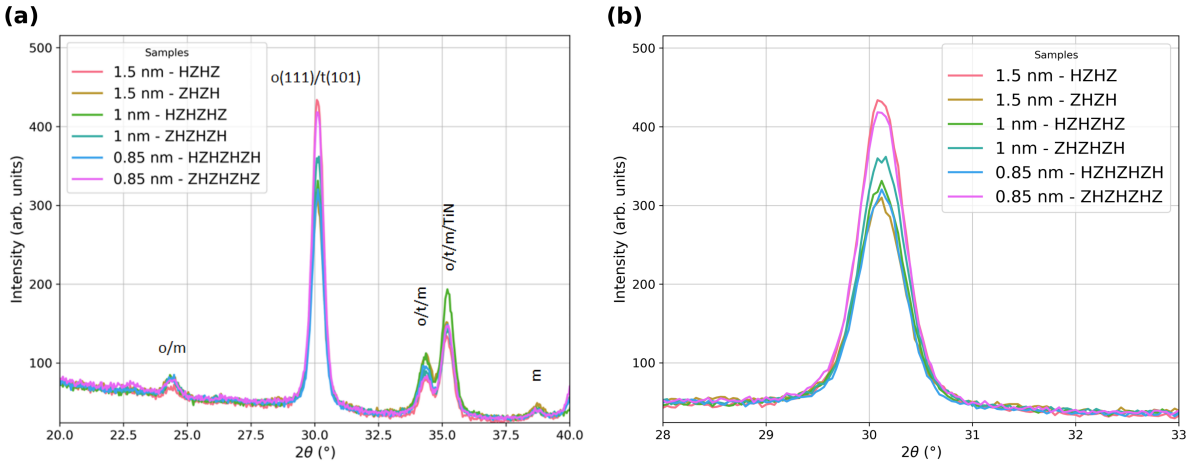

Figure 5.2: a. In-plane XRD measurements for multilayered HfO_2/ZrO_2 stacks after integration with TiN/W top electrode, annealing at 500°C for 15 min, and subsequent etching of the top electrode. All samples are 6 nm-thick with different stacking configurations. **b.** Zoomed view of the o(111)/t(101) region showing no noticeable shift in 2θ, but a difference in peak intensity depending on the stack.

In addition, a clear diffraction feature is observed near 35°, corresponding to the (200) planes of the orthorhombic (o-) phase, which is associated with a preferred crystallographic texture known to enhance ferroelectric polarization in HfO_2-based materials. The intensity of this peak varies among the different multilayer configurations, suggesting differences in crystallographic texture. In particular, an increased intensity of the (200) reflection has been linked in the litera-

ture to a preferred orientation of the o-phase, which enhances ferroelectric switching [129, 130]. This phenomenon has been confirmed by techniques such as transmission Kikuchi diffraction, which show that such texturing facilitates alignment of the polar axes. Therefore, the observed variation in (200) peak intensity may reflect different degrees of o-phase texture development in the samples, potentially influencing the macroscopic polarization behavior.

However, it is important to note that the peak near 35° also includes contributions from the (111) orientation of TiN, as well as from the t(002), t(110), m(200), and m(020) reflections of HZO. Consequently, caution is necessary when correlating these diffraction results directly to o-phase texture.

Fig. 5.2 b shows a zoomed view of the o(111)/t(101) region, where no shift in 2θ is observed for the peak at 30.5°, indicating no detectable phase change (t → o) through XRD analysis. Only differences in peak intensity are observed among the different stacking configurations.

2.2 Impact of multilayer design on ferroelectric response

The **Fig. 5.3 i**llustrates the evolution of the hysteresis loops with cycling for various multilayer structures with different unit layer thicknesses and initial starting layers. The capacitors had TiN/W top electrodes and were annealed at 500°C for 15 min, as described in 3.1.

As shown in **Fig. 5.3 f**or three representative cycling states (1, 10^3, and 10^6 cycles), all six multilayer configurations exhibit clear hysteresis loops, characteristic of switching behavior. Panels **Fig. 5.3 a** to **Fig. 5.3 c** correspond to structures where the first deposited layer is HfO_2, while panels **Fig. 5.3 d** to **Fig. 5.3 f** correspond to structures where the first layer is ZrO_2. Across all structures, the initial hysteresis loops exhibit a pinched shape, characteristic of the wake-up effect and antiferroelectric-like behavior. With cycling, the loop profiles evolve and become more open and ferroelectric-like.

The ferroelectricity observed in these stacking layers of HfO_2 and ZrO_2 is atypical. Under standard semiconductor processing conditions, HfO_2 typically crystallizes in a nonpolar monoclinic form, and ZrO_2 exists in a tetragonal antiferroelectric phase. However, literature references suggest that the emergence of ferroelectricity in these systems is due to the formation of artificial polycrystalline superlattices, with local epitaxy occurring within each columnar grain [96]. This phenomenon is believed to arise from local strain effects during crystallization, which, under specific conditions, promotes the stabilization of a noncentrosymmetric orthorhombic phase, thereby enabling the observed ferroelectric behavior.

According to [96], during annealing, the films initially crystallize into a high-temperature tetragonal phase, which is favored due to entropic contributions. As the system cools, phase transitions are governed by kinetic barriers. While the monoclinic phase is thermodynamically stable at room temperature, the transition from tetragonal to monoclinic involves a high activation energy, which can delay or suppress its formation. In contrast, the transition from tetragonal to orthorhombic has a significantly lower barrier, making it more accessible under certain conditions. The presence of local strain, arising from epitaxial alignment and lattice mismatch between layers, can further stabilize the orthorhombic phase by modifying the energy landscape and nucleation kinetics.

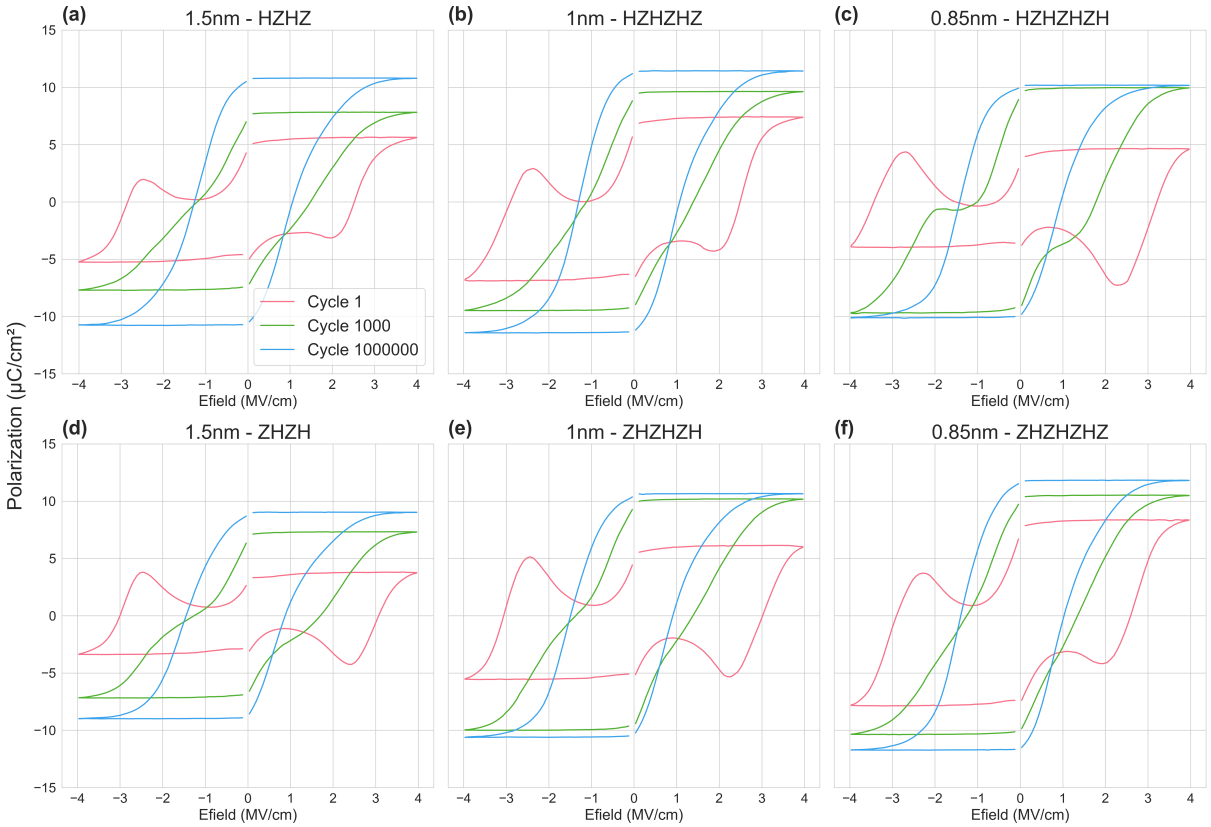

Figure 5.3: P-E loops of 6 nm multilayer samples annealed at 500°C for 15 min. The top row **a** to **c** corresponds to structures starting with HfO_2-starting layers, while the bottom row **d** to **f** starts with ZrO_2 layers. From left to right, the unit layer thickness decreases from 1.5 nm to 1 nm and finally 0.85 nm. The hysteresis loops illustrate ferroelectric behavior across multiple thickness scales and are shown for three representative cycling states (1, 10^3, and 10^6 cycles), highlighting how the stack sequence and thickness influence the capacitor's performance.

2.2.1 Evolution of remanent polarization and coercive voltage as a function of electrical cycling

Variation of remanent polarization during cycling, from 1 to 10^6 cycles, as seen in **Fig. 5.4 a**, provides insights into the ferroelectric behavior of the studied samples. All samples exhibit a characteristic wake-up effect, where $2P_R$ increases with cycling.

As seen in the results, the HZO 1:1 solid solution consistently displays the highest remanent polarization throughout the measurement range.

Among the multilayer samples, those with 0.85 nm unit layers demonstrate polarization values approaching those of the HZO 1:1 solid solution, particularly the ZrO_2-starting configuration, which reaches 25 $\mu C/cm^2$ at 10^6 cycles. This result is noteworthy, as the increased Zr content in this stack would typically be associated with a greater tendency toward the antiferroelectric tetragonal phase, which often leads to reduced remanent polarization.

The unexpectedly high performance suggests that interface engineering and nanoscale stacking effects may outweigh the expected influence of global composition, potentially favoring the stabilization of the orthorhombic ferroelectric phase. In contrast, multilayers with thicker unit

layers (1 nm and 1.5 nm) exhibit lower remanent polarization overall, with a clear trend of polarization degradation as unit thickness increases.

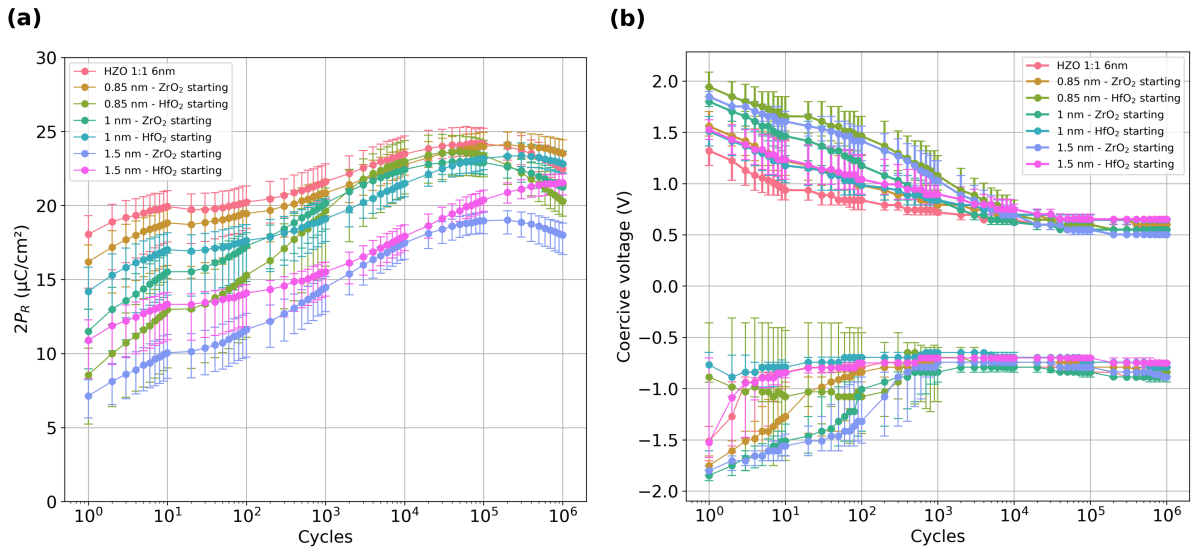

Figure 5.4: Evolution of **a.** remanent polarization ($2P_R$) and **b.** coercive voltage as a function of cycling, from 1 to 10^6 cycles, for various multilayer configurations.

The evolution of coercive voltage in **Fig. 5.4 b**, from 1 to 10^6 cycles, reflects the same wake-up effect observed for the polarization, with initial antiferroelectric-like behavior that stabilizes with cycling, leading to similar V_c values across all structures regardless of unit layer configuration. Unlike what has been reported in the literature [89], where superlattice-based devices demonstrated tunability of the coercive field compared to a homogeneous 10 nm (Hf,Zr)O_2 reference film, the present results indicate that coercive voltage evolution is primarily dictated by total thickness rather than the superlattice configuration.

2.2.2 Wake-up behavior and multilayer loop characteristics

Fig. 5.5 a shows the evolution of remanent polarization in 6 nm HfO_2/ZrO_2 multilayer structures with different unit layer thicknesses and starting oxides across various cycling stages. Thinner unit layers exhibit higher remanent polarization, approaching that of the homogeneous HZO 1:1 reference. In the first cycle (red region), polarization is influenced by both stacking order and unit thickness. However, after 10^5 cycles (blue region), polarization values converge for each unit thickness, regardless of the initial stacking sequence. This convergence suggests that the application of an electric field likely drives transformations within the samples, reducing the initial differences.

Fig. 5.5 b presents the analysis of the wake-up rate for the different multilayer structures. The wake-up rate is calculated as $(2P_{r,max} - 2P_{r,pristine})/2P_{r,pristine}$, where $2P_{r,max}$ corresponds to the maximum remanent polarization measured during cycling and $2P_{r,pristine}$ to the initial remanent polarization at the first cycle. The wake-up effect, characterized by an increase in polarization over cycling, was observed across all structures, with its magnitude varying signif-

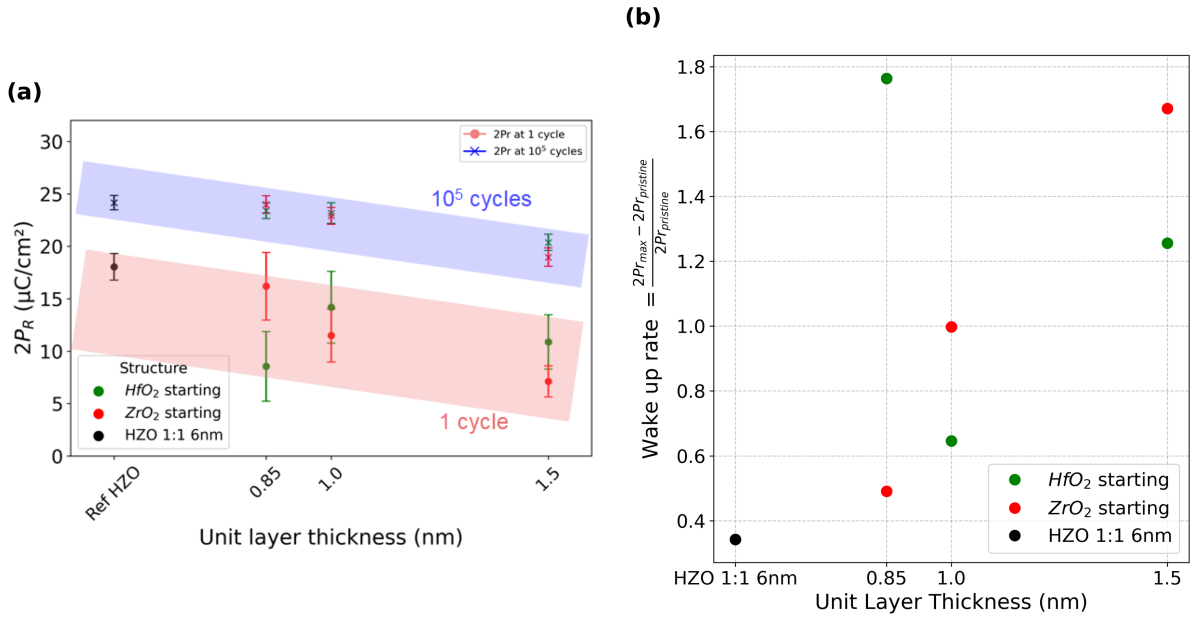

Figure 5.5: Trends in remanent polarization for 6 nm HfO_2/ZrO_2 based multilayer structures with different starting oxides (HfO_2 or ZrO_2) and varying unit layer thicknesses. **a.** show the remanent polarization ($2P_r$) at the first (red zone) and 10^5 cycles (blue zone), respectively. **b.** corresponds to the the wake-up rate. The wake-up rate is calculated as $\frac{2P_{r,\max} - 2P_{r,\text{pristine}}}{2P_{r,\text{pristine}}}$, with higher values indicating a more pronounced wake-up effect.

icantly depending on unit layer thickness and stacking configuration. As previously discussed, this effect may originate from a phase transformation, along with other contributing mechanisms such as oxygen vacancy migration and charge redistribution during electrical cycling.

The 1.5 nm and 1 nm unit layers starting with ZrO_2 show a significant wake-up effect, as seen in **Fig. 5.5 b**, especially when compared to their HfO_2-starting counterparts. According to [89], a ZrO_2-starting layer can promote enhanced crystallization of the antiferroelectric phase, thereby leading to a more pronounced wake-up effect as the phase transformation progresses throughout cycling.

Interestingly, the 0.85 nm structure starting and ending with HfO_2 shows the most pronounced wake-up among all samples, whereas the structure with the same unit thickness (0.85 nm) but starting and ending with ZrO_2 maintains a high polarization (comparable to the HZO 1:1 reference) value with lower wake-up. Notably, this configuration also corresponds to the most Zr-rich composition among the multilayers studied. While this reduced wake-up behavior may initially seem counterintuitive, it highlights that additional factors beyond global composition, may be influencing the ferroelectric response in these ultrathin multilayers.

2.2.3 Hypotheses on mechanisms influencing polarization in 6 nm multilayers

The electrical performance observed across the different 6 nm multilayer configurations, particularly the variation in wake-up behavior and remanent polarization, suggests the presence of additional underlying physical mechanisms beyond global composition alone. A key limitation

in interpreting these results is the uncertainty surrounding the structural state of the films, as it is not possible to precisely determine the fraction of each sample that is fully crystallized versus remaining amorphous. This structural ambiguity may influence the polarization response and contribute to the differences observed among the configurations.

Nonetheless, in this subsection, we explore two widely discussed hypotheses in the literature that may account for the observed behaviors: (i) the role of oxygen vacancy behavior, and (ii) stress effects arising from thermal expansion mismatch at the interfaces, including both internal stresses and those induced by the electrode materials, which may influence phase stability and polarization dynamics.

As reported in [47, 164, 165], differences in oxygen vacancy behavior between HfO_2 and ZrO_2 may contribute to the wake-up effect and polarization values observed in multilayer structure. According to these studies, HfO_2 tends to accumulate oxygen vacancies that act as charge trapping centers, gradually reducing switchable polarization, whereas ZrO_2 more effectively disperses vacancies, limiting charge trapping.

This behavior may explain the more pronounced wake-up and lower polarization observed in the 0.85 nm structure that begins and ends with HfO_2, where localized vacancy accumulation likely hinders efficient polarization switching. Conversely, the ZrO_2-starting configuration, identified by WDXRF as having the highest Zr content, stabilizes near 25 $\mu C/cm^2$ at 10^5 cycles and exhibits the highest polarization among the multilayer structures studied. This enhanced performance may result from a reduced density of charge traps, promoting a more efficient ferroelectric response.

However, quantifying oxygen vacancies remains challenging. Techniques like XPS or even HAXPES are surface-sensitive (typically probing 5 nm), making it difficult to assess buried ferroelectric layers without altering the sample. Advanced synchrotron-based HAXPES offers deeper probing and better spectral resolution, making it more suitable for correlating vacancy distribution with electrical behavior in cycled capacitors [51, 84].

In addition to oxygen vacancies, local stress also influences the performance of multilayer ferroelectric structures. Stress contributes to the initial stabilization of the orthorhombic phase and affects its evolution during cycling. While electrode-induced stress is common in single-layer films, multilayers are also subject to internal stresses due to mismatches in the thermal expansion coefficients (CTE) of adjacent layers.

CTE mismatches between materials like TiN (9.4×10^{-6} /K [137]), W (4.5×10^{-6} /K [137]), HfO_2 (8.5×10^{-6} /K [166]) and ZrO_2 (11×10^{-6} /K [166]) introduce localized tensile or compressive stress. ZrO_2, having the highest CTE, is particularly susceptible to stress accumulation when integrated into a superlattice structure [47, 50, 167]. Literature reports indicate that tensile stress can promote the tetragonal-to-orthorhombic phase transition, thereby enhancing ferroelectric properties [96].

Although ZrO_2 is generally more prone to forming the tetragonal phase, the lower CTE of W and HfO_2 relative to ZrO_2 likely induce tensile stress at ZrO_2 interfaces within the multilayers. This stress may suppress the stabilization of the tetragonal phase and instead favor the formation of the ferroelectric orthorhombic phase. Such effect could explain the reduced wake-up behavior

and enhanced polarization observed in the 0.85 nm multilayer configuration, which begins and ends with ZrO_2 and performs comparably to the HZO 1:1 reference. However, this behavior was observed for this specific sample and was not systematically investigated across other similar systems.

2.2.4 Leakage current and breakdown characteristics

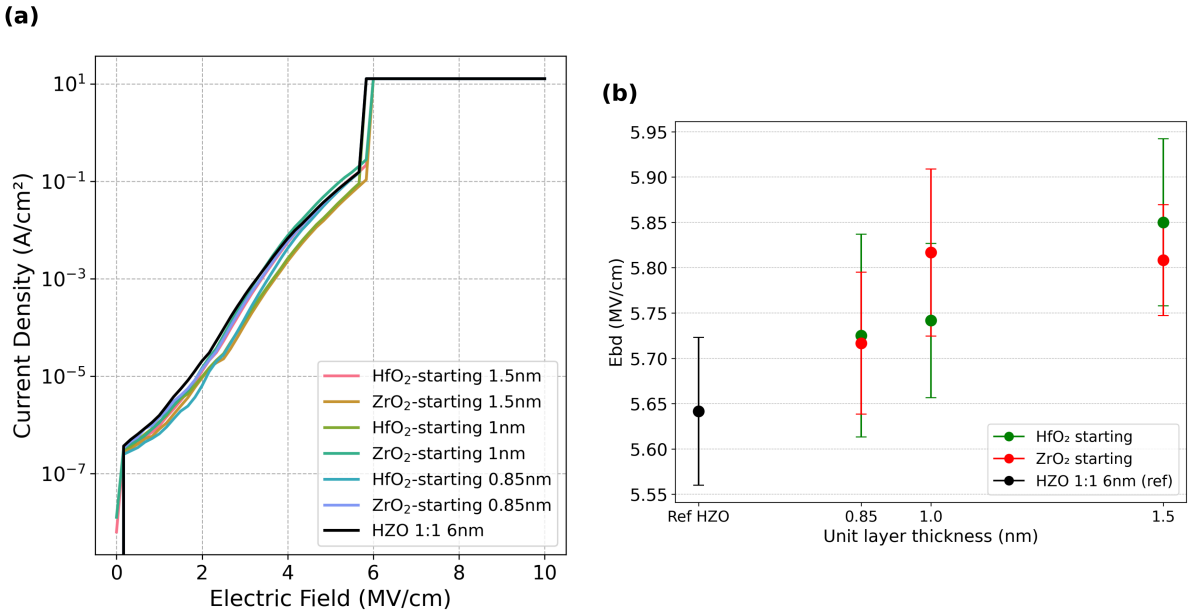

Figure 5.6: a. Current density as a function of the electric field and **b.** Breakdown field (E_{BD}) for different multilayer configurations and single-layer HZO.

The current density-electric field characteristics in **Fig. 5.6 a** reveal similar leakage current behavior across all samples, indicating that ferroelectric thickness, rather than the specific multilayer configuration, is the dominant factor governing leakage performance in structures. The overlapping J-E curves suggest that neither the starting layer nor the stacking sequence introduces significant differences in leakage mechanisms. However, a higher E_{BD} was observed for the multilayer structures compared to the homogeneous HZO reference film in **Fig. 5.6 b**. This suggests that, while total thickness remains the primary determinant of the overall leakage current behavior, the multilayer architecture may contribute to improved dielectric robustness.

This result contrasts with previous findings in the literature, where nanolaminate structures have been reported to significantly reduce leakage current compared to solid-solution HZO films. For example, Chen *et al.* demonstrated a reduction in leakage by up to three orders of magnitude in HfO_2/ZrO_2 multilayers compared to the HZO, attributing this behavior to the formation of space-charge-limited current regimes at the interfaces [168]. Similarly, other studies have reported approximately one order of magnitude decrease in leakage current for superlattice structures relative to the solid solution HZO [169, 170].

2.2.5 Correlation between crystallographic texture and ferroelectric performance

To further investigate the structural correlation with ferroelectric behavior in ultrathin films, a comparative analysis was performed between the XRD intensity at 30.5° and the initial remanent polarization. Each point in **Fig. 5.7 r**epresents a different 6 nm-thick multilayer structure, characterized by its unit layer thickness and whether it starts with HfO_2 (green) or ZrO_2 (red). The error bars reflect the standard deviation of $2P_R$ measurements across multiple devices.

As in Chapter 4 (Section 3), this study aims to assess whether improved crystallinity, reflected by higher diffraction intensity at 30.5°, corresponds to enhanced ferroelectric performance. As shown in **Fig. 5.7 ,** a trend is observed for the ZrO_2-starting multilayers: higher diffraction intensity tends to accompany higher $2P_R$ values. This suggests that greater crystallinity may support better ferroelectric performance in these systems.

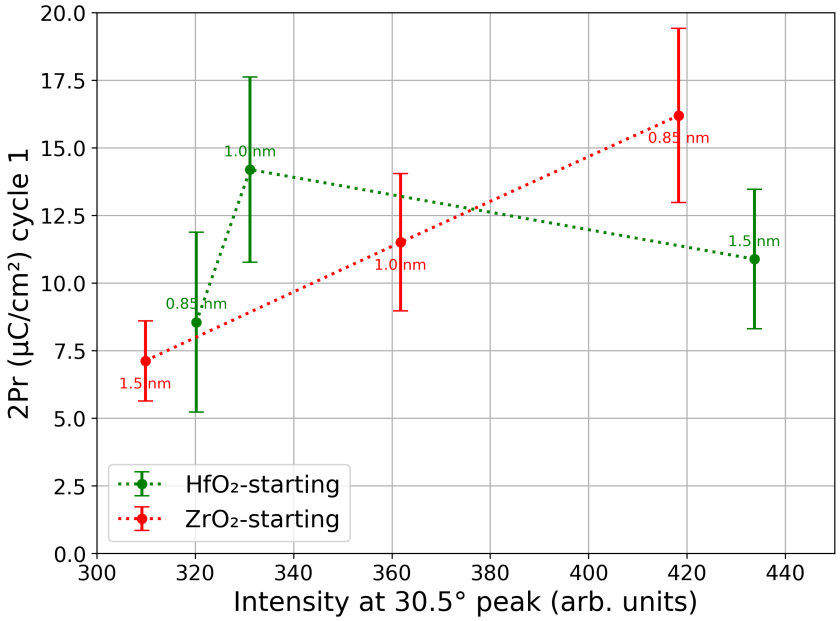

Figure 5.7: Correlation between remanent polarization at cycle 1 ($2P_R$) and the intensity of the 30.5° peak obtained from in-plane XRD for 6 nm HfO_2/ZrO_2 multilayers annealed at 500°C for 1 h. Green and red points indicate structures starting with HfO_2 and ZrO_2, respectively. Labels correspond to unit layer thickness. Error bars represent the standard deviation across $2P_R$ measurements.

However, the analysis based on the 30.5° peak is limited. This reflection includes overlapping contributions from both orthorhombic and tetragonal phases, which are difficult to distinguish due to similar *d*-spacings. This is particularly relevant for Zr-rich compositions, known to favor the formation of the tetragonal antiferroelectric phase. As a result, the presence of a stronger peak at 30.5° does not necessarily indicate enhanced ferroelectricity, and caution must be used when interpreting these results. To better understand the underlying mechanisms, a more refined structural investigation is necessary.

To gain further clarity, a complementary analysis was carried out by examining crystallographic texture. Inspired by the methodology proposed by Lehninger *et al.* [89], this second

analysis uses the area ratio between the (200) and (111) diffraction features as an indicator of texture development in the orthorhombic phase.

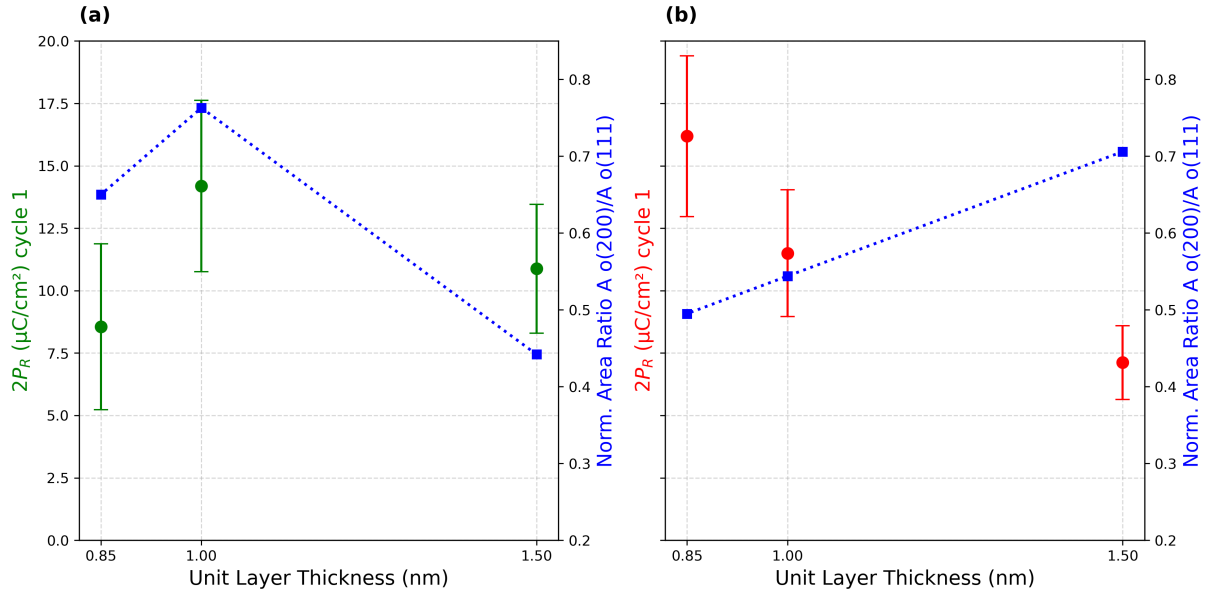

Figure 5.8: Correlation between unit layer thickness and both initial remanent polarization ($2P_r$) and normalized area ratio of the orthorhombic (200) to (111) XRD reflections ($A_{o(200)}/A_{o(111)}$) for **a.** HfO_2-starting and **b.** ZrO_2-starting multilayer stacks. Error bars indicate the standard deviation across measurements. The right y-axis represents the normalized area ratio extracted from in-plane XRD analysis, while the left y-axis shows the electrical response.

This approach focuses on a secondary feature near 35°, attributed to the (200) planes of the orthorhombic phase. An increased relative intensity or area of the (200) reflection has been linked in the literature to the development of crystallographic texture in the o-phase, which favors polarization switching by aligning the polar axes [129, 130]. Therefore, the ratio of the area under the (200) peak to that of the main peak at 30.5° can serve as an indirect indicator of texture development and ferroelectric phase dominance. However, it is important to note that this region also includes overlapping contributions from tetragonal and monoclinic phases of HZO, as well as from the (111) orientation of the TiN electrode, as noted earlier in the chapter.

This relationship is examined in **Fig. 5.8 ,** which presents the $2P_R$ extracted from the first cycle and the normalized area ratio $A_{o(200)}/A_{o(111)}$ for multilayers with different unit layer thicknesses, separated by initial sublayer **Fig. 5.8 a** HfO_2-starting and **Fig. 5.8 b** ZrO_2-starting.

In the HfO_2-starting structures **Fig. 5.8 a**, both $2P_R$ and the area ratio exhibit a similar trend. Although the evolution of polarization and area ratio is not perfectly identical, their general behavior suggests a link between structural texture and ferroelectric performance. This result aligns well with literature reports, where HfO_2-starting structures have enhanced (200) reflection is associated with better polarization performance due to stronger o-phase texturing [89, 96].

In contrast, the ZrO_2-starting structures **Fig. 5.8 b** exhibit an inverse trend. The area

ratio increases with unit thickness, but the polarization decreases. This divergence indicates that, although the structural texture becomes more pronounced, it does not necessarily lead to enhanced ferroelectric polarization behavior. Such a mismatch suggests that additional factors are influencing the electrical response beyond what can be inferred from XRD alone.

Nonetheless, these analyses assumes that the crystalline regions probed by XRD are representative of the entire film. Since the exact fraction of the sample that is fully crystallized versus remaining amorphous is not known, this correlation must be interpreted with caution. Amorphous regions, which do not contribute to the diffraction signal, may still impact the overall electrical response, potentially introducing additional variability in the observed trends.

2.3 General conclusion

This study evaluates the ferroelectric behavior of HfO_2/ZrO_2 multilayer structures with a total thickness of 6 nm, comparing different unit layer thicknesses and stacking sequences. All structures, including the homogeneous HZO solid solution reference, are fabricated under identical thermal processing conditions (500°C for 15 minutes), allowing for a direct comparison of the effects of the multilayer architecture.

Although all multilayer configurations exhibit ferroelectric switching, the homogeneous HZO reference sample consistently demonstrates superior remanent polarization values across all cycling conditions. The results further reveal that thinner unit layers, particularly those around 0.85–1.0 nm, provide higher remanent polarization, approaching the performance of homogeneous HZO at the same thickness. Notably, the ZrO_2-starting multilayer with 0.85 nm unit layers exhibits a remanent polarization comparable to the homogeneous HZO 1:1 sample. The starting and ending layers within the stack strongly influence polarization evolution during cycling and the wake-up behavior, highlighting the impact of stack configuration. Importantly, since crystallization occurs only after the deposition of the top electrode, the finishing layer plays also a role in the ferroelectric performance. In addition, the multilayer structures show a slightly higher breakdown field (E_{BD}) compared to the homogeneous film, suggesting that the multilayer design may enhance dielectric robustness

Structural analysis confirms successful crystallization in all samples, with no evidence of the most intense monoclinic peaks, even in ZrO_2-starting configurations. However, compositional analysis reveals deviations from the intended 1:1 Hf:Zr ratio in the multilayer stacks, which may contribute to differences in ferroelectric response. Furthermore, the correlation between crystallographic texture and electrical performance appears to be configuration-dependent: while HfO_2-starting stacks show a link between remanent polarization and the area ratio of the orthorhombic (200) to (111) XRD reflections, this trend is not observed in ZrO_2-starting structures, suggesting that additional factors also influence the ferroelectric behavior. Due to the complexity of the system and the limitations of current characterization techniques, the individual contributions of these factors remain difficult to isolate.

Overall, this work confirms that it is possible to obtain ferroelectric behavior in HfO_2/ZrO_2 nanolaminate structures even at ultrathin thicknesses, validating the possibility of the multilayer approach for ferroelectric integration. These findings open new opportunities for device opti-

mization in advanced memory and logic applications. However, the results also emphasize the complex interplay between structure, interfaces, and crystallographic orientation, which must be carefully managed to fully exploit the potential of ultrathin ferroelectric stacks to tune the desired properties.

3 6 nm multilayers with different compositions

As in the composition study of solid solution HZO in Chapter 4 4, the objective here is to investigate how different compositions influence the ferroelectric properties of a multilayer material structure. By analyzing multilayers with varying Hf/Zr ratios, it is possible to assess whether the trends observed in solid solution structures persist in a layered configuration or if interfacial effects introduce new behaviors.

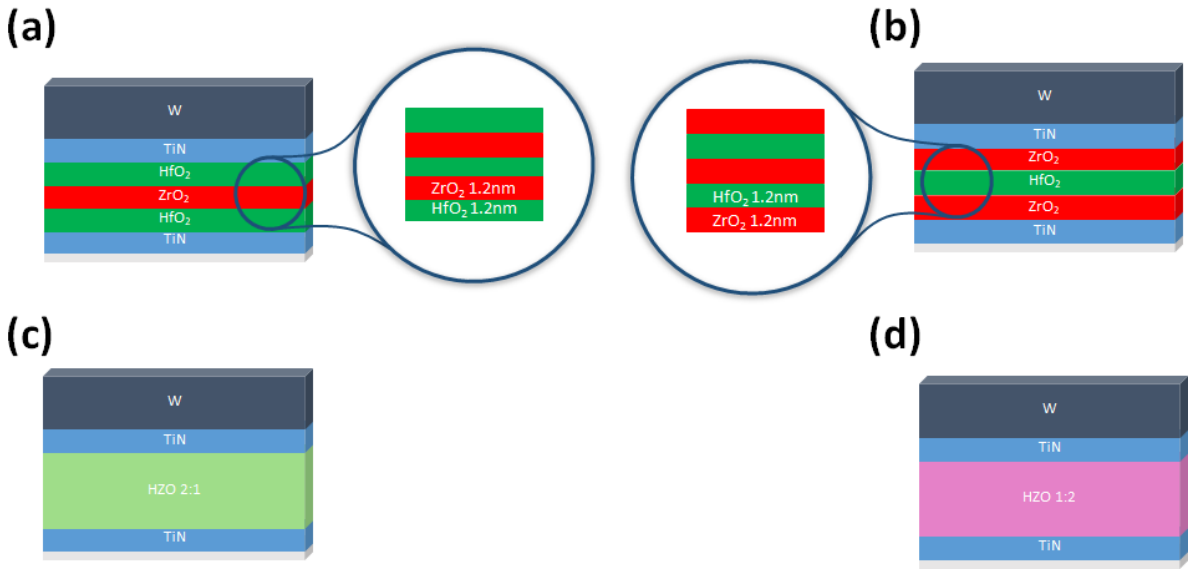

Figure 5.9: Schematic representation of the 6 nm multilayer with different compositions. **a** and **b** show 6 nm-thick multilayer structures with five alternating layers of HfO_2 and ZrO_2 with unit layer thickness of 1.2 nm. **c** and **d** represent 6 nm-thick HZO 2:1 and 1:2, respectively.

In this section, two multilayer structures were analyzed and compared to HZO solid solution references. The objective is to understand how ferroelectric behavior is influenced not only by the Hf:Zr ratio but also by the layered arrangement and interfacial characteristics. Both multilayers were composed of five layers with a targeted unit thickness of 1.2 nm, resulting in a total thickness of 6 nm. The first configuration (HZHZH) begins and ends with HfO_2, while the second (ZHZHZ) starts and ends with ZrO_2. These structures were compared to solid solution HZO samples with compositions of 2:1 and 1:2 Hf:Zr, respectively, to evaluate the impact of the multilayer configuration on polarization and wake-up behavior at the same thickness scale, as shown in **Fig. 5.9 .**

3.1 Structural and compositional analysis of 6 nm multilayers with varying Hf/Zr ratios

The composition results obtained from WDXRF analysis, presented in **Table 5.3**, show clear differences between the two multilayer configurations, despite being designed with the same number of layers and nominal unit thicknesses of 1.2 nm. The HZHZH configuration exhibits a global composition of 56:44 Hf:Zr, while the ZHZHZ configuration shows 35:65 Hf:Zr. These

variations suggest that the stacking order may influence the final elemental distribution. However, it is also likely that these differences arise, at least in part, from variations in the actual thickness of each layer, which cannot be precisely confirmed due to the challenges encountered in fitting the XRR data, seen in **Table 5.3**. The corresponding XRR fitting curves for both configurations are provided in the appendix 7.

Table 5.3: Experimental details for 6 nm multilayer configurations with alternating HfO_2 (H) and ZrO_2 (Z) layers. Atomic compositions were determined by WDXRF, and layer thicknesses were extracted by XRR fitting. Densities used in the fitting were fixed at 4.5 g/cm^3 for Ti, 4.95 g/cm^3 for TiN, 9.68 g/cm^3 for HfO_2, and 5.68 g/cm^3 for ZrO_2. Interface roughness was limited to 0.5 nm.

Target Unit Thickness	No. of Layers	Hf (at%)	Zr (at%)	Ti / TiN (nm)	Fitted H/Z Thicknesses (nm)
1.2 nm - HZHZH	5	56	44	4.2 / 9.7	1.1, 1.2, 1.1, 1.2, 1.4
1.2 nm - ZHZHZ	5	35	65	5.3 / 9.2	1.0, 1.4, 1.2, 1.4, 1.3

In theory, both multilayer configurations were designed to achieve global compositions close to 60:40 and 40:60 Hf:Zr, respectively. These expected theoretical compositions guided the comparison with HZO solid solution references having nominal Hf:Zr ratios of 2:1 and 1:2. However, the measured compositions deviate from these targets, which may be due to uncertainties in the WDXRF measurements or, as discussed previously, to differences in oxide-to-oxide growth rates during deposition that lead to variations in layer thickness, further contributing to these discrepancies.

These observations reinforce the need to account not only for the local stacking sequence but also for the resulting global composition when interpreting the electrical behavior of multilayer systems. As discussed in previous chapters, composition is a key factor influencing ferroelectric properties, with variations in the Hf:Zr ratio leading to changes in polarization and phase stability.

Fig. 5.10 shows the in-plane XRD patterns of multilayer and solid-solution HZO structures with equivalent thickness, where the most intense peak at approximately 30° (o(111)/t(101)) was normalized to enable direct comparison. Despite this normalization, the peak near 35°, associated with a mixture of orthorhombic, tetragonal, and monoclinic phases, and potentially influenced by the TiN electrode, shows different intensities across the structures. In **Fig. 5.10 a**, the HZHZH multilayer exhibits a more intense 35° peak compared to the HZO 2:1 solid solution, while in **Fig. 5.10 b**, both the ZHZHZ multilayer and the HZO 1:2 reference show similar intensities at this position.

It is important to note that the observed differences in intensity may also reflect variations in global composition between the multilayers and their solid-solution references, as they do not share exactly the same Hf:Zr ratio. Therefore, these XRD comparisons should be interpreted with caution, as crystallization behavior can be influenced by both composition and structural configuration.

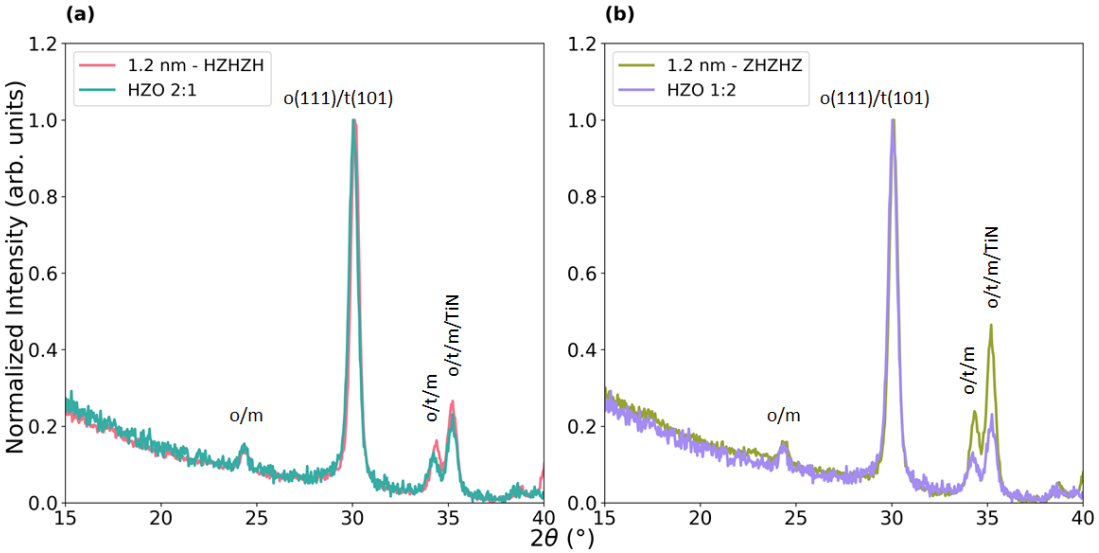

Figure 5.10: Normalized in-plane XRD patterns of 6 nm: **a.** HZHZH multilayer (1.2 nm unit layers, 56:44 Hf:Zr) and the HZO 2:1 solid solution and **b.** ZHZHZ multilayer (1.2 nm unit layers, 35:65 Hf:Zr) and the HZO 1:2 solid solution. All samples were integrated with TiN/W electrodes and annealed at 500°C for 15 min, and subsequently underwent top electrode etching.

3.2 Electrical properties of 6 nm HfO_2/ZrO_2 multilayers with varying composition

Fig. 5.11 shows the evolution of P–E loops during cycling for four 6 nm-thick structures annealed at 500°C. The HZHZH and ZHZHZ multilayers both exhibit pinched hysteresis loops in the initial cycles, which progressively evolve with cycling, reflecting the characteristic wake-up effect. In comparison, the HZO 2:1 sample shows less pinching from the beginning, suggesting a lower antiferroelectric contribution and a more favorable initial ferroelectric state. On the other hand, the HZO 1:2 composition remains strongly pinched even after cycling, consistent with the stabilization of the tetragonal antiferroelectric phase commonly observed in Zr-rich compositions.

These observations are supported by the remanent polarization evolution in **Fig. 5.12 a**. The HZHZH multilayer exhibits the highest $2P_r$ at 10^4 cycles, along with a significant wake-up effect. In the Zr-rich structures, the ZHZHZ multilayer maintains higher $2P_r$ than its solid-solution counterpart throughout cycling, reinforcing the impact of stacking order and interfacial configuration. These results emphasize how both composition and structural design influence the stabilization of the ferroelectric phase in ultrathin films.

The superior ferroelectric performance observed in the multilayer structure could, in part, be attributed to differences in global composition, as variations in the Hf:Zr ratio are known to influence polarization behavior and phase stability. Additionally, mechanisms previously discussed, such as localized stress at HfO_2/ZrO_2 interfaces arising from thermal expansion mismatches, may induce tensile strain and suppress the formation of the tetragonal antiferroelectric phase. These combined effects make it difficult to attribute the enhanced performance to a single factor.

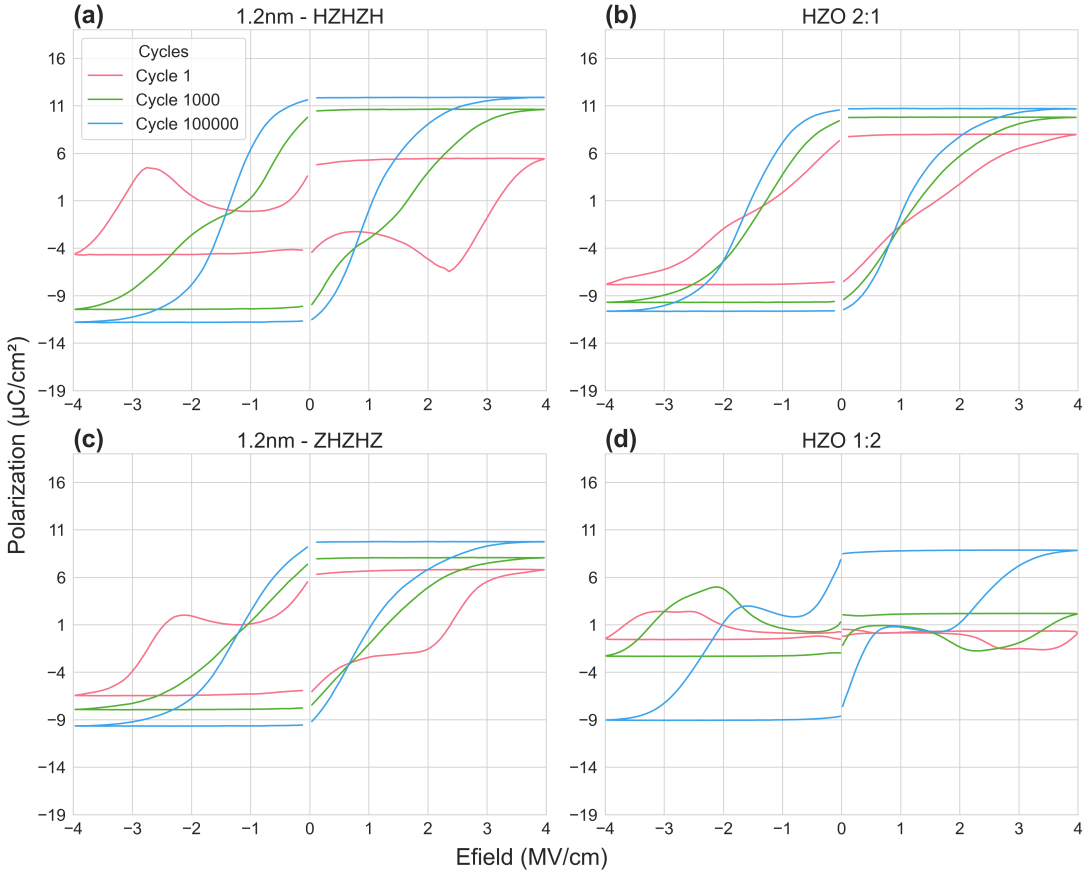

Figure 5.11: P–E loops as a function of cycling for different 6 nm structures annealed at 500°C for 15 min.**a.** HfO_2 (1.2 nm)/ZrO_2 (1.2 nm) multilayer (HZHZH); **b.** solid solution HZO 2:1; **c.** ZrO_2 (1.2 nm)/HfO_2 (1.2 nm) multilayer (ZHZHZ); **d.** solid solution HZO 1:2.

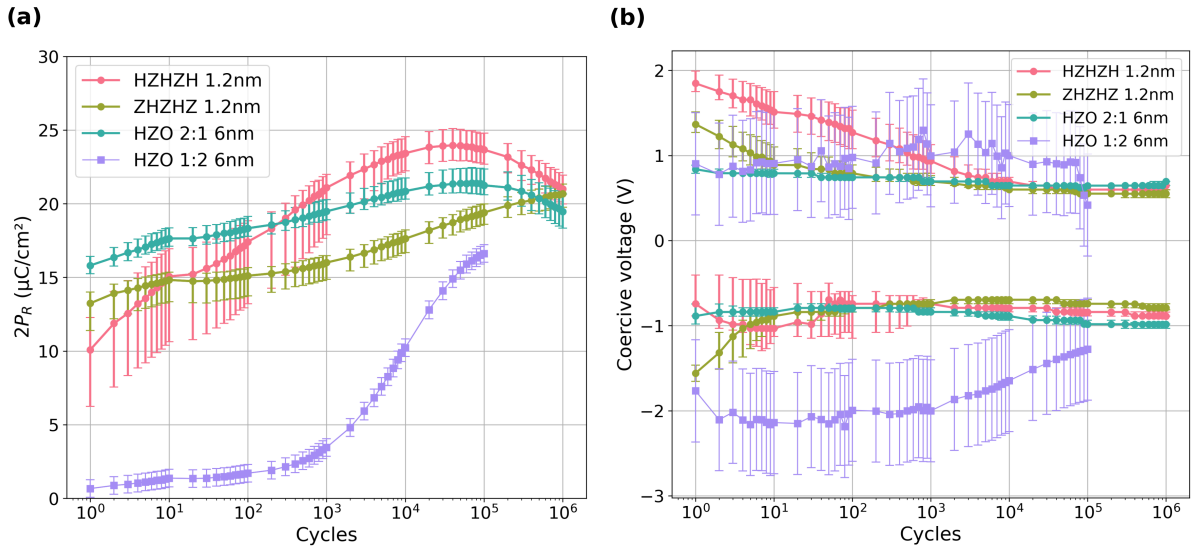

Figure 5.12: Evolution of **a.** remanent polarization ($2P_R$) and **b.** coercive voltage as a function of cycling for different structures and compositions.

The V_C evolution over cycling in **Fig. 5.12 b** reveals distinct behaviors depending on composition and structural configuration. The HZO 1:2 sample presents large variability and broad error bars during early cycles, reflecting its initial antiferroelectric character. In contrast, the HZO 2:1 sample remains stable from the initial cycles, indicating that this composition favors ferroelectric ordering. Its multilayer counterpart HZHZH shows a more pronounced wake-up effect, suggesting an initially non-polar state that gradually stabilizes. Despite these initial variations, the coercive voltage of all compositions tends to converge after extensive cycling, suggesting that the total thickness of the layer ultimately plays a dominant role in the long-term stability of the switching process.

Another key observation is the asymmetry in coercive voltages, where positive and negative V_C values do not coincide for the studied multilayer stacks. This asymmetry is not observed in other multilayer configurations or in the solid-solution films discussed previously; it becomes more pronounced only when the stack starts and ends with different oxides. While TiN oxidation from air exposure between process steps is possible, this effect would occur in all stacks and therefore cannot fully explain the behavior. Instead, interface-related differences, such as variations in the local HfO_2/ZrO_2 contact or interfacial layers formed during processing [171, 172], may contribute when such asymmetry appears.

Fig. 5.13 illustrates the influence of both composition and multilayer architecture on the dielectric breakdown strength of the thin films at 6 nm thickness. As expected, the solid solution HZO 2:1 exhibits a higher E_{BD} than the more Zr-rich HZO 1:2, in agreement with the known trend that higher Hf content increases the bandgap, thereby improving breakdown performance.

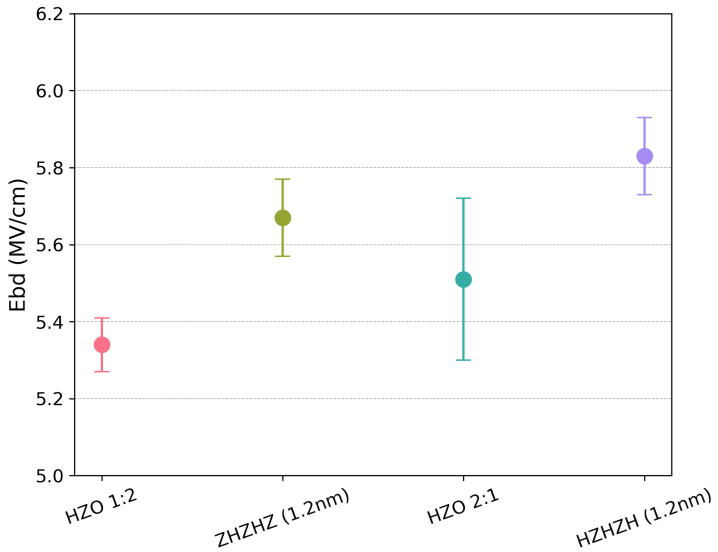

Figure 5.13: Breakdown field (E_{BD}) comparison for four configurations: solid solution HZO 1:2, multilayer ZHZHZ (1.2 nm unit layers thickness), solid solution HZO 2:1, and multilayer HZHZH (1.2 nm unit layers thickness). All structures used a TiN/W top electrode and were annealed at 500°C for 15 minutes. Error bars represent the standard deviation across the 20 measured devices.

Interestingly, both multilayer structures (ZHZHZ and HZHZH), despite having different com-

positions from the solid solution references, demonstrate even higher breakdown fields. This suggests that, beyond chemical composition, the presence of well-defined interfaces in the multilayers plays a key role. These interfaces can act as barriers to charge transport, suppressing defect propagation or leakage paths, and thereby enhancing dielectric robustness.

The HZHZH structure (1.2 nm unit layers, 56% Hf) shows the highest E_{BD} value among the samples studied. This is especially notable given that the HZO 2:1 solid solution contains more Hf (66%) and should, in principle, benefit from a wider bandgap. The superior performance of the HZHZH multilayer highlights the importance of interface engineering: it suggests that structural modulation through nanolaminate design can outweigh the advantages of composition alone, offering enhanced breakdown strength via charge-blocking interfaces.

3.3 General conclusion

This study investigates how composition variations and multilayer configurations influence the structural and electrical behavior of 6 nm HfO_2/ZrO_2 ferroelectric stacks. In-plane XRD measurements reveal distinct structural differences between the multilayer and solid-solution counterparts. The Hf-rich multilayer exhibits an overall higher intensity across the diffraction pattern, including a more pronounced (200) peak near 35°, often associated in the literature with orthorhombic phase texture favorable to ferroelectricity. For the Zr-rich compositions, XRD patterns are similar between the multilayer and solid solution, showing only a slight increase in the (200) peak for the multilayer structure, which alone does not explain the electrical behavior.

Electrical measurements provide further insight into the impact of composition and stacking configuration. For the Hf-rich compositions, the multilayer structure shows a significant wake-up effect, eventually surpassing the remanent polarization of the corresponding HZO film after extended cycling. This suggests that, despite a lower initial polarization, the multilayer evolves toward a state with greater maximum remanent polarization over cycling.

Interestingly, the Zr-rich multilayer exhibits enhanced ferroelectric polarization behavior compared to its solid-solution counterpart, achieving higher polarization already at early cycles. While Zr-rich films are typically associated with the stabilization of the non-polar tetragonal phase, leading to antiferroelectric-like behavior, the improved performance observed in the multilayer indicates that its architecture may help suppress the formation of the tetragonal phase. This suggests that other effects also contribute to promoting ferroelectric behavior despite the Zr-rich composition.

These findings indicate that, for the compositions studied here, the multilayer architecture enhances ferroelectric behavior over time, suggesting that stacking order and interface configuration positively influence phase stabilization and polarization evolution in nanoscale ferroelectric devices. In addition, the multilayer configuration demonstrates superior dielectric breakdown strength compared to solid solutions, reinforcing the beneficial role of interface engineering in enhancing electrical reliability.

4 Ultra-thin multilayers: tuning ferroelectric performance with reduced ZrO_2 content

As part of the strategy to reduce the total thickness of the ferroelectric material and lower the operating voltage, this section investigates ultra-thin multilayers with reduced ZrO_2 content. The objective is to assess whether these modifications enhance polarization stability, suppress antiferroelectric-like behavior, and promote a well-defined ferroelectric phase in the ultra-thin regime.

Previous results have shown that reducing the amount of Zr is effective in stabilizing ferroelectricity at thin thicknesses, as discussed in Chapter 4 Section 4. To further investigate this trend, two multilayer structures are analyzed: a 5 nm multilayer composed of alternating 1 nm HfO_2 and 1 nm ZrO_2 layers, arranged in a five layers and therefore starting and ending with HfO_2, and a 4 nm multilayer with 1 nm HfO_2 and 0.5 nm ZrO_2, also forming a five-layer structure with HfO_2 as the initial and final layer. The latter design aims to further reduce the tetragonal phase fraction and mitigate antiferroelectric behavior by decreasing the ZrO_2 layer thickness. By comparing these structures, the study aims to determine how composition control impact polarization properties in ultra-thin ferroelectric multilayers.

4.1 Structural and composition characterization of ZrO_2-reduced ultra-thin multilayers

Table 5.4 summarizes the experimental compositions of the 5 and 4 nm multilayer systems, as determined by WDXRF. Each configuration was designed with a targeted Hf/Zr ratio, approximately 60:40 for the 5 nm sample and 75:25 for the 4 nm one, based on the number and thickness of HfO_2 and ZrO_2 layers in the ALD cycles. WDXRF analysis confirms that the targeted compositions were achieved.

Although the compositions are not strictly identical between the two structures, they represent the closest matching configurations available for a relevant comparison of thickness and layering effects.

Table 5.4: Experimental details and structural parameters for 5 and 4 nm multilayer configurations. The stack includes Ti/TiN bottom electrodes followed by alternating HfO_2 (H) and ZrO_2 (Z) layers. Atomic compositions were determined by WDXRF and thicknesses were extracted from XRR analysis.

Target Unit Thickness	No. of Layers	Hf (at%)	Zr (at%)	Ti / TiN (nm)	Fitted H/Z Thicknesses (nm)
1 nm/1 nm - HZHZH	5	58	42	3.6 / 11.2	0.8, 0.9, 1.2, 0.9, 0.9
1 nm/0.5 nm - HZHZH	5	71	29	3.5 / 11.2	1.0, 0.5, 1.1, 0.5, 0.9

The presented XRR results in appendix 8 (**Fig. 34**) and **Table 5.4** correspond to as-deposited HfO_2/ZrO_2 multilayers fabricated on a bottom electrode consisting of 5 nm Ti and 10 nm TiN. The total thicknesses of the multilayers are 5 nm and 4 nm, respectively. These multilayers were designed with unit sublayers of 1 nm/1 nm and 1 nm/0.5 nm, respectively, making their characterization particularly challenging due to the ultra-thin nature of the individual

layers.

Accurately fitting XRR data for such ultrathin multilayers is difficult due to limited contrast between HfO_2 and ZrO_2, potential intermixing at interfaces, and the influence of surface roughness. As described previously, constraints were applied during the XRR fitting process to improve convergence and reduce overfitting.

The in-plane XRD analysis in **Fig. 5.14** was conducted after the fabrication of the MFM structures with TiN/W top electrodes, followed by annealing at 500°C for 15 minutes, and the measurements were performed after the etching of the top electrode. The results compare multilayered HfO_2/ZrO_2 structures with their corresponding solid solution HZO compositions at 5 and 4 nm thicknesses, providing insight into the structural evolution of these different configurations.

For the 5 nm structures in **Fig. 5.14**a, the solid solution sample exhibits higher-intensity diffraction peaks, indicating better crystallinity. In contrast, for the 4 nm structures in **Fig. 5.14**b, the multilayer sample exhibits less intense peaks, whereas the solid solution of the same composition remains amorphous, as indicated by the absence of discernible crystallographic peaks. This suggests that the introduction of layering promotes crystallization, even at this reduced thickness, while the solid solution structure lacks sufficient crystallization under the given annealing conditions.

Additional low-intensity features between 18–27°, labeled as "oxidation" in **Fig. 5.14**, are likely due to surface oxidation of the exposed electrodes after etching. This effect was previously discussed in Chapter 4, Section 3.

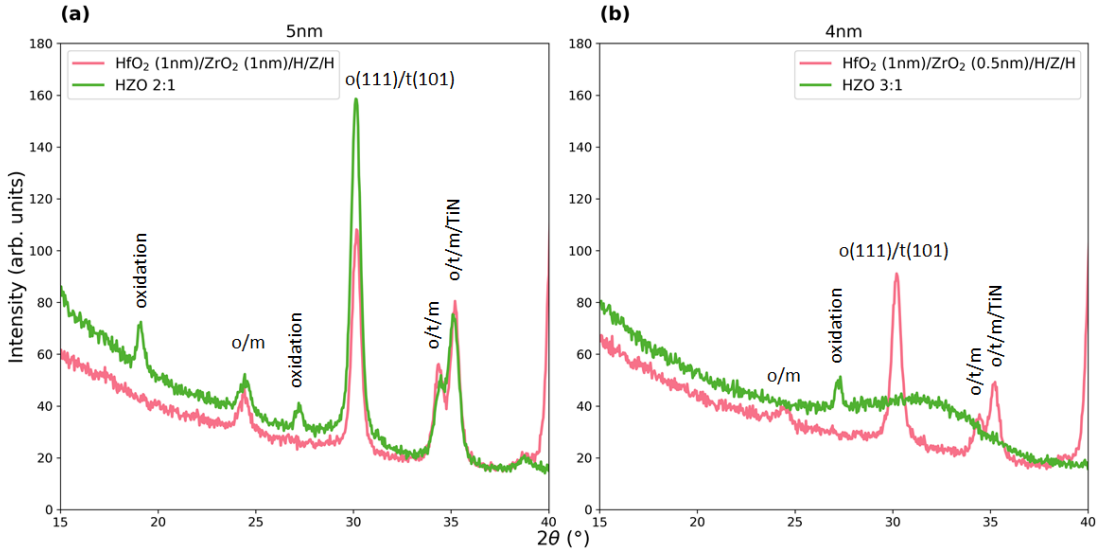

Figure 5.14: In-plane XRD characterization of **a.** 5 and **b.** 4 nm multilayer structures after TiN/W deposition and annealing at 500°C for 15 minutes. The pink curve corresponds to the multilayer structures, while the green curve represents the solid solution of similar composition for comparison. XRD scans were performed after etching the top electrode.

To further explore the preservation of the multilayer architecture, cross-sectional TEM anal-

ysis was conducted to assess the conservation of the unit layers after the complete fabrication process, as shown in **Fig. 5.15**. One of the main objectives was to determine whether the individual HfO_2 and ZrO_2 sublayers remained distinguishable, as their ultrathin dimensions pose challenges for precise modeling in XRR due to resolution limitations.

Regarding the 5 nm structure, evidence of unit layers is observed in **Fig. 5.15**a, though the interfaces between the HfO_2 and ZrO_2 sublayers are not sharply defined. This could suggests a possible degree of mixing or diffusion between the layers, however, the overall layered structure remains preserved after processing.

Similarly, for the 4 nm structure, a contrast variation is still visible in **Fig. 5.15**b, suggesting the potential conservation of the ultrathin layers, despite the lack of sharply defined boundaries. This points out the challenges in resolving them due to their ultrathin dimensions or significant intermixing of the sublayers. Similar to the 5 nm structure, some level of diffusion or interfacial modification is observed at the top electrode-multilayer interface. Additionally, lattice fringes are also present, further confirming that the sample has undergone crystallization, despite the reduced thickness. Nonetheless, the presence of residual amorphous regions cannot be ruled out, especially considering the limited volume sampled by TEM and the lower crystallization efficiency typically associated with thinner films.

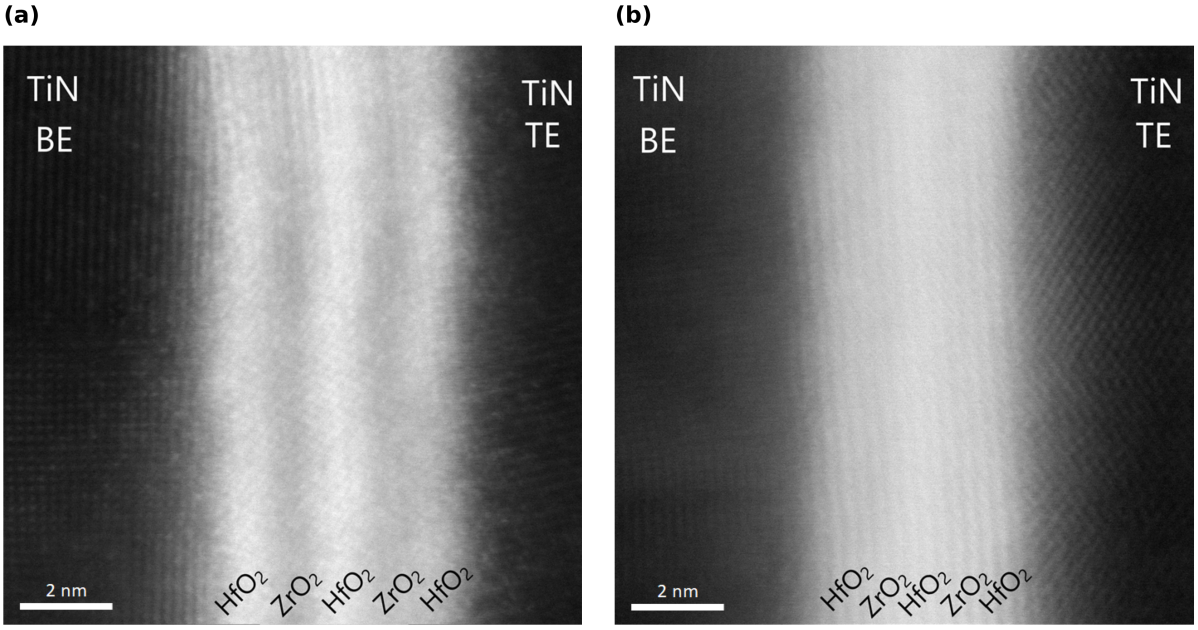

Figure 5.15: Cross-sectional TEM characterization of **a.** 5 nm multilayer composed of alternating 1 nm HfO_2 and 1 nm ZrO_2 layers, and **b.** 4 nm multilayer structures with 1 nm HfO_2 and 0.5 nm ZrO_2, after TiN/W deposition and annealing at 500°C for 15 minutes. BE and TE refer to the bottom and top electrodes, respectively.

4.2 Ferroelectric stability in sub-6 nm capacitor structures

The developed structures were fabricated using TiN 10 nm CVD + W 70 nm SSP as the top electrode, followed by annealing at 500°C for 15 minutes. However, one exception is the HZO

2:1 5 nm structure, which was processed with a TiN 10 nm CVD + TiN 50 nm PVD electrode, as previously discussed in Chapter 4 Section 4.

The **Fig. 5.16** and **Fig. 5.17** compare P–E loops of multilayers and solid solutions HZO at 5 and 4 nm. The observed differences in electrical performance can be correlated with the crystallographic characteristics in the in-plane XRD analysis (**Fig. 5.14**), which provides insight into the structural evolution of these materials.

At 5 nm, the HfO_2 (1 nm)/ZrO_2 (1 nm)/H/Z/H multilayer exhibits a pronounced wake-up effect, with 2Pr increasing beyond 10^4 cycles. However, its total polarization remains lower than that of the HZO 2:1 solid solution, which displays consistently higher $2P_R$ from the beginning, suggesting a more readily stabilized ferroelectric phase. In-plane XRD in **Fig. 5.14**a shows that the solid solution has stronger diffraction peaks, indicating better crystallinity, while the multilayer exhibits weaker peaks, suggesting reduced crystallization. This difference in structural order may explain the initially lower polarization in the multilayer and its need for additional cycling to enhance ferroelectric performance.

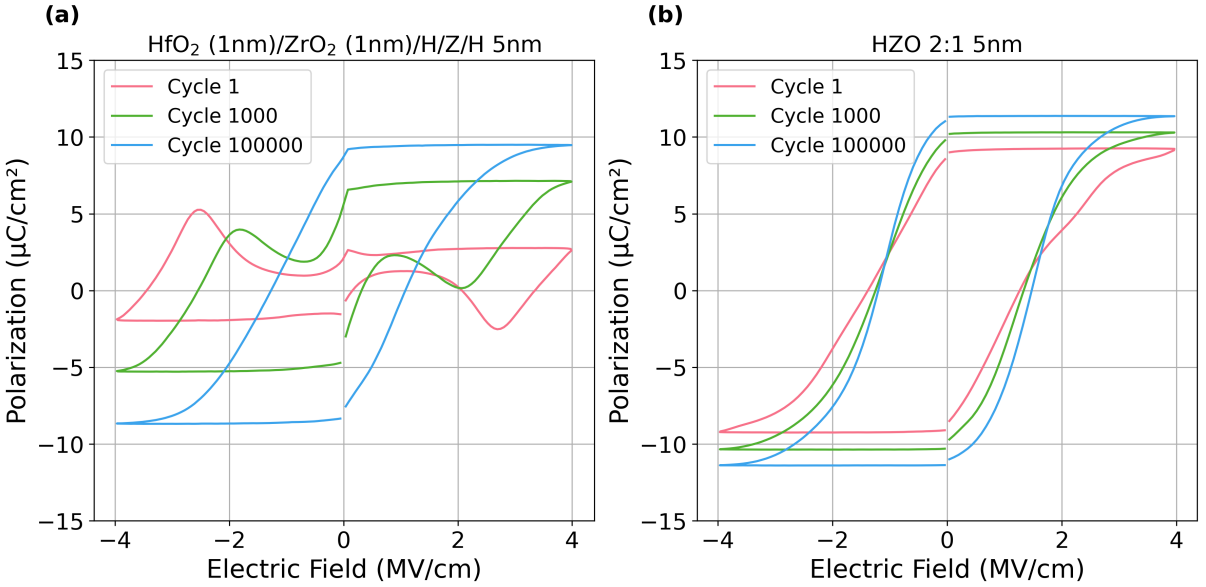

Figure 5.16: P-E loops of 5 nm ultrathin structures at different cycling stages annealed at 500°C for 15 min. **a.** HfO_2 (1 nm)/ZrO_2 (1 nm)/H/Z/H multilayer exhibits a characteristic wake-up effect, with polarization increasing over cycling. **b.** HZO 2:1 5 nm single layer shows a higher total remanent polarization ($2P_r$) compared to the multilayer at the same thickness, indicating better ferroelectric performance in this structure and composition.

At 4 nm, the HfO_2 (1 nm)/ZrO_2 (0.5 nm)/H/Z/H multilayer exhibits a weaker wake-up effect and achieves a lower total $2P_r$ compared to the 5 nm multilayer structure presented previously. In contrast, the HZO 3:1 solid solution displays no measurable polarization, indicating difficulty in forming a ferroelectric phase at this thickness. This behavior is consistent with the in-plane XRD results (**Fig. 5.14**b), which show that the multilayer exhibits some structural order, while the solid solution remains amorphous. These findings suggest that layering promotes crystallization and helps stabilize ferroelectricity in ultrathin films, whereas the solid solution fails to crystallize

under the same annealing conditions.

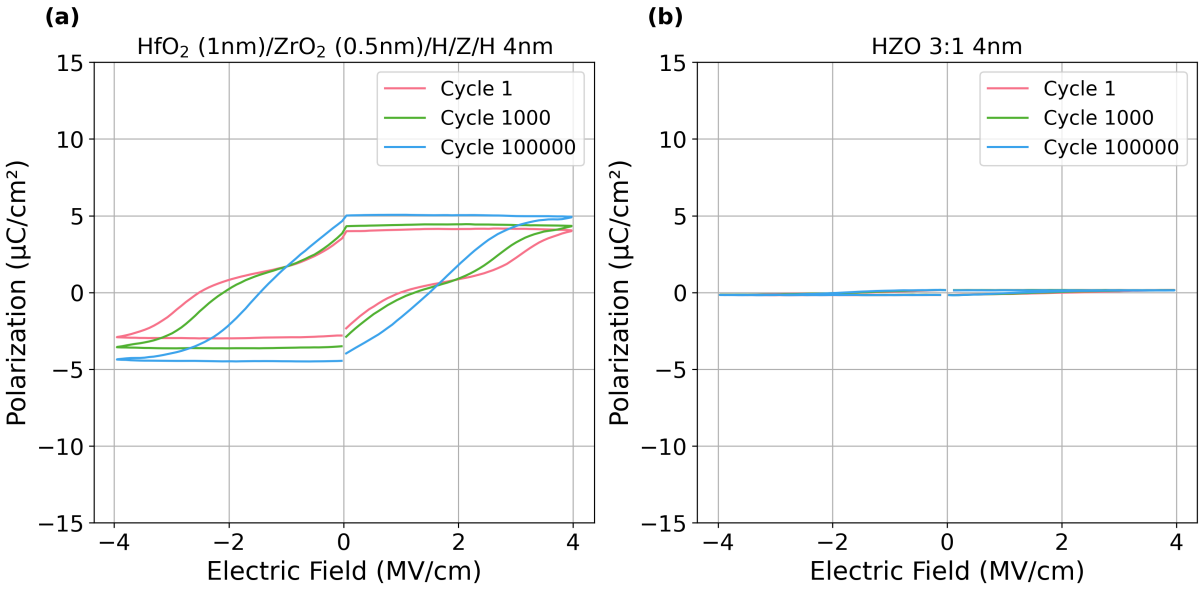

Figure 5.17: P-E loops of 4 nm ultrathin structures at different cycling stages annealed at 500°C for 15 min. **a.** HfO_2 (1nm)/ZrO_2 (0.5 nm)/H/Z/H multilayer exhibits clear ferroelectric behavior with polarization evolution over cycling. **b.** HZO 3:1 4 nm single layer shows no significant polarization, indicating a non-ferroelectric response at this thickness.

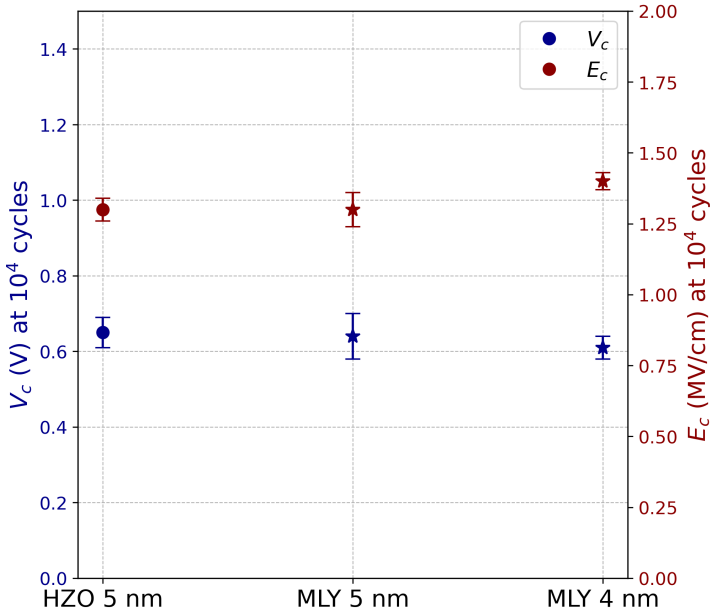

Figure 5.18: Coercive voltage (V_c) and coercive field (E_c) values at 10^4 cycles for HZO 5 nm 2:1, MLY 5 nm (HfO_2 (1 nm)/ZrO_2 (1 nm)/H/Z/H), and MLY 4 nm (HfO_2 (1 nm)/ZrO_2 (0.5 nm)/H/Z/H) samples.

Fig. 5.18 presents the V_c and E_c values measured at 10^4 cycles for three ultrathin ferroelectric structures: HZO 5 nm 2:1, MLY 5 nm 2:1 (HfO_2 (1 nm)/ZrO_2 (1 nm)/H/Z/H), and MLY

4 nm 3:1 (HfO_2 (1 nm)/ZrO_2 (0.5 nm)/H/Z/H). The HZO solid solution 4 nm 3:1 structure was not considered due to the absence of crystallization of the film. Contrarily with previous observations presented in Chapter 4 sections 3 and 4, E_c and V_c remains constant across all investigated structures.

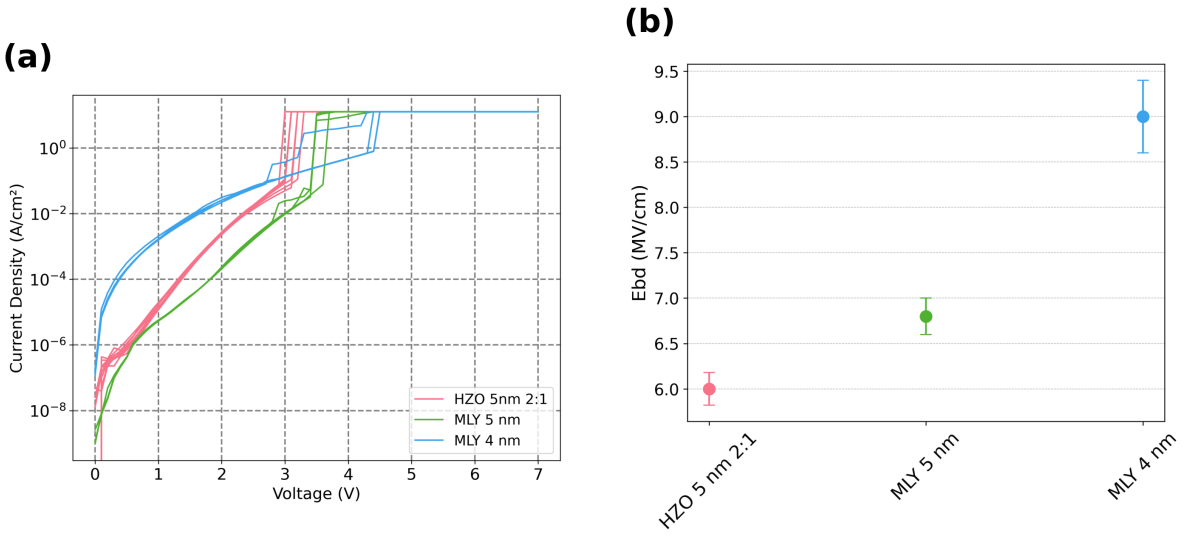

Figure 5.19: a. Leakage current density as a function of applied voltage for each sample configuration. **b.** Breakdown field (E_{BD}) comparison highlighting differences between the samples.

Fig. 5.19a illustrates the leakage current density as a function of applied voltage for each ultrathin film configuration. The MLY 4 nm structure (blue curves) exhibits the highest breakdown voltage among the studied samples, although it simultaneously presents elevated leakage currents relative to the 5 nm structures. This increased leakage is attributed primarily to direct tunneling effects occurring between the TiN electrodes and the ultrathin ferroelectric layer, as previously reported for films thinner than 5 nm [99]. Both 5 nm structures demonstrate comparable leakage current characteristics at lower voltages, although the multilayer structure shows a slightly improved dielectric robustness, as indicated by its higher breakdown field compared to the single-layer HZO structure in **Fig. 5.19**b. This enhancement in breakdown field is likely related to the presence of internal interfaces in the multilayer system, which not only hinder the movement of defects, but also act as localized charge trapping sites, together helping to prevent premature breakdown.

4.3 General conclusion

The investigation of ultra-thin ferroelectric multilayers with reduced ZrO_2 content provides critical insights into the stabilization of ferroelectricity at ultra-thin thicknesses. Structural characterization through XRD confirms that multilayers facilitate crystallization, even at 4 nm, whereas solid solution HZO at the same thickness remains amorphous and non-ferroelectric. The preservation of unit layers in the multilayer structures showed through TEM, suggests that engineered interfaces play a crucial role in promoting crystallization at such reduced dimensions.

However, interdiffusion at the interfaces cannot be ruled out in such thin films.

Electrical measurements reveal a strong dependence of polarization stability on both composition and structure configuration. At 5 nm, the multilayer structure exhibits a pronounced wake-up effect, with $2P_R$ increasing significantly over cycling, whereas the solid solution HZO 2:1 maintains a consistently higher polarization from the outset. In contrast, at 4 nm, the multilayer exhibits lower ferroelectricity, while the solid solution HZO 3:1 remains entirely amorphous, underscoring the challenge of stabilizing polarization in ultra-thin films. These findings suggest that interface engineering can aid crystallization and improve polarization in such thin films.

Quasi-static I–V tests highlight another advantage of the multilayer approach. The 4 nm multilayer exhibits the highest breakdown field, suggesting that the layering strategy contributes to improved resistance to breakdown. However, this benefit comes at the cost of increased leakage current, likely due to direct tunneling effects exacerbated by ultra-thin dimensions. In contrast, the 5 nm multilayer shows slightly improved dielectric robustness compared to its solid solution counterpart, while maintaining comparable leakage characteristics.

This research provides valuable insights into the feasibility of ultra-thin ferroelectrics for next-generation memory applications. By demonstrating how multilayer structuring influences phase stability and electrical performance, these findings contribute to strategies for extending ferroelectricity to sub-5 nm thicknesses. Importantly, the use of ALD provides control over both layer thickness and composition, making it an ideal technique for fabricating complex multilayer stacks. Future efforts should aim to optimize processing conditions and ensure compatibility with BEOL integration for successful implementation in advanced microelectronics.

5 Benchmark

The benchmark comparison in **Fig. 5.20 h**ighlights the variation in remanent polarization across different multilayer (MLY) total thicknesses, emphasizing the role of fabrication processes, deposition conditions, and annealing treatments. Notably, 10 nm films exhibit the highest remanent polarization (45–48.6 $\mu C/cm^2$), particularly in studies by Lehninger *et al.* and Kang *et al.*, suggesting optimized processing parameters that enhance ferroelectric properties [89, 173]. In contrast, thinner films (6 nm) tend to show lower polarization, with this PhD samples (P_r = 25 $\mu C/cm^2$) presenting comparable values relative to reports from Liang *et al.* and Bai *et al.* [47, 164]. Additionally, annealing temperature appears to play a key role, as higher temperatures (550°C) correlate with enhanced polarization. However, there is no clear consensus on the results, as the performance of these systems is not solely dictated by thickness or annealing temperature but is instead influenced by a complex interplay of factors, including layer system configuration, unit layer thickness, precursor chemistry, deposition temperature, electrode materials, and interfacial effects.

Taking into consideration prior research, understanding these performance differences requires analyzing the various processing parameters that influence the final material properties. Despite having a superior polarization compared to this PhD work, the 10 nm samples from Lehninger *et al.* and Kang *et al.* were fabricated using different approaches. Lehninger's *et al.* study utilized an ALD process similar to this work (chlorinated precursors and 300°C deposition), but with TiN electrodes and a 400°C RTA for 60 s, which may have contributed to differences in the resulting ferroelectric properties [89]. Notably, Lehninger *et al.* found that 1 nm unit layers provided the best results, a trend that was also observed in this PhD work, indicating that ultrathin unit layers promote favorable ferroelectric phase formation in nanolaminates. Importantly, his multilayer structures showed superior performance compared to homogeneous HZO films of the same total thickness.

On the other hand, Kang *et al.* used a system with 100 nm TaN electrodes and ALD deposition using organometallic precursors, followed by a higher-temperature annealing at 550°C for 60 s [173]. Interestingly, Kang *et al.* found better results for even thinner unit layers (<1 nm), suggesting that in certain processing conditions, further reducing the individual layer thickness can enhance polarization. As in Lehninger's *et al.* work, the multilayer structures developed by Kang *et al.* outperformed the solid solution HZO of identical total thickness. Both processes incorporated an initial HfO_2 layer, a factor known to impact nucleation and phase formation in multilayers. The differences in electrode materials (TiN vs. TaN), precursor chemistry (chlorinated vs. organometallic), and annealing temperature likely contributed to variations in stress, crystallization dynamics, and defect formation, all of which can significantly influence polarization stability and wake-up behavior in ferroelectric capacitors.

For 6 nm multilayer systems, polarization results are comparable, with this PhD work achieving similar polarization at a lower annealing temperature (500°C), while literature typically reports higher temperatures. Although slightly lower than other reports, this reduction in annealing temperature may be advantageous for thermal budget constraints in device integration.

Liang's *et al.* study, which also obtained high polarization at 6 nm, employed W electrodes, organometallic precursors, and ALD deposition at 250°C, followed by a 600°C annealing step [47]. Unlike this work, Liang *et al.* found that an initial ZrO_2 layer combined with 1 nm unit layers produced better results, highlighting the influence of initial layer selection on phase formation. However, his study also differed in electrode choice and annealing conditions, which can significantly affect interface properties, defect densities, and switching mechanisms. The higher annealing temperature (600°C vs. 500°C in this work) could have contributed to further phase stabilization, leading to differences in observed polarization behavior.

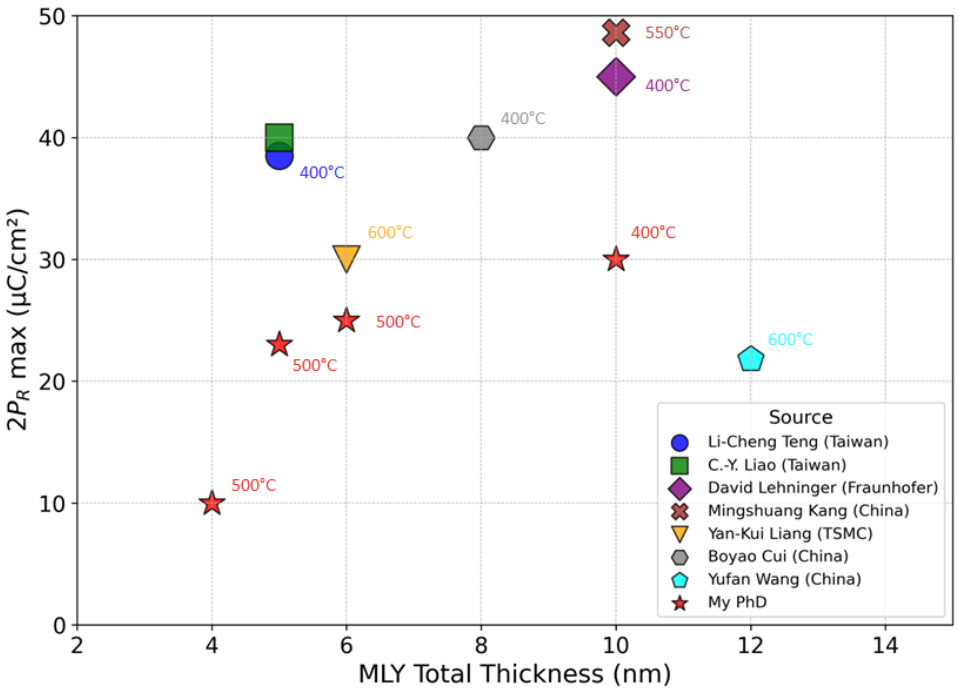

Figure 5.20: Benchmark of remanent polarization for HfO_2/ZrO_2 multilayers (MLY) thin films across various total thicknesses.

For the 5 nm system, Liao *et al.* did not specify key processing parameters, such as precursor type, ALD conditions, electrode materials, or annealing details, making direct comparisons challenging [174]. The low thickness of the superlattice system suggests that higher annealing temperatures may have been necessary to induce crystallization into the ferroelectric phase. However, the available details indicate that Teng *et al.* used a PEALD process with Mo electrodes and a 400°C annealing step for 1 min, highlighting the potential for different optimizations in terms of electrode compatibility and crystallization kinetics.

Moreover, measurement strategies employed by different studies can also contribute to the observed performance variations. Differences in capacitor size and electrical testing conditions, such as cycling protocols, frequencies, and field strengths, often not fully specified in the literature, can significantly influence the measured electrical properties. In particular, changes in capacitor size can affect the stress distribution, which in turn may impact the crystallization behavior and phase formation of the ferroelectric material. As discussed previously, these fac-

tors must be taken into account when comparing reported ferroelectric performance, as they introduce variability and can influence the interpretation of experimental results.

Finally, the 4 nm nanolaminate structure with good electrical performance appears to be the first of its kind reported in the literature. Given the challenges associated with crystallization at such ultrathin thicknesses, this result represents a significant advancement in the field, demonstrating the feasibility of ferroelectricity in ultra-scaled multilayers and opening new possibilities for future optimizations.

6 Chapter Summary and Conclusions

Based on the findings presented across the different sections, this study provides a comprehensive evaluation of the ferroelectric behavior in ultrathin HfO_2/ZrO_2-based structures, with a particular focus on multilayer configurations. Through systematic analysis of 6 nm multilayers, it was shown that the combination of precise unit layer thickness control and interface engineering plays a critical role in enhancing remanent polarization. The most promising results were obtained for multilayers with unit layers close to 1 nm, which approached the performance of homogeneous HZO while offering additional tunability through stacking sequence and interfacial configuration. Moreover, the importance of the initial and final layers in each stack was emphasized, as they significantly influenced wake-up behavior, texture formation, and polarization.

When comparing different compositions, the study demonstrated that the multilayer architecture is not only effective for 1:1 Hf:Zr systems, but can also enhance ferroelectric response in asymmetric compositions. The Hf-rich multilayer exhibited a significantly stronger wake-up effect compared to the solid-solution HZO 2:1, ultimately surpassing its polarization after cycling, suggesting a phase stabilization mechanism along cycling. For the Zr-rich composition, the multilayer delivered a much better performance, as the solid-solution HZO 1:2 starts with an almost negligible polarization and requires extensive cycling to exhibit ferroelectric behavior, whereas the multilayer form showed higher polarization, highlighting how stacking can effectively improve ferroelectric response. A similar trend was observed for dielectric breakdown, where both multilayers exhibited higher breakdown fields than the solid-solution compositions, suggesting that the presence of interfaces may hinder charge transport and potentially enhance electrical endurance.

At reduced thicknesses of 5 and 4 nm, the benefits of multilayer structuring became even more apparent. Solid-solution HZO films struggled to crystallize and exhibited limited ferroelectric response, especially at 4 nm. In contrast, multilayer structures facilitated crystallization and preserved electrical performance, though challenges remained, particularly high annealing temperature to crystallize the film and the lowest polarization. These results underline the multilayer approach as a viable strategy to push ferroelectricity toward sub-5 nm regimes, though further improvements are needed to balance electrical robustness with minimal leakage.

Benchmarking against state-of-the-art studies confirms that while the absolute polarization values obtained in this work are slightly lower than the best-reported results for 10 nm films, they are competitive for 6 nm systems and represent a significant advancement for 4 nm structures. Although the 500°C annealing used here is moderate compared to other studies, it remains relatively high for full BEOL integration. Overall, this research highlights the powerful role of multilayer design in enabling ferroelectric behavior at ultrathin dimensions and offers practical pathways to optimize these systems for future memory technologies.

Conclusion et perspectives

1 Discussion and conclusions

This thesis provided an in-depth investigation into ultrathin HfO_2-based ferroelectric structures, focusing on the development, fabrication, and optimization of these materials for potential application in non-volatile memory devices. By combining systematic material characterization and electrical testing with careful control over composition, structure, and processing, this work has contributed to valuable insights into how ferroelectricity can be stabilized and maintained at nanometric dimensions.

The first part of the study is dedicated to establishing the reference system of this thesis by demonstrating how the fabrication and characterization methodologies enable the development and analysis of ferroelectric HZO thin films. The manufacturing techniques, particularly atomic layer deposition (ALD), with its precise control over composition, thickness uniformity, and interface quality, made it possible to produce a well-defined ferroelectric system whose properties are consistent with those reported in the literature. Building on this foundation, the suite of characterization techniques employed in this work allowed us to probe the structural, electrical, and local-atomic mechanisms governing the behavior of this reference material.

This reference system consisted of 10 nm HZO films with a 1:1 Hf:Zr composition, used as a reference to investigate the influence of electrode configurations. It was shown that the top electrode affects ferroelectric performance. In particular, weaker TiN (002) crystalline orientation correlated with improved polarization and reduced wake-up. No clear correlation was found between global stress and material performance. These results provide initial insight into how electrode properties and mechanical conditions influence the behavior of the ferroelectric phase.

The second part of the thesis explored the role of composition and thickness scaling in single-layer HZO films. At 10 nm, the 50% Zr composition (1:1) exhibited the highest remanent polarization, confirming its effectiveness in stabilizing the orthorhombic ferroelectric phase. As the Zr content increased, stronger wake-up effects and antiferroelectric behavior were observed. Hf-rich films, although exhibiting lower polarization, showed more stable cycling behavior. When the thickness was reduced to 6 nm, 5 nm, and 4 nm, polarization decreased significantly, especially for the 1:1 composition, due to phase destabilization and the emergence of amorphous or non-polar phases. Among thinner films, particularly at 4 nm, the 33% Zr composition offered a better balance between crystallization and electrical performance.

In response to these scaling challenges, the third part of the thesis investigated HfO_2/ZrO_2 multilayers as an alternative structural approach. The results confirmed that multilayering, particularly with thinner unit layers, can improve polarization at ultrathin total thicknesses. Results showed that stacking order, unit layer thickness, and the choice of starting and ending layers had significant impact on polarization and wake-up behavior. Notably, Hf-rich (HZHZH with 1.2 nm of unit layer thickness) and Zr-rich (ZHZHZ with 1.2 nm of unit layer thickness) multilayers both outperformed their single-layer counterparts. This advantage was especially evident at 4 nm, where solid-solution HZO remained mostly amorphous or antiferroelectric, whereas multilayer stacks achieved measurable and relatively stable polarization after cycling.

Material characterization supported the electrical findings but also highlighted certain limitations. X-ray diffraction (XRD), while essential for confirming global crystallinity, showed limited sensitivity to subtle structural changes, particularly in ultrathin films. As a result, electrical measurements proved indispensable for evaluating ferroelectric behavior. The use of atomic layer deposition (ALD) was a key advantage throughout this work, enabling precise control over thickness and composition and allowing the fabrication of complex multilayer architectures.

Beyond the specific experimental findings, this work successfully addressed the core objectives defined at the outset of the thesis. The role of composition was systematically analyzed across a wide range of Hf:Zr ratios and thicknesses, confirming its dominant influence on phase stability and polarization. The impact of different top electrodes and annealing temperatures was also thoroughly explored, showing how they affect crystallization and stress. By directly comparing single-layer and multilayer structures, the study demonstrated that multilayers can enhance ferroelectric performance and crystallize at dimensions, particularly at 4 nm, where conventional films fail. Finally, the study advanced the understanding of ferroelectricity at reduced thickness, particularly in the 4–6 nm range, where trade-offs between scaling, crystallinity, and electrical behavior were evaluated.

In the context of the broader literature, the results obtained here are in agreement with prior reports that identify 50% Zr as the optimal composition for phase stabilization at 10 nm-thick, while also offering new insights into the behavior of asymmetric compositions and multilayer configurations. While some benchmark studies report higher polarization values for 10 nm films, often achieved through aggressive annealing or doping, this work achieves state of the art polarization for 6 nm multilayers (approximately 20–25 $\mu C/cm^2$ after wake-up) using moderate annealing conditions (500°C), a critical step toward BEOL integration. Furthermore, this thesis contributes to unique findings on 4 nm multilayer structures, an area scarcely explored in the literature, positioning this study at the forefront of ferroelectric scaling research.

In conclusion, this thesis demonstrates that composition engineering and stacking modulation via multilayers are effective strategies for enhancing ferroelectricity in ultrathin HfO_2-based devices. These findings lay a solid foundation for further process optimization and support the integration of ferroelectric materials into next-generation memory technologies.

2 Perspectives

Building on the findings of this work, several promising directions emerge for future research. First, the use of alternative organometallic precursors during ALD growth could be explored to study how precursor chemistry affects phase formation, crystallization dynamics, and overall ferroelectric performance. Different ligands or metal centers may influence film quality, defect concentration, and phase stability, potentially leading to improved uniformity and electrical reliability, particularly in ultrathin regimes.

Additionally, optimizing the electrode stack remains a key opportunity for enhancing ferroelectric device performance. The use of electrodes deposited via ALD could provide improved interface control, better conformality over high aspect ratio features, and enhanced compatibility with CMOS processes. Exploring the effects of different electrode materials, not only in terms of their mechanical stress and texture, but also their chemical reactivity with the HZO layer, could lead to significant gains in both polarization and endurance.

A particularly critical area for future study is the role of the bottom electrode in influencing the initial nucleation and crystallization of the HZO layer. Since the early stages of growth often dictate phase orientation and stability, understanding how bottom electrode material, crystallinity, and surface energy affect the formation of the orthorhombic phase could unlock new strategies for performance optimization, especially in sub-5 nm films, where these effects are magnified.

Future work should also investigate alternative annealing approaches to meet the stringent thermal budgets of BEOL integration. Ultrafast annealing techniques such as laser annealing or rapid thermal annealing (RTA) could offer lower thermal exposure while still enabling sufficient crystallization of the ferroelectric phase. This would be especially valuable for maintaining material integrity in scaled devices and for integrating ferroelectric layers in more advanced process flows.

Furthermore, the interpretation of EXAFS and GIWAXS results remains ongoing, particularly with the aim of understanding the structural mechanisms underlying the wake-up effect observed in electrical measurements. These synchrotron-based techniques have already shown preliminary evidence of phase evolution during early cycling, but more detailed analysis is necessary to fully elucidate the role of disorder, local structure, and phase transition dynamics in ferroelectric behavior.

Another promising research avenue involves exploring the antiferroelectric nature of certain HfO_2-based layers, particularly in Zr-rich compositions. Given their double hysteresis loops and field-dependent polarization behavior, these materials could be suitable for emerging memory applications beyond conventional FeRAM, such as energy-efficient capacitive devices. Investigating their switching characteristics, stability, and integration potential could open new functional opportunities in device engineering.

Finally, the compatibility of these materials and architectures with 3D memory structures represents an exciting research direction. Given the conformal nature of ALD and the potential scalability of HZO-based ferroelectrics, implementing these films in vertical capacitor stacks

or gate-all-around transistor configurations could lead to new forms of high-density, low-power, non-volatile memories. Understanding how factors like stress, leakage, and phase stability evolve in such 3D geometries will be essential for bringing this class of materials closer to industrial adoption.

In summary, this thesis lays a solid foundation for the integration of ultrathin HfO_2-based ferroelectrics, and the proposed future directions offer both practical and forward-looking strategies to advance this field. From material innovation to structural design and process integration, these perspectives aim to support the development of reliable, scalable, and high-performance ferroelectric memory technologies for future generations of computing.

Appendices

1 Spectroscopic Ellipsometry

Spectroscopic ellipsometry allows to measure the optical constants (refractive index n and extinction coefficient k) and the thickness of a thin film. It is an indirect technique because, to retrieve this information, ellipsometry data must be modelled.

A linearly polarized light is sent on the thin film. The polarization of a wave can be decomposed into two orthogonal contributions: one oriented parallel to the plane of incidence, called *p-polarization*, and the other oriented perpendicular to the plane of incidence, called *s-polarization*. When a linearly polarized incident light (for both p- and s-components) is sent on a sample, the reflected light undergoes a change in polarization [175, 176].

The ellipsometry technique measures this polarization change, in particular the ratio ρ between the reflection coefficients r of the two polarization components (r_s for s-polarization and r_p for p-polarization):

$$\rho = \frac{r_p}{r_s} = \tan\Psi \cdot e^{j\Delta} \tag{1}$$

where $\tan\Psi$ corresponds to the ratio of the moduli of the reflection coefficients, and Δ is the phase shift introduced by the reflection between the two polarization components.

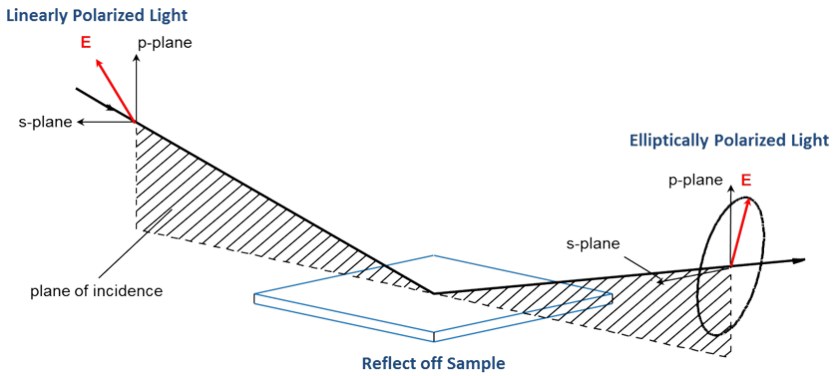

Figure 21: Schematic representation of spectroscopic ellipsometry, where a linearly polarized light is decomposed into s- and p-components, and after reflection the polarization becomes elliptical, described by Ψ and Δ [177].

The reflection coefficients r_s and r_p depend on the optical constants of the materials on which the reflection takes place, namely the refractive index (n) and the extinction coefficient (k). Knowing the amplitude ratio Ψ and the phase difference Δ (also called ellipsometric angles)

as a function of the wavelength of the incident light allows one to determine the optical constants and the thickness of the film by modelling.

Using the Atlas® XP+ equipment, thickness of $Hf_{0.5}Zr_{0.5}O_2$ (HZO) films is determined by fitting optical data (typically reflectance or ellipsometry spectra) with a multilayer model. The stack includes the Si substrate with a native SiO_2 layer of approximately 7 Å, the HZO film, and optionally a surface roughness or interface layer. For this study, the optical dispersion of HZO was described using the Bruggeman effective medium approximation (EMA), which treats the material as an effective mixture of HfO_2 and ZrO_2 optical responses. The fitting algorithm then adjusts film thickness, roughness, and composition fractions until the simulated optical response matches the measured data.

As the composition and structure of the ferroelectric layer were systematically varied in this work, ranging from solid solution HZO films to multilayer configurations, the optical models required for ellipsometry fitting become increasingly complex and difficult to constrain reliably. Each structural variation would demand distinct assumptions for dispersion functions, interface layers, or effective medium approximations, introducing a high degree of uncertainty in the extracted thickness values. For this reason, X-ray reflectometry (XRR) was preferred as the primary technique to estimate film thickness, providing a more direct and composition-independent measurement.

2 EDX-based chemical composition analysis throughout the fabrication of 10 nm HZO films

EDX elemental maps acquired at three key stages, **Fig. 22 a**s-deposited, **Fig. 23 a**fter top electrode deposition, and **Fig. 24 a**fter annealing, show that the Hf, Zr, and O elements are homogeneously distributed across the 10 nm HZO film. This indicates the formation of a solid solution rather than phase separation into distinct HfO_x and ZrO_x regions.

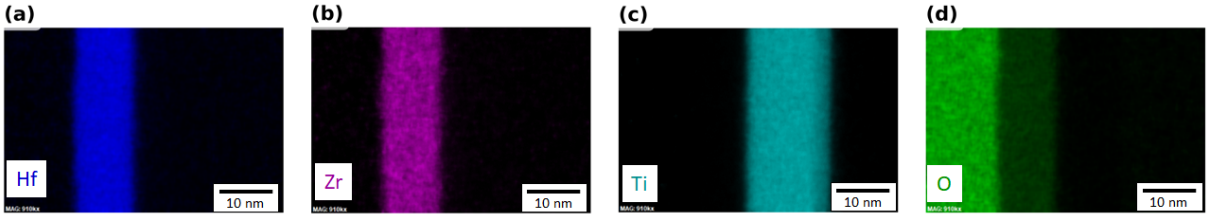

Figure 22: Energy-dispersive X-ray spectroscopy (EDX) elemental map of a 10 nm HZO as-deposited thin film confirming the uniform distribution of **a.** Hf (blue), **b.** Zr (violet), **c.** Ti (cyan) and **d.** O (green).

The Ti signal, corresponding to the TiN electrode, remains well confined to the interfaces and shows no significant diffusion into the ferroelectric layer under any of the conditions, confirming interface stability. The oxygen map also remains uniform in intensity across all process steps, suggesting consistent oxidation of the film. These observations are further supported by the EDX depth profiles, which reveal stable elemental distributions across the film thickness before and

after annealing, confirming the compositional homogeneity of the stack throughout processing.

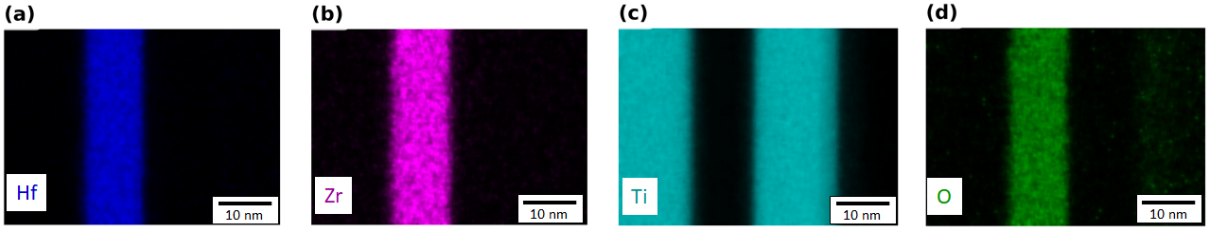

Figure 23: Energy-dispersive X-ray spectroscopy (EDX) elemental map of a 10 nm HZO thin film after top electrode deposition confirming the uniform distribution of **a.** Hf (blue), **b.** Zr (violet), **c.** Ti (cyan) and **d.** O (green). The uniform elemental distribution indicates a well-mixed HZO layer with no significant phase segregation.

However, the possible formation of a thin interfacial TiO_xN_y layer cannot be excluded, particularly after annealing, due to the known oxygen-scavenging behavior of TiN. While no clear intermixing is detected, the spatial resolution of cross-sectional EDX may not be sufficient to resolve ultrathin interfacial modifications at the atomic scale.

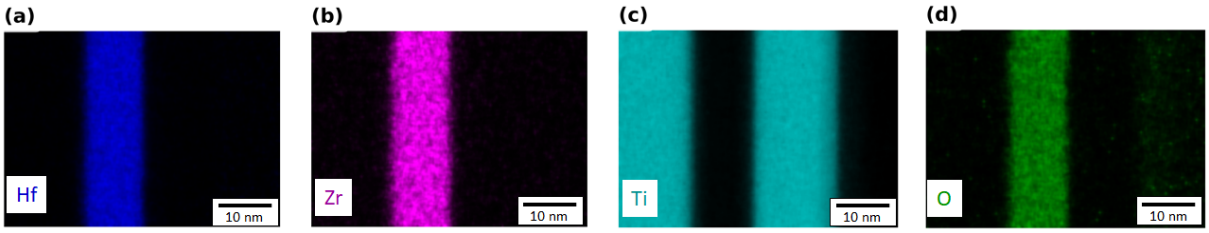

Figure 24: EDX elemental map confirming the uniform distribution of **b.** Hf (blue), **c.** Zr (violet), **c.** Ti (cyan) and **d.** O (green) with TiN as the bottom and top electrode after 400°C anneal for 1 hour.

3 ToF-SIMS profiling of 10 nm HZO with TiN top electrode

The 10 nm HZO film, capped with a 50 nm TiN top electrode deposited by PVD, underwent furnace annealing at 400°C for 1 hour to promote crystallization. After annealing, ToF-SIMS analysis was carried out (**Fig. 25)** to assess the elemental depth distribution within the HZO layer. The use of a 50 nm TiN top electrode served to facilitate abrasion during depth profiling.

The resulting depth profile reveals clear signals for Hf, Zr, and O-related ions throughout the film. Notably, a Cs_2Cl^- signal is observed across the entire thickness, confirming the presence of chlorine originating from the ALD precursors, as discussed previously. Carbon-related ions show a slight decrease compared to the as-deposited sample (Chapter 3 Section 2.1 and **Fig. 3.5)**, likely due to the removal of surface organic contaminants during the annealing process.

The analysis does not allow for a definitive observation of interfacial diffusion between the HZO layer and the TiN electrodes, but such interactions cannot be ruled out, particularly at the upper interface, given the known oxygen-scavenging behavior of TiN.

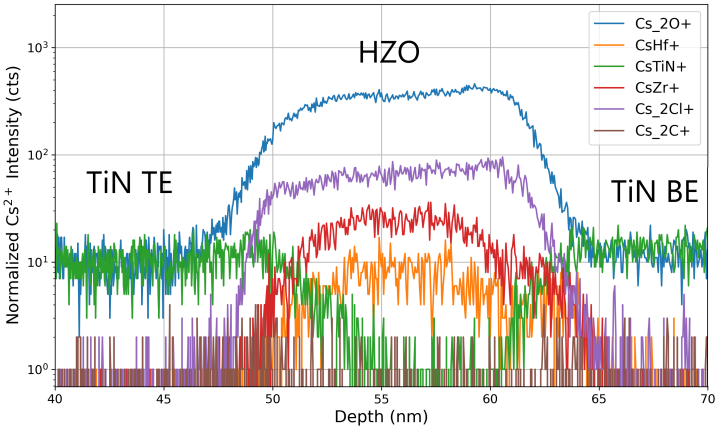

Figure 25: Depth-resolved ToF-SIMS analysis of a 10 nm HZO film with a top electrode after annealing at 400°C for 1 hour. The graph illustrates the normalized Cs^{2+}-based secondary ion intensities for key elements and species, where BE refers to the bottom electrode and TE to the top electrode.

4 Fine characterization of 10 nm HZO: investigating wake-up mechanisms

The ferroelectric behavior of HZO thin films is closely linked to their crystalline phase composition. While the orthorhombic ($Pca2_1$) phase enables ferroelectricity, it is not thermodynamically stable in bulk at room temperature [52]. Stabilizing this phase through compositional and structural engineering is therefore a key goal in hafnia-based ferroelectric research.

One common phenomenon in HZO capacitors is the wake-up effect, where remanent polarization increases during early electrical cycling [178, 179]. Its origin remains under debate, with proposed mechanisms including oxygen vacancy redistribution, phase transitions from monoclinic or tetragonal to orthorhombic, and stress relaxation [74, 76]. Some studies suggest that charged oxygen vacancies migrate under electric field, facilitating domain switching or phase transitions, especially near interfaces [77, 180, 181].

Standard techniques like XRD often struggle to distinguish between orthorhombic and tetragonal phases due to overlapping peaks. To overcome this, this study uses synchrotron-based grazing-incidence wide-angle X-ray scattering (GIWAXS) and extended X-ray absorption fine structure (EXAFS). EXAFS provides local, element-specific information on atomic coordination, making it useful for identifying subtle structural changes. For instance, the orthorhombic phase features seven-fold Hf–O coordination, while the tetragonal phase shows distinct short and long Hf–O bonds [182].

The samples analyzed in the synchrotron experiments were manufactured following the process described in Section 4.1, using similar fabrication steps to those of the 300 mm wafers to ensure comparability.

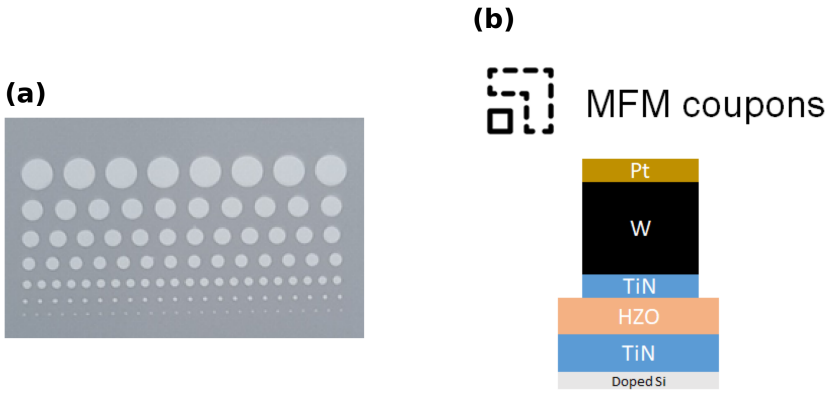

Figure 26: a. PTA photolithography mask layout used to pattern the FE stack to realize MFM capacitors. The capacitors analyzed in this study correspond to the 100 µm diameter structures, located in the last row of the mask shown in the image. **b.** Sketches of the tested MFM coupons strucutres

4.1 MFM coupons

MFM coupons were derived from previously fabricated 300 mm wafers to facilitate tests that required smaller sample formats, as shown in **Fig. 26**b. This approach enabled more flexible and efficient experimental workflows while preserving the integrity and relevance of the integration process.

The BE was made of Ti/TiN (5 nm/10 nm) deposited on Si substrates by PVD. The deposition of the HfO_2-based FE film was made by ALD at 300°C. Before the deposition of the top electrode, a cleavage step was performed on the 300 mm wafer, allowing the acquisition of smaller samples. On top of 10 nm-thick TiN TE, 70 nm-thick W layers was deposited by CVD and SSP.

Following the deposition of the top electrode, the samples were further cut into smaller pieces ($\sim 2 \times 2$ cm^2) before annealing. The samples underwent annealing under the same conditions and equipment as the 300 mm wafers. From this stage, the integration processes continued on the PTA platform (Upstream Technological Platform).

A positive-negative photoresist was spin-coated on the annealed cleaved MFM coupon prepared in the cleanroom environment of CEA-Leti. Circular patterns with a diameter of 100 µm were then defined by photolithography, corresponding to the final capacitor layout.

Subsequently, a 10 nm platinum layer was deposited via evaporation across the entire surface of the sample. A lift-off process in an acetone bath followed by isopropanol enabled the formation of Pt plots, with the mask displayed in **Fig. 26**a.

Finally, coupled plasma reactive ion etching (ICP-RIE) with SF_6 gas was performed to etch the top electrode. For ICP, the etching plasma power source had 100 W and the bias power was set at 30 W. The gas flow rate was set to 50 sccm for SF_6, while mantaining a chamber pressure of 1.3 Pa. The reactor used for this process was a PLASMALAB100 from Oxford.

4.2 Grazing incident wide angle X-ray scattering

GIWAXS using a synchrotron source is a powerful technique to probe the structural properties of thin films with nanometric sensitivity. In this method, a highly collimated and intense synchrotron X-ray beam is directed at a shallow incident angle relative to the sample surface, enhancing surface sensitivity and enabling the detection of weak diffraction signals from ultra-thin layers. The wide-angle configuration captures scattering from a broad range of in-plane and out-of-plane lattice spacings, allowing the identification of crystalline phases, texture, and preferential orientation. The use of a synchrotron source significantly improves signal-to-noise ratio and angular resolution, which is essential for distinguishing subtle structural features.

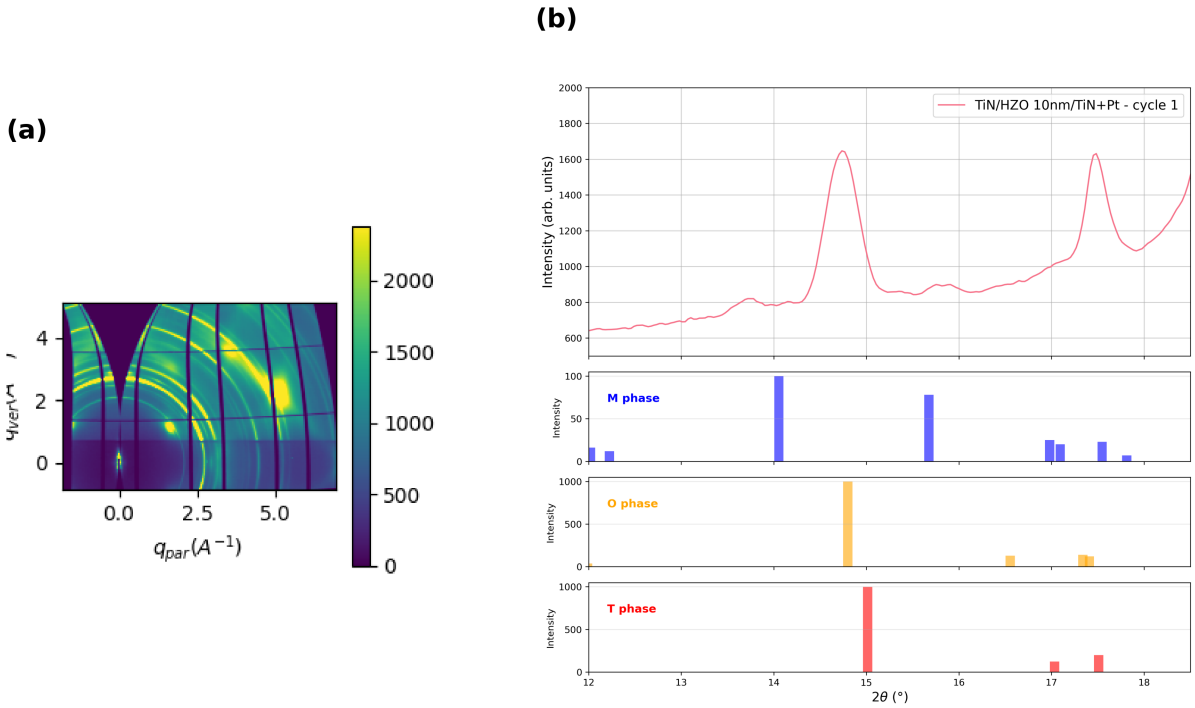

Figure 27: a. Out-of-plane GIWAXS reciprocal space map of a TiN (15 nm) bottom electrode / HZO (10 nm) / TiN (50 nm) + Pt (20 nm) top electrode stack, measured after annealing at 400°C for 1 hour and following one electrical cycling. **b.** Corresponding integrated diffraction profile showing the experimental curve (top) along with reference diffraction patterns for monoclinic (M, blue), orthorhombic (O, orange), and tetragonal (T, red) phases.

This technique is particularly relevant for thin films of $Hf_{0.5}Zr_{0.5}O_2$, where conventional XRD is often insufficient to clearly resolve the different non-centrosymmetric phases. Due to the close similarity of the crystallographic patterns associated with orthorhombic, tetragonal, and cubic phases, conventional θ–2θ scans may not provide unambiguous phase identification. GIWAXS, with its enhanced angular resolution and surface sensitivity, enables a more comprehensive mapping of reciprocal space, offering additional insight into the phase composition and crystallographic orientation of HZO thin films, critical factors that directly influence their ferroelectric behavior.

In this study, GIWAXS measurements were performed at the Soft Matter Interface beamline

at the National Synchrotron Light Source II (NSLS-II) to investigate both in-plane and out-of-plane structural characteristics of the HZO thin films. The 2D images were collected on a Pilatus 900K-W detector, with a pixel size of 172 µm placed at 279 mm from the sample. The incident angle was 5.0° and an X-ray energy of 16.10 keV. Sector averaging were done from -20 to 20° around the vertical direction and horizontal direction for the out-of-plane and in-plane analysis respectively, allowing the assessment of grain orientation and texturing. These combined configurations enabled a comprehensive investigation of phase distribution and anisotropy, complementing conventional XRD and offering a more accurate understanding of the structural landscape in ultrathin HZO films (**Fig. 28**).

This research used the Soft Matter Interfaces (SMI) beamline (Beamline 12-ID) of the National Synchrotron Light Source II, a U.S. Department of Energy (DOE) Office of Science User Facility operated for the DOE Office of Science by Brookhaven National Laboratory under contract no. DE-SC0012704.

The measurements were conducted at the NSLS-II SMI beamline using synchrotron radiation with an X-ray energy of 16.10 keV, corresponding to a wavelength of 0.770 Å (calculated using $\lambda = 12.398/E$, with E in keV). Compared to conventional lab-based XRD (Cu Kα, 1.54 Å), this shorter wavelength results in the same lattice spacings being observed at lower 2θ values. An incidence angle of 5° was used, and the beam footprint was approximately $20 \times 25\,\mu m^2$, enabling localized probing of the film area.

4.3 Crystallinity results via GIWAXS measurements

Fig. 28 presents GIWAXS diffractograms acquired in vertical geometry, predominantly probing the out-of-plane crystallographic orientation of the films. The data correspond to the 10 nm HZO capacitors described earlier, measured after 1 PUND cycle and after 10^5 PUND cycles.

The detected patterns reveal structural evolution in the HZO solid solution during electrical cycling. In the sample measured after Cycle 1, diffraction features attributed to the monoclinic (m) phase are visible at around 14° and 15.7°, consistent with known reflections of this non-ferroelectric phase. After 10^5 cycles, these monoclinic features are no longer detectable, indicating a suppression of the monoclinic component. Additionally, the main diffraction peak near 15° shifts slightly toward lower 2θ values, which may reflect changes in lattice strain or phase composition. Since the orthorhombic phase typically exhibits peaks at lower angles than the tetragonal phase, this evolution supports an increased contribution of the ferroelectric orthorhombic phase following wake-up.

4.4 Extended X-ray absorption fine structure

Extended X-ray Absorption Fine Structure (EXAFS) is a technique within the broader field of X-ray absorption spectroscopy (XAS), which also includes X-ray Absorption Near Edge Structure (XANES). EXAFS focuses on the oscillatory part of the absorption spectrum beyond the absorption edge. These oscillations arise from the interaction of the ejected photoelectron with neighboring atoms, as illustrated in **Fig. 29**a, making EXAFS particularly sensitive to the local

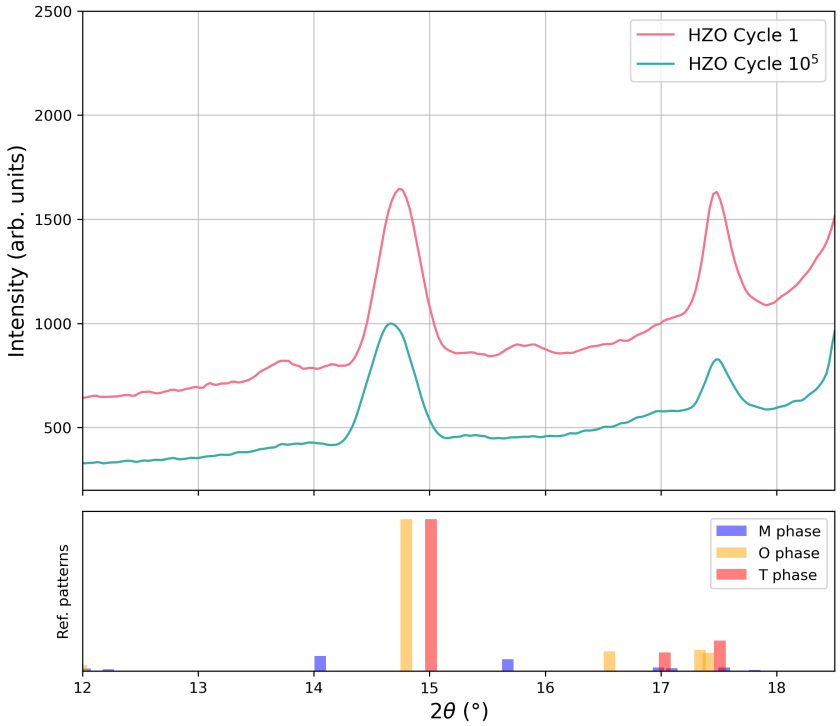

Figure 28: Out-of-plane grazing-incidence wide-angle X-ray scattering (GIWAXS) patterns of HZO solid solution capacitors after 1 and 10^5 electrical cycles. Below each diffraction profile, reference peak positions for the monoclinic (m), orthorhombic (o), and tetragonal (t) phases are shown, based on JCPDS files 00-034-0104 (m), 04-005-5597 (o), and 04-011-8820 (t), respectively.

atomic environment. By analyzing these oscillations, EXAFS provides detailed insights into the geometric structure around a specific atom within a material.

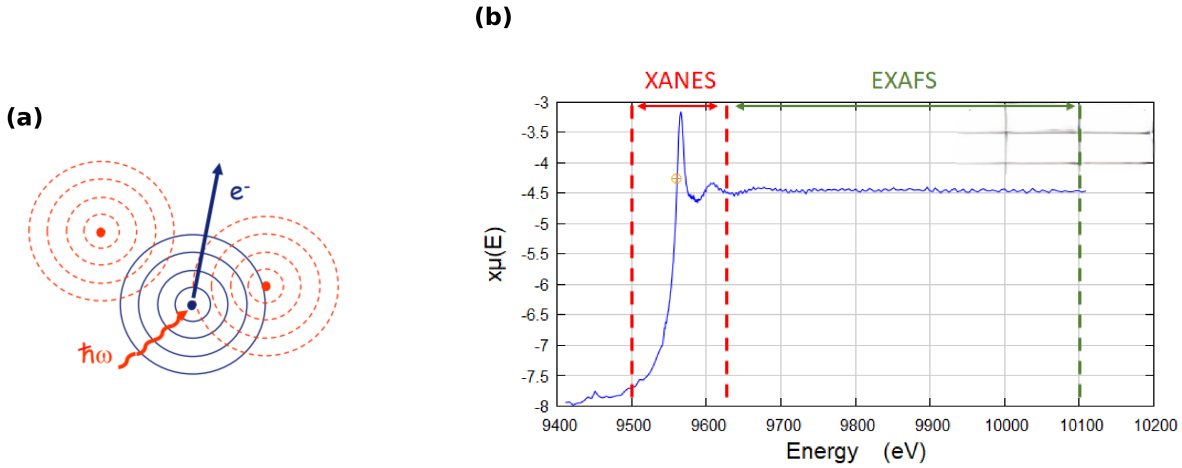

Figure 29: a. Photoelectron scattering process. **b.** EXAFS spectra of HZO cycled capacitor in the energy range of Hf L-edge.

EXAFS is widely used to study coordination numbers, the disorder of neighboring atoms, and the radial distance between an atom and its neighbors. Among these properties, the radial

distance is the most reliably measured, achieving theoretical accuracy to within ~ 0.02 Å under ideal conditions. This precision is critical for structural analysis, particularly in crystalline or well-ordered systems. In practice, the accuracy of EXAFS measurements improves in materials with low thermal or static disorder, as these conditions reduce noise in the oscillatory signals.

X-ray spectroscopy involves the interaction of X-rays with atoms, leading to the ejection of a core electron when the X-ray energy exceeds the electron's ionization energy. This process creates a vacancy in the core shell, followed by the relaxation of an outer electron to fill the vacancy. The probability of this interaction is described by the X-ray absorption coefficient, μ, which relates the intensity of an X-ray beam before and after passing through a material [183]. According to Beer's Law, it is expressed as:

$$I = I_0 e^{-\mu t} \tag{2}$$

where I_0 is the incident X-ray intensity, I is the transmitted intensity, t is the sample thickness. Peaks in the absorption spectrum, called edges, correspond to the ionization of specific core orbitals, such as K-edges for the 1s orbital and L-edges or M-edges for higher orbitals. These edges, unique to each element, serve as a basis for EXAFS analysis.

Beyond the absorption edge, the EXAFS region begins with oscillations in the absorption coefficient, driven by wave interactions between the ejected photoelectron and surrounding atom [184]. These oscillations are described by the function $\chi(k)$, which captures the fine structure of the absorption signal:

$$\chi(k) = \frac{\mu(k) - \mu_0(k)}{\mu_0(k)} \tag{3}$$

Here, $\mu(k)$ is the measured absorption coefficient, $\mu_0(k)$ is the smooth background absorption due to the isolated atom, and k is the wavevector of the ejected photoelectron, defined as:

$$k = \sqrt{\frac{2m_e}{\hbar^2}(E - E_0)} \tag{4}$$

where E is the photon energy, E_0 is the absorption edge energy, m_e is the electron mass, and $\hbar$ is the reduced Planck constant. These oscillations, characteristic of the absorbing atom's local environment, depend on the distances to neighboring atoms, their type, and the disorder in their arrangement.

The physical description of all these properties is encapsulated in the EXAFS equation, which models $\chi(k)$ as a sum of contributions from each shell of neighboring atoms:

$$\chi(k) = \sum_j \frac{N_j f_j(k) e^{-2k^2\sigma_j^2} e^{-2R_j/\lambda(k)}}{kR_j^2} \sin\left[2kR_j + \delta_j(k)\right] \tag{5}$$

In this equation, N_j represents the coordination number of the j-th shell, indicating the number of neighboring atoms, while R_j is the radial distance to that shell. The term $f_j(k)$ corresponds to the scattering amplitude of the photoelectron due to neighboring atoms, and σ_j^2 is the Debye-Waller factor, which accounts for both thermal and static disorder in the system.

$\lambda(k)$ denotes the mean free path of the photoelectron, and $\delta_j(k)$ represents the phase shift experienced by the photoelectron as a result of scattering. This phase shift results not only from the scattering by neighboring atoms but also from the photoelectron's passage through the electron cloud of the absorber atom itself. Together, these parameters describe how the photoelectron wave interacts with the surrounding atomic structure, enabling detailed analysis of the local environment.

An example of an EXAFS spectrum obtained at the Hf L_3-edge from a cycled HZO capacitor is presented in **Fig. 29**b, revealing oscillatory features that reflect the local bonding environment around Hf atoms. This analysis enables the extraction of structural parameters such as bond lengths, coordination, and disorder, making EXAFS a powerful tool in material characterization.

XAS measurements were performed at the LISA beamline (BM08) of the European Synchrotron Radiation Facility (ESRF) on 10-nm-thick HZO thin films. XAS data were collected at the Hf-L_3 (E = 9561 eV) and Zr-K (E = 17998 eV) absorption edges using a liquid-nitrogen-cooled Si(111) monochromator and vertically focusing Pd-coated mirrors. Fluorescence signals were recorded using either a 12-element energy-resolving high-purity Ge detector or a Si photodiode.

4.5 Local atomic environment analysis via EXAFS

EXAFS spectroscopy was performed to investigate the local structural evolution of the ferroelectric layer during the wake-up process. Measurements were conducted at the Hf and Zr L3 and K-edges for samples collected after ALD deposition (amorphous according to XRD), full sheet film after complete MFM stack fabrication and annealing and finally after electrical cycling at 1, 10, 10^3 and 10^5 cycles. The goal was to correlate changes in local atomic structure with the ferroelectric behavior and identify phase transformations occurring during cycling. The complete list and description of analyzed samples are summarized in **Table 5**.

Table 5: Description of EXAFS samples analyzed.

Sample #	Description
1	After ALD deposition (amorphous film)
2	Full MFM stack after annealing, prior to lithography (no defined capacitors)
3	After 1 cycle (PUND) on 100 µm capacitor
4	After 10 cycles on 100 µm capacitor
5	After 10^3 cycles on 100 µm capacitor
6	After 10^5 cycles on 100 µm capacitor

Among the measured spectra, the most noticeable structural changes were observed between Samples 3 and 4, corresponding to 1 and 10 electrical cycles, respectively. The k^2-weighted EXAFS signals in **Fig. 30 s**how a marked evolution in oscillation amplitude and frequency between these two conditions, particularly from approximately 6 $Å^{-1}$ onward. This suggests significant atomic rearrangement during early cycling. After 10 cycles, however, the spectra appear to stabilize, with only minor changes observed up to 10^5 cycles (Sample 6). This indicates

that the most substantial reorganization of the local structure occurs within the first few cycles, consistent with the electrical wake-up behavior.

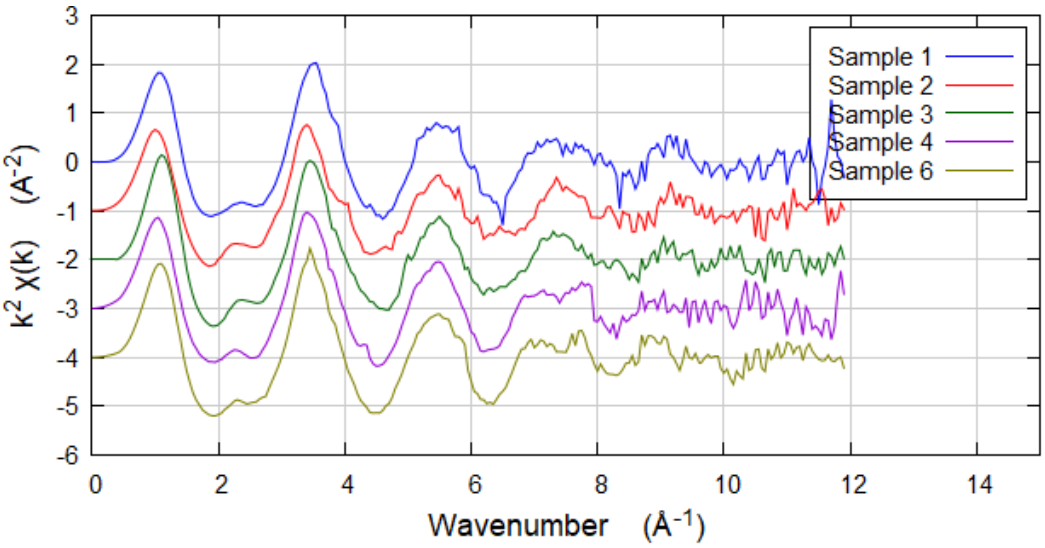

Figure 30: k^2-weighted EXAFS spectra at the Hf L_3-edge for samples 1, 2, 3, 4, and 6. The oscillatory behavior reflects differences in the local structural environment, suggesting variations in short- and long-range order among the samples, with the most prominent variation occurring between samples 3 and 4.

It is important to note that this is a preliminary analysis based on the Hf L_3-edge spectra. Further data processing, including quantitative fitting and linear combination analysis, is required to determine the relative phase fractions in each cycled sample and confirm the nature of the structural transitions.

5 Effect of etching sequence on ferroelectric response

To assess the potential influence of processing sequence on ferroelectric performance, we investigated whether performing the etching step before or after annealing affects the polarization behavior of HZO-based capacitors.

This experiment was carried out using 10 nm-thick HZO capacitors with a Ti/TiN (15 nm) bottom electrode and a 60 nm TiN top electrode deposited by PVD using a DC-only generator. All samples were annealed at 400°C for 1 hour in N_2 ambient. Two process flows were compared: in the first, the etching step was performed before annealing, while in the second, the etching was done after annealing.

Polarization loops were recorded, and both configurations exhibited nearly identical initial $2P_R$ values and wake-up behaviors over cycling (**Fig. 31)**. Despite the stress relaxation observed after annealing, no significant difference in ferroelectric performance was detected between the two process sequences. This result supports the conclusion that global stress plays a limited role in determining polarization at this stage, although localized interfacial stress effects cannot be ruled out.

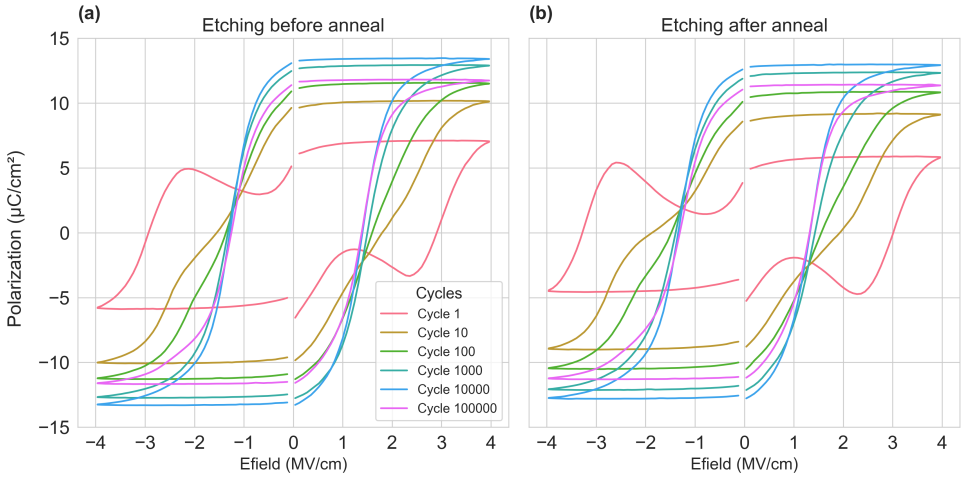

Figure 31: P–E loops of HZO 10 nm 1:1 samples for different process sequences: **a.** etching before annealing and **b.** etching after annealing at 400°C for 1 h. Both configurations show nearly identical ferroelectric behavior and wake-up effect across all measured cycles.

6 XRR analysis of 6 nm multilayer structures

Fig. 32 presents the XRR experimental data and corresponding fit curves for six multilayer structures with a total thickness of 6 nm, deposited on TiN bottom electrodes. The samples vary in unit layer thickness (1.5 nm, 1.0 nm, and 0.85 nm) and stacking sequence, with half of the configurations starting with HfO_2 layers (top row, panels a–c) and the others with ZrO_2 (bottom row, panels d–f).

The goal of this analysis was to estimate individual layer thicknesses and confirm the presence of a multilayer architecture. The successful observation of well-defined interference fringes in all configurations, especially visible in samples with higher periodicity, confirms the formation of a layered structure. Despite the visual confirmation, fitting these curves was particularly complex due to the number of sublayers, interface roughness, and potential variations in local density.

This figure complements **Table 5.2**, which lists the fitted thicknesses of individual HfO_2 and ZrO_2 sublayers, as well as the Ti/TiN electrode layers, highlighting the modeling effort required for multilayer systems.

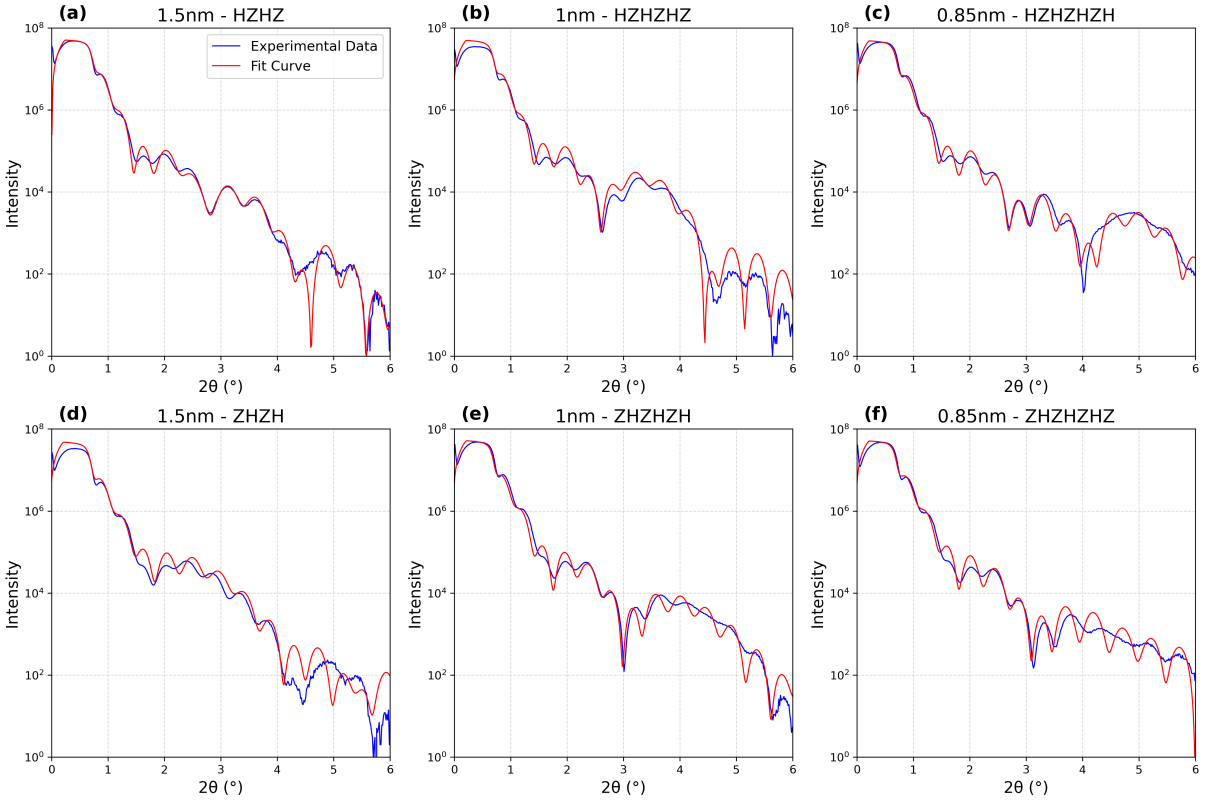

Figure 32: XRR experimental data (blue) and corresponding fit curves (red) for six different as deposited multilayer structures on TiN bottom electrode. **a** to **c** corresponds to structures starting with HfO_2-starting layers, while the bottom row **d** to **f** starts with ZrO_2 layers. From left to right, the unit layer thickness decreases from 1.5 nm to 1 nm and finally 0.85 nm.

7 XRR analysis of 6 nm multilayer structures with different compositions

Fig. 33 shows the XRR experimental data and corresponding fit curves for two multilayer structures with a total thickness of 6 nm and a targeted unit layer thickness of approximately 1.2 nm. Both samples consist of five alternating HfO_2 and ZrO_2 layers, differing only in stacking sequence: the configuration in panel (a) begins and ends with HfO_2, while the configuration in panel (b) begins and ends with ZrO_2.

While the fits capture the general fringe periodicity of the experimental data, noticeable deviations remain. These discrepancies highlight the complexity of accurately modeling such multilayer systems, where factors like interfacial roughness, density variations, and local layer non-uniformity are difficult to fully account for. Nevertheless, the analysis confirms the presence of a periodic structure and the extracted thickness values summarized in **Table 5.3**.

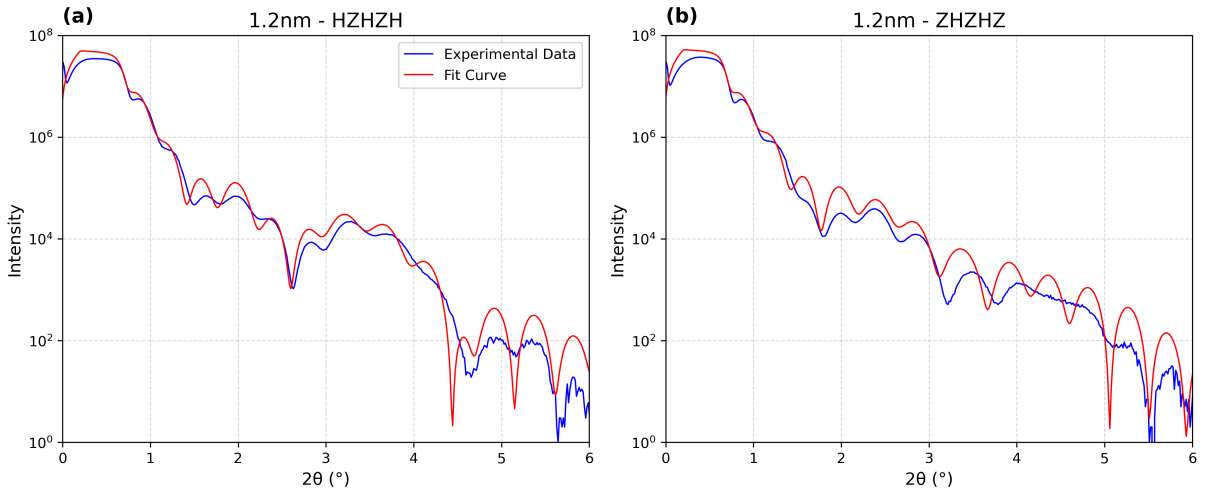

Figure 33: XRR experimental data (blue) and corresponding fit curves (red) for six different as deposited multilayer structures on TiN bottom electrode for **a.** H/Z/H/Z/H configuration and **b.** Z/H/Z/H/Z configuration.

8 XRR analysis of ultra-thin multilayers

Fig. 34 presents the XRR experimental data and fitted curves for two ultrathin multilayer structures with total thicknesses of 5 nm and 4 nm. These stacks consist of alternating HfO_2 and ZrO_2 layers with targeted unit thicknesses of 1 nm/1 nm and 1 nm/0.5 nm, respectively. The samples were deposited on Ti/TiN bottom electrodes.

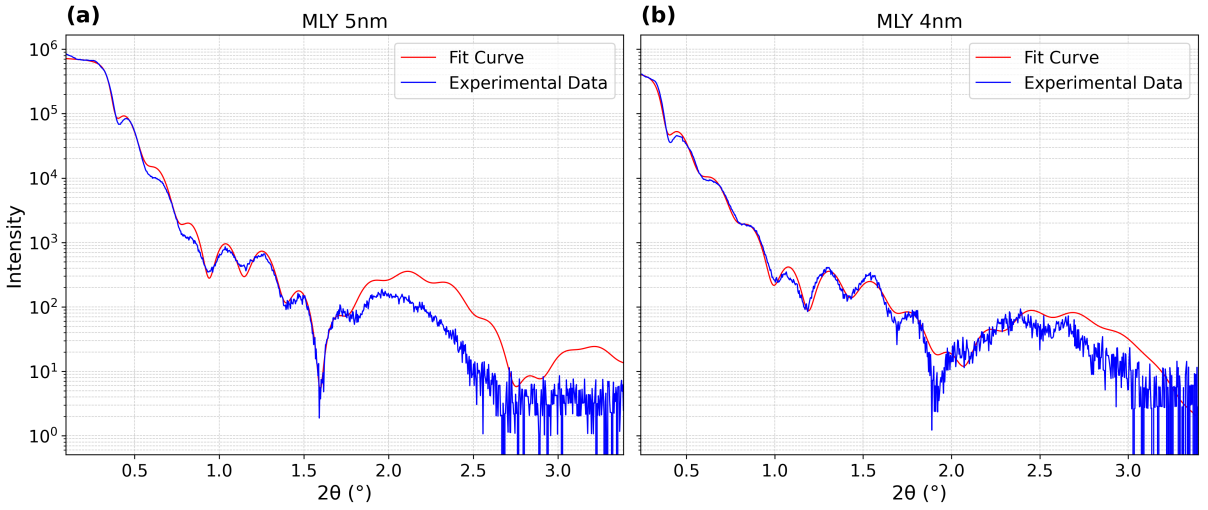

Figure 34: XRR results of as-deposited multilayer (MLY) structures. **a.** MLY 5 nm with a HfO_2 (1 nm) /ZrO_2 (1 nm) /H/Z/H stack and **b.** MLY 4 nm with a HfO_2 (1 nm) /ZrO_2 (0.5 nm) /H/Z/H stack, both deposited on a 15 nm TiN bottom electrode.

While the fits reproduce the general fringe periodicity observed in the experimental data, deviations remain, reflecting the complexity of modeling ultrathin multilayers. Challenges include limited contrast between HfO_2 and ZrO_2, possible intermixing at interfaces, and surface

roughness effects. Despite these limitations, the data confirm the presence of periodic multilayer structures and support the extracted thickness values shown in **Table 5.4**.

Texte de synthèse en français

9 Contexte et opportunités des matériaux ferroélectriques à base d'oxyde d'hafnium

À mesure que l'informatique progresse, la limite dite du mur de la mémoire devient un obstacle majeur : la taille et la complexité des modèles d'intelligence artificielle (IA) et d'apprentissage automatique croissent beaucoup plus vite que les capacités des mémoires actuelles. Le calcul massif, les systèmes autonomes et l'Internet des objets exigent des dispositifs de stockage et de traitement de données toujours plus rapides et économes en énergie.

Or, les mémoires traditionnelles atteignent leurs limites. Les mémoires volatiles comme la SRAM et la DRAM nécessitent une alimentation constante, engendrant une forte consommation d'énergie, tandis que la mémoire flash, bien que non volatile, présente des vitesses d'accès plus lentes et une endurance limitée. Toutes rencontrent des difficultés de miniaturisation liées aux fuites électriques, à la variabilité et à la fiabilité. Ces contraintes ont conduit à l'exploration de nouvelles mémoires dites émergentes, capables d'allier vitesse, non-volatilité et faible consommation énergétique.

Parmi elles, les oxydes à base d'hafnium (HfO_2), "dopés" notamment avec du zirconium, se distinguent par leur compatibilité avec les procédés de fabrication du silicium et leur capacité à devenir ferroélectriques à très faible épaisseur. Cette propriété repose sur la stabilisation d'une phase orthorhombique non centro-symétrique, qui confère une polarisation même en l'absence de champ électrique. Déposées par couches atomiques successives, ces structures offrent une maîtrise nanométrique de l'épaisseur et une excellente homogénéité, indispensables pour les dispositifs intégrés.

Les condensateurs métal–ferroélectrique–métal (MFM) constitués de ces films ouvrent la voie à des mémoires non volatiles rapides et sobres en énergie. Cependant, plusieurs défis persistent : la compréhension et le contrôle des phénomènes internes (comme l'évolution de la polarisation au cours des cycles, la dérive du champ interne et la fatigue), l'influence des interfaces électrode/oxyde, ainsi que la réduction de l'épaisseur du film tout en maintenant des propriétés ferroélectriques stables.

La réduction de l'épaisseur constitue un levier essentiel pour abaisser la tension de commutation et améliorer la durabilité des dispositifs, mais elle rend la cristallisation plus complexe. Les électrodes jouent aussi un rôle clé, car leur nature (par exemple le nitrure de titane ou le tungstène) modifie la contrainte mécanique, la chimie interfaciale et la compensation des charges de polarisation.

Dans ce contexte, ce travail de recherche vise à développer et à comprendre le comportement de couches ferroélectriques ultraminces à base d'oxyde d'hafnium intégrées dans des condensateurs MFM. Il s'agit d'étudier l'influence de la composition, des électrodes, de la structure en multicouches et de la réduction d'épaisseur sur les propriétés structurales et électriques, afin d'identifier les conditions permettant de maximiser la ferroélectricité.

En outre, cette étude contribue à mieux comprendre les mécanismes qui influencent la ferroélectricité dans les oxydes d'hafnium ultraminces et à évaluer leur potentiel pour surmonter les limites énergétiques et technologiques des mémoires actuelles.

10 Dépôt par ALD des couches ferroélectriques à base d'HfO_2 et ZrO_2

Le dépôt par couches atomiques, ou Atomic Layer Deposition (ALD), est une technique de dépôt en phase vapeur reposant sur des réactions chimiques auto-limitantes à la surface du substrat. Les précurseurs gazeux sont introduits de manière séquentielle : chacun réagit uniquement avec la surface active et non avec lui-même, permettant ainsi la formation d'une seule couche atomique par cycle. Des étapes de purge intermédiaires éliminent les excès de réactifs et les sous-produits, garantissant un contrôle précis et uniforme de l'épaisseur du film à l'échelle atomique.

Chaque cycle d'ALD comprend quatre étapes principales : (1) adsorption du premier précurseur métallique ($HfCl_4$ ou $ZrCl_4$) sur les groupes hydroxyles de surface, (2) purge des gaz résiduels, (3) réaction avec l'oxydant (H_2O) pour former la couche oxyde et régénérer les sites –OH, puis (4) nouvelle purge. La répétition de ces cycles permet une croissance linéaire du film, définie par la croissance par cycle (Growth Per Cycle, GPC), stable dans une fenêtre de température spécifique appelée fenêtre ALD.

Les films ferroélectriques étudiés ont été déposés par ALD thermique à 300 °C dans un réacteur ASM Polygon Pulsar. Les précurseurs $HfCl_4$ et $ZrCl_4$ ont été utilisés avec H_2O comme oxydant, et des purges d'azote ont permis d'éliminer les espèces résiduelles. L'épaisseur finale a été ajustée en fonction du GPC de chaque matériau, assurant une grande précision sur la composition et l'épaisseur totale du dépôt.

Deux approches de fabrication ont été employées :

- **La solution solide $\mathbf{Hf_{1-x}Zr_xO_2}$** : obtenue par la méthode des supercycles, consiste à alterner les cycles individuels de HfO_2 et ZrO_2. Cette alternance favorise un mélange homogène des atomes à l'échelle atomique et permet d'ajuster la composition globale (par exemple 1:1 pour $Hf_{0.5}Zr_{0.5}O_2$).

- **La structure multicouche $\mathbf{HfO_2/ZrO_2}$** : formée par empilement séquentiel de plusieurs cycles de HfO_2 suivis de ZrO_2, conduit à des sous-couches distinctes et à des interfaces bien définies. Le contrôle du nombre de cycles de chaque oxyde permet d'ajuster à la fois la composition moyenne et l'épaisseur unitaire des couches.

Cette flexibilité dans la conception et la maîtrise des couches fait de l'ALD une méthode particulièrement adaptée à la fabrication de structures ferroélectriques ultraminces et homogènes,

essentielles pour l'intégration dans des dispositifs mémoire avancés.

11 Approches expérimentales de caractérisation

Les techniques de caractérisation utilisées dans cette étude visent à établir la corrélation entre les propriétés structurales, chimiques et électriques des couches ferroélectriques à base d'oxyde d'hafnium.

Les méthodes de caractérisation des matériaux comprennent la réflectométrie des rayons X (XRR), utilisée pour déterminer l'épaisseur, la densité et la rugosité des films, et la fluorescence X à dispersion en longueur d'onde (WDXRF), permettant de quantifier la composition élémentaire et le rapport Hf/Zr. La diffraction des rayons X (XRD), en configurations rasante et in-plane, fournit des informations sur la cristallinité, la texture et les contraintes internes des films. La microscopie électronique en transmission (TEM), combinée à la spectroscopie à dispersion d'énergie des rayons X (EDX), permet d'observer les interfaces et la microstructure tout en cartographiant la distribution chimique à l'échelle nanométrique. La spectrométrie de masse des ions secondaires en temps de vol (ToF-SIMS) est utilisée pour obtenir des profils de composition en profondeur et identifier d'éventuelles interdiffusions entre couches, tandis que la spectroscopie de photoélectrons X (XPS) fournit des informations sur la composition chimique de surface et les états de liaison. Enfin, la mesure de la courbure des plaquettes (bow) permet d'évaluer la contrainte résiduelle dans les films déposés.

Du point de vue électrique, la méthode PUND (Positive-Up Negative-Down) est employée pour extraire les paramètres ferroélectriques clés tels que la polarisation rémanente ($2P_r$) et la tension coercitive (V_c), en isolant le courant de commutation du courant de fuite et du déplacement diélectrique. Les mesures quasi-statiques courant–tension (I–V) complètent cette analyse en caractérisant le courant de fuite et le champ de claquage, offrant ainsi une compréhension globale des performances électriques des condensateurs ferroélectriques.

12 Comportement ferroélectrique des films de solution solide $\mathbf{Hf_{1-x}Zr_xO_2}$

Les études menées sur les films de solution solide $Hf_{1-x}Zr_xO_2$ ont permis de mettre en évidence le rôle déterminant des conditions de dépôt, des électrodes et des traitements thermiques sur leurs propriétés structurales et ferroélectriques. Les couches de 10 nm d'épaisseur présentent un état amorphe après dépôt, et le recuit à 400°C est déjà suffisant pour induire la cristallisation et présenter de la ferroélectricité. Un recuit à 500°C entraîne une légère amélioration de la polarisation, accompagnée d'une diminution de l'effet de réveil (wake-up), c'est-à-dire l'augmentation progressive de la polarisation remanente au cours des premiers cycles électriques, mais sans modification majeure du comportement ferroélectrique global.

L'influence de l'électrode supérieure s'est révélée significative, notamment à travers la texture cristallographique. Les électrodes de TiN induisent des contraintes compressives, tandis que celles de tungstène génèrent des contraintes tensiles après dépôt. Ces contraintes se relâchent

toutefois largement après gravure et recuit, et aucune corrélation directe n'a été observée entre la contrainte résiduelle et la polarisation finale. En revanche, la texture du TiN s'avère déterminante : une orientation TiN(002) plus faible est associée à une polarisation rémanente plus élevée et à un effet de réveil réduit, ce qui suggère que certaines orientations cristallines favorisent la stabilisation de la phase orthorhombique ferroélectrique.

Les analyses structurales complémentaires (GIWAXS, Grazing Incidence Wide Angle X-ray Scattering, et EXAFS, Extended X-ray Absorption Fine Structure) réalisées sur des condensateurs cyclés ont montré que les principales réorganisations de la structure cristalline se produisent dès les premiers cycles électriques. Cette évolution rapide indique une réorganisation locale et à longue portée du matériau lors de l'activation ferroélectrique initiale.

Au-delà de ces résultats de référence, l'étude de la composition et de la réduction d'épaisseur a permis de préciser les conditions nécessaires à la stabilisation de la phase orthorhombique. La composition 1:1 (Hf:Zr) présente la polarisation rémanente la plus élevée pour les films de 10 nm, confirmant sa capacité à stabiliser la phase ferroélectrique. Les compositions riches en zirconium montrent un effet de réveil plus marqué et des caractéristiques partiellement antiferroélectriques, tandis que les compositions riches en hafnium contiennent une proportion plus importante de phase monoclinique, thermodynamiquement la plus stable pour le HfO_2 mais de nature paraélectrique, moins polarisable mais réputée plus endurante.

Lorsque l'épaisseur est réduite à 6, 5 et 4 nm, des changements structurels et électriques significatifs apparaissent. À 4 nm, la composition 1:1 ne présente pas de réponse ferroélectrique : le film reste amorphe à 400 °C et adopte un comportement antiferroélectrique après recuit à 500 °C. La diminution de la teneur en zirconium atténue cet effet en favorisant une polarisation plus marquée. En revanche, les films riches en hafnium restent majoritairement amorphes ou partiellement monoclinique, ce qui limite leur aptitude à des applications ferroélectriques en très faible épaisseur.

Les mesures électriques montrent que les compositions riches en hafnium présentent un courant de fuite plus faible et un champ de claquage plus élevé, en accord avec un élargissement du gap et une densité de défauts réduite. Toutefois, à 4 nm, les courants de fuite augmentent nettement en raison des effets de conduction par effet tunnel direct, soulignant la nécessité d'une optimisation supplémentaire pour garantir la fiabilité diélectrique à ces épaisseurs extrêmes.

Dans l'ensemble, ces résultats démontrent que la ferroélectricité des films $Hf_{1-x}Zr_xO_2$ dépend d'un équilibre subtil entre composition, contraintes, texture et conditions de recuit. Si la réduction d'épaisseur permet de diminuer la tension de commutation, le maintien d'une polarisation stable sous 6 nm requiert une température de cristallisation plus élevée et un ajustement précis de la teneur en zirconium. Ces conclusions posent les bases pour la conception de structures optimisées, notamment les configurations multicouches, qui sont étudiées dans la suite du travail.

13 Structures multicouches HfO_2/ZrO_2 : vers la ferroélectricité à l'échelle nanométrique

L'étude des structures multicouches ultrafines à base de HfO_2/ZrO_2 a mis en évidence le rôle essentiel du contrôle nanométrique des sous-couches et de la nature des interfaces, à la fois entre les couches d'oxyde et entre le matériau ferroélectrique et les électrodes, sur le comportement ferroélectrique. Pour les empilements de 6 nm, les meilleures performances ont été obtenues avec des sous-couches d'environ 1 nm, présentant une polarisation rémanente comparable à celle des films homogènes de HZO tout en offrant une flexibilité supplémentaire liée à la séquence d'empilement et à la configuration des interfaces. La première et la dernière couche de chaque structure se révèlent particulièrement importantes, influençant directement l'effet de réveil et la texture cristallographique, ainsi que la polarisation observée dès les premiers cycles électriques.

L'analyse comparative entre différentes compositions montre que l'architecture multicouche ne se limite pas aux systèmes symétriques Hf:Zr = 1:1, mais améliore également la réponse ferroélectrique dans les compositions asymétriques. Le multicouche riche en hafnium présente un effet de réveil plus marqué que la solution solide HZO 2:1, mais atteint une polarisation supérieure après cyclage, suggérant une stabilisation progressive de la phase ferroélectrique. Pour les compositions riches en zirconium, le multicouche se distingue nettement : alors que la solution solide HZO 1:2 montre une polarisation initiale quasi nulle nécessitant un cyclage prolongé, l'empilement multicouche présente une polarisation plus élevée dès les premiers cycles. Ces observations confirment que les interfaces jouent un rôle important dans la stabilisation de la phase orthorhombique et dans la réduction des fuites, comme l'indiquent les valeurs plus élevées du champ de claquage observées pour les multicouches, synonymes d'une meilleure endurance électrique.

Lorsque l'épaisseur est réduite à 5 nm et 4 nm, les avantages de la configuration multicouche deviennent encore plus évidents. Les films de solution solide HZO peinent à se cristalliser et présentent une réponse ferroélectrique limitée, voire absente à 4 nm, tandis que les structures multicouches favorisent la cristallisation et conservent une réponse électrique mesurable. Cependant, ces structures demeurent sensibles aux conditions de recuit : une température de 500°C est encore nécessaire pour activer la phase ferroélectrique, et la polarisation reste plus faible qu'à plus grande épaisseur. Ces résultats confirment que l'approche multicouche constitue une voie prometteuse pour étendre la ferroélectricité à l'échelle sub-5 nm, tout en soulignant la nécessité d'un équilibre entre robustesse électrique, limitation des fuites et maintien de la phase ferroélectrique.

Comparées aux résultats de l'état de l'art, les valeurs de polarisation obtenues restent légèrement inférieures à celles rapportées pour des films de 10 nm, mais demeurent compétitives pour les épaisseurs de 6 nm et représentent une avancée significative à 4 nm. Bien que le recuit à 500°C utilisé ici soit modéré par rapport à d'autres études, il reste relativement élevé pour une intégration complète en technologie de fin de ligne (BEOL). Dans l'ensemble, ces résultats soulignent le rôle déterminant de la configuration multicouche et du contrôle précis de l'épaisseur des sous-couches dans le maintien de la ferroélectricité à des dimensions nanométriques et ou-

vrent des perspectives concrètes pour l'optimisation des dispositifs ferroélectriques de prochaine génération.

14 Avancées et perspectives sur les films ferroélectriques ultrafins de HfO_2

Cette thèse a permis d'approfondir la compréhension du comportement ferroélectrique des structures ultrafines à base de HfO_2, en explorant de manière systématique les effets de la composition, de l'épaisseur et de l'architecture multicouche sur les propriétés électriques.

Les travaux menés ont démontré que la composition Hf:Zr = 1:1 présente la meilleure polarisation à 10 nm, confirmant sa capacité à stabiliser la phase orthorhombique ferroélectrique. Les compositions riches en Zr révèlent un comportement antiferroélectrique marqué et un effet de réveil plus important, tandis que les compositions riches en Hf, bien que présentant des $2P_r$ plus faibles, présentent une meilleure endurance au cyclage.

La réduction d'épaisseur jusqu'à 6, 5 et 4 nm a montré la difficulté croissante à maintenir la ferroélectricité, en raison de la perte de cristallinité et de la prédominance de phases amorphes ou non polaires. Cependant, la structuration en multicouches HfO_2/ZrO_2 s'est révélée être une stratégie efficace pour restaurer la polarisation dans ces régimes ultrafins, grâce au contrôle précis de l'épaisseur unitaire et de la séquence d'empilement. Les résultats les plus prometteurs ont été obtenus pour des sous-couches proches de 1 nm, démontrant que le contrôle de la configuration du matériau permet de préserver la ferroélectricité même à 4 nm.

Les études structurelles (XRD, GIWAXS, EXAFS) ont confirmé la cristallisation des films après recuit et suggéré une réorganisation structurale rapide lors des premiers cycles électriques, liée à l'effet de réveil. Ces observations, couplées aux mesures électriques, ont permis de relier les propriétés ferroélectriques aux mécanismes d'évolution locale du matériau. L'utilisation du dépôt par couches atomiques (ALD) s'est imposée comme un atout majeur, permettant un contrôle nanométrique de la composition et de l'épaisseur, et offrant une voie privilégiée pour la fabrication d'architectures complexes compatibles avec les procédés CMOS.

Au-delà de ces résultats, plusieurs perspectives se dégagent pour la poursuite de ce travail. L'exploration de nouveaux précurseurs ALD pourrait permettre d'améliorer la qualité cristalline, de réduire les défauts et d'accroître l'uniformité des films ultrafins. L'ingénierie des électrodes, notamment par l'utilisation de couches déposées par ALD, offrirait un meilleur contrôle des interfaces et une compatibilité renforcée avec les procédés industriels. L'étude du rôle de l'électrode inférieure dans la nucléation initiale de la phase orthorhombique constitue également un axe clé pour favoriser une cristallisation préférentielle en phase ferroélectrique à très faible épaisseur.

Sur le plan thermique, l'adoption de procédés de recuit ultrarapide (laser annealing, RTA) permettrait de limiter le budget thermique tout en assurant une cristallisation suffisante du matériau, rendant le procédé plus compatible avec la technologie de fin de ligne (BEOL). Par ailleurs, les analyses avancées par EXAFS et GIWAXS devront être poursuivies pour élucider les mécanismes atomiques sous-jacents à l'effet de réveil et aux transitions de phase lors des premiers cycles électriques.

Enfin, l'étude des comportements antiferroélectriques observés dans les compositions riches en Zr ouvre de nouvelles voies fonctionnelles, notamment pour des dispositifs à double hystérésis ou des applications capacitives à faible consommation. L'intégration tridimensionnelle de ces matériaux, rendue possible par la nature conforme du dépôt ALD, représente également une perspective prometteuse pour le développement de mémoires haute densité et à faible puissance.

Dans l'ensemble, cette étude a permis d'établir une base solide pour la compréhension et l'optimisation des films ferroélectriques ultrafins à base de HfO_2. Le couplage entre ingénierie de la composition, structuration multicouche, maîtrise des électrodes et contrôle du procédé de cristallisation apparaît comme la voie la plus crédible pour garantir la stabilité, la fiabilité et la performance de ces matériaux dans les technologies mémoire de prochaine génération.

Bibliography

1. Labs, A. *What is the memory wall?* https://ayarlabs.com/glossary/memory-wall (2025).
2. Sastry, G., Heim, L., Belfield, H., Anderljung, M., Brundage, M., Hazell, J., O'Keefe, C., Hadfield, G. K., Ngo, R., Pilz, K., Gor, G., Bluemke, E., Shoker, S., Egan, J., Trager, R. F., Avin, S., Weller, A., Bengio, Y. & Coyle, D. *Computing Power and the Governance of Artificial Intelligence* (2024).
3. Kompas AI. *AI Research & Report Engine* 2024.
4. Carvalho, C. *The Gap between Processor and Memory Speeds* (2002).
5. TaheriNejad, N. *In-Memory Computing: Global Energy Consumption, Carbon Footprint, Technology, and Products Status Quo 2024 IEEE 24th International Conference on Nanotechnology (NANO)* (2024), 495–500. doi:10.1109/NANO61778.2024.10628809.
6. Chi, P., Li, S., Cheng, Y., Lu, Y., Kang, S.-H. & Xie, Y. *Architecture design with STT-RAM: Opportunities and challenges 2016 21st Asia and South Pacific Design Automation Conference (ASP-DAC)* (2016), 109–114. doi:10.1109/ASPDAC.2016.7427997.
7. Lee, S.-H. *Technology Scaling Challenges and Opportunities of Memory Devices 2016 IEEE International Electron Devices Meeting (IEDM)* (2016), 1.1.1–1.1.8. doi:10.1109/IEDM.2016.7838026.
8. Rizk, R., Rizk, D., Kumar, A. & Bayoumi, M. *Demystifying Emerging Nonvolatile Memory Technologies: Understanding Advantages, Challenges, Trends, and Novel Applications 2019 IEEE International Symposium on Circuits and Systems (ISCAS)* (2019), 1–5. doi:10.1109/ISCAS.2019.8702390.
9. Mannocci, P., Farronato, M., Lepri, N., Cattaneo, L., Glukhov, A., Sun, Z. & Ielmini, D. In-memory computing with emerging memory devices: Status and outlook. *APL Machine Learning* **1,** 010902. doi:10.1063/5.0136403 (2023).
10. Chen, A. A Review of Emerging Non-Volatile Memory (NVM) Technologies and Applications. *Solid-State Electronics* **125,** 25–38. doi:10.1016/j.sse.2016.07.006 (2016).
11. Van Houdt, J. Memory Technology for the Terabit Era: From 2D to 3D. *2017 Symposium on VLSI Technology,* T24–T25. doi:10.23919/VLSIT.2017.7998186 (2017).
12. Chen, L., Pam, M. E., Li, S. & Ang, K.-W. Ferroelectric Memory Based on Two-Dimensional Materials for Neuromorphic Computing. *Neuromorphic Computing and Engineering* **2,** 022001. doi:10.1088/2634-4386/ac57cb (2022).
13. Lu, C., Lue, H. & Chen, Y. State-of-the-art flash memory devices and post-flash emerging memories. *Science China Information Sciences* **54,** 1039–1060. doi:10.1007/s11432-011-4221-z (2011).
14. Navarro, G., Bourgeois, G., Kluge, J., Serra, A. L., Verdy, A., Garrione, J., Cyrille, M.-C., Bernier, N., Jannaud, A., Sabbione, C., Bernard, M., Nolot, E., Fillot, F., Noe, P., Fellouh, L., Rodriguez, G., Beugin, V., Cueto, O., Castellani, N., Coignus, J., Delaye, V., Socquet-Clerc, C., Magis, T., Boixaderas, C., Barnola, S. & Nowak, E. *Phase-Change Memory: Performance, Roles and Challenges 2018 IEEE International Memory Workshop (IMW)* (2018), 1–4. doi:10.1109/IMW.2018.8388845.
15. Slesazeck, S. & Mikolajick, T. Nanoscale resistive switching memory devices: a review. *Nanotechnology* **30,** 352003. doi:10.1088/1361-6528/ab2084 (2019).
16. Bhatti, S., Sbiaa, R., Hirohata, A., Ohno, H., Fukami, S. & Piramanayagam, S. N. Spintronics based random access memory: a review. *Materials Today* **20,** 530–548. doi:10.1016/j.mattod.2017.07.007 (2017).
17. Keshavarzi, A., Ni, K., Van Den Hoek, W., Datta, S. & Raychowdhury, A. FerroElectronics for Edge Intelligence. *IEEE Micro* **40,** 33–48. doi:10.1109/MM.2020.3026667 (2020).

18. Mikolajick, T., Slesazeck, S., Mulaosmanovic, H., Park, M.-H., Fichtner, S., Lomenzo, P. D., Hoffmann, M. & Schroeder, U. Next generation ferroelectric materials for semiconductor process integration and their applications. *Journal of Applied Physics* **129,** 100901. doi:10.1063/5.0037617 (2021).

19. Terry, F. *Caractérisation électrique et analyse de mémoires non-volatiles embarquées à base de matériaux ferroélectriques* PhD thesis (Ecole doctoral de Marseille, 2023).

20. Banerjee, W. Challenges and Applications of Emerging Nonvolatile Memory Devices. *Electronics* **9,** 1029. doi:10.3390/electronics9061029 (2020).

21. Du, Y., Tang, J., Li, Y., Xi, Y., Gao, B., Qian, H. & Wu, H. Monolithic 3D Integration of FeFET, Hybrid CMOS Logic and Analog RRAM Array for Energy-Efficient Reconfigurable Computing-In-Memory Architecture. *2023 IEEE Symposium on VLSI Technology and Circuits (VLSI Technology and Circuits),* 1–2. doi:10.23919/VLSITechnologyandCir57934.2023.10185221 (2023).

22. Barbot, J. *Electrical Characterization of Ferroelectric Tunnel Junctions Based on Hafnium Oxide for Neuromorphic Applications* PhD thesis (Université Grenoble Alpes, 2023).

23. Ishiwara, H. Recent Progress in Ferroelectric Random Access Memory Technology. *MRS Online Proceedings Library* **997,** 805. doi:10.1557/PROC-0997-I08-05 (2008).

24. Chanthbouala, A., Garcia, V., Cherifi, R. O., Bouzehouane, K., Fusil, S., Moya, X., Xavier, S., Yamada, H., Deranlot, C., Mathur, N. D., Bibes, M., Barthélémy, A. & Grollier, J. A ferroelectric memristor. *Nature Materials* **11,** 860–864. doi:10.1038/nmat3415 (2012).

25. Valasek, J. Piezo-Electric and Allied Phenomena in Rochelle Salt. *Physical Review* **17,** 475–481. doi:10.1103/PhysRev.17.475 (1921).

26. Fousek, J. *Joseph Valasek and the Discovery of Ferroelectricity Proceedings of 1994 IEEE International Symposium on Applications of Ferroelectrics* (1994), 1–5. doi:10.1109/ISAF.1994.522283.

27. *CRC Handbook of Chemistry and Physics* 90th (ed Lide, D. R.) 4–83 (CRC Press, 2010).

28. Mueller, S. F. *Development of HfO_2-Based Ferroelectric Memories for Future CMOS Technology Nodes* (Technogical University of Dresden, 2016).

29. Forsbergh, P. W. Domain Structures and Phase Transitions in Barium Titanate. *Physical Review* **76,** 1187–1201. doi:10.1103/PhysRev.76.1187 (1949).

30. Merz, W. J. Domain Properties in $BaTiO_3$. *Physical Review* **88,** 421–422. doi:10.1103/PhysRev.88.421 (1952).

31. Randall, C. A., Newnham, R. E. & Cross, L. E. *History of the First Ferroelectric Oxide, $BaTiO_3$* tech. rep. (Materials Research Institute, The Pennsylvania State University, University Park, PA, USA, 2004).

32. Pramanik, S., Pingguan-Murphy, B. & Abu Osman, N. A. Developments of Immobilized Surface Modified Piezoelectric Crystal Biosensors for Advanced Applications. *International Journal of Electrochemical Science* **8,** 8863–8892. doi:10.1016/S1452-3981(23)12933-6 (2013).

33. *F-RAM Technology Brief* [Online] Available: https://studylib.net/doc/18729109/f-ram-technology-brief (2007).

34. Zhang, J., Zhang, Y., Chen, Q., Chen, X., Wang, G., Dong, X., Yang, J., Bai, W. & Tang, X. Enhancement of Energy-Storage Density in PZT/PZO-Based Multilayer Ferroelectric Thin Films. *Nanomaterials* **11,** 2141. doi:10.3390/nano11082141 (2021).

35. Dawber, M., Rabe, K. M. & Scott, J. F. Physics of Thin-Film Ferroelectric Oxides. *Reviews of Modern Physics* **77,** 1083–1130. doi:10.1103/RevModPhys.77.1083 (4 2005).

36. Pandey, R., Vats, G., Yun, J., Bowen, C. R., Ho-Baillie, A. W. Y., Seidel, J., Butler, K. T. & Seok, S. I. Mutual Insight on Ferroelectrics and Hybrid Halide Perovskites: A Platform for Future Multifunctional Energy Conversion. *Advanced Materials* **31,** 1807376. doi:10.1002/adma.201807376 (2019).

37. *Nanoscale Phenomena in Ferroelectric Thin Films* (ed Hong, S.) (Kluwer Academic Publishers, Boston, 2004).

38. Hennessey, G., Peters, T., Tipsawat, P., Checa, M., Collins, L. & Trolier-McKinstry, S. Domain wall motion across microstructural features in polycrystalline ferroelectric films. *Acta Materialia* **250,** 118871. doi:10.1016/j.actamat.2023.118871 (2023).

39. Zhao, X. & Vanderbilt, D. First-Principles Study of Structural, Vibrational, and Lattice Dielectric Properties of Hafnium Oxide. *Physical Review B* **65,** 233106. doi:10.1103/PhysRevB.65.233106 (2002).

40. Wang, J., Li, H. P. & Stevens, R. Hafnia and Hafnia-Toughened Ceramics. *Journal of Materials Science* **27,** 5397–5430 (1992).

41. Wilk, G. D., Wallace, R. M. & Anthony, J. M. High-κ gate dielectrics: Current status and materials properties considerations. *Journal of Applied Physics* **89,** 5243–5275. doi:10.1063/1.1361065 (2001).

42. Lomenzo, P. D. *Ferroelectric and Antiferroelectric Properties of HfO_2-Based Thin Films* Ph.D. Dissertation (University of Florida, 2016).

43. Böscke, T. S., Müller, J., Bräuhaus, D., Schröder, U. & Böttger, U. Ferroelectricity in Hafnium Oxide Thin Films. *Applied Physics Letters* **99,** 102903. doi:10.1063/1.3634052 (2011).

44. Silva, J. P. B., Alcala, R., Avci, U. E., Barrett, N., Bégon-Lours, L., Borg, M., Byun, S., Chang, S.-C., Cheong, S.-W., Choe, D.-H., Coignus, J., Deshpande, V., Dimoulas, A., Dubourdieu, C., Fina, I., Funakubo, H., Grenouillet, L., Gruverman, A., Heo, J., Hoffmann, M., Hsain, H. A., Huang, F.-T., Hwang, C. S., Íñiguez, J., Jones, J. L., Karpov, I. V., Kersch, A., Kwon, T., Lancaster, S., Lederer, M., Lee, Y., Lomenzo, P. D., Martin, L. W., Martin, S., Migita, S., Mikolajick, T., Noheda, B., Park, M. H., Rabe, K. M., Salahuddin, S., Sánchez, F., Seidel, K., Shimizu, T., Shiraishi, T., Slesazeck, S., Toriumi, A., Uchida, H., Vilquin, B., Xu, X., Ye, K. H. & Schroeder, U. Roadmap on Ferroelectric Hafnia- and Zirconia-Based Materials and Devices. *APL Materials* **11,** 089201. doi:10.1063/5.0148068 (2023).

45. Lee, D. H., Lee, Y., Yang, K., Park, J. Y., Kim, S. H., Reddy, P. R. S., Materano, M., Mulaosmanovic, H., Mikolajick, T., Jones, J. L., Schroeder, U. & Park, M. H. Domains and domain dynamics in fluorite-structured ferroelectrics. *Applied Physics Reviews* **8,** 021312. doi:10.1063/5.0047977 (2021).

46. Kim, J.-H., Song, S., Narayan, D. M., Le, D. N., Chu, T. T. H., Lee, M., Park, G., Lee, S., Kang, J., Spiegelman, J., Benham, M., Kim, S. J., Choi, R. & Kim, J. Impact of Tetrakis(ethylmethylamino)-based precursor and oxygen source selection on atomic layer deposition of ferroelectric HfxZr1-xO2 thin films. *Applied Surface Science* **686,** 162197. doi:https://doi.org/10.1016/j.apsusc.2024.162197 (2025).

47. Liang, Y.-K., Liu, Z., Cai, Z., Han, X., Huang, H.-Y., Lin, Y.-M., Yi Chang, E., Lin, C.-H., Takenaka, M., Toprasertpong, K. & Takagi, S. Demonstration of Wake-Up Free 6 nm Ultrathin ZrO_2-HfO_2 Superlattice Ferroelectric Capacitors with High Endurance Against Fatigue. *IEEE Electron Device Letters* **45,** 1468–1471. doi:10.1109/LED.2024.3410378 (2024).

48. Park, H. S., Choi, S., Kim, K. D., Yeom, M. K., Lee, S. H., Ryoo, S. K. & Hwang, C. S. Optimization of the 4 nm-Thick Hf1-xZrxO2 Film with Low Operating Voltage and High Endurance for Ferroelectric Random Access Memory. *ACS Applied Electronic Materials* **6,** 6826–6836. doi:10.1021/acsaelm.4c01216 (2024).

49. Wunderwald, F., Xu, B., Kersch, A., Holsgrove, K. M., Kao, Y.-C., Richter, C., Enghardt, S., Mikolajick, T. & Schroeder, U. Interaction Between Strain and Phase Formation in $Hf_xZr_{1-x}O_2$ Thin Films. *Small* **21,** 2408133. doi:10.1002/smll.202408133 (2025).

50. Cui, B., Ye, S., Wang, X., Wu, M., Li, Y., Wu, Y., Wen, Y., Liu, J., Li, X., Ren, P., Ji, Z., Lu, H., Zhang, D. W., Wang, R. & Huang, R. Unveiling the Role of Local Stress in Enhancing Ferroelectric Properties and Endurance of HfO_2/ZrO_2 Superlattice Structures. *IEEE Electron Device Letters* **46,** 107–110. doi:10.1109/LED.2024.3496720 (2025).

51. Iung, T., Pérez Ramírez, L., Gloskovskii, A., Cho, C.-Y., Lao, M.-Y., De, S., Hou, T.-H., Lubin, C., Gros-Jean, M. & Barrett, N. Oxygen vacancy distribution and phase composition in scaled, $Hf_{0.5}Zr_{0.5}O_2$-based ferroelectric capacitors. *Applied Physics Letters* **126,** 062903. doi:10.1063/5.0245595 (2025).

52. Hoffmann, M., Schroeder, U., Schenk, T., Shimizu, T., Funakubo, H., Sakata, O., Pohl, D., Drescher, M., Adelmann, C., Materlik, R., Kersch, A. & Mikolajick, T. Stabilizing the Ferroelectric Phase in Doped Hafnium Oxide. *Journal of Applied Physics* **118,** 072006. doi:10.1063/1.4927805 (2015).

53. Hsain, H. A., Lee, Y., Materano, M., Mittmann, T., Payne, A., Mikolajick, T., Schroeder, U., Parsons, G. N. & Jones, J. L. Many routes to ferroelectric HfO2: A review of current deposition methods. *Journal of Vacuum Science & Technology A* **40,** 010803. doi:10.1116/6.0001317 (2021).

54. Mittmann, T., Materano, M., Lomenzo, P. D., Park, M. H., Stolichnov, I., Cavalieri, M., Zhou, C., Chung, C.-C., Jones, J. L., Szyjka, T., Müller, M., Kersch, A., Mikolajick, T. & Schroeder, U. Origin of Ferroelectric Phase in Undoped HfO_2 Films Deposited by Sputtering. *Advanced Materials Interfaces* **6,** 1900042. doi:10.1002/admi.201900042 (2019).

55. Lyu, J., Fina, I., Solanas, R., Fontcuberta, J. & Sánchez, F. Growth Window of Ferroelectric Epitaxial $Hf_{0.5}Zr_{0.5}O_2$ Thin Films. *ACS Applied Electronic Materials* **1,** 220–228. doi:10.1021/acsaelm.8b00065 (2019).

56. Ritala, M. & Leskelä, M. *Handbook of Thin Films* (ed Nalwa, H. S.) 103–159 (Academic Press, Burlington, 2002). doi:10.1016/B978-012512908-4/50005-9.

57. Putkonen, M. & Niinistö, L. *Precursor Chemistry of Advanced Materials* (ed Fischer, R. A.) 125–145 (Springer Berlin Heidelberg, Berlin, Heidelberg, 2005). doi:10.1007/b136145.

58. Cho, A.-J., Jeon, J., Chung, H. K., Baek, I.-H., Yang, K., Park, M. H., Baek, S.-H. & Kim, S. K. Effects of oxygen sources on properties of atomic-layer-deposited ferroelectric hafnium zirconium oxide thin films. *Ceramics International* **48,** 3280–3286. doi:https://doi.org/10.1016/j.ceramint.2021.10.102 (2022).

59. Kim, B. S., Hyun, S. D., Moon, T., Do Kim, K., Lee, Y. H., Park, H. W., Lee, Y. B., Roh, J., Kim, B. Y., Kim, H. H., Park, M. H. & Hwang, C. S. A Comparative Study on the Ferroelectric Performances in Atomic Layer Deposited $Hf_{0.5}Zr_{0.5}O_2$ Thin Films Using Tetrakis(ethylmethylamino) and Tetrakis(dimethylamino) Precursors. *Nanoscale Research Letters* **15,** 72. doi:10.1186/s11671-020-03301-4 (2020).

60. Park, M. H., Lee, Y. H., Kim, H. J., Schenk, T., Lee, W., Kim, K. D., Fengler, F. P. G., Mikolajick, T., Schroeder, U. & Hwang, C. S. Surface and Grain Boundary Energy as the Key Enabler of Ferroelectricity in Nanoscale Hafnia-Zirconia: A Comparison of Model and Experiment. *Nanoscale* **9,** 9973–9986. doi:10.1039/C7NR02121F (2017).

61. Park, M. H., Lee, Y. H., Kim, H. J., Kim, Y. J., Moon, T., Kim, K. D., Hyun, S. D., Mikolajick, T., Schroeder, U. & Hwang, C. S. Understanding the Formation of the Metastable Ferroelectric Phase in Hafnia–Zirconia Solid Solution Thin Films. *Nanoscale* **10,** 716–725. doi:10.1039/C7NR06342C (2018).

62. Nyns, L., Delabie, A., Caymax, M., Heyns, M. M., Van Elshocht, S., Vinckier, C. & De Gendt, S. HfO_2 Atomic Layer Deposition Using $HfCl_4/H_2O$: The First Reaction Cycle. *ECS Transactions* **16,** 257. doi:10.1149/1.2980001 (2008).

63. Xu, L., Xiao, Y., van Sandwijk, A., Xu, Q. & Yang, Y. Production of Nuclear Grade Zirconium: A Review. *Journal of Nuclear Materials* **466,** 21–28. doi:10.1016/j.jnucmat.2015.07.010 (2015).

64. Mueller, S., Mueller, J., Singh, A., Riedel, S., Sundqvist, J., Schroeder, U. & Mikolajick, T. Incipient Ferroelectricity in Al-Doped HfO_2 Thin Films. *Advanced Functional Materials* **22,** 2412–2417. doi:10.1002/adfm.201103119 (2012).

65. Mueller, S., Adelmann, C., Singh, A., Van Elshocht, S., Schroeder, U. & Mikolajick, T. Ferroelectricity in Gd-Doped HfO_2 Thin Films. *ECS Journal of Solid State Science and Technology* **1,** N123. doi:10.1149/2.002301jss (2012).

66. Kim, S. J., Mohan, J., Summerfelt, S. R. & Kim, J. Ferroelectric $Hf_0.5Zr_0.5O_2$ Thin Films: A Review of Recent Advances. *JOM* **71,** 246–255. doi:10.1007/s11837-018-3140-5 (2019).

67. Siannas, N., Zacharaki, C., Tsipas, P., Chaitoglou, S., Bégon-Lours, L., Istrate, C., Pintilie, L. & Dimoulas, A. Metastable ferroelectricity driven by depolarization fields in ultrathin $Hf_{0.5}Zr_{0.5}O_2$. *Communications Physics* **5,** 178. doi:10.1038/s42005-022-00951-x (2022).

68. Kim, S. J., Narayan, D., Lee, J.-G., Mohan, J., Lee, J. S., Lee, J., Kim, H. S., Byun, Y.-C., Lucero, A. T., Young, C. D., Summerfelt, S. R., San, T., Colombo, L. & Kim, J. Large Ferroelectric Polarization of $TiN/Hf_{0.5}Zr_{0.5}O_2/TiN$ Capacitors Due to Stress-Induced Crystallization at Low Thermal Budget. *Applied Physics Letters* **111,** 242901. doi:10.1063/1.4995619 (2017).

69. Liu, B., Cao, Y., Zhang, W. & Li, Y. Excellent ferroelectric $Hf_{0.5}Zr_{0.5}O_2$ thin films with ultra-thin Al_2O_3 serving as capping layer. *Applied Physics Letters* **119,** 172902. doi:10.1063/5.0064700 (2021).

70. Zhu, S.-B., Geng, Y., Lu, H.-L., Zhang, Y., Sun, Q.-Q., Ding, S.-J. & Zhang, D. W. Effects of Rapid Thermal Annealing on Hf-Doped ZnO Films Grown by Atomic Layer Deposition. *Journal of Alloys and Compounds* **577,** 340–344. doi:10.1016/j.jallcom.2013.05.181 (2013).

71. Shekhawat, A., Walters, G., Chung, C.-C., Garcia, R., Liu, Y., Jones, J., Nishida, T. & Moghaddam, S. Effect of furnace annealing on the ferroelectricity of $Hf_{0.5}Zr_{0.5}O_2$ thin films. *Thin Solid Films* **677,** 142–149. doi:10.1016/j.tsf.2019.03.031 (2019).

72. Grenouillet, L., Francois, T., Coignus, J., Kerdilès, S., Vaxelaire, N., Carabasse, C., Mehmood, F., Chevalliez, S., Pellissier, C., Triozon, F., Mazen, F., Rodriguez, G., Magis, T., Havel, V., Slesazeck, S., Gaillard, F., Schroeder, U., Mikolajick, T. & Nowak, E. *Nanosecond Laser Anneal (NLA) for Si-Implanted HfO_2 Ferroelectric Memories Integrated in Back-End of Line (BEOL) 2020 IEEE Symposium on VLSI Technology* (2020), 1–2. doi:10.1109/VLSITechnology18217.2020.9265061.

73. Lee, Y., Goh, Y., Hwang, J., Das, D. & Jeon, S. The Influence of Top and Bottom Metal Electrodes on Ferroelectricity of Hafnia. *IEEE Transactions on Electron Devices* **68,** 523–528. doi:10.1109/TED.2020.3046173 (2021).

74. Bouaziz, J., Romeo, P. R., Baboux, N. & Vilquin, B. Huge Reduction of the Wake-Up Effect in Ferroelectric HZO Thin Films. *ACS Applied Electronic Materials* **1,** 1740–1745. doi:10.1021/acsaelm.9b00367 (2019).

75. Grimley, E. D., Schenk, T., Sang, X., Pešić, M., Schroeder, U., Mikolajick, T. & LeBeau, J. M. Structural Changes Underlying Field-Cycling Phenomena in Ferroelectric HfO_2 Thin Films. *Advanced Electronic Materials* **2,** 1600173. doi:10.1002/aelm.201600173 (2016).

76. Chouprik, A., Zakharchenko, S., Spiridonov, M., Zarubin, S., Chernikova, A., Kirtaev, R., Buragohain, P., Gruverman, A., Zenkevich, A. & Negrov, D. Ferroelectricity in $Hf_{0.5}Zr_{0.5}O_2$ Thin Films: A Microscopic Study of the Polarization Switching Phenomenon and Field-Induced Phase Transformations. *ACS Applied Materials & Interfaces* **10,** 8818–8826. doi:10.1021/acsami.7b17482 (2018).

77. Kashir, A., Oh, S. & Hwang, H. Defect Engineering to Achieve Wake-up Free HfO_2-Based Ferroelectrics. *Advanced Engineering Materials* **23,** 2000791. doi:10.1002/adem.202000791 (2021).

78. Schenk, T., Hoffmann, M., Ocker, J., Pešić, M., Mikolajick, T. & Schroeder, U. Complex Internal Bias Fields in Ferroelectric Hafnium Oxide. *ACS Applied Materials & Interfaces* **7,** 20224–20233. doi:10.1021/acsami.5b05773 (2015).

79. Oh, S., Kim, H., Kashir, A. & Hwang, H. Effect of dead layers on the ferroelectric property of ultrathin HfZrOx film. *Applied Physics Letters* **117,** 252906. doi:10.1063/5.0030856 (2020).

80. Lomenzo, P. D., Richter, C., Mikolajick, T. & Schroeder, U. Depolarization as Driving Force in Antiferroelectric Hafnia and Ferroelectric Wake-Up. *ACS Applied Electronic Materials* **2,** 1583–1595. doi:10.1021/acsaelm.0c00184 (2020).

81. Fengler, F. P. G., Hoffmann, M., Slesazeck, S., Mikolajick, T. & Schroeder, U. On the Relationship Between Field Cycling and Imprint in Ferroelectric $Hf_{0.5}Zr_{0.5}O_2$. *Journal of Applied Physics* **123,** 204101. doi:10.1063/1.5026424 (2018).

82. Takada, K., Takarae, S., Shimamoto, K., Fujimura, N. & Yoshimura, T. Time-Dependent Imprint in $Hf_{0.5}Zr_{0.5}O_2$ Ferroelectric Thin Films. *Advanced Electronic Materials* **7,** 2100151. doi:10.1002/aelm.202100151 (2021).

83. Sünbül, A., Lehninger, D., Lederer, M., Mähne, H., Hoffmann, R., Bernert, K., Thiem, S., Schöne, F., Döllgast, M., Haufe, N., Roy, L., Kämpfe, T., Seidel, K. & Eng, L. M. A Study on Imprint Behavior of Ferroelectric Hafnium Oxide Caused by High-Temperature Annealing. *physica status solidi (a)* **220,** 2300067. doi:10.1002/pssa.202300067 (2023).

84. Hamouda, W., Mehmood, F., Mikolajick, T., Schroeder, U., Mentes, T. O., Locatelli, A. & Barrett, N. Oxygen vacancy concentration as a function of cycling and polarization state in $TiN/Hf_{0.5}Zr_{0.5}O_2/TiN$ ferroelectric capacitors studied by x-ray photoemission electron microscopy. *Applied Physics Letters* **120,** 202902. doi:10.1063/5.0093125 (2022).

85. Vecchi, S., Puglisi, F. M., Appelt, P., Guido, R., Wang, X., Slesazeck, S., Mikolajick, T. & Lancaster, S. Evaluation of Imprint and Multi-Level Dynamics in Ferroelectric Capacitors. *Advanced Electronic Materials* **11,** 2400204. doi:10.1002/aelm.202400204 (2025).

86. Hsain, H. A., Lee, Y., Lancaster, S., Lomenzo, P. D., Xu, B., Mikolajick, T., Schroeder, U., Parsons, G. N. & Jones, J. L. Reduced Fatigue and Leakage of Ferroelectric $TiN/Hf_{0.5}Zr_{0.5}O_2/TiN$ Capacitors by Thin Alumina Interlayers at the Top or Bottom Interface. *Nanotechnology* **34,** 125703. doi:10.1088/1361-6528/acad0a (2023).

87. Chernikova, A. G., Kozodaev, M. G., Negrov, D. V., Korostylev, E. V., Park, M. H., Schroeder, U., Hwang, C. S. & Markeev, A. M. Improved Ferroelectric Switching Endurance of La-Doped $Hf_{0.5}Zr_{0.5}O_2$ Thin Films. *ACS Applied Materials & Interfaces* **10,** 2701–2708. doi:10.1021/acsami.7b15110 (2018).

88. Lehninger, D., Olivo, R., Ali, T., Lederer, M., Kämpfe, T., Mart, C., Biedermann, K., Kühnel, K., Roy, L., Kalkani, M. & Seidel, K. Back-End-of-Line Compatible Low-Temperature Furnace Anneal for Ferroelectric Hafnium Zirconium Oxide Formation. *Physica Status Solidi (a)* **217,** 1900840. doi:10.1002/pssa.201900840 (2020).

89. Lehninger, D., Prabhu, A., Sünbül, A., Ali, T., Schöne, F., Kämpfe, T., Biedermann, K., Roy, L., Seidel, K., Lederer, M. & Eng, L. M. Ferroelectric $[HfO_2/ZrO_2]$ Superlattices with Enhanced Polarization, Tailored Coercive Field, and Improved High Temperature Reliability. *Advanced Physics Research* **2,** 2200108. doi:10.1002/apxr.202200108 (2023).

90. Liang, Y.-K., Li, W.-L., Wang, Y.-J., Peng, L.-C., Lu, C.-C., Huang, H.-Y., Yeong, S. H., Lin, Y.-M., Chu, Y.-H., Chang, E.-Y. & Lin, C.-H. ZrO_2-HfO_2 Superlattice Ferroelectric Capacitors with Optimized Annealing to Achieve Extremely High Polarization Stability. *IEEE Electron Device Letters* **43,** 1451–1454. doi:10.1109/LED.2022.3193383 (2022).

91. Lu, Y. W., Shieh, J. & Tsai, F. Y. Induction of Ferroelectricity in Nanoscale ZrO_2/HfO_2 Bilayer Thin Films on $Pt/Ti/SiO_2/Si$ Substrates. *Acta Materialia* **115,** 68–75. doi:10.1016/j.actamat.2016.05.029 (2016).

92. Weeks, S. L., Pal, A., Narasimhan, V. K., Littau, K. A. & Chiang, T. Engineering of Ferroelectric HfO_2–ZrO_2 Nanolaminates. *ACS Applied Materials & Interfaces* **9,** 13440–13447. doi:10.1021/acsami.7b00776 (2017).

93. Wang, Y., Zhu, C., Sun, H., Wang, W., Zou, L., Yi, Y., Xu, J., Ren, J., Hu, S., Ye, L., Cheng, W., He, Q. & Miao, X. Phase Transition Kinetics and Sublayer Optimization of HfO_2/ZrO_2 Superlattice Ferroelectric Thin Films. *Applied Physics Letters* **125,** 083503. doi:10.1063/5.0221607 (2024).

94. Pavoni, E., Mohebbi, E., Mencarelli, D., Stipa, P., Laudadio, E. & Pierantoni, L. The Effect of Y Doping on Monoclinic, Orthorhombic, and Cubic Polymorphs of HfO_2: A First Principles Study. *Nanomaterials* **12.** doi:10.3390/nano12234324 (2022).

95. Reyes-Lillo, S. E., Garrity, K. F. & Rabe, K. M. Antiferroelectricity in thin-film ZrO_2 from first principles. *Physical Review B* **90,** 140103. doi:10.1103/PhysRevB.90.140103 (2014).

96. Park, M. H., Kim, H. J., Lee, G., Park, J., Lee, Y. H., Kim, Y. J., Moon, T., Kim, K. D., Hyun, S. D., Park, H. W., Chang, H. J., Choi, J.-H. & Hwang, C. S. A Comprehensive Study on the Mechanism of Ferroelectric Phase Formation in Hafnia-Zirconia Nanolaminates and Superlattices. *Applied Physics Reviews* **6,** 041403. doi:10.1063/1.5118737 (2019).

97. Cheema, S. S., Shanker, N., Wang, L.-C., Hsu, C.-H., Hsu, S.-L., Liao, Y.-H., San Jose, M., Gomez, J., Chakraborty, W., Li, W., Bae, J.-H., Volkman, S. K., Kwon, D., Rho, Y., Pinelli, G., Rastogi, R., Pipitone, D., Stull, C., Cook, M., Tyrrell, B., Stoica, V. A., Zhang, Z., Freeland, J. W., Tassone, C. J., Mehta, A., Saheli, G., Thompson, D., Suh, D. I., Koo, W.-T., Nam, K.-J., Jung, D. J., Song, W.-B., Lin, C.-H., Nam, S., Heo, J., Parihar, N., Grigoropoulos, C. P., Shafer, P., Fay, P., Ramesh, R., Mahapatra, S., Ciston, J., Datta, S., Mohamed, M., Hu, C. & Salahuddin, S. Ultrathin Ferroic HfO_2–ZrO_2 Superlattice Gate Stack for Advanced Transistors. *Nature* **604,** 65–71 (2022).

98. Migita, S., Ota, H., Asanuma, S., Morita, Y. & Toriumi, A. Accelerated Ferroelectric Phase Transformation in HfO_2/ZrO_2 Nanolaminates. *Applied Physics Express* **14,** 051006. doi:10.35848/1882-0786/abfa75 (2021).

99. Toprasertpong, K., Tahara, K., Hikosaka, Y., Nakamura, K., Saito, H., Takenaka, M. & Takagi, S. Low Operating Voltage, Improved Breakdown Tolerance, and High Endurance in $Hf_{0.5}Zr_{0.5}O_2$ Ferroelectric Capacitors Achieved by Thickness Scaling Down to 4 nm for Embedded Ferroelectric Memory. *ACS Applied Materials & Interfaces* **14,** 51137–51148. doi:10.1021/acsami.2c15369 (2022).

100. Park, M. H., Lee, Y. H., Mikolajick, T., Schroeder, U. & Hwang, C. S. Review and Perspective on Ferroelectric HfO_2-Based Thin Films for Memory Applications. *MRS Communications* **8,** 795–808 (2018).

101. Kim, S. J., Mohan, J., Kim, H. S., Lee, J., Young, C. D., Colombo, L., Summerfelt, S. R., San, T. & Kim, J. Low-Voltage Operation and High Endurance of 5-nm Ferroelectric $Hf_{0.5}Zr_{0.5}O_2$ Capacitors. *Applied Physics Letters* **113,** 182903. doi:10.1063/1.5052012 (2018).

102. Lyu, J., Song, T., Fina, I. & Sánchez, F. High Polarization, Endurance and Retention in Sub-5 nm $Hf_{0.5}Zr_{0.5}O_2$ Films. *Nanoscale* **12,** 11280–11287. doi:10.1039/D0NR02204G (2020).

103. Niinistö, J., Mäntymäki, M., Kukli, K., Costelle, L., Puukilainen, E., Ritala, M. & Leskelä, M. Growth and Phase Stabilization of HfO_2 Thin Films by ALD Using Novel Precursors. *Journal of Crystal Growth* **312,** 245–249. doi:10.1016/j.jcrysgro.2009.10.028 (2010).

104. Yuan, G.-J., Xie, J.-F., Li, H.-H., Lu, H.-L. & Tian, Y.-Z. Atomic Layer Deposition of Inorganic Films for the Synthesis of Vertically Aligned Carbon Nanotube Arrays and Their Hybrids. *Coatings* **9.** doi:10.3390/coatings9120806 (2019).

105. Ritala, M., Leskelä, M., Rauhala, E. & Haussalo, P. Atomic Layer Epitaxy Growth of TiN Thin Films. *Journal of The Electrochemical Society* **142,** 2731. doi:10.1149/1.2050083 (1995).

106. Puurunen, R. L., Root, A., Sarv, P., Viitanen, M. M., Brongersma, H. H., Lindblad, M. & Krause, A. O. I. Growth of Aluminum Nitride on Porous Alumina and Silica through Separate Saturated Gas-Solid Reactions of Trimethylaluminum and Ammonia. *Chemistry of Materials* **14,** 720–729. doi:10.1021/cm011176i (2002).

107. George, S. M. Atomic Layer Deposition: An Overview. *Chemical Reviews* **110,** 111–131. doi:10.1021/cr900056b (2010).

108. Johnson, R. W., Hultqvist, A. & Bent, S. F. A Brief Review of Atomic Layer Deposition: From Fundamentals to Applications. *Materials Today* **17,** 236–246. doi:10.1016/j.mattod.2014.04.026 (2014).

109. Nolot, E. *Towards inline metrology of thin materials in semiconductor environment* Habilitation à diriger des recherches (Université Grenoble Alpes, 2023).

110. Parratt, L. G. Surface Studies of Solids by Total Reflection of X-Rays. *Physical Review* **95,** 359–369. doi:10.1103/PhysRev.95.359 (1954).

111. Pessoa, W. B. *Probing chalcogenide films by advanced X-ray metrology for the semiconductor industry* PhD thesis (Université Paris Saclay (COmUE), 2018).

112. Harrington, G. F. & Santiso, J. Back-to-Basics Tutorial: X-ray Diffraction of Thin Films. *Journal of Electroceramics* **47,** 141–163. doi:10.1007/s10832-021-00263-6 (2021).

113. Cervasio, R., Amzallag, E., Verseils, M., Hemme, P., Brubach, J.-B., Infante, I. C., Segantini, G., Rojo Romeo, P., Coati, A., Vlad, A., Garreau, Y., Resta, A., Vilquin, B., Creuze, J. & Roy, P. Quantification of Crystalline Phases in Hf0.5Zr0.5O2 Thin Films through Complementary Infrared Spectroscopy and Ab Initio Supercell Simulations. *ACS Applied Materials & Interfaces* **16,** 3829–3840. doi:10.1021/acsami.3c13848 (2024).

114. Fields, S. S., Jaszewski, S. T. & Ihlefeld, J. F. A Perspective on Ferroelectricity in Hafnium Oxide: Mechanisms and Considerations Regarding its Stability and Performance. *Applied Physics Letters* **121,** 240502. doi:10.1063/5.0129546 (2022).

115. *Encyclopedia of Materials Characterization—Surfaces, Interfaces, Thin Films* (eds Brundle, C. R., Evans, C. A. & Wilson, S.) (Elsevier, New York, 1992).

116. Vandenbroucke, A. *Abatement of Volatile Organic Compounds by Combined Use of Non-Thermal Plasma and Heterogeneous Catalysis* PhD thesis (Ghent University, 2015).

117. Barnes, J.-P., Guyot, C., Hirchenhahn, P., Maindron, T., Renault, O. & Fisher, G. L. *The importance of sample preparation in time-of-flight secondary ion mass spectrometry analysis for semiconductor applications SISS-22 – The Scientific International Symposium on SIMS and Related Techniques Based on Ion-Solid Interactions* (Kanazawa, Japan, 2023).

118. Barnes, J.-P., Guyot, C., Hirchenhahn, P., Gauthier, N., Moreno, M., Maindron, T., Mazel, Y., Nolot, E., Renault, O., Chevalier, N., Priebe, A., Gautier, B., Tempez, A., Legendre, S. & Fisher, G. L. *Correlative microscopy and data analysis for semiconductor technology applications SIMS23 – 23rd International Conference on Secondary Ion Mass Spectrometry* (Minneapolis, United States, 2022).

119. Vignoud, L., Morin, C., Assigbe, N., Parry, G. & Estevez, R. *The advantages of coupling experimental methods and analytical modelling to fix deformation problems in devices conception and manufacturing 2018 IEEE CPMT Symposium Japan (ICSJ)* (2018), 11–14. doi:10.1109/ICSJ.2018.8602522.

120. Natsu, W., Ito, Y., Kunieda, M., Naoi, K. & Iguchi, N. Effects of Support Method and Mechanical Property of 300mm Silicon Wafer on Sori Measurement. *Precision Engineering* **29,** 19–26. doi:10.1016/j.precisioneng.2004.03.004 (2005).

121. Martin, S. *Caractérisation électrique multi-échelle d'oxydes minces ferroélectriques* Thesis (Université de Lyon, 2016).

122. Müller, J., Böscke, T. S., Schröder, U., Mueller, S., Bräuhaus, D., Böttger, U., Frey, L. & Mikolajick, T. Ferroelectricity in Simple Binary ZrO_2 and HfO_2. *Nano Letters* **12,** 4318–4323. doi:10.1021/nl302049k (2012).

123. Kim, H.-G., Hong, D.-H., Yoo, J.-H. & Lee, H.-C. Effect of process temperature on density and electrical characteristics of $Hf_{0.5}Zr_{0.5}O_2$ thin films prepared by plasma-enhanced atomic layer deposition. *Nanomaterials* **12,** 548. doi:10.3390/nano12030548 (2022).

124. Jung, Y. C., Kim, J.-H., Hernandez-Arriaga, H., Mohan, J., Hwang, S. M., Le, D. N., Sahota, A., Kim, H. S., Kim, K., Choi, R., Nam, C.-Y., Alvarez Daniel, J., Spiegelman, J., Kim, S. J. & Kim, J. Robust low-temperature (350 °C) ferroelectric $Hf_{0.5}Zr_{0.5}O_2$ fabricated using anhydrous H_2O_2 as the ALD oxidant. *Applied Physics Letters* **121,** 222901. doi:10.1063/5.0126695 (2022).

125. Fang, Z. & Dixon, D. A. Hydrolysis of ZrCl4 and HfCl4: The Initial Steps in the High-Temperature Oxidation of Metal Chlorides to Produce ZrO2 and HfO2. *The Journal of Physical Chemistry C* **117,** 7459–7474. doi:10.1021/jp400228d (2013).

126. Jeloaica, L., Estève, A., Djafari Rouhani, M. & Estève, D. Density functional theory study of HfCl4, ZrCl4, and Al(CH3)3 decomposition on hydroxylated SiO2: Initial stage of high-k atomic layer deposition. *Applied Physics Letters* **83,** 542–544. doi:10.1063/1.1587261 (2003).

127. Cao, R., Wang, Y., Zhao, S., Yang, Y., Zhao, X., Wang, W., Zhang, X., Lv, H., Liu, Q. & Liu, M. Effects of Capping Electrode on Ferroelectric Properties of $Hf_0.5Zr_0.5O_2$ Thin Films. *IEEE Electron Device Letters* **39,** 1207–1210. doi:10.1109/LED.2018.2846570 (2018).

128. Ye, K. H., Yeu, I. W., Han, G., Jeong, T., Yoon, S., Kim, D., Hwang, C. S. & Choi, J.-H. Comprehensive interpretations of thermodynamic and kinetic effects on the phase fractions in Hf1-xZrxO2 by first principle calculations. *Applied Physics Reviews* **10,** 031419. doi:10.1063/5.0160719 (2023).

129. Lederer, M., Lehninger, D., Ali, T. & Kämpfe, T. Review on the Microstructure of Ferroelectric Hafnium Oxides. *physica status solidi (RRL) - Rapid Research Letters* **16,** 2200168. doi:https://doi.org/10.1002/pssr.202200168 (2022).

130. Lederer, M., Olivo, R., Lehninger, D., Abdulazhanov, S., Kämpfe, T., Kirbach, S., Mart, C., Seidel, K. & Eng, L. M. On the Origin of Wake-Up and Antiferroelectric-Like Behavior in Ferroelectric Hafnium Oxide. *physica status solidi (RRL) - Rapid Research Letters* **15,** 2100086. doi:https://doi.org/10.1002/pssr.202100086 (2021).

131. Segantini, G., Manchon, B., Cañero Infante, I., Bugnet, M., Barhoumi, R., Nirantar, S., Mayes, E., Rojo Romeo, P., Blanchard, N., Deleruyelle, D., Sriram, S. & Vilquin, B. Interplay between Strain and Defects at the Interfaces of Ultra-Thin $Hf_{0.5}Zr_{0.5}O_2$-Based Ferroelectric Capacitors. *Advanced Electronic Materials* **9,** 2300171. doi:10.1002/aelm.202300171 (2023).

132. Park, M. H., Kim, H. J., Kim, Y. J., Lee, W., Moon, T. & Hwang, C. S. Evolution of phases and ferroelectric properties of thin $Hf_{0.5}Zr_{0.5}O_2$ films according to the thickness and annealing temperature. *Applied Physics Letters* **102,** 242905. doi:10.1063/1.4811483 (2013).

133. Yun, S., Kim, H., Seo, M., Kang, M.-H., Kim, T., Cho, S., Park, M. H., Jeon, S., Choi, Y.-K. & Hong, S. Effect of Annealing Temperature on Minimum Domain Size of Ferroelectric Hafnia. *ACS Applied Electronic Materials* **6,** 2134–2141. doi:10.1021/acsaelm.3c01104 (2024).

134. Bouaziz, J., Rojo Romeo, P., Baboux, N., Negrea, R., Pintilie, L. & Vilquin, B. Dramatic impact of pressure and annealing temperature on the properties of sputtered ferroelectric HZO layers. *APL Materials* **7,** 081109. doi:10.1063/1.5110894 (2019).

135. Khakimov, R. R., Chernikova, A. G., Lebedinskii, Y., Koroleva, A. A. & Markeev, A. M. Influence of the Annealing Temperature and Applied Electric Field on the Reliability of TiN/Hf0.5Zr0.5O2/TiN Capacitors. *ACS Applied Electronic Materials* **3,** 4317–4327. doi:10.1021/acsaelm.1c00511 (2021).

136. Athle, R., Persson, A. E. O., Irish, A., Menon, H., Timm, R. & Borg, M. Effects of TiN Top Electrode Texturing on Ferroelectricity in Hf1-xZrxO2. *ACS Applied Materials & Interfaces* **13,** 11089–11095. doi:10.1021/acsami.1c01734 (2021).

137. Han, R., Hong, P., Zhang, B., Bai, M., Hou, J., Yang, J., Xiong, W., Yang, S., Gao, J., Lu, Y., Liu, F., Luo, F. & Huo, Z. Understanding the stress effect of TiN top electrode on ferroelectricity in $Hf_0.5Zr_0.5O_2$ thin films. *Journal of Applied Physics* **134,** 194104. doi:10.1063/5.0176345 (2023).

138. Zhang, L., Yang, H., Pang, X., Gao, K. & Volinsky, A. A. Microstructure, residual stress, and fracture of sputtered TiN films. *Surface and Coatings Technology* **224,** 120–125. doi:https://doi.org/10.1016/j.surfcoat.2013.03.009 (2013).

139. Xi, Y., Gao, K., Pang, X., Yang, H., Xiong, X., Li, H. & Volinsky, A. A. Film thickness effect on texture and residual stress sign transition in sputtered TiN thin films. *Ceramics International* **43,** 11992–11997. doi:https://doi.org/10.1016/j.ceramint.2017.06.050 (2017).

140. Cao, Y., Tang, X., Allen, A. M. & Gung, T.-J. US9499901B2 (United States) (2016).

141. Raaif, M. Investigating the structure and tribo-mechanical performance of PVD TiN on bearing TiN substrate constructed by rf plasma. *Materials Chemistry and Physics* **224,** 117–123. doi:10.1016/j.matchemphys.2018.12.004 (2019).

142. Larsson, M., Bromark, M., Hedenqvist, P. & Hogmark, S. Deposition and mechanical properties of multilayered PVD Ti-TiN coatings. *Surface and Coatings Technology* **76–77,** 202–205. doi:10.1016/0257-8972(95)02589-8 (1995).

143. Park, M. H., Kim, H. J., Kim, Y. J., Lee, Y. H., Moon, T., Kim, K. D., Hyun, S. D., Fengler, F., Schroeder, U. & Hwang, C. S. Effect of Zr Content on the Wake-Up Effect in $Hf_1 - xZr_xO_2$ Films. *ACS Applied Materials & Interfaces* **8,** 15466–15475. doi:10.1021/acsami.6b03586 (2016).

144. Choudhury, D., Mandia, D. J., Langeslay, R. R., Yanguas-Gil, A., Letourneau, S., Sattelberger, A. P., Balasubramanium, M., Mane, A. U., Delferro, M. & Elam, J. W. Atomic layer deposition of HfO_2 films using carbon-free tetrakis(tetrahydroborato)hafnium and water. *Journal of Vacuum Science & Technology A* **38,** 042407. doi:10.1116/6.0000053 (2020).

145. Callister, W. D. & Rethwisch, D. G. *Materials Science and Engineering: An Introduction* 10th (John Wiley & Sons, Hoboken, NJ, 2018).

146. Kim, H.-G., Hong, D.-H., Yoo, J.-H. & Lee, H.-C. Effect of Process Temperature on Density and Electrical Characteristics of Hf(0.5)Zr(0.5)O(2) Thin Films Prepared by Plasma-Enhanced Atomic Layer Deposition. *Nanomaterials (Basel)* **12,** 2134–2141. doi:10.3390/nano12032134 (2022).

147. Min, S.-Y., Toprasertpong, K., Nako, E., Nakane, R., Takenaka, M. & Takagi, S. *Reservoir computing using nonlinear polarization and charge dynamics of anti-ferroelectric HZO/Si FETs 2024 IEEE Silicon Nanoelectronics Workshop (SNW)* (2024), 37–38. doi:https://doi.org/10.1109/SNW63608.2024.10639235.

148. Chavan, A., Rajagopal, A., Yan, Y., Asano, I., Ettisserry, D., Antonov, V., Servalli, G., Calderoni, A. & Ramaswamy, N. *Materials Engineering for High Performance Ferroelectric Memory 2024 IEEE International Memory Workshop (IMW)* (2024), 1–4. doi:10.1109/IMW59701.2024.10536948.

149. Song, T., Estandía, S., Tan, H., Dix, N., Gàzquez, J., Fina, I. & Sánchez, F. Positive Effect of Parasitic Monoclinic Phase of Hf0.5Zr0.5O2 on Ferroelectric Endurance. *Advanced Electronic Materials* **8,** 2100420. doi:https://doi.org/10.1002/aelm.202100420 (2022).

150. Ye, P. *Fundamental Properties of Ferroelectric and Anti-Ferroelectric Hafnium Zirconium Oxides: Scaling Limit, Switching Speed and Polarization Density 2020 International Symposium on VLSI Technology, Systems and Applications (VLSI-TSA)* (2020), 145–145. doi:10.1109/VLSI-TSA48913.2020.9203666.

151. Wang, C.-I., Chen, H.-Y., Wang, C.-Y., Chang, T.-J., Jiang, Y.-S., Chang, C.-S. & Chen, M.-J. Evolution of pronounced ferroelectricity in Hf0.5Zr0.5O2 thin films scaled down to 3 nm. *J. Mater. Chem. C* **9,** 12759–12767. doi:10.1039/D1TC01778K (37 2021).

152. Zacharias, M. & Streitenberger, P. Crystallization of amorphous superlattices in the limit of ultrathin films with oxide interfaces. *Phys. Rev. B* **62,** 8391–8396. doi:10.1103/PhysRevB.62.8391 (2000).

153. Zhou, X., Lu, Z. & Jing, X. Pinning growth of TiN films toward porous Ti matrix. *Journal of Materials Science* **57,** 18949–18968. doi:10.1007/s10853-022-07798-1 (2022).

154. Pirrotta, O., Larcher, L., Lanza, M., Padovani, A., Porti, M., Nafría, M. & Bersuker, G. Leakage current through the poly-crystalline HfO2: Trap densities at grains and grain boundaries. *Journal of Applied Physics* **114,** 134503. doi:10.1063/1.4823854 (2013).

155. Kobayashi, M., Wu, J., Sawabe, Y., Saraya, T. & Hiramoto, T. Mesoscopic-scale grain formation in HfO_2-based ferroelectric thin films and its impact on electrical characteristics. *Nano Convergence* **9,** 50. doi:10.1186/s40580-022-00342-6 (2022).

156. Kashir, A., Kim, H., Oh, S. & Hwang, H. Large Remnant Polarization in a Wake-Up Free Hf0.5Zr0.5O2 Ferroelectric Film through Bulk and Interface Engineering. *ACS Applied Electronic Materials* **3,** 629–638. doi:10.1021/acsaelm.0c00671 (2021).

157. Lyu, X., Si, M., Sun, X., Capano, M. A., Wang, H. & Ye, P. D. *Ferroelectric and Anti-Ferroelectric Hafnium Zirconium Oxide: Scaling Limit, Switching Speed and Record High Polarization Density Symposium on VLSI Technology and Circuits* (2019).

158. Qi, Y., Xu, X., Krylov, I. & Eizenberg, M. Ferroelectricity of as-deposited HZO fabricated by plasma-enhanced atomic layer deposition at 300 °C by inserting TiO_2 interlayers. *Applied Physics Letters* **118,** 032906. doi:10.1063/5.0037887 (2021).

159. Aich, A., Senapati, A., Lou, Z.-F., Chen, Y.-P., Huang, S.-Y., Maikap, S., Lee, M.-H. & Liu, C. W. Low Voltage High Polarization by Optimizing Scavenged WN_x Interfacial Capping Layer at the $Ru/Hf_xZr_{1-x}O_2$ Interface and Evidence of Fatigue Mechanism. *Advanced Materials Interfaces* **11,** 2400185. doi:10.1002/admi.202400185 (2024).

160. Wang, C.-I., Wang, C.-Y., Chang, T.-J., Jiang, Y.-S., Shyue, J.-J., Lin, H.-C. & Chen, M.-J. Atomic layer deposited TiN capping layer for sub-10 nm ferroelectric $Hf_{0.5}Zr_{0.5}O_2$ with large remnant polarization and low thermal budget. *Applied Surface Science* **570,** 151152. doi:10.1016/j.apsusc.2021.151152 (2021).

161. Niinistö, J., Putkonen, M., Niinistö, L., Kukli, K., Ritala, M. & Leskelä, M. Structural and dielectric properties of thin ZrO_2 films on silicon grown by atomic layer deposition from cyclopentadienyl precursor. *Journal of Applied Physics* **95,** 84–91. doi:10.1063/1.1630696 (2004).

162. Yang, X., Zhou, T., Hua, E., Wang, Z., Liu, Z., Wang, H. & Liu, Q. Composition-dependent structure and bandgaps in HfxZr1-xO2 thin films. *Applied Physics Letters* **124,** 122902. doi:10.1063/5.0197282 (2024).

163. Huang, J., Mao, G.-Q., Xue, K.-H., Yang, S., Ye, F., Sun, H. & Miao, X. Impact of Zr substitution on the electronic structure of ferroelectric hafnia. *Journal of Applied Physics* **133,** 184101. doi:10.1063/5.0146092 (2023).

164. Bai, N., Xue, K.-H., Huang, J., Yuan, J.-H., Wang, W., Mao, G.-Q., Zou, L., Yang, S., Lu, H., Sun, H. & Miao, X. Designing Wake-Up Free Ferroelectric Capacitors Based on the HfO2/ZrO2 Superlattice Structure. *Advanced Electronic Materials* **9,** 2200737. doi:https://doi.org/10.1002/aelm.202200737 (2023).

165. Xue, K.-H. & Miao, X.-S. Oxygen vacancy chain and conductive filament formation in hafnia. *Journal of Applied Physics* **123,** 161505. doi:10.1063/1.4989621 (2017).

166. Haggerty, R. P., Sarin, P., Apostolov, Z. D., Driemeyer, P. E. & Kriven, W. M. Thermal Expansion of HfO2 and ZrO2. *Journal of the American Ceramic Society* **97,** 2213–2222. doi:https://doi.org/10.1111/jace.12975 (2014).

167. Onaya, T., Nabatame, T., Sawamoto, N., Ohi, A., Ikeda, N., Chikyow, T. & Ogura, A. Improvement in ferroelectricity of $Hf_xZr_{1-x}O_2$ thin films using ZrO_2 seed layer. *Applied Physics Express* **10,** 081501. doi:10.7567/APEX.10.081501 (2017).

168. Chen, H., Tang, L., Luo, H., Yuan, X. & Zhang, D. Modulation of Ferroelectricity in Atomic Layer Deposited HfO_2/ZrO_2 Multilayer Films. *Materials Letters* **313,** 131732. doi:10.1016/j.matlet.2022.131732 (2022).

169. Cui, B., Wang, X., Li, Y., Wu, M., Wu, Y., Liu, J., Li, X., Ren, P., Ye, S., Ji, Z., Lu, H., Wang, R., Zhang, D. W. & Huang, R. Back-End-of-Line Compatible HfO_2/ZrO_2 Superlattice Ferroelectric Capacitor With High Endurance and Remnant Polarization. *IEEE Electron Device Letters* **44,** 1011–1014. doi:10.1109/LED.2023.3265516 (2023).

170. Peng, Y., Xiao, W., Liu, Y., Jin, C., Deng, X., Zhang, Y., Liu, F., Zheng, Y., Cheng, Y., Chen, B., Yu, X., Hao, Y. & Han, G. HfO2-ZrO2 Superlattice Ferroelectric Capacitor With Improved Endurance Performance and Higher Fatigue Recovery Capability. *IEEE Electron Device Letters* **43,** 216–219. doi:10.1109/LED.2021.3135961 (2022).

171. Wang, Q., Zhang, Y., Yang, P., Cao, R., Liu, H., Xu, H., Liu, S. & Li, Q. Improved Symmetry of Ferroelectric Switching in HZO Based MFM Capacitors Enabled by High Pressure Annealing. *IEEE Journal of the Electron Devices Society* **10,** 1009–1014. doi:10.1109/JEDS.2022.3221727 (2022).

172. Yu, S., Zhang, Y., Yang, P., Luo, X., Sun, Z., Liu, H. & Liu, S. Inhibiting the Imprint Effect of the TiN/HZO/TiN Ferroelectric Capacitor by Introducing a Protective HfO_2 Layer. *AIP Advances* **14,** 085012. doi:10.1063/5.0222725 (2024).

173. Kang, M., Peng, Y., Xiao, W., Zhang, Y., Wang, Z., Du, P., Jiang, H., Liu, F., Liu, Y., Hao, Y. & Han, G. HfO_2-ZrO_2 Ferroelectric Capacitors with Superlattice Structure: Improving Fatigue Stability, Fatigue Recovery, and Switching Speed. *ACS Applied Materials & Interfaces* **16,** 2954–2963. doi:10.1021/acsami.3c15732 (2024).

174. Liao, C.-Y., Lou, Z.-F., Lin, C.-Y., Senapati, A., Karmakar, R., Hsiang, K.-Y., Li, Z.-X., Ray, W.-C., Lee, J.-Y., Chen, P.-H., Chang, F.-S., Tseng, H.-H., Wang, C.-C., Tsai, J.-H., Tang, Y.-T., Chang, S. T., Liu, C. W., Maikap, S. & Lee, M. H. *Superlattice HfO 2 -ZrO 2 based Ferro-Stack HfZrO 2 FeFETs: Homogeneous-Domain Merits Ultra-Low Error, Low Programming Voltage 4 V and Robust Endurance 10 9 cycles for Multibit NVM 2022 International Electron Devices Meeting (IEDM)* (IEEE, San Francisco, CA, USA, 2022), 36.6.1–36.6.4.

175. Woollam, J. A., Johs, B. D., Herzinger, C. M., Hilfiker, J. N., Synowicki, R. A. & Bungay, C. L. *Overview of variable-angle spectroscopic ellipsometry (VASE): I. Basic theory and typical applications Optical Metrology: A Critical Review* **10294** (July 1999), 1029402. doi:10.1117/12.351660.

176. *Ellipsometry in the Measurement of Surfaces and Thin Films Natl. Bur. Std. Misc. Publ.* **256** (U.S. Government Printing Office, 1964).

177. Company, J. W. *What is Ellipsometry?* https://www.jawoollam.com/resources/ellipsometry-tutorial/what-is-ellipsometry.

178. Jiang, P., Luo, Q., Xu, X., Gong, T., Yuan, P., Wang, Y., Gao, Z., Wei, W., Tai, L. & Lv, H. Wake-Up Effect in HfO_2-Based Ferroelectric Films. *Advanced Electronic Materials* **7,** 2000728. doi:10.1002/aelm.202000728 (2021).

179. Kim, H. J., Park, M. H., Kim, Y. J., Lee, Y. H., Moon, T., Kim, K. D., Hyun, S. D. & Hwang, C. S. A Study on the Wake-Up Effect of Ferroelectric $Hf_{0.5}Zr_{0.5}O_2$ Films by Pulse-Switching Measurement. *Nanoscale* **8,** 1383–1389. doi:10.1039/C5NR05339K (3 2016).

180. Schenk, T., Schroeder, U., Pešić, M., Popovici, M., Pershin, Y. V. & Mikolajick, T. Electric Field Cycling Behavior of Ferroelectric Hafnium Oxide. *ACS Applied Materials & Interfaces* **6,** 19744–19751. doi:10.1021/am504837r (2014).

181. Pešić, M., Fengler, F. P. G., Larcher, L., Padovani, A., Schenk, T., Grimley, E. D., Sang, X., LeBeau, J. M., Slesazeck, S., Schroeder, U. & Mikolajick, T. Physical Mechanisms behind the Field-Cycling Behavior of HfO_2-Based Ferroelectric Capacitors. *Advanced Functional Materials* **26,** 4601–4612. doi:10.1002/adfm.201600590 (2016).

182. McBriarty, M. E., Narasimhan, V. K., Weeks, S. L., Pal, A., Fang, H., Petach, T. A., Mehta, A., Davis, R. C., Barabash, S. V. & Littau, K. A. Crystal Phase Distribution and Ferroelectricity in Ultrathin HfO_2–ZrO_2 Bilayers. *physica status solidi (b)* **257,** 1900285. doi:10.1002/pssb.201900285 (2020).

183. Newville, M. *Fundamentals of XAFS* Consortium for Advanced Radiation Sources, University of Chicago. Version Revision 1.6. 2004.

184. Pascarelli, S. *Fundamentals of X-ray Absorption Fine Structure* Undergraduate Summer School Lecture, European Synchrotron Radiation Facility. Grenoble, France, 2016.